Universität Rostock

Traditio et Innovatio

Experimental methods for measurement and analysis of quantum fluctuations and correlations in bright comb-like pulses

Dissertation

zur Erlangung des akademischen Grades

doctor rerum naturalium (Dr. rer. nat.)

der Mathematisch-Naturwissenschaftlichen Fakultät

der Universität Rostock

vorgelegt von:

Kai Barnscheidt

INSTITUT FÜR PHYSIK

Rostock, August 2022

https://doi.org/10.18453/rosdok_id00004170

Gutachter:

Prof. Dr. Boris Hage

Institut für Physik,
Universität Rostock

Prof. Dr. Michael Kues

Hannoversches Zentrum für Optische Technologien,
Leibniz Universität Hannover

Einreichung: 11.08.2022
Verteidigung: 13.01.2023

Abstract

Previously, a quantum state reconstruction of a fs pulse, squeezed in a fibre by the Kerr effect, was not feasible due to the strong carrier pulse. This measurement is enabled here by the separation of both classical and quantum fluctuations from the carrier pulse. Based on the comb structure of fs pulses, emitted by mode-locked lasers, an adequate optical resonator is used for this spectral separation. Thereby the separated fluctuations can be analysed in a balanced homodyne detection (BHD) setup by a local oscillator (LO) pulse. Furthermore, the introduced setup allows to shape the LO pulse and thereby facilitates the characterisation of correlations between different parts of the pulse.

The separation resonator was experimentally characterised as its properties influences the observed interference patterns. Furthermore, for the evaluation of the BHD data, an approach was used that enabled necessary corrections as well as the simultaneous evaluation of the vacuum reference.

One mayor limiting factor for the observed squeezing was the phase noise from Brillouin scattering on thermally excited vibrational modes of the fibre. This was verified by observation a reduction in phase noise after submerging the fibre in liquid nitrogen.

Zusammenfassung

Bisher war eine Quantenzustandsrekonstruktion von in Glasfasern Kerr-gequetschten fs-Pulsen aufgrund des starken Trägerpulses nicht praktikabel. Eine solche Messung wird hier ermöglicht, indem sowohl klassische als auch quantische Fluktuationen von dem Trägerpuls getrennt werden. Dies geschieht unter Ausnutzung der Frequenzkammstrukur des von einem modengekoppelten Lasern erzeugten fs-Puls und einem abgestimmten optischen Resonator zur spektralen Trennung. Die getrennten Fluktuationen können dann in einer balancierten homodynen Detektion (BHD) mit einem weiteren Puls als Lokaloszillator (LO) vermessen werden. Zusätzlich kann der realisierte Messaufbau den LO-Puls formen und vereinfacht die Charakterisierung von Korrelationen zwischen verschiedenen Teilen des Pulses.

Der zur Trennung benutzte Resonator wurde experimentell charakterisiert, da seine Eigenschaften die aufgenommenen Interferogramme beeinflussen. Zur Auswertung der BHD-Daten wurde ein Ansatz benutzt, welcher von gängigen Methoden abweicht und sowohl benötigte Korrekturen als auch die zeitgleiche Aufnahme einer Vakuumreferenz ermöglicht.

Phasenrauschen durch Brillouin-Streuung an thermisch angeregten Vibrationsmoden der Glasfaser wurde als ein hauptsächlich limitierender Faktor für den gemessenen Quetschgrad ausgemacht. Dies wurde durch die Beobachtung der Abnahme von Phasenrauschen unter der Kühlung der Glasfaser mit flüssigem Stickstoff beobachtet.

Contents

Acronyms

AR	anti-reflective 132, 148
BHD	balanced homodyne detection . . . . . iii, 2 f., 7, 28, 32, 38 f., 42 f., 45 f., 48, 50–56, 58 ff., 62, 66 f., 70 f., 74 f., 77, 80–83, 85 f., 90 f., 96 f., 128, 131 f., 165, 167
BS	beamsplitter 2, 9, 26, 32, 39 f., 50 ff., 55, 58, 81, 85, 91–94, 96
CDC	climate data center 17
CEO	carrier-envelope offset 2, 12 ff., 16, 26–30, 33–38, 42 ff., 60, 78, 99, 147 ff.
CEP	carrier-envelope phase . . . . . 29 ff., 34 f.
CO_2	carbon dioxide . . . . . 36, 147 f.
CW	continuous-wave 3, 12, 15 f., 26 ff., 31, 33, 36, 38, 48, 54, 65 f., 85, 91, 96, 126, 131, 151 ff., 163 f.
EOM	electro-optic modulator . . . . . 6, 9, 26 ff., 58, 72, 160, 163
FM	flip mirror 8, 55
FROG	frequency-resolved optical gating 34
FSR	free spectral range 7, 24–27, 33
FWHM	full width at half maximum 10, 16, 24, 31, 33
GAWBS	guided acoustic-wave Brillouin scattering 3, 8, 53, 62 f., 65–75, 78 f., 83, 86–91, 94, 97 f., 153, 156, 176, 181 f., 187
GDD	group delay dispersion . . . . . 29, 36 f., 42, 84, 147, 149
GVD	group velocity dispersion 15, 29, 34, 37, 147
HCCM	homodyne cross-correlation measurement 3, 9, 91–96
HITRAN	high-resolution transmission molecular absorption . . 36, 147
HWP	half-wave plate 7, 82, 132
LN_2	liquid nitrogen . . . . iii, 3, 31, 65, 68–72, 74, 97 f., 179, 181
LO	local oscillator . . iii, 2 f., 7 ff., 43, 45, 51–60, 62, 66 f., 75 f., 78–86, 88, 90–93, 95, 97–100, 153, 155 f., 163 f., 176
LabVIEW	Laboratory Virtual Instrumentation Engineering Workbench 159 f., 165
MFD	mode field diameter (intensity drops to $1/e^2$) . . . . 20 ff., 66

1. Introduction

Physics in the twentieth century was driven by quantum mechanics and has revealed a quantum world beyond classical physics. Since the beginning of the century when Planck [1] and Einstein [2] discovered that electromagnetic waves come in discrete energy quanta (photons), the world of physics has changed due to subsequent discoveries.

Many of these discovered quantum effects are directly related to fundamental constants yielding very reproducible measurements. As a consequence, the SI base units were redefined to be derived from these fundamental constants in 2019 [3].

With the invention of the laser [4] in 1960, a bright new coherent source of light became available. Not only can it provide uttermost accuracy [5, 6], directly linked to the SI base units, but also immense intensity [7, 8]. These properties gave rise to countless, today commonly used applications material processing and for measurements. Low losses in light-guiding optical fibres combined with the available bandwidth provided by laser light builds the backbone of today's communication [9, 10].

Aside from its vast technical applications, the quantum properties of laser light are described by coherent states [11]. While coherent light and its properties, such as shot noise, can be explained by classical physics, it can be manipulated to show non-classical behaviour such as squeezing [12] using quantum mechanics. Elaborate present-day lasers and laser-based measurements are currently limited by quantum noise, and non-classical properties are required to overcome classical limits. The principle of a quantum-enhanced measurement is illustrated in chapter 2 based on an experimental setup to which a contribution was made during this thesis [13]. This experiment was the first quantum-enhanced measurement that was carried out at the damage threshold of a biological sample [13].

Furthermore, such non-classical states of light offer a manifold of opportunities to enhance existing instruments [14, 15], decouple interaction and detection [16], encrypt communication [17, 18] and operate quantum computers [19, 20].

The intensity-dependent nonlinear Kerr effect (a $\chi^{(3)}$ nonlinearity) in optical fibres creates squeezing and was among the first realised sources of squeezed light [21]. But as the overall number of photons is conserved by the Kerr effect [22], the resulting squeezing cannot by observed directly.

Using a Sagnac interferometer, the squeezing was revealed by the interference of two pulses [23] and by using an optimised splitting ratio and a fibre-based BS[1], a stable sources of amplitude-squeezed light can be built [24]. This light can then be transferred to arbitrary spatial modes [25] or used as a basis for other quantum optical experiments [26, 27]. Furthermore, the Kerr effect creates quantum correlations between different spectral components within the pulse and aside from interference, spectral filtering can be used to reveal Kerr squeezing [28, 29]. All prior experimental setups did verify some non-classical properties but by design they cannot perform a full tomography of the quantum state. By using two orthogonally polarised co-propagating pulses, polarisation squeezing was observed [30] and quantum polarisation tomography was carried out within such a setup [31].

A measurement scheme that gives access to arbitrary quadratures, such as BHD [32, 33], cannot be implemented straightforward due to limited available optical power and saturation of detectors [34] as for this scheme the LO has to be significantly more intense than the already bright non-classical pulse.

At the beginning of the experimental work for this thesis, there was the naïve idea of simply using an optical resonator to separate the quantum fluctuations of a Kerr-squeezed fs pulse from its coherent carrier and to implement a BHD to characterise the remaining quantum fluctuations by using the separated carrier as LO. This separation resonator and the corresponding idea is detailed in chapter 3. Utilising the equidistant frequency modes of mode-locked lasers [35], the experimental setup introduced and realised in this thesis can separate the coherent amplitude of the carrier pulse of the bright squeezed pulse. In reflection of the resonator, a squeezed state with significantly depleted carrier remains (chapter 4). While each experimental component behaved as expected, the experimental observations differed drastically from the initial expectations as no squeezing was measured.

From this starting point, fault diagnosis started and in an extensive analysis, the dispersive properties of the resonator as well as the relative mismatch in CEO[2] between resonator and laser were examined. Based upon these properties, slight deviations from the idealised behaviour were expected and indeed observed after conducting and evaluating targeted measurements. However, these properties did not explain the absence of quantum features, *i.e.* squeezing in the measured data.

Squeezing was first observed in the experimental setup only close to one optical power but once found, it was quite unaffected by both intentional disturbances and misalignment. A change in the used optical fibre and a reduction of the propagation distance led to the

[1] beamsplitter
[2] carrier-envelope offset

observation of squeezing for a wider range of optical powers but the observed squeezing was still far behind the expectations (chapter 5).

Essentially, the used pulses are too short to be significantly affected by thermally driven GAWBS[3] in optical fibres but, as other contemplated influences were either experimentally excluded or beyond the reach of available experimental characterisation, the fibre was submerged in LN_2. This provided a reduction in GAWBS and its effect in the measurement. In opposition to the expectation of GAWBS having no significant influence, the observed squeezing increased while simultaneously anti-squeezing decreased.

No individual pulse is significantly affected by GAWBS but an explanation for the introduction of GAWBS into the separation resonator–based BHD was found that matches the experimental observations (chapter 6).

As the limiting factor was found, an additional SLM[4] was implemented to shape the LO and to extent the measurement scheme. This allowed analysis of the quantum fluctuations in and between different temporal modes.

The experimental setup allows to analyse Kerr-squeezed fs pulses with almost arbitrary LO pulses (chapter 7) and thereby provides a versatile method hat can be extended, in principle, to other bright comb-based states in a single spatial mode.

Other experiments [36, 37] have already used pulsed light as well as a $\chi^{(2)}$ nonlinearity to create a squeezed vacuum, and implemented multi-mode measurements [38]. Their experimental setup required a SHG[5] generation and a complexly stabilised resonator around the used $\chi^{(2)}$ media. Compared to this, Kerr squeezing depends solely on the physical properties of the optical fibre and the parameters of the used pulse, which both usually do not require additional stabilisation. In the used setup presented presented within this thesis, the analysis requires a stabilised resonator but the creation of the non-classical light itself is a stable process.

Furthermore, the non-classicality of the used Kerr-squeezed fs pulses was verified by the fibre-based HCCM[6] implemented for the Kerr-squeezed pulses (chapter 8). This method to verify non-classicality was previously only applied once with a CW[7] laser [39].

Aside from this work in Rostock, a specialised detector for short and intense pulses was designed and provided for a quantum-enhanced experimental setup of the University of Queensland (Australia), which is briefly introduced in chapter 2. Using the supplied detector enabled the quantum-enhanced microscope to operate at the maximum optical

[3] guided acoustic-wave Brillouin scattering
[4] spatial light modulator
[5] second harmonic generation
[6] homodyne cross-correlation measurement
[7] continuous-wave

power a biological sample could handle and to resolve more detail than achievable with classical light.

All the experiments named above and their properties are based upon several different areas of both classical and quantum optics. A well structured and fundamental overview on these, prior to the experimental work, would far exceed the 100 page limit given for a PhD thesis. Hence, the structure of this thesis differs from the typical structure of a dissertation in experimental physics, *e.g.* a theory and background chapter prior to the experimental setup, measurements and their discussion. Instead, this thesis is structured in discrete chapters on the experimental setup and its theoretical properties. Additional background information is given within the corresponding chapter and each chapter builds on the previous one and the presented findings.

2. Quantum-enhanced nonlinear microscopy

By using squeezed light, the work published in [13] extended the limits of coherent Raman microscopy beyond the limits achievable by the use of classical light. Within this chapter, the operational principle of the used microscope is briefly introduced[1] prior to the principle of quantum enhancement via squeezed light. Compared to previous quantum-enhanced measurements [14, 41], this experimental setup operates at and above the damage threshold of the sample. The personal contribution, the photodetector, is discussed in appendix A. Within this appendix, a description and a subsequent solution are given for the rather general engineering problems and technical challenges occurring in the detection of sub-ps pulses with a repetition rate of 80 MHz at average optical powers in the mW regime. While those aspects are also relevant for the detection in the other experimental setups within this thesis, it has no relation to the actual physical processes.

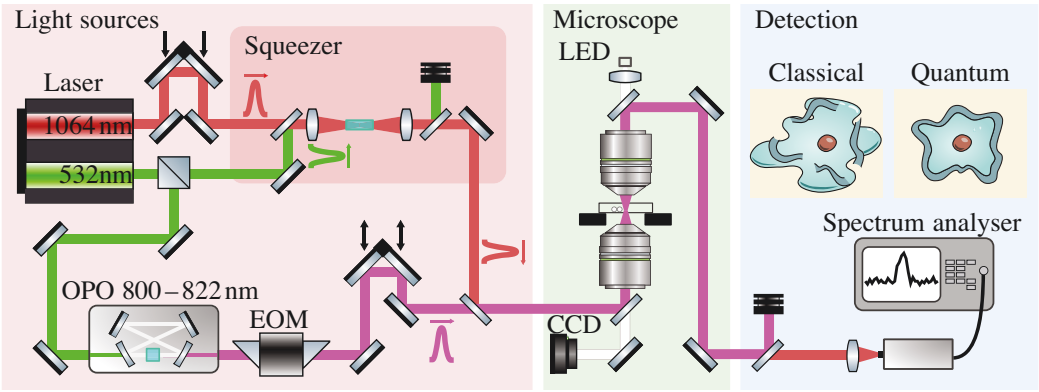

Figure 2.1 Quantum-enhanced coherent Raman microscope (Illustration as published in [13] with edited fonts.)

2.1 Coherent Raman spectroscopy

Raman spectroscopy is a linear spectroscopy technique that probes the vibrational and rotational spectra of molecules [42, 43]. Stokes scattering at the molecular transitions

[1] More and detailed information can be found in [40].

shifts the photon energy and molecular bonds can be identified from measured spectra [44].

For coherent Raman spectroscopy, a coherent pump and a detuned Stokes beam are used to probe transitions in molecular bonds. If the detuning matches a transition, it is resonantly enhanced [45]. Compared to the linear case, an additional photon from the Stokes beam is involved, making it a nonlinear process that improves more than linearly with optical intensity and hence, it is often used specifically with short intense pulses. In this experimental setup, stimulated Raman scattering, increasing quadratically with intensity [46], was used as illustrated in figure 2.1. Spatial resolution is achieved by scanning over the probe and in doing so, this technique can be used to map the concentration of specific molecular bonds in a complex biological sample.

2.2 Classical limit and quantum enhancement

In stimulated Raman scattering, a modulation, applied by the EOM[2] in figure 2.1, is transferred from the pump beam to the Stokes beam[3] and its detected intensity is directly proportional to the concentration of molecular bonds that match the chosen detuning within the illuminated area of the sample. For low concentrations, this signal vanishes in the background noise which limits the sensitivity of the microscope, and increased intensity or measurement time is required for meaningful imaging.

State-of-the-art Raman microscopes use classical light and are in practice already limited by the shot noise of the laser [47–49]. This limit is set by the Poissonian photon statistics and it can be overcome by using quantum mechanics to create light with sub-Poissonian photon statistics, so called squeezed light [50][4]. Using a squeezed Stokes beam, the SNR[5] was improved by 35 % which led to a 14 % increase in concentration sensitivity at the limit for photodamage.

The increased SNR and sensitivity allow for identical image quality at lower optical intensities or with shorter measurement times, both of which are important parameters for measurements on sensitive biological samples or fast processes.

[2] electro-optic modulator

[3] The change in intensity due to the scattered photons in the Stokes beam is minuscule and cannot be observed without the applied modulation.

[4] The used squeezer is shown and described in the supplemental of [13] or in [40]. Properties of squeezed light itself are discussed later in section 5.3.

[5] signal-to-noise ratio

3. Experimental idea and setup

As indicated in chapter 1, Kerr-squeezed pulses cannot be analysed in a BHD setup due to their inherent intensity. The required intensity for the LO in such a measurement scheme has to be provided by the laser system and it also has to be detected with a high efficiency. Tremendous technical efforts are neccessary to meet these requirements. To avoid these efforts, a sophisticated solution is proposed and implemented in this thesis to reduce the intensity of the Kerr-squeezed pulses without notably affecting its quantum properties. This chapter elucidates the underlying experimental principles.

3.1 Summary of the experimental scheme

The experimental procedure is shown in figure 3.1 and composed of the following steps:

- The laser emits a fs pulse with equally spaced modes.
- Optical power is adjusted by a combination of HWP[1] and PBS[2] and the pulse propagates through a PM[3] optical fibre undergoing a $\chi^{(3)}$ nonlinear process, the nonlinear Kerr effect (discussed in more detail in appendix F), and evolves into a non-classical state [21, 51] represented by b).
- The fibre output is mode-matched to the separation resonator which FSR[4] matches the comb emitted by the laser, shown in c), and thereby transmits a clean carrier pulse [52, 53] shown in e).
- Sidebands containing the information for quantum state tomography shown in f) are reflected and thereby separated from the transmitted carrier pulse by the resonator [54].
- Both reflected and transmitted beams are sent as SI[5] and LO into a BHD scheme.

[1] half-wave plate
[2] polarising beamsplitter
[3] polarisation-maintaining
[4] free spectral range
[5] signal

- Using an SLM, see figure 7.3, the LO can be shaped (this path is not shown here for simplification).

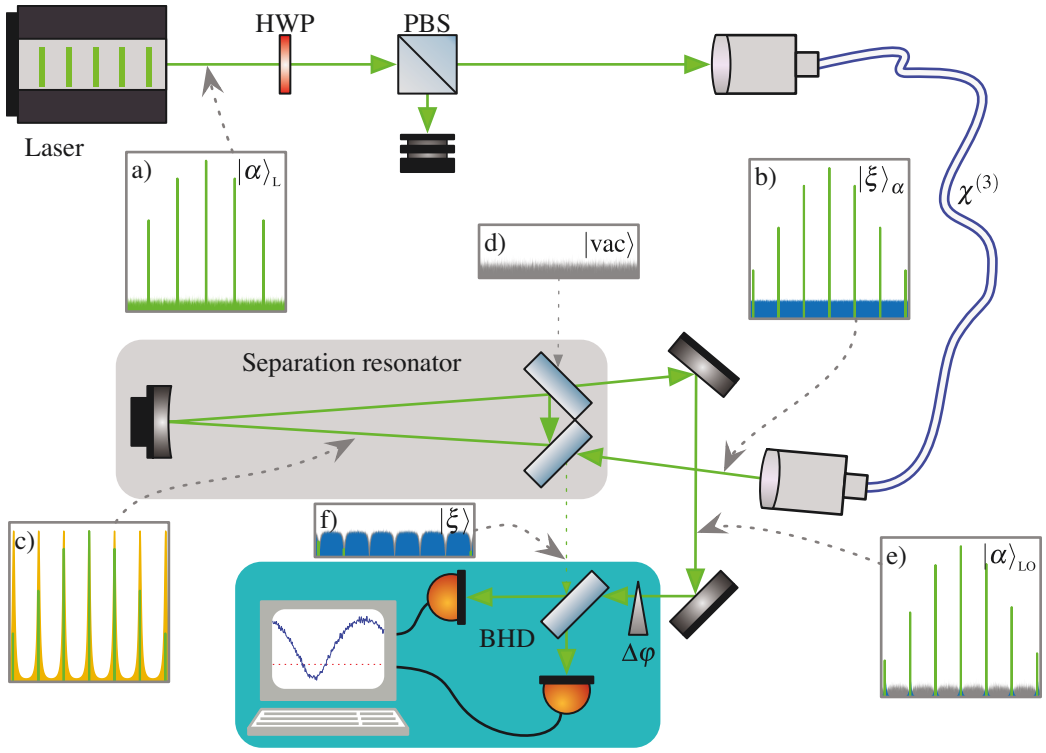

Figure 3.1 Schematic representation of the experimental idea
A coherent pulse *a*) propagates through a $\chi^{(3)}$ nonlinear media and evolves into a bright non-classical state *b*). A resonator *c*) transmits the coherent amplitudes of the pulse and separates it from its sidebands *e*). The reflected state is then sent into a BHD setup to be analysed.

The experimental idea was successfully demonstrated during this thesis in section 5.6. Measured squeezing was limited by thermally driven GAWBS (chapter 6) that can be overcome by appropriate cooling.

Furthermore, the temporal structure of the non-classical state can be accessed (chapter 7) and the transmitted pulse can be replaced by a shapeable LO to improve the measured squeezing (section 7.8) or observe correlations between spectral components (section 7.9). Using an FM[6], this shapeable LO can replace the LO transmitted by the separation resonator which is not shown in figure 3.1 due to its complexity.

As the separation and measurement is based solely upon the transversal and longitudinal modes of the separation resonator, it could be applied to any process where pulses from mode-locked lasers are involved and a separation from the coherent amplitude or even a recombination may be useful.

[6] flip mirror

3.2 Laser system and its distribution

As the parameters of the laser system are relatively fixed and many aspects of the experimental setup are related to them, they are given at this early stage of this thesis in table 3.1.

In figure 3.2, the distribution of pulsed light to the individual experimental sub-setups is described. Each sub-setup is shown in its respective chapter.

First, an adjustable portion of the available optical power is directed into the HCCM setup (chapter 8). In this setup, a fibre-based verification of a non-classicality criterion, based on correlation measurements in an unbalanced detection scheme [55, 56] with a strongly asymmetric BS and equally strong SI and LO [57, 39], is realised for Kerr-squeezed fs pulses[7].

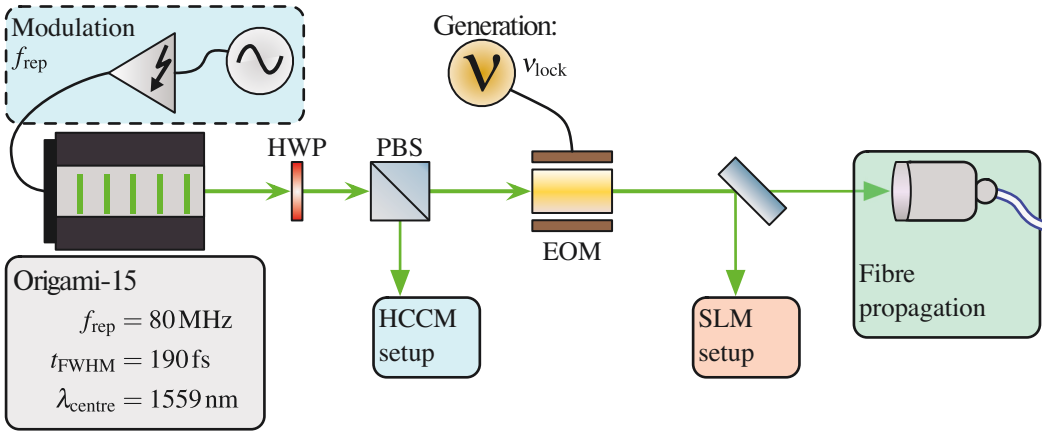

Figure 3.2 Laser distribution to the individual parts of the experimental setup
Laser power is split between the setup for HCCM and the setups for BHD measurements using a combination of HWP and PBS.
After an EOM generates the modulation for resonator stabilisation (section 4.3.2), the optical power is split in a fixed ratio between the SLM setup, used to shape the LO pulse, and the coupling into PM fibre for propagation prior to the resonator.

Subsequently, an EOM generates a phase modulation for stabilising the separation resonator (section 4.3.1) as well as the filter cavity in the SLM setup (section 7.4). The modulation frequency for the EOM is applied using waveform generator (*PXI-5404* [58]) integrated into the data acquisition setup (appendix G). All individual components use a PLL[8] with the same clock source which yields a known frequency and stable phase for the modulation in the recorded data. Using a BS with fixed splitting ratio, the light is split into the SLM setup, enabling the use of a shaped LO (chapter 7), and the propagation through an optical fibre, altering the quantum state and directing the light onto the separation resonator

[7] In the HCCM setup, both used paths differ by two pulse distances and therefore the pulse repetition rate is used to shift the phase between both arms in the HCCM setup.

[8] phase-locked loop

Basis performance:	f_{rep}	λ_c	λ_{FWHM}	τ_{FWHM}	TBWP
	80 MHz	1558.8 nm	13.1 nm	192 fs	0.31
Frequency tuning:	coarse (temperature)			fine (piezo)	
	3.585 kHz 80 steps of 44.8 Hz			180 Hz 0 V to 100 V	
Pump current:		Input	λ_c	λ_{FWHM}	$[\tau_{FWHM}]$
	min:	−5 V	1557.9 nm	10.8 nm	[236 fs]
	max:	1.5 V	1559.0 nm	13.4 nm	[191 fs]

Table 3.1 Specification of Origami 15 SN 3369
Tuning ranges were read from the specification sheet (appendix B). Pulse is assumed to be limited by the TBWP, as specified, for the calculated pulse durations (τ_{FWHM}).

(section 4.5 and figures 4.13 and 5.5). The SLM setup is shown in figure 7.3 and discussed in section 7.4.

Centre wavelength λ_c and the FWHM[9] of the pulse for the used laser system are consolidated in table 3.1 with the tuning range of the repetition rate. Factory characterisation states a bandwidth limited $sech^2$ pulse with minimal TBWP[10]. For further details, the provided specification sheet of the laser is given in appendix B.

The following chapter focusses on the core of the experimental setup and describes the separation resonator in detail and relates it to the properties of the laser.

[9] full width at half maximum
[10] time-bandwidth product

4. Laser and separation resonator

At the core of the experimental setup (figure 3.1), a spectral separation resonator is used to separate the coherent amplitude of the carrier pulse from the classical and quantum fluctuations. The used separation resonator is described and characterised in this chapter.

First, the comb-like spectral structure of mode-locked lasers and frequency combs is explained as the separation is based upon it. The required and claimed stability of the used laser[1] on short timescales (sub-ms regime) cannot be resolved directly by the measurement instruments available in the laboratory. The manufacturer only points out the stability compared to fibre-based fs laser systems [59] and states a low timing jitter ($< 70\,\mathrm{as}$) for individual systems [60] but does not provide a detailed specification for the individual system due to the complex characterisation. In the laboratory, it is only possible to compare it relative to the separation resonator, discussed later. Nevertheless, research published prior to the commercial production can provide some information. To compare the obtained resonator measurements to available information, the properties of frequency combs and related measurements are examined.

In this chapter, the frequency comb properties of the laser, the fundamental properties of resonators and their spatial modes are presented and related to the modes of an optical fibre before active stabilisation schemes are discussed. These are the fundamental principles on which the separation resonator and thereby the intended experimental setup rely.

After detailing these principles, the effects of dispersion are reviewed in context with their characterisation of the used resonator. This is required for the interpretation and evaluation of measurements in the following chapters. A comparable application of optical resonators are enhancement cavities which are used in the regime of short intense pulses. Methods for their precise characterisation have emerged in recent years [61, 62]. Stabilisation dependencies and possible improvements are discussed at the end of this chapter.

[1] The Origami 15 from NKT Photonics is a solid state laser with SESAM-based soliton mode locking.

4.1 Frequency comb-like lasers and stability

This section treats fundamental properties of mode-locked lasers as well as their frequency comb properties [63, 64]. Dispersive effects are discussed later in relation to the experimental setup in section 4.4. Detailed information on short pulses and further applications can be found in specific textbooks such as [65].

4.1.1 Mode-locked lasers

Mode-locked lasers generally emit short pulses with pulse durations in the ps and fs regime. As their name suggests, these are created by combing (locking) multiple longitudinal modes of the laser to create a short and intensive pulse as shown in figure 4.1. Active or passive mode-locking techniques can be used to increase the overall gain for the pulsed operation compared to the CW operation of the laser. Passive techniques such as the SESAM[2] or Kerr-lens mode locking can provide stable and short pulses as they interact almost immediately with the pulse.

A stable pulse pattern is only formed if all modes are equally spaced by the repetition rate f_{rep} of the laser. This leads to a comb in the spectrum as show in figure 4.2. The pulse shape depends on several parameters such as available bandwidth of the gain media, dispersion, and losses inside the resonator. An effective way to describe one pulse of such a laser is the slowly-varying envelope approximation using a carrier frequency[3] ω_{c} and a complex envelope $a(t)$. Table 4.1 lists important properties of Gaussian and sech^2 shaped pulses in time and frequency domain. As discussed later, the experimental setup relies on the equally spaced frequencies of the repetitive pulse pattern and hence mostly the frequency domain[4] (ω, ν, f) is chosen. Depending on the context, the wavelength λ or the wavenumber k may also be used for illustrative purposes or by convention.

The sech^2 pulse is an important pulse shape as it describes the fundamental soliton in optical fibres [66, 67] as well as the emitted pulse shape of the used laser [68–70].

4.1.2 Frequency combs

Aside from the equidistant modes, another important property of a mode-locked laser is the offset frequency, the closest frequency of the extension of comb structure, centred around hundredths of THz, to 0 Hz as shown in figure 4.2. This frequency is called carrier-envelope offset (f_{CEO}) as it describes the frequency offset at which the carrier passes the

[2] semiconductor saturable absorber mirror

[3] Note that the angular frequency ω is used instead of the actual optical frequency for consistency with literature.

[4] Depending on the context either the angular frequency ω, the optical frequency ν or f for frequencies accessible in the RF regime is used.

Shape:	$\lvert a(t)\rvert$	$\lvert A(\omega)\rvert^2$	Δt	$\Delta t \cdot \Delta \nu$
Gaussian:	$\exp\left(-\left(\frac{t}{t_\mathrm{p}}\right)^2\right)$	$\exp\left(-\frac{(\omega-\omega_\mathrm{c})^2 t_\mathrm{p}^2}{2}\right)$	$1.177 \cdot t_\mathrm{p}$ $\sqrt{2\ln 2} \cdot t_\mathrm{p}$	0.441 $2 \cdot \ln(2)/\pi$
sech^2:	$\mathrm{sech}\left(\frac{t}{t_\mathrm{p}}\right)$	$\mathrm{sech}^2\left(\frac{\pi t_\mathrm{p}(\omega-\omega_\mathrm{c})}{2}\right)$	$1.763 \cdot t_\mathrm{p}$ $2\,\mathrm{acosh}\left(\sqrt{2}\right) \cdot t_\mathrm{p}$	0.315 $\left(\frac{2\ln(1+\sqrt{2})}{\pi}\right)^2$

Table 4.1 Ideal temporal ($\lvert a(t)\rvert$) and spectral $\lvert A(\omega)\rvert^2$ shapes for Gaussian and sech^2 pulses with their temporal FWHM (Δt) and their corresponding TBWP
Pulse envelope is simplified by using t_p instead of Δt. The commonly found numerical values as well as their analytical expression are stated. Additional shapes and details can be found for example in [65].

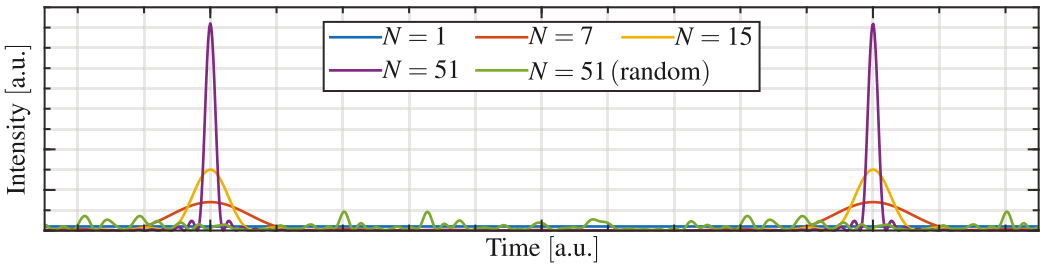

Figure 4.1 Visualisation of pulses created by equally spaced modes
If multiple modes interfere constructively at one point, a repeating pulse is formed. An increased number of modes leads to a shorter pulse and reduced intensity between the pulses. A random phase leads to a fluctuating intensity. All shown patterns have the same integrated intensity split equally between all used modes.

envelope for two consecutive pulses at the same position. With f_CEO and f_rep, all optical frequencies (ν_j) in the comb can be expressed using a corresponding integer number j:

$$\nu_j = f_\mathrm{CEO} + j \cdot f_\mathrm{rep} \tag{4.1}$$

Assuming a mode-locked laser has a repetition rate of 80 MHz and a CEO of 40 MHz, the phase of the carrier would be shifted by π between consecutive pulses and only every second pulse would be exactly equal (figure 4.2). The duration of an optical cycle[5] is short compared to the pulse duration and most applications aside from high harmonic generation [71] are not significantly affected by the CEO.

While the frequencies of the modes are not connected to the actual pulse shape, they are each solely defined by two frequencies and an integer, and can be linked directly to a frequency reference. They can provide precise absolute measurements if both frequencies are known. In astronomy [72], they allow precise measurements of frequency shifts across

[5] For 1560 nm, it is ≈ 5.2 fs and the pulse duration in the experiment is close to 200 fs.

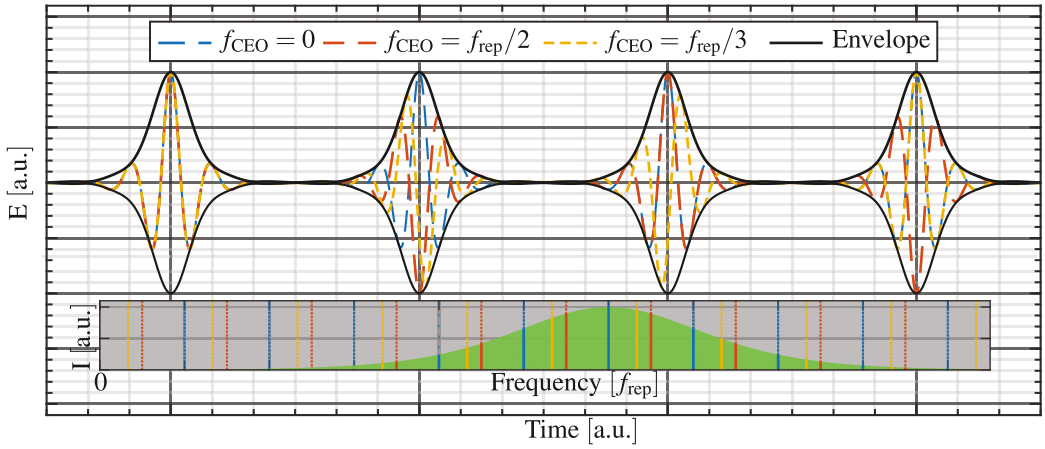

Figure 4.2 Pulse pattern for identical repetition rates with different CEO
Depending on the CEO, the phase between carrier and envelope is shifted from pulse to pulse. Frequencies and spectral structure are indicated in the grey area. (Pulse shape and repetition rate are chosen for illustrative purposes and do not represent experimental parameters.)

the optical spectrum. Furthermore, comb-based distance measurements [5, 73] were used to obtain for example a three-dimensional surface profile of a shoe sole from a distance of more than 10 m with µm absolute accuracy under normal atmosphere [74]. In spectroscopy, the use of two frequency combs allows simultaneous measurements of amplitude and phase with kHz resolution [75].

While f_{rep} can be measured directly, the f_{CEO} cannot be measured as easily. If the spectrum of the laser is either broad enough or broadened accordingly, the beat frequency between the 2nd harmonic of mode j and the mode $2j$ can be obtained in a $f-2f$ measurement [76].

$$2\cdot(f_{CEO}+j\cdot f_{rep})-(f_{CEO}+2j\cdot f_{rep})=f_{CEO} \tag{4.2}$$

In the laboratory, we cannot measure the CEO and the measured repetition rate itself does not yield useful information about the optical frequencies as the central optical frequency near 192 THz is the 2.4 millionth harmonic of the repetition rate of 80 MHz. It only provides information about long-term drifts as shown in section 4.1.5.

As the stability of the laser cannot be directly measured in the laboratory, the next sections will discuss the operational principle of the laser and published measurements on comparable laser systems to obtain an educated expectation for its influences.

4.1.3 SESAM mode locking

The Origami laser uses a SESAM to obtain passive soliton mode locking[6] [78]. A SESAM introduces higher losses for the CW operation compared to the pulsed operation. While fast mode-locking schemes like Kerr-lens mode locking or fast SESAM can provide fs pulses, they do not provide stable soliton pulses. The formation of a soliton pulse requires an additional loss mechanism [79].

By using a slowly saturable SESAM, the response of the SESAM leads to SPM[7] [80] which in balance with the GVD[8] inside the resonator forms a stable soliton pulse. This is ideal for the experiment as the soliton pulse is also a solution for optical fibres [66, 67]. Additionally, the soliton mode locking is a self-starting process which further reduces the complexity of the laser. As the manufacturer does not provide complete information on the laser resonator or its components, its properties can only be estimated from related research papers [81, 82]. For the resonator length, folding mirrors with engineered dispersion properties are used. The beam is focussed into an approximately 2 mm thin Eb:Yb:glass gain media, pumped by a low-noise fibre-coupled CW pump laser. The transmission of the output coupling mirror is likely below 2 % and as all other components do not introduce high losses, the overall finesse of the laser resonator is likely above 200.

Aside from the 2 mm gain media, the resonator is filled with air. Due to likely solid mounts for the optical components, temperature stabilisation and low-noise pump, the laser can in theory be extremely stable. In practice the measured stability is limited by external influences for low frequencies. Due to the low linewidth of the resonator, higher frequencies above 100 kHz are likely limited by quantum noise as the quotation of the manufacturer (appendix C) states. Additionally, the output coupler may be integrated into the SESAM [83], leading to a further reduction in required optical components. Commercially sold laser systems may be cost optimised which could impede the stability as only the stated specifications have to be achieved.

Within the next sections, the stability of the laser in the used experimental setup is discussed and measured to the extend of the experimental capabilities in the laboratory.

4.1.4 Short-term stability

To be able to use an optical resonator in the experimental setup, multiple consecutive pulses of the laser need to interfere with each other. In comparison with the resonator linewidth, the linewidths of the modes contributing the comb-like laser have to be low. For both CW and pulsed lasers, the Schawlow-Townes limit [84] gives an approximate limit

[6] For a comprehensive overview of soliton mode locking see [77].
[7] self-phase modulation
[8] group velocity dispersion

for the linewidth a laser can obtain. The more accurate form for equation (4.3) is derived in [85] and spontaneous emission is considered in [86] but due to limited information on the gain media this cannot be evaluated here.

$$\Delta\nu_{\mathrm{FWHM}} = \frac{\pi \cdot h \cdot \nu}{P_{\mathrm{out}}} (\Delta\nu_{\mathrm{res}})^2 \tag{4.3}$$

Using equation (4.3) and parameters of the used laser[9], this limit is below 1 µHz[10]. In practice the laser linewidth is broadened at least by fluctuations in pump current and resonator length. A beat measurement between the used pulsed laser and a CW laser of ≈ 5 kHz linewidth did not reveal a significant difference in linewidth between the CW laser and the closest mode of the laser. The laboratory is not equipped to verify the specifications provided by the manufacturer. Using a 1.5 GHz spectrum analyser with 100 Hz RBW[11], the Gordon-Haus jitter [89, 90] was not resolved as the measurement was limited by the RBW. Further measurements were not performed as the measured linewidth of 3.6 kHz for the CEO frequency on a similar laser [91] indicates that a significantly higher resolution would be required. To truly verify the manufacturers claims, more complex measurements such as a balanced optical correlation measurement [92] or comparable schemes like [59] are required. Based on the claims of the manufacturer, the pulsed laser is by far the most stable reference on short timescales available in the laboratory at this time.

4.1.5 Environmental influences on long-term stability

In the experimental setup, stability is required on two different timescales as in the separation resonator the pulse must interfere with multiple preceding pulses requiring a low linewidth which, as previously stated, is beyond the resolution of any instrument available in the laboratory. At the same time, the overall system has to be stable over multiple minutes or even hours for complex measurements (chapter 7) without significant changes for the reflection and transmission of pulses by the separation resonator.

Observations have shown that the length of the separation resonator needed to be adjusted within 2 µm during stable environmental conditions. The adjustments needed under stable conditions are consistent with expected thermal expansion of the optical table[12] in the stabilised temperature of the laboratory.

At apparent random times, the stabilisation between laser and resonator reached the boundaries of the used piezo. This happened significantly more often during the week and especially during windy weather than during the weekend.

[9] 3 % roundtrip losses estimated from [87] giving a finesse of 206.
[10] Measurements on fibre-based frequency combs have shown mHz linewidths [88].
[11] resolution bandwidth
[12] Thermal expansion coefficient of stainless steel is around 10^{-5} K.

The laser repetition rate is directly connected to the optical path length and hence the refractive index of air (under normal conditions: $n_{\mathrm{air}} = 1.00027$ for 1559 nm [93]):

$$f_{\mathrm{rep}} = \frac{c}{L_{\mathrm{RT}}} = \frac{c_0}{n_{\mathrm{air}} \cdot L_{\mathrm{RT}}} \tag{4.4}$$

Assuming that at least in a first order approximation the light is slowed down linearly with the air pressure (p), the change in repetition rate can be estimated from known start values for repetition rate $(f_{\mathrm{rep},0})$ and air pressure (p_0):

$$f_{\mathrm{rep}}(p) = \frac{c_0}{\left(1 + \frac{p}{p_0}(n_{\mathrm{air}} - 1)\right) \cdot L_{\mathrm{RT}}} \implies \frac{\Delta f_{\mathrm{rep}}}{f_0} = 1 - \frac{f_{\mathrm{rep}}}{f_{\mathrm{rep},0}} = -\frac{1 + (n_{\mathrm{air}} - 1)\frac{p}{p_0}}{n_{\mathrm{air}}} \tag{4.5}$$

Monitoring the laser repetition rate over longer time periods by using a frequency counter has shown a strong correlation with the local atmospheric conditions (figure 4.3). Solely a significant temporal offset is observed which can be explained by the distance of 11.5 km between laboratory and the location of the CDC[13] weather station in Warnemünde. As the separation resonator is not isolated from atmospheric influences, these drifts are expected to affect it in almost the same manner and do not require additional stabilisation. Otherwise, the measured long-term pressure fluctuations would exceed the range of the piezo in the separation resonator.

The measured drifts alone cannot explain the occurring instabilities. Due to the correlation with workdays and windy weather, a likely cause are quick fluctuations in air pressure caused by doors opening in the institute. As the resonator is built directly on the optical table, it is directly affected. The laser is well encapsulated which suggest that it takes some time to equalise pressure inside the laser with room pressure. To verify this hypothesis, faster sampling of both the room pressure and the laser repetition rate is required. Better compensation of quick pressure fluctuations is possible by increasing the piezo stroke.

The occurring overall pressure fluctuations of 60 hPa [94][14] in Rostock can lead to changes in the repetition rate close to 1 kHz which is well beyond the fast tuning range of the laser of around 200 Hz (table 3.1). On shorter timescales, the repetition rate of the laser shows a triangular drift of 10 Hz in time (figure 4.4). A likely cause for those could be any control loop such as the internal temperature stabilisation of the laser changing between heating and cooling. A change in the laboratory temperature did not significantly change this pattern. As the temperature of the laser is set to a defined temperature, a change in environmental temperature should have changed the duration of cooling and heating periods. Hence, it is unlikely linked to the laser itself. All frequency measurements are limited by the resolution and accuracy of the frequency counter used [95].

[13] climate data center

[14] Data of station 4271 Rostock-Warnemünde, accessed April 2021.

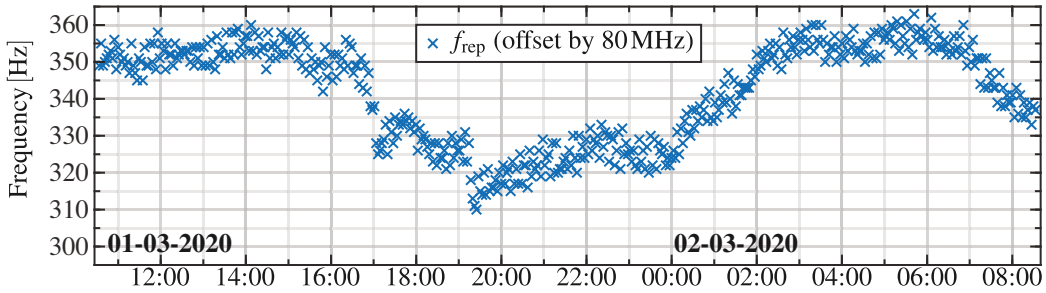

(4.3a) Measured laser repetition rates (Only every 30th point is shown.)

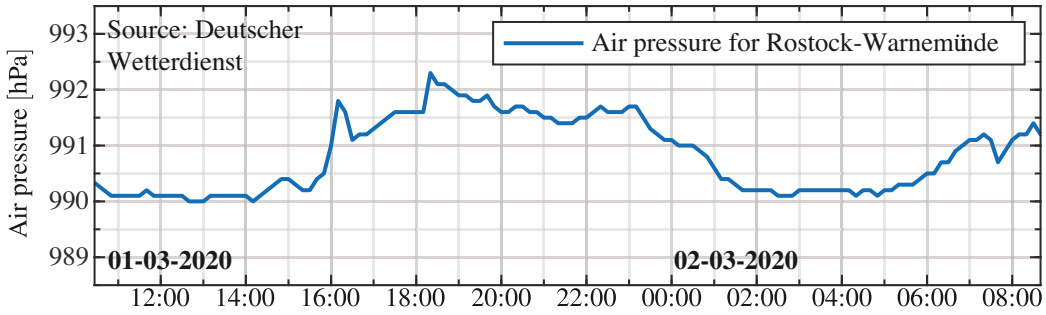

(4.3b) Air pressure in Rostock-Warnemünde during measurement

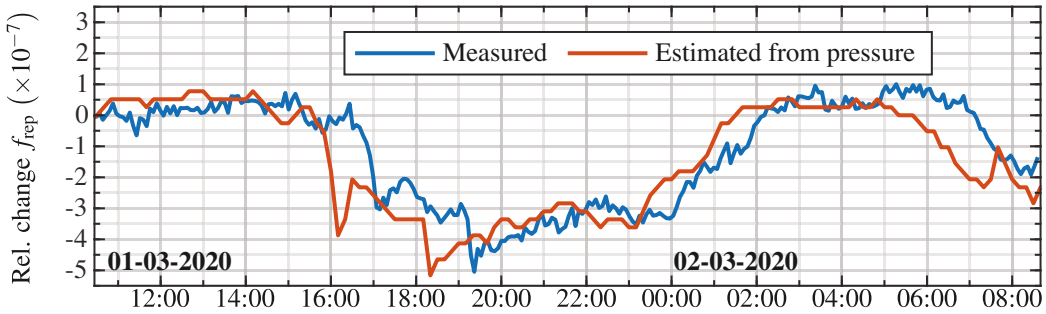

(4.3c) Deviation from initial repetition rate and expected change from pressure fluctuations

Figure 4.3 Measured stability of the repetition rate is shown in **(4.3a)** Pressure data in **(4.3b)** is accessed from the CDC [94]. Measured and estimated frequency change is compared in **(4.3c)**. The visible offset is likely due to the spatial separation (11.5 km) of laboratory and weather station.

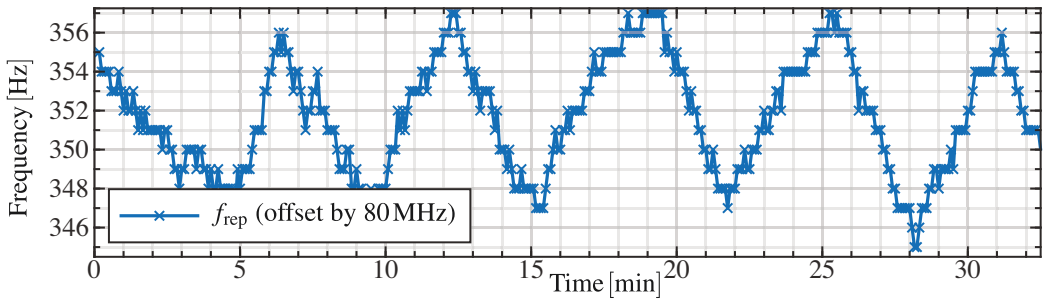

Figure 4.4 Measured stability of the repetition rate on shorter timescales A repetitive drift pattern with a period close to 6 min is observed.

4.2 Field and intensity in optical resonators

Within this section, the field inside a passive optical resonator driven by a coherent light field is discussed. A special focus lies on the reflected and transmitted fields for a single frequency. Additionally, the spatial modes as well as the experimental mode matching to the optical fibre are discussed. A comprehensive overview on optical resonators can be found in [96, Ch. 9]. The behaviour of a dispersive resonator for a frequency comb is discussed based on the single frequency response. Experimental schemes to stabilise the resonator and measure its dispersive properties are presented and applied. Especially in reflection, where the carrier pulse frequencies are depleted, the shape of the pulse is changed and hence all observed interference patterns in the actual experimental setup are affected. As a result, the interference pattern between pulses in the experiment cannot be perfectly mapped to the actual detuning.

4.2.1 Spatial modes

An optical resonator is generally formed by a closed optical path, usually created by reflective surfaces such as mirrors which can be arranged in complex setups, or a simple linear resonator with one or two concave mirrors (figure 4.5).

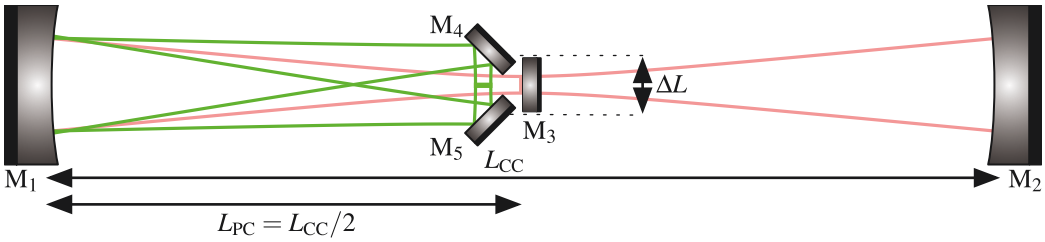

Figure 4.5 Gaussian beams in simple resonator configurations
Concave mirrors M_1 and M_2 form a linear symmetric resonator. M_1 and M_3 form a linear plano-concave resonator. A ring resonator is formed by M_1, M_4 and M_5.

In a linear symmetric resonator formed by two identical concave mirrors with curvature R, such as M_1 and M_2 in figure 4.5, the waist (W_0) of the Gaussian beam is centred between both mirrors and its value is given by [96]:

$$W_0^2 = \frac{\lambda \cdot L_{CC}}{2\pi} \sqrt{2\frac{|R|}{L_{CC}} - 1} \tag{4.6}$$

The mode remains identical if the concave mirror M_1 and the planar mirror M_3 are used:

$$W_0^2 = \frac{\lambda \cdot L_{PC}}{\pi} \sqrt{\frac{|R|}{L_{PC}} - 1} \tag{4.7}$$

Size of the waist is almost unaffected if instead of one mirror M_3 two mirrors M_4 and M_5 are used if $\Delta L \ll L_{PC}$. The overall roundtrip length is then:

$$L_{RT} = 2L_{PC} \cdot \sqrt{1 + \left(\frac{\Delta L}{2L_{PC}}\right)^2} + \Delta L \approx 2L_{PC} + \Delta L \left(1 + \frac{\Delta L}{L_{PC}}\right) \tag{4.8}$$

Such a three mirror ring cavity has the advantage that the s- and p-polarisation degeneracy is lifted but the beam waist is still well approximated by equation (4.7) and positioned between the two coupling mirrors. In the actual setup ($|R| = 3\,\mathrm{m}$; $L_{RT} \approx 3.75\,\mathrm{m}$; $\Delta L \approx 5\,\mathrm{cm}$), this results in a Rayleigh length of 1.45 m and a waist of 850 µm at a wavelength of 1560 nm.

Based on the fundamental TEM[15] mode, the higher order Hermite-Gaussian modes can also be excited.

4.2.2 Mode matching between fibre and resonator

In the experimental setup (figure 4.13), the laser is coupled from a PM fibre to the separation resonator. The optical fibre guides only its fundamental mode, similar to the TEM_{00} mode. To estimate the experimentally achievable coupling from the optical fibre to the separation resonator, this section focusses on the wavelength-dependent properties of the fibre modes as well as their matching to the TEM_{00} mode of the separation resonator.

Fibre mode field diameter

As for the resonator, the beam properties depend on the actual wavelength but due to the refractive index profile, they do not exactly match a TEM_{00} mode. For an idealised step index fibre, an analytic expression can be found depending on the fibre parameters[16] [97]. An empiric formula [98] is given in equation (4.9) for the MFD[17] of a TEM_{00} mode approximating the profile in an optical fibre. As illustrated in figure 4.6, both modes have a good overlap and the TEM_{00} mode contains 99.4 % of the optical power at 1560 nm[18]. Calculations are based on parameters of the used fibre (*PM1550-XP*) estimated from its specification sheet.

Fibre collimator and mode matching

Obtaining a good mode matching requires precisely matching both the beam waist and its position. The usual scheme is to characterise the beam that has to be matched and use multiple lenses to obtain the right diameter at the right distances. Simultaneously, two

[15] transverse electromagnetic

[16] These wavelength-depended parameters are merged into the V number (equation (4.10)).

[17] mode field diameter

[18] This percentage is wavelength-dependent and changes from 99.5 % at 1510 nm to 99.3 % at 1610 nm as the MFD increases for longer wavelengths and more light is guided in the cladding.

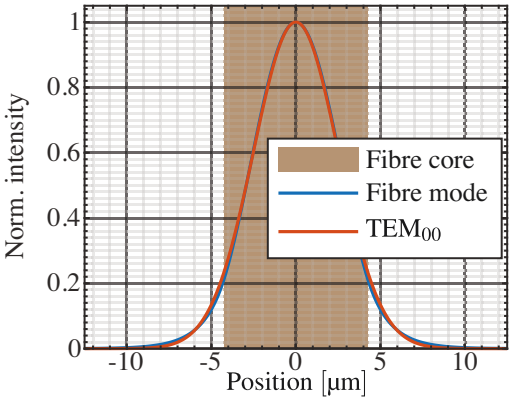

$$\mathrm{MFD} = 2a_\mathrm{c}\left(0.65 + \frac{1.619}{V^{3/2}} + \frac{2.879}{V^6}\right) \tag{4.9}$$

$$V = \frac{2\pi}{\lambda}\cdot a_\mathrm{c}\cdot \mathrm{NA} \tag{4.10}$$

Parameters used for *PM1550-XP* are:

$$a_\mathrm{c} = 4.25\,\mu\mathrm{m} \qquad \mathrm{NA} = 0.125$$

Figure 4.6 Intensity profile of the fundamental mode in a step index fibre
For comparison, the TEM_{00} mode according to equation (4.9) is shown. Wavelength is set to 1560 nm and fibre parameters are based on *PM1550-XP*.

steering mirrors are required to adjust the position and direction of the beam. Aside from being very time-consuming, this complex setup is prone to aberration and misalignment, especially the alignment of the 10 µm mode from the optical fibre is critical. Optical fibres are industrially mass-manufactured with tight tolerances and well aligned assemblies for coupling are available. These allow for a precise adjustment of the distance between fibre and one well aligned aspheric lens. Using a collimator assembly, optimised to deliver a collimated beam with a 2 mm MFD, the fine adjustment for the lens (figure 4.7a) can be used to obtain the right MFD for the separation resonator.

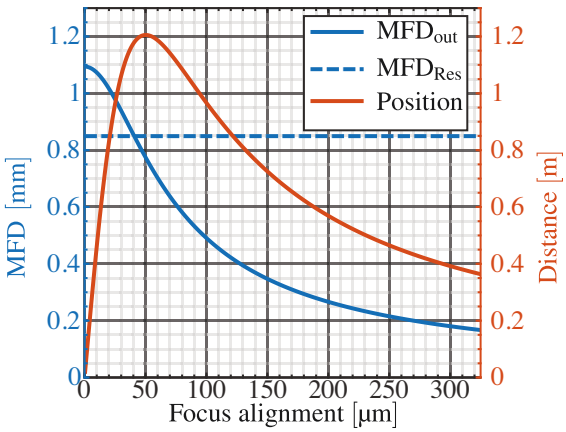

(4.7a) MFD and waist position

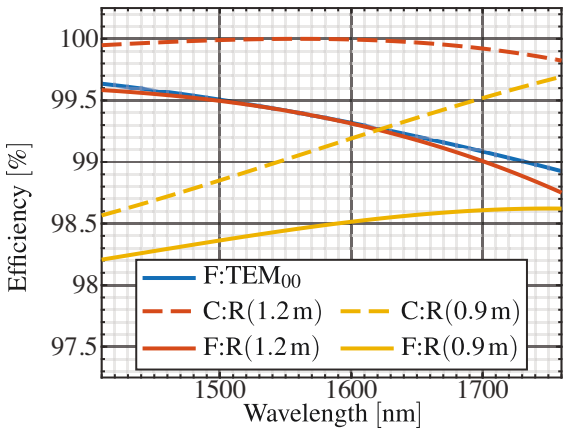

(4.7b) Theoretical coupling efficiencies

Figure 4.7 Estimated theoretical fibre to resonator mode matching
(4.7a) shows the expected MFD and waist position relative to the fibre depending on the detuning from focus point of a 11 mm lens. **(4.7b)** shows the expected power coupling efficiency to the TEM_{00} mode $(\mathrm{F:TEM}_{00})$, the matching of the TEM_{00} mode to the resonator by the coupler $(\mathrm{C:R})$ and the overall efficiency $(\mathrm{F:R})$ in dependence of the wavelength for two lengths.

Calculations lead to a distance of 1.2 m between collimator and waist of the separation resonator and indeed excellent mode matching was observed. Due to changes in the experimental setup, this distance was changed to ≈ 0.9 m and the observed mode matching

further improved. This improvement may be caused by a deviation of the fibre MFD or the focal length. In figure 4.7, the estimated wavelength-dependent mode matching for both distances is shown.

The expected achievable mode matching for the pulse is 98.5 % to 99.4 % which is hard to verify in the experiment (section 4.5.1). This estimation does not account for additional aberrations of the lens and changes in the spectrum during propagation which may slightly change the overall coupling efficiency to the separation resonator.

4.2.3 Longitudinal modes and coupling

Assuming an external light beam with matching parameters, *e.g.* direction, waist size and position, in a single TEM mode excites the resonator at one of its mirrors, a field inside the resonator builds up. Reflected and transmitted fields can be written down straightforward depending on the field(s) inside the resonator using the field reflection (r) and transmission (τ) coefficients of the mirrors:

$$E_{\mathrm{refl}} = r_{\mathrm{IC}} \cdot E_{\mathrm{in}} - \tau_{\mathrm{IC}} \cdot E_{\mathrm{R_3}} \qquad E_{\mathrm{trans}} = \tau_{\mathrm{IC}} \cdot E_{\mathrm{R_1}} \tag{4.11}$$

Fields inside the resonator can be put in relation to each other.

$$E_{\mathrm{R_2}} = r_{\mathrm{OC}} \cdot E_{\mathrm{R_1}} \qquad E_{\mathrm{R_3}} = \eta_{\mathrm{F}} \cdot E_{\mathrm{R_2}} \tag{4.12}$$

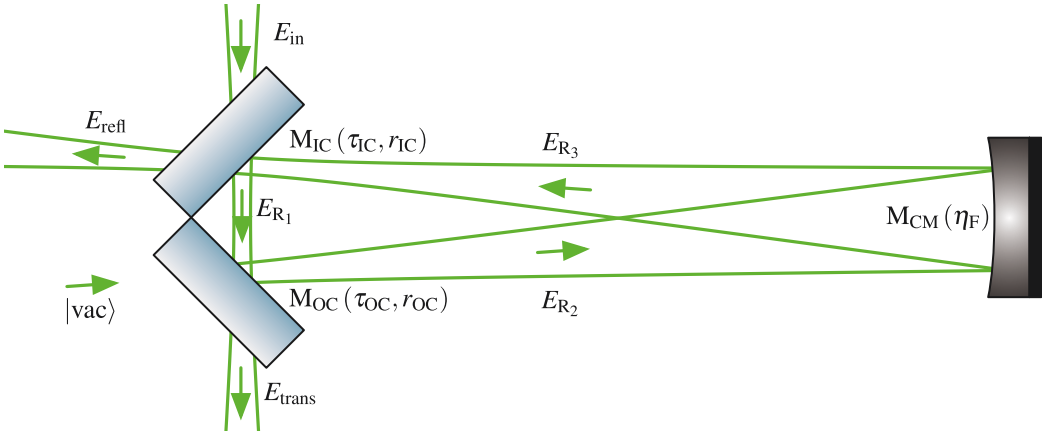

Figure 4.8 Fields inside the ring resonator ($E_{\mathrm{R}_{1,2,3}}$) are excited by the incident field (E_{in}) on the input coupling mirror ($\mathrm{M_{IC}}$). Transmitted (E_{trans}) and reflected field (E_{refl}) are shown. Field incident on the output coupling mirror ($\mathrm{M_{OC}}$) is in vacuum state. The curved mirror ($\mathrm{M_{CM}}$) accounts for the all roundtrip losses η_{F} aside from the reflection coefficients of the coupling mirrors. All coefficients refer to the corresponding fields.

Only on the input coupling mirror, multiple fields interfere with each other and, combined with the overall phase accumulated during one roundtrip (φ_{RT}), E_{R_1} can be calculated:

$$E_{R_1} = \tau_{IC} \cdot E_{in} + e^{i\varphi_{RT}} \cdot r_{IC} \cdot E_{R_3} = \underbrace{\tau_{IC} \cdot E_{in}}_{A_0} + \underbrace{e^{i\varphi_{RT}} \cdot r_{IC} \cdot r_{OC} \cdot \eta_F}_{r_{RT}} \cdot \underbrace{E_{R_1}}_{A} \tag{4.13}$$

$$= A_0 + r_{RT} \cdot A_0 + r_{RT}^2 \cdot A = \cdots = A_0 \sum_{j=0}^{\infty} r_{RT}^j \tag{4.14}$$

As $|r_{RT}| < 1$, the geometric series of equation 4.14 converges to $A_0/(1 - r_{RT})$ resulting in:

$$E_{R_1} = \frac{\tau_{IC}}{1 - e^{i\varphi_{RT}} \cdot r_{IC} \cdot r_{OC} \cdot \eta_F} \cdot E_{in} \tag{4.15}$$

The absolute value of the field inside the resonator reaches its minimum value if the denominator has its maximum absolute value and vice versa. Maximum and minimum absolute values for the denominator are: $1 \pm r_{IC} \cdot r_{OC} \cdot \eta_F$. Hence for φ_{RT} being a multiple of 2π, the resonator is on resonance and the field inside obtains its maximum value.

Reflected and transmitted fields are given by:

$$E_{refl} = \left(r_{IC} - \frac{\tau_{IC}^2 \cdot r_{OC} \cdot \eta_F \cdot e^{i\varphi_{RT}}}{1 - e^{i\varphi_{RT}} \cdot r_{IC} \cdot r_{OC} \cdot \eta_F} \right) \cdot E_{in} \quad E_{trans} = \frac{\tau_{IC}\tau_{OC}}{1 - e^{i\varphi_{RT}} \cdot r_{IC} \cdot r_{OC} \cdot \eta_F} \cdot E_{in} \tag{4.16}$$

If the reflectivity of the input coupler matches all other losses during one roundtrip, i.e. $r_{IC} = r_{OC} \cdot \eta$, impedance matching is achieved and the reflected field vanishes independent of the actual reflectivity of the mirror:

$$E_{refl,\,res} = \left(r_{IC} - \frac{\tau_{IC}^2 \cdot r_{IC}}{\underbrace{1 - r_{IC}^2}_{=\tau_{IC}^2}} \right) \cdot E_{in} = 0 \cdot E_{in} \tag{4.17}$$

If furthermore no internal losses occur, i.e. $\eta_F = 1$ and $r_{IC} = r_{OC}$, all optical power is transmitted:

$$E_{trans} = \underbrace{\frac{\tau_{IC}^2}{1 - r_{IC}^2}}_{=1} \cdot E_{in} \tag{4.18}$$

Most parameters of a resonator are linked to the transmitted and reflected intensity as shown in figures 4.9 and 4.10. This is due to the simplicity of intensity measurements compared with measurements of the actual amplitude and phase.

The finesse of an optical resonator is the ratio of its FSR and its FWHM shown in figure 4.9. It can be calculated from overall roundtrip losses:

$$\mathcal{F} = \pi / \left(2 \cdot \operatorname{asin} \left(\frac{1 - |r_{\mathrm{RT}}|}{2\sqrt{|r_{\mathrm{RT}}|}} \right) \right) \tag{4.19}$$

Using equation (4.16) and the detuning phase φ_{RT}, the transmitted intensity can be written as:

$$I_{\mathrm{trans}} = \frac{\tau_{\mathrm{IC}}^2 \cdot \tau_{\mathrm{OC}}^2}{1 + r_{\mathrm{RT}}^2 - 2|r_{\mathrm{RT}}| \cos(\varphi_{\mathrm{RT}})} I_{\mathrm{in}} \tag{4.20}$$

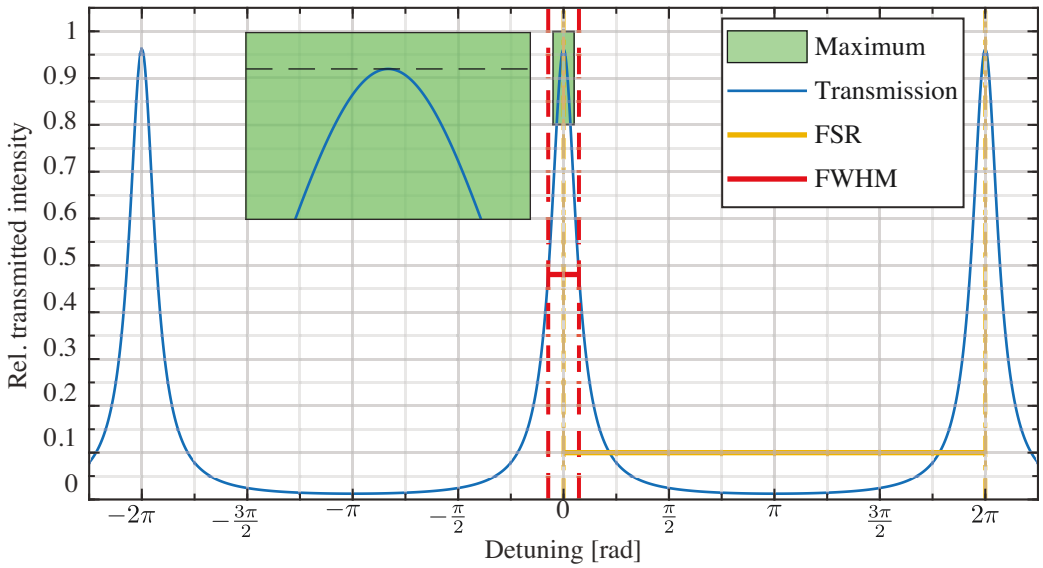

Figure 4.9 Intensity transmission of a resonator
Parameters used are $r_{\mathrm{IC}}^2 = r_{\mathrm{OC}}^2 = 0.8$ and $\eta_{\mathrm{F}}^2 = 0.99$, resulting in a finesse of 14. Near its maximum value (green area), the transmitted intensity is flat.

The condition for a standing wave requires the overall phase[19], acquired during one roundtrip, to be an integer multiple of 2π. As the refractive optical path length inside the resonator depends on the wavelength $\left(\lambda = \frac{2\pi \cdot c_0}{\omega}\right)$ and wavelength-dependent phase shifts from the used mirrors $(\Phi(\omega))$, these modes are strictly speaking not spaced equidistant as the modes of a mode-locked laser:

$$2\pi \cdot N = \frac{n(\omega) \cdot L \cdot \omega}{2\pi \cdot c_0} + \Phi(\omega) \tag{4.21}$$

Commonly, the FSR and FWHM are given in hertz which is quite accurate. Nevertheless, equation (4.21) shows they depend on the frequency of the used light which is critical for pulsed light as in this case the spectral FWHM spans roughly 2 THz or 25000 times the

[19] The additionally acquired Gouy phase, depending on the actual Hermite-Gaussian mode, is neglected in the discussion as the mode matching suggests the TEM_{00} to be dominant in the aligned state.

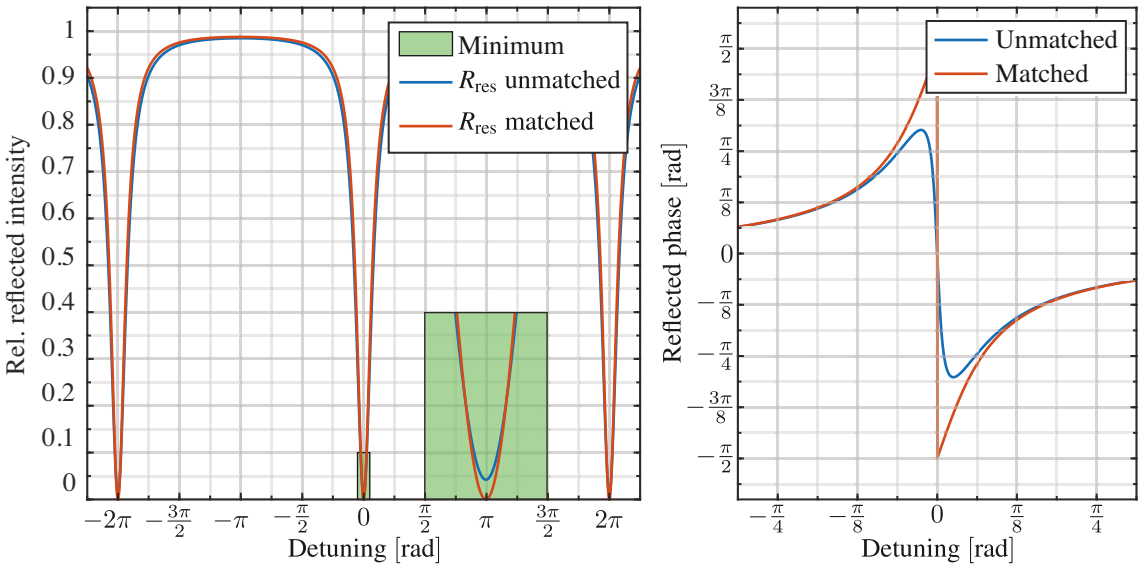

(4.10a) Intensity of reflected light

(4.10b) Phase of reflected field

Figure 4.10 Intensity and phase upon reflection of an unmatched resonator
Parameters are $r_{\text{IC}}^2 = r_{\text{OC}}^2 = 0.8$ with $\eta_{\text{F}}^2 = 0.99$ and $\eta_{\text{F}}^2 = 1$.
(4.10a): Near its minimum value (shown in the green area), the reflected intensity is flat and vanishes only for perfectly matched impedance.
(4.10b): The slope of the reflected phase is steep close to the minimum of reflected intensity. In case of impedance matching, the sign flips.

FSR (80 MHz). In particular for the reflection on which the experimental setup relies, even small deviations significantly affect the intensity and phase.

As the dispersive properties of the mirrors and the atmosphere cannot be influenced, at least with feasible effort, only the length can be used to stabilise the resonator relative to the frequency comb emitted by the laser system discussed in section 4.3. The characterisation of the dispersion (section 4.4) follows after the stabilisation scheme as its measurements requires the resonator to be stabilised.

4.3 Stabilisation schemes

To obtain stable transmission and reflection, the separation resonator roundtrip length of 3.75 m has to be actively stabilised in the sub-nm regime. A simple method of stabilisation is the SFL[20]. By measuring either reflected or transmitted intensity, the resonator can be stabilised on either side of the transmission peak. This scheme is used in the experiment for the alignment of both spatial modes as it splits the optical power between them. Nevertheless, it cannot be used to stabilise the resonator upon resonance as both reflected (figure 4.10) and transmitted (figure 4.9) intensities are flat near the resonance.

[20] side-of-fringe lock

4.3.1 PDH locking scheme

The PDH[21] technique [99, 100] is a locking scheme for stabilising either the frequency of a laser to an optical resonator or vice versa.

As shown in figure 4.10b, the sign of the phase changes upon resonance. For imperfect impedance matching, the phase depends linearly on the detuning near the resonance. This dependence can be used to stabilise the resonator if the phase can be accessed.

This can be achieved by using modulated sidebands with a frequency offset by f_{mod} . As the frequencies of the sidebands experience a different phase shift than the laser, the corresponding beat signal changes. Commonly, a phase modulation applied by an EOM is used. As the carrier component drastically changes upon resonance, the initial phase modulation can be observed as an amplitude modulation[22] in reflection. By demodulating this amplitude modulation with f_{mod}, an error signal (figure 4.11b) for stabilising the resonator upon maximum transmission can be obtained. As the comb structure is described by two independent parameters, f_{CEO} and f_{rep}, and only one linear error signal is obtained, the resulting stabilisation cannot be well defined.

4.3.2 Dual laser lock

As shown in figure 4.13, a CW laser can be added to the experimental setup using a BS. By stabilising the beat frequency of the CW laser and the next mode of the frequency comb, a modulation is created that can be used for stabilisation.

This method results in an error signal for one specific mode (here called n_1) of the pulse at a wavelength of 1550 nm, given by the available CW laser. This does not match the central wavelength of the laser $\lambda_{\mathrm{CW}}\,(1559\,\mathrm{nm})$ and additionally the modulation is proportional to the power in one specific comb mode, which is only a fraction of the overall power.

By evaluating this error signal, the deviation is proportional to the deviation of $f_{\mathrm{CEO}} + n_1 \cdot f_{\mathrm{rep}}$ from a chosen setpoint. As a result, a drift in f_{rep} or separation resonator length is perfectly accounted for as the required length adjustment is identical[23] for all modes of the frequency comb. But a drift in f_{CEO} requires different detunings for all modes.

If f_{CEO} drifts by Δf_{CEO}, the control loop adjusts the length of the resonator and thereby its FSR by:

$$\Delta\mathrm{FSR} = -\frac{\Delta f_{\mathrm{CEO}}}{n_1} \tag{4.22}$$

[21] Pound-Drever-Hall

[22] Information on classical amplitude and phase modulation of light can be found in chapter 2 of [101].

[23] Neglecting the dispersion of air caused by changing the length of a 3.75 m long optical path by a few µm.

As a result of following the CEO in this way, other modes, offset by Δn modes, are shifted from resonance by:

$$\Delta\varphi\,(\Delta n) = 2\pi \cdot \frac{\Delta f_{\mathrm{CEO}}}{f_{\mathrm{rep}}} \frac{\Delta n}{n_1} \tag{4.23}$$

Using this locking scheme, the stabilisation can be excellently close to the CW laser but will generally worsen with increasing spectral distance (Δn) from λ_{CW}.

4.3.3 Influences of the comb structure

As shown in figure 3.2, an EOM is used to apply a phase modulation on all modes of the pulsed laser. As a result, the overall error signal also depends on all modes. From each mode, a contribution similar to the one previously discussed (section 4.3.2) is expected. These individual error signals may be shifted away from resonance due to a mismatch of CEO, FSR or other dispersive effects. This influences the overall error signal in a complex way as indicated in figure 4.11b even if neither the CEO nor dispersive effects are considered and the error signal for one peak detuning is already altered. Nevertheless, the complex structure is irrelevant as long as a linear error signal close to resonance is available for stabilisation. It is expected that the error signal is proportional to the deviation of the FSR from f_{rep} for all modes yielding a good error signal to stabilise.

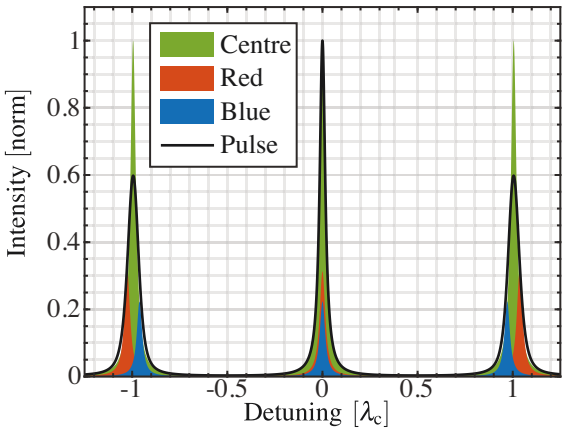

(4.11a) Transmitted intensity

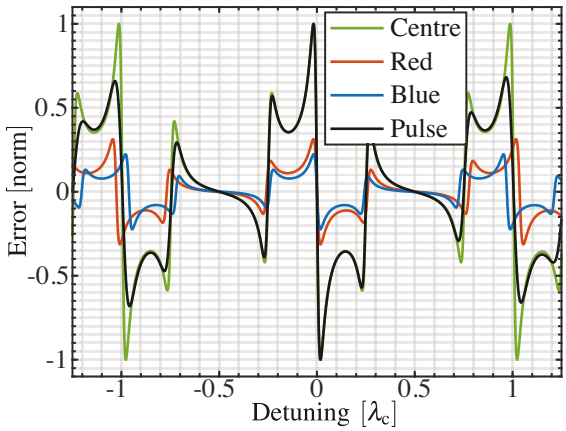

(4.11b) Error signal for stabilisation

Figure 4.11 PDH error signal for pulses and individual spectral components **(4.11a)** shows the normalised transmitted intensity of the overall pulse, the central spectral component as well as shorter (blue) and longer (red) wavelengths. **(4.11b)** shows the corresponding error signals. Spectral transmission is normalised to the strongest/central component.

A deviation in CEO on the other hand has a different impact on the actual stabilisation. The CEO depends on the phase shift between pulse envelope and the wavelength of the carrier close to the central wavelength of the pulse. As the spectrum is approximately symmetric around its central wavelength, the effect discussed in equation (4.23) leads

to a phase detuning linear in the distance from the central frequency. A drifting CEO is expected to change the slope of this detuning. Nonlinear pulse propagation may change the spectrum of the pulse and particularly a red shift due to Raman scattering may alter the error signal and thereby lead to a detuning from maximum transmission. If a component with a longer wavelength already left the linear range of the error signal, its contribution has the wrong sign (similar to the detuning of $-\lambda_c$ in figure 4.11b). These influences are merely perceptible in the laboratory and cannot be resolved currently without tremendous effort.

4.3.4 EOM frequency choice

For demodulation, a double balanced mixer[24] is used which demodulates the signal at all odd harmonics. While the detector can be designed for almost any frequency, the pulse repetition rate and its harmonics cannot be filtered out perfectly. Additionally, a modulation is created on all spectral components. This leads to signals at $(n \cdot f_{\mathrm{rep}} \pm f_{\mathrm{mod}})$. Any odd harmonic of f_{mod} close to these frequencies will lead to a beat signal in the derived error signal[25]. As the locking loop is limited by the piezo speed, the intended bandwidth for the error signal is in the range of 50 kHz. Beat signals within this bandwidth will influence the achieved stability of the resonator, hence they need to be avoided. This can be generally achieved by either driving the EOM with a high voltage or using a resonant EOM design to obtain a strong phase modulation which would yield a better SNR for the error signal and allow for additional filtering prior to demodulation.

In the experimental setup the electronics were designed for the weak error signal from the beat with the CW laser and driving the EOM with an amplitude of only 1 V generated a more than sufficient error signal. By choosing a modulation frequency of 17.25 MHz, the odd harmonics widely avoid the discussed problems while still being well apart from the frequencies around 5.6 MHz used in the BHD.

4.4 Dispersion effects

In this section, the effects of dispersion on short pulses will be briefly discussed and related to the properties of the separation resonator.

[24] For the operational principle see for example [102].
[25] As the used demodulation technique essentially uses a square wave with f_{mod}.

4.4.1 Dispersion for short pulses

The frequency-dependent wavenumber depends on the refractive index:

$$k(\omega) = \frac{\omega}{c_0} n(\omega) \tag{4.24}$$

For pulsed light around a carrier frequency, a Taylor expansion yields:

$$k(\omega) \approx k_c + \left.\frac{\partial k}{\partial \omega}\right|_{\omega_c} (\omega - \omega_c) + \frac{1}{2} \left.\frac{\partial^2 k}{\partial \omega^2}\right|_{\omega_c} (\omega - \omega_c)^2 + \frac{1}{6} \left.\frac{\partial^3 k}{\partial \omega^3}\right|_{\omega_c} (\omega - \omega_c)^3 + \dots \tag{4.25}$$

The first order $\frac{\partial k}{\partial \omega}$ is the inverse group velocity v_g:

$$\left(\frac{\partial k}{\partial \omega}\right)^{-1} = \left(\frac{n(\omega)}{c_0} + \omega \frac{n'(\omega)}{c_0}\right)^{-1} = \frac{c_0}{n(\omega) + \omega \cdot n'(\omega)} = v_g \tag{4.26}$$

It describes at which velocity the envelope of the pulse travels and does not change the shape of the envelope. The difference to the phase velocity $v_p = c_0/n(\omega)$ at the carrier frequency determines how the CEP[26] changes during propagation. Generally, this is related to group-phase offset frequency f_{GPO} which can well exceed f_{rep}. For the comb properties and the experimental setup, only the phase shift between two consecutive pulses after $1/f_{rep}$ is relevant and will be used within this thesis. This frequency is the CEO frequency which is the difference between f_{GPO} and the nearest multiple of f_{rep}.

The second derivative is called GVD[27] and affects the shape of the envelope as it elongates a transform-limited pulse in time as shown in figure 4.12. Depending on its sign, the wavelength inside the envelope changes from shorter to longer or vice versa which is called a chirp. For a material, it is usually stated using $\mathrm{fs}^2/\mathrm{mm}$ as it increases with the propagation distance but for a fixed optical component, like a mirror, a value in fs^2 is stated as its GDD[28].

4.4.2 Dispersive effects within the resonator

As the pulse consists of equidistant frequency modes and the resonance frequencies of the resonator are not absolutely equidistant, they do not match perfectly and lead to a strongly nonlinear behaviour upon detuning. While the frequency description is a good choice for characterisation, it is not particularly suited for illustrative purposes.

[26] carrier-envelope phase
[27] group velocity dispersion
[28] group delay dispersion

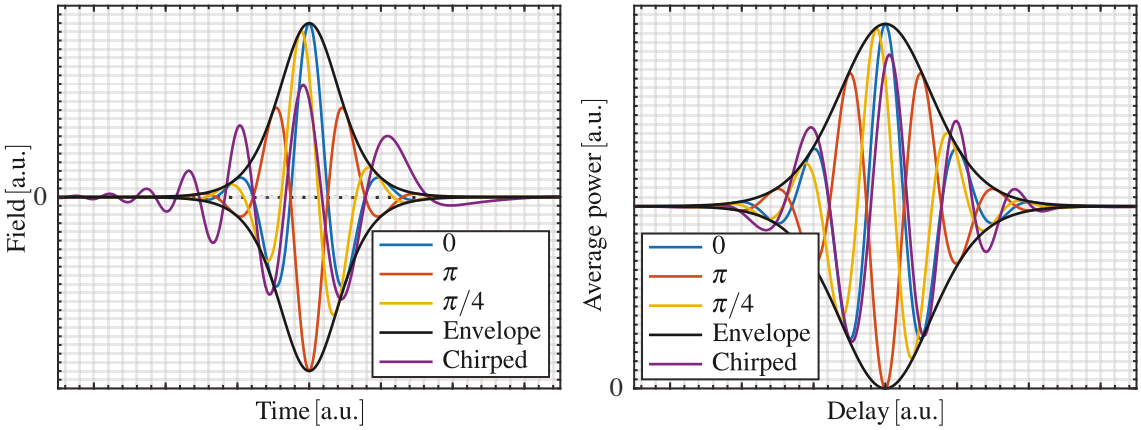

(4.12a) Field in time (Chirp broadens pulse compared to envelope)

(4.12b) Average power of interference depending on delay

Figure 4.12 Interfering pulses with different CEP and chirp
(4.12a) depicts the field in time for different CEP with the pulse envelope. Additionally, a chirped pulse is shown.
(4.12b) displays the resulting average power from interference with the 0-CEP pulse depending on the delay between the pulses.

Wavelength	media	$n_\mathrm{p}\ (c_0/v_\mathrm{p})$	$n_\mathrm{g}\ (c_0/v_\mathrm{g})$	ΔL	GVD
1064 nm:	air	1.00027398	1.00027673	0.387 m	16.735 fs^2/m
	FS	1.4496	1.4624	255 µm	16.476 $\mathrm{fs}^2/\mathrm{mm}$
	BK7	1.5005	1.5201	186 µm	$-25.864\ \mathrm{fs}^2/\mathrm{mm}$
1560 nm:	air	1.00027325	1.00027452	1.23 m	10.734 fs^2/m
	FS	1.4439	1.4627	253 µm	$-29.140\ \mathrm{fs}^2/\mathrm{mm}$
	BK7	1.5066	1.5206	285 µm	22.369 $\mathrm{fs}^2/\mathrm{mm}$

Table 4.2 Dispersion parameters for air, fused silica (FS) and BK7 glass from [103]
The calculated distance ΔL indicates the propagation distance required for a 2π-shift between carrier and envelope.

Due to the limited bandwidth of the pulse, the main contribution comes from the group and phase velocity which will be briefly discussed.

A portion of the pulse is transmitted by the in-coupling mirror and propagates one roundtrip until it interferes with the transmitted portion of the next pulse. Considering only group and phase velocity if both pulse envelopes perfectly overlap, all wavelengths will interfere exactly in the same way. But as the CEP has changed during one roundtrip and the next pulse has a different CEP due to the CEO of the laser, this leads to an equal detuning for all components. To obtain constructive interference inside the resonator and destructive interference upon reflection, the roundtrip length of the resonator has to be increased or decreased by up to half the carrier wavelength. In doing so, the resonator becomes resonant for the carrier wavelength but the pulse envelopes do not perfectly overlap. This results in better but not perfect overall interference as indicated in figure 4.12b. A perfect

constructive interference is only possible if the pulse after one roundtrip is exactly equal to the following incident pulse.

The illustrations in figure 4.12 uses few cycle pulses where these effects are clearly visible. Within the actual parameters[29], these effects are rather subtle and cannot be clearly distinguished from other parameters such as mode matching or losses inside the resonator.

If for example for perfect overlap of the envelopes all components are detuned by $\pi/2$ at a carrier wavelength of 1560 nm, a detuning of 390 nm is required. While on average the best possible constructive interference is obtained, the spectral component at 1510 nm will experience a detuning close to $\left(\frac{1}{2}+\frac{1}{60}\right)\pi$ and will not be perfectly on resonance as the detuning is too long. For longer wavelengths, the detuning will not be long enough. Due to the resonator's highly nonlinear reflection of both amplitude and phase (figure 4.10), the reflected carrier pulse shape will be affected as well as all measurements depending on this carrier pulse.

Another method of shifting the CEP obtained during one roundtrip would be to vary v_g and v_p inside the resonator (table 4.2). Adding less than 300 µm fused silica or BK7 and correcting the length accordingly would be sufficient to shift the CEP by more than 2π. The contribution from the atmosphere to the CEP is close to 6π (table 4.2). Translated to f_{GPO}, this would translate to 240 MHz and depending on the pressure fluctuations in the atmosphere[30], a drift of 20 MHz is expected. This would have significant influence on the experimental setup but this drift was not observed as the stability of the laser is also limited by the same atmospheric pressure fluctuations (section 4.1.5).

4.5 Separation resonator setup and measurements

Within this section, the setup of the separation resonator and its characterisation with respect to mode matching, finesse and the dispersive effects within the resonator are discussed.

Figure 4.13 shows the schematic experimental setup used to lock and align the separation resonator. The expected mode matching (98.5 % to 99.4 %) to the optical fibre was discussed in section 4.2.2 and the optional locking scheme using a CW laser in section 4.3.2. For later measurements (chapter 6), the fibre was submerged in LN_2.

By adjusting the offset of the error signal used for stabilising the resonator, it can be detuned by roughly[31] ±5 nm from the maximum transmission. Both reflected and transmitted

[29] Around 200 fs long pulses (FWHM) and ≈ 5 fs per field oscillation, *i.e.* 40 cyclces, within the FWHM of the pulse.

[30] Usually atmospheric pressures of 960 hPa to 1060 hPa can be expected [94].

[31] Actual range for stable detuning depends on the width of the linear section of the error signal which itself depends on several factors.

beams enter the BHD setup (chapter 5) where both can be analysed using a fibre-coupled OSA[32] (figure 5.5). For the coupling into the OSA, similar optical components are used indicating also excellent obtainable spatial mode matching[33].

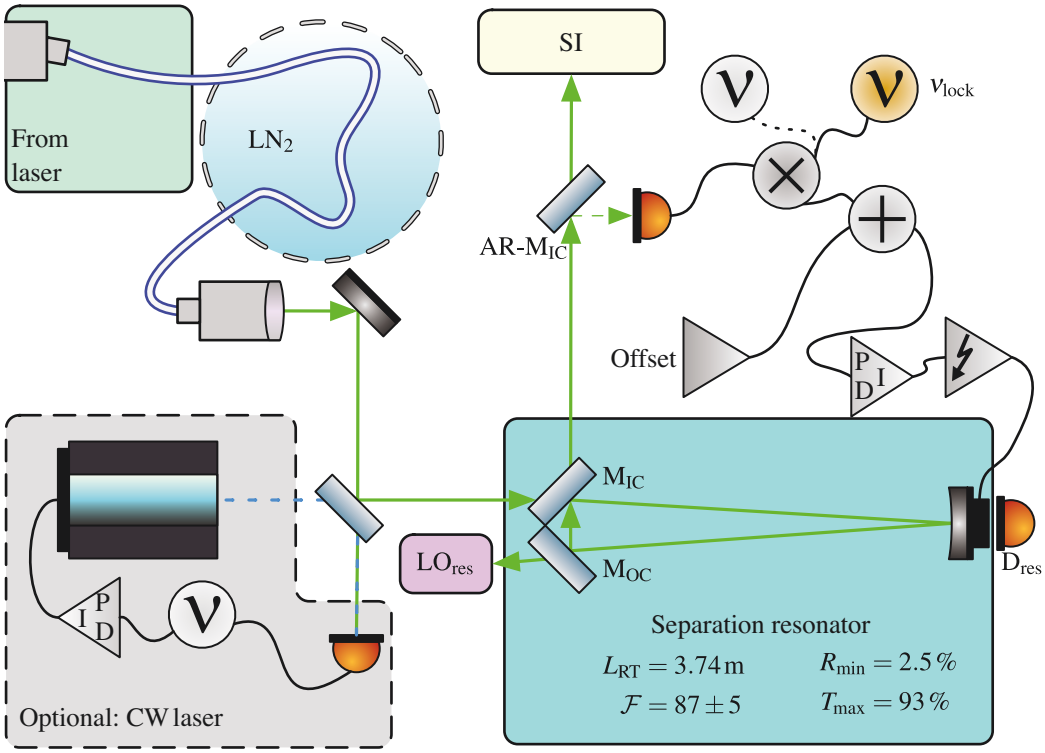

Figure 4.13 Separation resonator setup
The output beam of the fibre (optionally submerged in LN_2) is coupled via a steering mirror and a BS where the CW laser can be added (section 4.3.2). Shown as a separate part, a reflection from the AR coating on the input coupling mirror M_{IC} is used for the PDH locking scheme. Circulating power can be monitored using D_{res}. Transmitted (LO_{res}) and reflected SI beams are directed to the BHD shown in figure 5.5.

4.5.1 Measured mode matching

While the resonator length is scanned using a triangular ramp, the signals from the detectors in BHD are recorded in transmission and reflection in two consecutive measurements. Both measurements are aligned to each other using the signal of D_{res} that monitors the optical power within the resonator (figure 4.13). Due to a strong polarisation dependence of the BS used for the BHD, the contribution from p-polarised light, for which the resonator has a lower finesse, has a visible contribution on one detector as seen on the processed data (figure 4.14).

Overall for the measurement shown in figure 4.14, the achieved measured transmission is 89 % while the reflection dropped to 3 %. These parameters cannot necessarily be

[32] optical spectrum analyser
[33] Close to 90 % transmission through the optical fibre was observed.

compared between different measurements as they actually depend on the alignment, the CEO difference between resonator and laser and whether additional losses from a Brewster window inside the resonator occur. In figure 4.13, the maximum observed values are stated.

The sum of all perceptible modes is close to 1 % accounting all modes and well below 1 % if the p-polarised modes are neglected, yielding an overall mode matching in s-polarisation of 97 % to 99.5 % for the laser pulse matching the previous estimations. The lower bound results from the remaining optical power on resonance and the upper bound results from remaining observable modes.

As the scan covers almost the full range of the piezo, the detuning is not linear in time and by measuring the times for scanning the FWHM (66 µs) and the FSR (5.726 ms), an estimate of 87 ± 5 for the finesse is obtained. Additional measurements with a narrow CW laser gave a value of 92 ± 5. For the pulsed measurement, the transmission peak is broadened. Broadening is caused by the dispersive properties as not all spectral components are simultaneously on resonance (section 4.4.2).

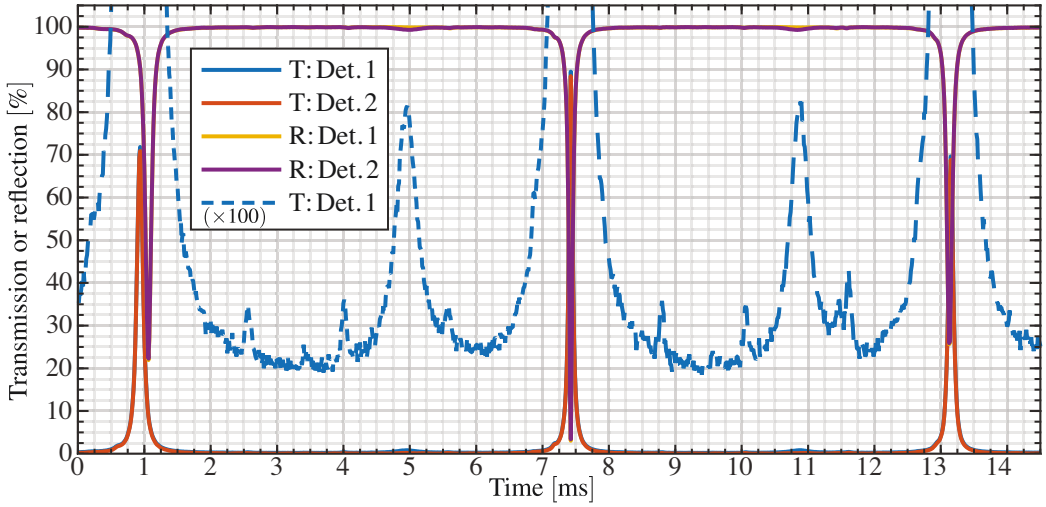

Figure 4.14 Mode matching of the built resonator
Reflection and transmission data were recorded in subsequent measurements. Data is centred on the central transmission peak measured on D_{res} (figure 4.13) and reduced to one slope of the used ramp. Data is normalised to the maximum of reflected power.

4.5.2 Dispersion measurement problems

One method to resolve the dispersive properties of individual optical components uses white-light interferometry [104]. Such a setup measures only relative differences by comparing with a reference arm. The properties of the components usually change depending on polarisation and angle of incidence. Such a setup is not available in the laboratory and cannot provide a measurement for the actual aligned resonator.

For the precise measurement of resonators for pulsed light, so-called fs-enhancement cavities, different approaches have been implemented. One approach uses the transmitted pulse and compares it with the pulse prior to the resonator [61]. In this approach, both pulses interfere under an angle, resulting in interference fringes. The phase shift is resolved in one direction and the spectral components are resolved in the orthogonal direction. From this two dimensional interference pattern, the phase difference between the spectral components can be calculated. As in [61], the resonator is placed inside a vacuum chamber. The high sensitivity was verified by measurements on the dispersion of nitrogen for various pressures inside the resonator. This setup operates at a wavelength close to 1 µm and the used pulse has a duration below 20 fs [62] and as a result a large bandwidth.

In the experimental setup for this thesis, the laser operates near 1560 nm and a similar setup would require an InGaS array which is far less common than a normal CCD sensor and not available in the laboratory. Furthermore within such a setup, the difference between a mismatch in CEO cannot be directly separated from a temporal detuning, similar to the data shown in figure 4.20b. As in the cited research, the CEO of the laser is stabilised to obtain maximum intracavity power, the CEO of the fs-enhancement cavity is not of a particular interest.

Research on fs-enhancement cavities is aimed at enhancing the intensity of a fs pulse used to provide coherent extreme ultraviolet radiation via high harmonics generation at high repetition rates [105] and hence also focussed on the improvement of the mirrors [106]. The influence of the stabilised CEO of the used laser on the enhancement factor was analysed in [107] and [108]. These were used as an inspiration for the used setup built from existing resources to characterise the dispersive properties of the separation resonator.

Another implemented method is based on the analysis of the difference in pulse shape prior and after the resonator by measuring both pulse shapes using a FROG[34] [109]. In principle, this can resolve for example the GVD but it also cannot directly measure the CEP[35].

4.5.3 Dispersion measurement setup

As shown in figure 4.13, an offset can be applied to the error signal used for stabilising the resonator and the transmitted spectra can be measured automatically for fine detuning steps by a written measurement program. The available OSA can obtain high resolution spectra[36] by sweeping through a set wavelength range leading to a high measurement time. An array-based spectrum analyser could vastly improve measurement times.

[34] frequency-resolved optical gating

[35] In principle as the higher orders can be resolved and full spectra are recorded, the linear detuning could be deduced. This approach was not followed as it requires a sufficient resolution of the FROG traces and the existing FROG mechanically influenced the resonator stabilisation.

[36] The minimum bandwidth is 30 pm or close to 3 GHz.

The error signal is not completely linear and hence a nonlinear fit between detuning step and detuning is used to fit the resonator transmission peak figure 4.15. Recorded spectra are normalised showing for which detuning which wavelengths are resonant. In figure 4.16, two almost indistinguishable measurements on two consecutive days are shown.

Figure 4.17 shows the alignment of a 2 mm thick Brewster window inside the resonator. Slight variation of the angle can be used to change the optical path length through amount of fused silica in the resonator and compensate for the CEO difference between resonator and laser as it shifts the CEP of the pulse in the resonator.

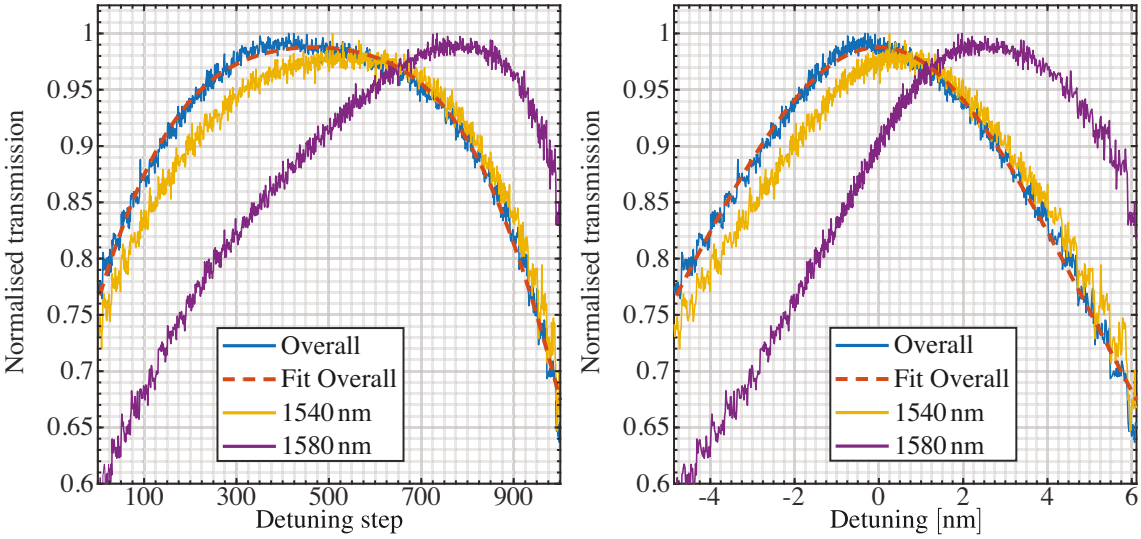

(4.15a) Spectrally resolved and normalised intensity transmission depending on detuning step
For complete data see figure 4.16b.

(4.15b) Data of **(4.15a)** in dependence of the detuning in nm
A third order polynomial was used to assign a detuning to each step.

Figure 4.15 Exemplary data for dispersion measurement and detuning fit
A finesse of 87, as measured in section 4.5.1, was used for the detuning shown in figure 4.15b.

4.5.4 Dispersion measurement evaluation

From the recored data shown in figure 4.16b, a resonator transmission peak can be fitted for each wavelength resulting in a detuning phase for each component shown in figure 4.19.

The two consecutive measurements look nearly identical indicating a high relative stability of the laser and resonator over multiple hours. While no measurements on the CEO stability of a similar free-running laser were found, in [91] it is stated that: "The free-running CEO frequency is very stable and not subject to constant drifts or sudden shifts as long as the pump current is stable". Based on the performed measurements, no significant drift in CEO between the laser and the separation resonator was observed. As the repetition rate is influenced by atmospheric pressure, the CEO is expected to drift by $\approx 15\,\mathrm{MHz}$ with atmospheric pressure over a year and less than one MHz within a day (section 4.1.5 and

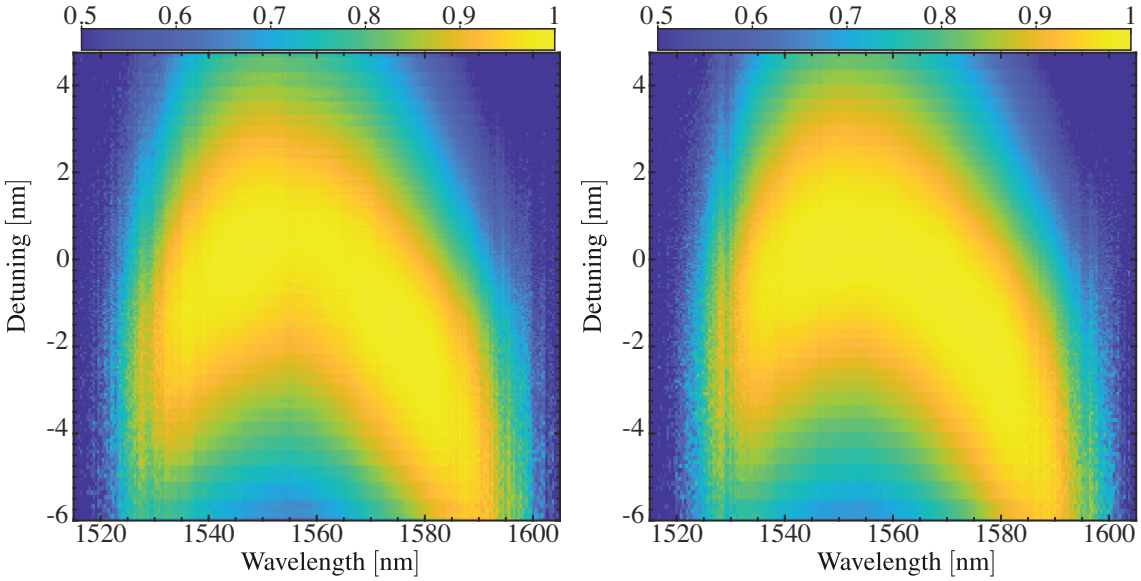

(4.16a) Measurement started on 19.10.2020 at 15:14 and finished 61 min later.

(4.16b) Measurement started on 20.10.2020 at 09:57 and finished 61 min later.

Figure 4.16 Dispersion measurement data for the separation resonator as used in the experiment
Shown is the spectrally resolved detuning dependence of intensity transmission normalised to the maximally transmitted intensity of each wavelength.

table 4.2). Nevertheless, long-term drifts due to degradation of optical components or drifts in pump power cannot be excluded.

Evaluating figure 4.19, values for GDD and CEO difference between resonator and laser can be obtained as shown in table 4.3.

The data for the CW locking method was recorded prior to a factory realignment and hence its relative CEO may significantly differ. The CEO difference between laser and resonator seems to be stable on the timescale of single measurements (1 h) and only a minor drift of 200 kHz is estimated between both shown measurements. This drift may also be due to drifts in alignment or the accuracy of the method itself.

Using the Brewster window, the difference in CEO can be cancelled out but the remaining curve is highly asymmetrical and does not match the expectations for the dielectric mirrors and air. Molecular transitions of CO_2[37] were found in the HITRAN[38] database [110] within this spectral region. Increasing CO_2 concentration in the resonator increased this influence as shown in the appendix E. As no effective measures against this were found and no dual-comb measurements for a precise characterisation [75, 111, 112] were possible with the available resources, this dispersive behaviour has to be accepted. Numerical analysis of the refractive index of air with respect to these transitions could be done [113] and may match the experimental findings. Nevertheless, these transitions are not in the

[37] carbon dioxide
[38] high-resolution transmission molecular absorption

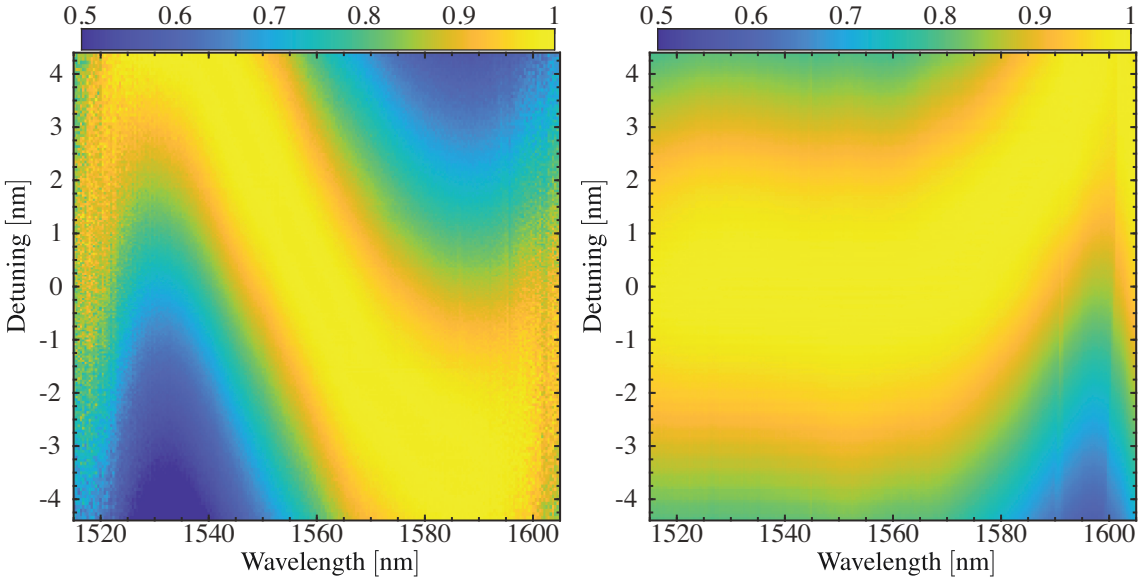

(4.17a) Brewster window during alignment

(4.17b) Brewster window aligned

Figure 4.17 Dispersion measurement data with Brewster window
Shown is the spectrally resolved detuning dependence of intensity transmission normalised to the maximally transmitted intensity of each wavelength.

centre of the spectrum and the available experimental resolution is limited, hence this effort was not made.

Additionally by tuning the angle of the Brewster window, the negative GVD of fused silica[39] compensated the positive GVD of air (around 40 fs^2 from table 4.2) and expected positive GDD of the coupling mirrors[40] (around 17 fs^2 each estimated from figure D.1 in the appendix D). All three obtained GDD values are close to the estimated GDD of air and mirrors but deviate by 5 fs^2 around 59 fs^2. With a Brewster window installed, the mean value is $-19.5\,\mathrm{fs}^2$ resulting in a difference of $-78.5\,\mathrm{fs}^2$ close to the expected value of $-71\,\mathrm{fs}^2$.

While the Brewster window can be used to precisely match the CEO, its initial alignment is time consuming and additionally imperfect alignment leads to losses in the order of 0.1 % per surface that affect the impedance matching and lead to both higher reflected and lower transmitted intensities. Long-term drifts in CEO would require realignments and ideally regular monitoring. For these reasons, it was not implemented in the final experimental setup. Aside from using a Brewster window, the pump current can also be used to align the CEO between laser and resonator. Lowering the spectral and detuning resolution, the shown measurements were repeated for 41 different pump currents and were measured in 150 min measurement time. As the direct voltage was not measured, the shift in CEO was evaluated with respect to the wavelength shift to be $-13.1 \pm 1.5\,\mathrm{MHz/nm}$. According to the laser specification (table 3.1), this can be translated to roughly $4.2 \pm 0.5\,\mathrm{MHz/V}$.

[39] For the 2 mm thick window close to the Brewster angle of 55.3 °, a dispersion of $-71\,\mathrm{fs}^2$ is expected.
[40] For the curved mirror, no data was provided.

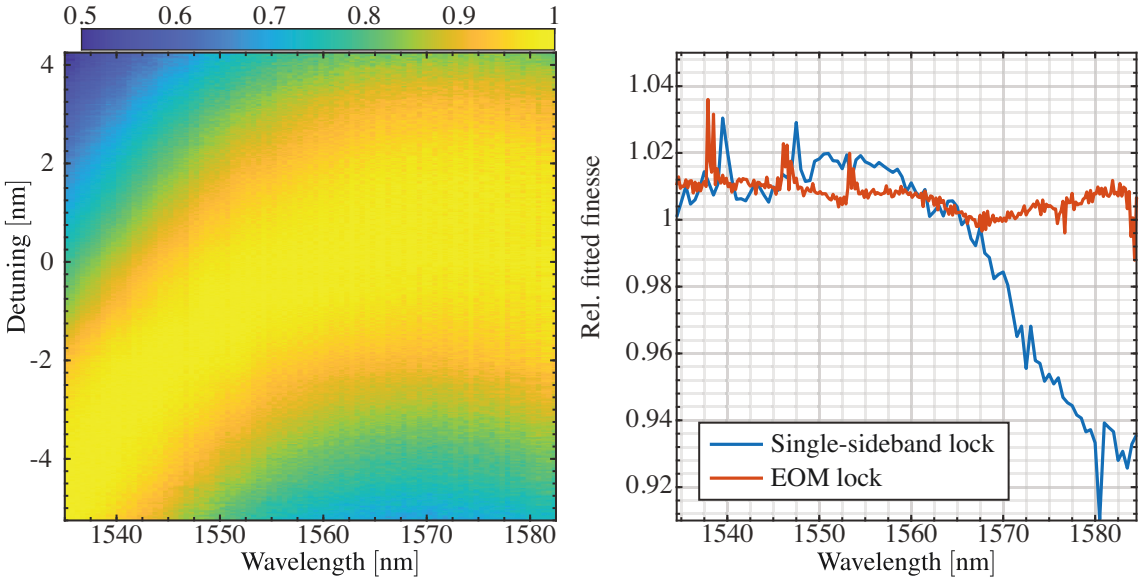

(4.18a) Spectrally resolved normalised intensity transmission detuning

(4.18b) Wavelength-dependent finesse relative to finesse used in detuning calculation

Figure 4.18 Single sideband lock dispersion measurement data and examples of the spectral dependence of fitted finesse values

Nevertheless, its stabilisation would require a faster and more accurate error signal and a low noise controller to minimise additional pump current noise or another adjustment method for the CEO [82].

Aside from the detuning, also the with of the transmission can be investigated. In figure 4.18b the results are shown. For most wavelengths, the individual finesse is well above the finesse of 87 used for determining the detuning which is expected as the dispersive effects broaden the transmission peaks for pulse as seen in figure 4.14. For locking scheme with the CW laser, the finesse decreases with distance to the 1550 nm used for locking. This is also expected from minor drifts in the CEO (equation (4.23)).

The estimation of an overall error for this measurement is difficult as the measured low values ($< 1 \cdot 10^{-28}\,\mathrm{s}^2$) scatter by about 10 % but are derived from less than 6 nm detuning of a 3.75 m long resonator affected by the atmosphere in the laboratory. The accuracy itself is limited by the determined detuning which is calculated from the measured finesse for the overall pulse. But as this measurement is already affected by the dispersion, it is not perfectly accurate. For a better result, the exact shape measured in figure 4.14 could be used to obtain a more accurate detuning estimate but this measurement is mainly limited by the linearity of the piezo.

Remaining deviations between consecutive measurements may be caused by drifts in optical alignment, readjustment of the error signal, in CEO and pulse shape of the laser. As the length is scanned in a long measurement, drifts may occur and also influence the measurement. Nevertheless, the measurement is accurate enough to estimate the influence on the actual BHD measurement.

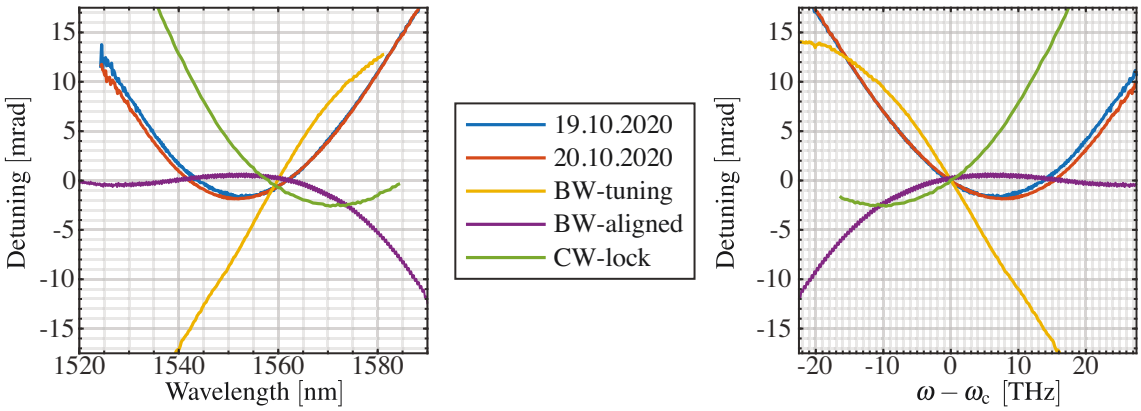

Figure 4.19 Results of dispersion measurements shown as detuning in mrad in dependence of wavelength (left) and angular frequency (right).

	19.10.2020	20.10.2020	BW-detuned	BW-aligned	CW-lock
CEO	−4.9 MHz	−4.7 MHz	−13.5 MHz	1 MHz	5.3 MHz
GDD	60 fs^2	63 fs^2	−18 fs^2	−21 fs^2	54 fs^2

Table 4.3 Results GDD and relative CEO between laser and separation resonator at 1560 nm, derived from the data shown in figure 4.19.

4.5.5 Influence of dispersion on the BHD

In the previous section, the transmitted light was used to characterise the dispersive effects in the separation resonator. In the later discussed BHD, the more severely affected reflected light is analysed. In the actual BHD measurement, off-resonant sidebands are analysed for which the separation resonator is highly reflective and has a flat frequency dependence for the phase and hence they are not significantly affected by the occurring dispersive properties. The observed interference pattern between the carrier components on the other hand strongly depends on the depleted carrier pulse in reflection. As the reflected intensity also consists of other spatial modes and the orthogonal polarisation (figure 4.14), the remaining intensity of reflected depleted carrier cannot be accessed directly in the experiment and most of the expected effects have to be evaluated numerically.

Experimental data

As both reflected and transmitted beam path interfere on a BS in the BHD (figure 5.5), they can be coupled into the OSA. A spectrally resolved interference pattern recorded in discrete steps is shown in figure 4.20. It was observed prior to a factory realignment of the laser system. As the distance between both arms is scanned, the interference patterns of the individual spectral components are not in phase showing the phase shift in reflectance of the resonator. Only close to the central frequency, the reflection is dominated by other

spatial modes than TEM_{00}. These do not interfere with the transmitted TEM_{00} mode if the mirrors are aligned properly.

While this data visualises the effect of the resonator, it is based on an interferometric measurement and aside from the resonator effects, it also depends on the temporal overlap of both pulses at the BS and a larger detuning range is required for an actual evaluation. For this reason and the contribution from unmatched optical power, these measurements were not repeated.

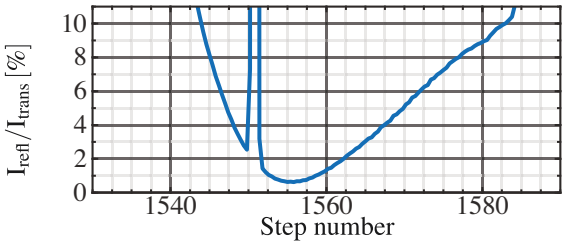

(4.20a) Spectrally resolved ratio of reflected to transmitted intensity

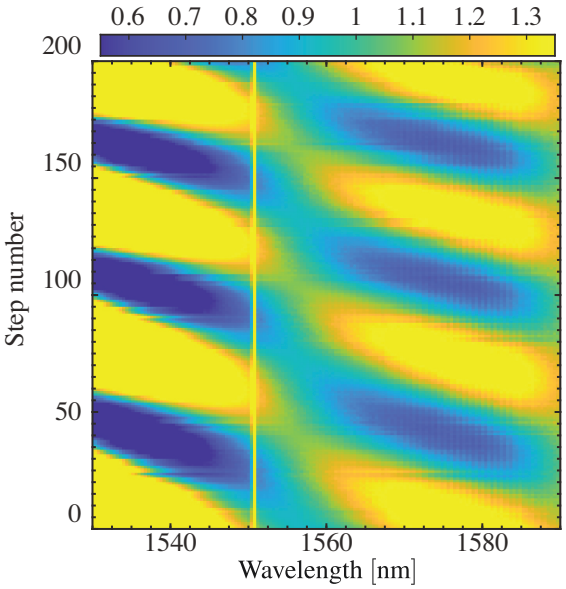

(4.20b) Spectrally resolved interference of transmission and reflection in one port of the BHD
Clipped to preserve detail.

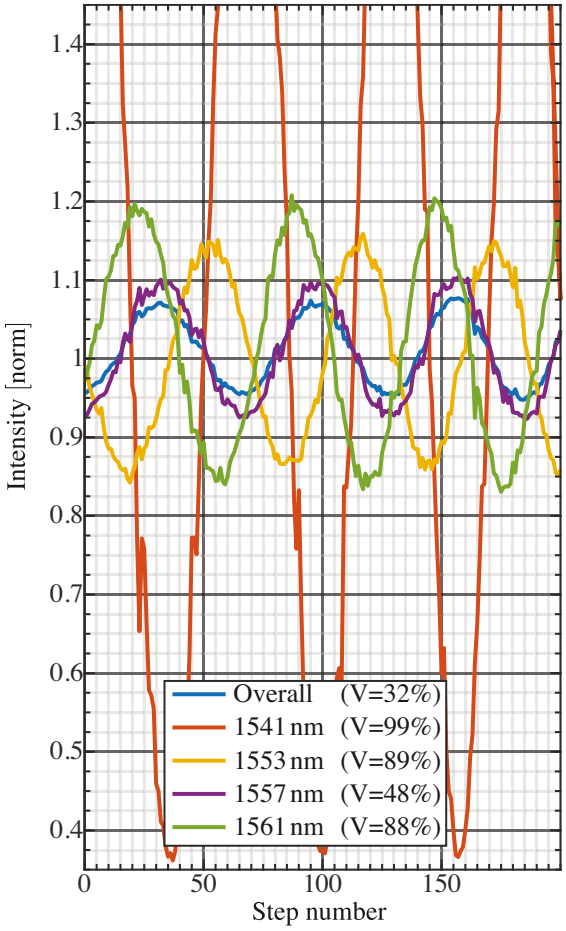

(4.20c) Interference shown for overall pulse and individual spectral components
The stated V is the ratio of observed visibility to maximal theoretical visibility.

Figure 4.20 Spectrally resolved interference in BHD
Data in **(4.20b)** and **(4.20c)** is normalised to the intensity measured in transmission. Data measured using a lock with the CW laser. Pulse is centred at 1557 nm prior to factory realignment. In reflection **(4.20a)**, the CW laser has a significant contribution at 1550 nm.

Simulated influence of the resonator dispersion on the interference pattern

The interference pattern depends on the actual pulse after the nonlinear propagation through the optical fibre and the actual resonator parameters. For the numerical evaluation, the

following parameters are used:

$$\text{Finesse: } 100 \qquad \eta_F^2 = 0.997 \qquad \lambda_c = 1560\,\text{nm} \qquad \Delta t = 150\,\text{fs}$$

Different dispersion effects up to the ToD[41] are considered and shown in figure 4.21a. The amount of dispersion was chosen to be comparable to the actual experimental setup. A detuning is used to obtain maximum overall transmission as depending on the order of dispersion, maximum transmission for the centre wavelength does not necessarily also coincide with maximum overall transmission.

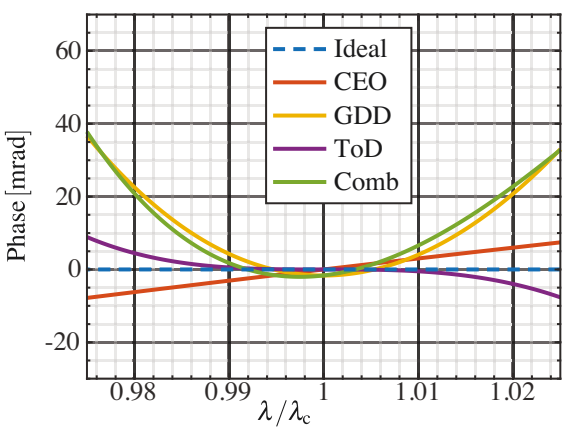

(4.21a) Detuning used in simulation

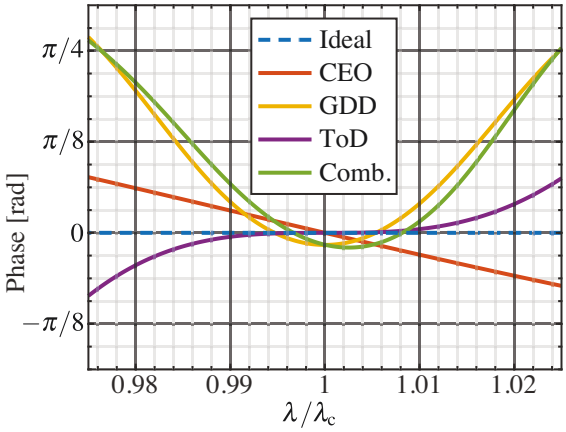

(4.21b) Optical phase in transmission

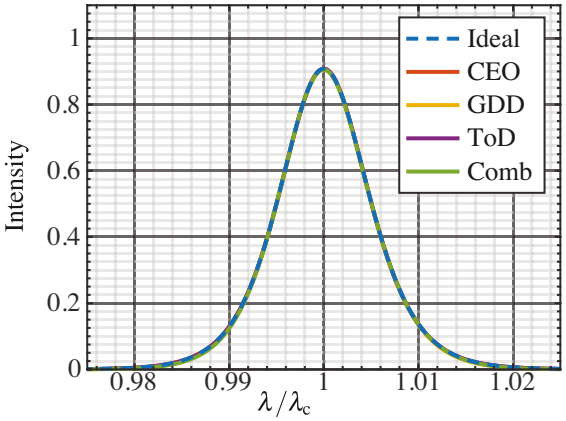

(4.21c) Absolute transmitted intensity

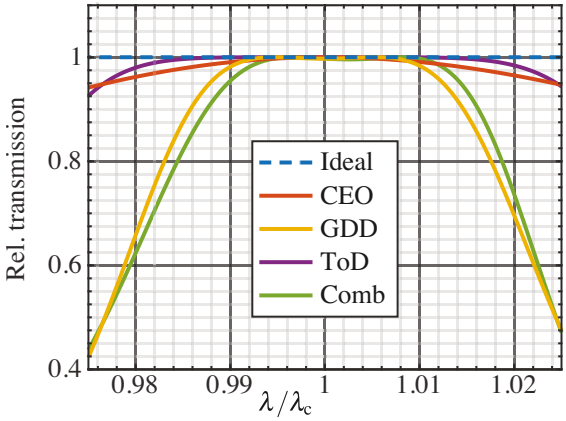

(4.21d) Compared to maximum transmission

Figure 4.21 Simulated spectrally resolved transmission of a resonator
Corresponding detuning indicated in **(4.21a)**. Resulting optical phase is illustrated in **(4.21b)**. **(4.21c)** shows transmitted intensity normalised to the incident intensity at centre wavelength while **(4.21d)** compares it relative to the ideal resonator.

As shown in figure 4.21, the transmitted spectra is only slightly affected by the separation resonator. The reflected spectrum on the other hand is significantly affected as shown in figure 4.22. Its phase is drastically altered as well as the shape of the spectral intensity

[41] third order dispersion

which shows additional peaks. For the CEO, two peaks arise as the effect is symmetric around the central wavelength. GDD on the other hand is also symmetric but increases quadratically. Due to this quadratic behaviour for both shorter and longer wavelengths, the resonator is either too short or too long if it is resonant for the central wavelength. By changing the length of the resonator, the optical power of the transmitted central wavelength is reduced but for all other components the optical power is increased, leading to an overall increased transmission. For ToD, no visible detuning is required. This is an idealisation and additional influences are expected for more complex spectra than the considered perfectly symmetric pulses.

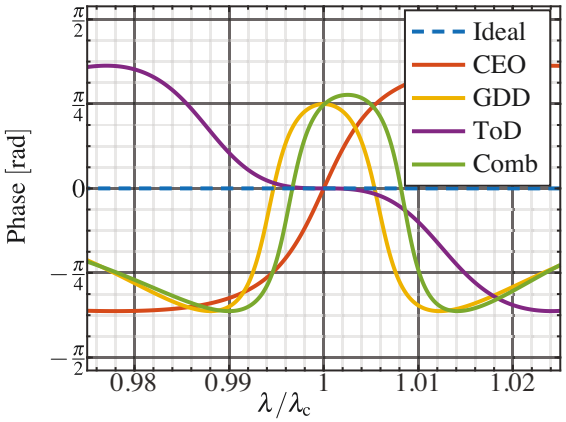

(4.22a) Optical phase in reflection

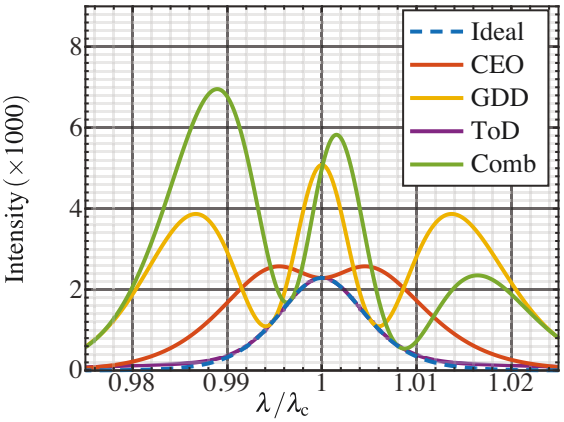

(4.22b) Absolute reflected intensity

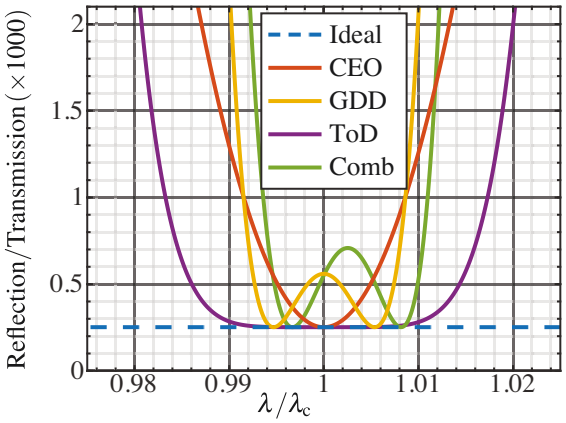

(4.22c) Ratio reflection to transmission

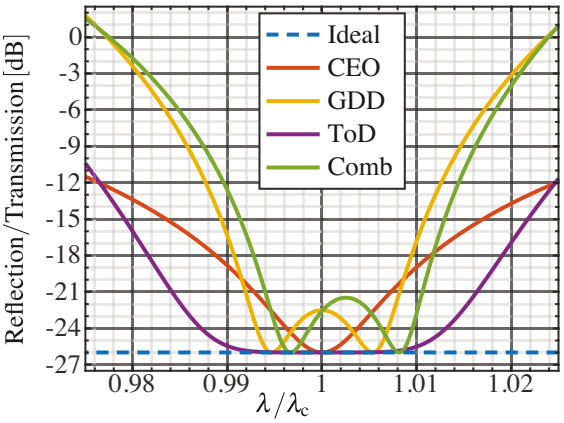

(4.22d) Ratio of transmission and reflection

Figure 4.22 Simulated spectrally resolved reflection of a resonator
Corresponding detuning shown in **(4.21a)**. Resulting phase is illustrated in **(4.22a)**. Reflected intensity is displayed in **(4.22b)**. The ratio between transmitted and reflected intensity is plotted in **(4.22c)** and **(4.22d)** on linear and logarithmic sale.

The reflected depleted carrier pulse is not directly accessible in the experiment but influences the interference pattern observed in the BHD as shown in figure 4.23. For the off-resonant sidebands analysed in BHD, the ideal (unaffected) pulse shape is relevant but as shown figure 4.23a, the envelope of the interference patterns has not only a different shape but its maximum is shifted by several wavelengths. This implies that in the

experimental BHD setup, the interference pattern is not the best indicator for the temporal alignment, *i.e.* the delay between LO and SI.

In figure 4.23b, the difference between the phase of the interference pattern and the ideal interference pattern is shown. For the full evaluation of BHD data, the phase information is required. This information is usually obtained from the interference pattern and will have an error. From figure 4.23b, the extracted phase is expected to differ by roughly 2.5 ° per full period. For the visualisation, a perfect sech^2 pulse was assumed. In the experimental setup, this deviation could be enhanced by the actual pulse shape after the optical fibre or by drifts in the error signal offset. Therefore, the resulting error in the experiment may be higher in the range of 1 % to 2 % which has to be considered in the evaluation.

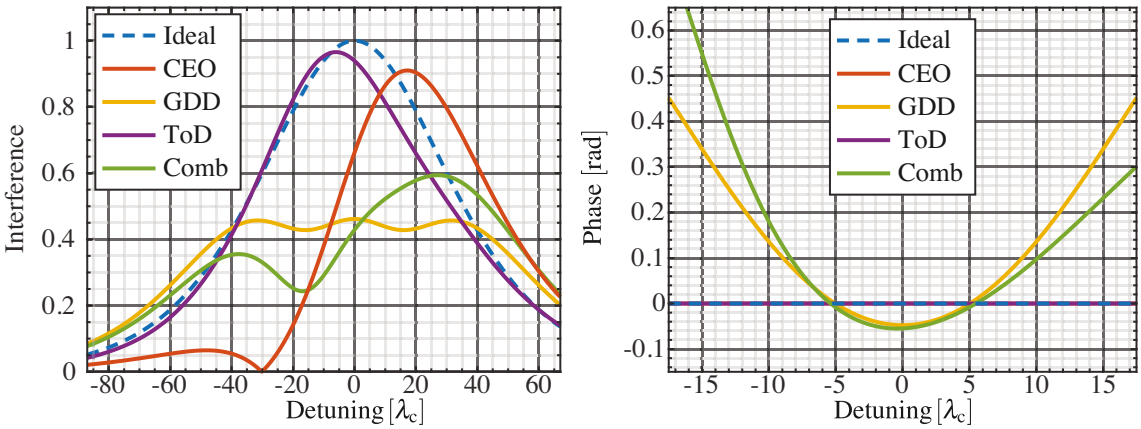

(4.23a) Interference pattern envelope

(4.23b) Phase difference

Figure 4.23 Simulated interference pattern in BHD for dispersive resonators
The envelope of the interference pattern is shown in **(4.23a)** while **(4.23b)** shows the phase difference to an interference pattern with the period λ_c.

4.5.6 Further stabilisation

This section briefly discusses possible methods to further stabilise repetition rate and CEO as at the moment their stability can only be seen as given. Their influences have to be estimated based on separate measurements that are not recorded at the same time. These measurements were recorded weeks or months prior to or after the other measurements.

Presented measurements on the stability indicate that the atmospherical conditions in the laboratory have a strong influence on the laser. This influence is common-mode between laser and resonator and does not necessarily require stabilisation. Any stabilisation of the laser to an external stable reference will destroy these common-mode effects and hence the resonator would additionally require a well stabilised atmosphere. Nevertheless, either a stabilisation or a simultaneous measurement of the stability (and atmospheric conditions) is required as otherwise long-term drifts due to degradation of optical components will affect the measurements and their evaluation.

Repetition rate stabilisation

An external frequency reference can be used to stabilise the repetition rate of the laser. This requires a highly stable frequency reference for a high harmonic of the repetition rate in the GHz regime in order to minimise added phase noise on shorter timescales [114]. Such a system is in principle available directly from the manufacturer.

CEO stabilisation

A portion of the optical power could be sent into an amplifier and a nonlinear fibre to broaden the spectrum for a f-$2f$ measurement to stabilise the CEO. Due to the influence of the air, the CEO difference between resonator and laser is expected to drift by about $0.24\,\mathrm{MHz/hPa}$.

Stabilisation to an optical reference

A stable optical reference [115, 116] could be used to fix one spectral component of the laser. Combined with the CEO stabilisation, this would yield a stable frequency comb. Nevertheless with the current capabilities, the change in stability could not be verified and electronic noise in the required control loops may even decrease the stability.

Relative stabilisation to the separation resonator or a reference resonator

In the existing scheme, the resonator follows the drifts in repetition rate of the laser as the laser resonator is assumed to be the more stable reference. The CEO of the laser is neither measured nor controlled. By spectrally splitting the light used to generate the error signal (figure 4.11b), an error signal for the relative CEO mismatch could be generated and used to also stabilise the CEO similar to the timing jitter characterisation scheme in [117]. To verify a possible improvement in stability, separate measurements of CEO and repetition rate would be required.

Using a monolithic resonator made of low thermal expansion glass may provide a stable low-noise reference for both repetition rate and CEO of a frequency comb. For 80 MHz, a monolithic resonator is very challenging but this idea may become more feasible using either repetition rates above 400 MHz or harmonics of the fundamental repetition rate as the required length decreases from roughly 2 m to only 0.4 m.

5. Balanced homodyne detection

Within the previous chapters, the overall idea of the experimental setup was presented prior to its investigation and experimental characterisation regarding classical properties of laser and resonator estimating their influences on measurements. This chapter focusses on BHD, the method that is used to measure both classical as well as quantum fluctuations of the pulses after propagation through the optical fibre.

Fundamentals of quantum optics and non-classicality cannot be discussed in detail within the extent of this thesis. If additional reading is required, several textbooks either focussing more on theoretical [118–120] or experimental [101, 121, 122] aspects can be recommended.

Nevertheless, a short recapitulation on non-classicality, coherent states, quadrature operators and squeezed light is given before BHD and its measured signals are discussed. Based on these signals, the evaluation of the data is presented in the commonly used strong LO approximation. Additional evaluation methods and approaches tailored to the experimental circumstances in the experimental setup are presented as well.

Last focus of this chapter is the evaluation and discussion of experimentally recorded data on which the further measurements in the following chapters are based.

5.1 Non-classical light

A quantum state is non-classical if quantum mechanics is required for its description as quantum theory can also be used to describe all classical properties[1] of light fields and its photon statistics but classical theories cannot explain quantum behaviour.

To verify non-classicality in a measurement, its result has to be incompatible with classical theories. For example, states with sub-Poissonian photon statistics, such as Fock states[2], or amplitude-squeezed states are non-classical. In contrast, super-Poissonian photon statistics are not necessarily classical. Indeed, a state is only classical if the results of all imaginable measurements are compatible with classical theories.

[1] Assuming the classical state does not violate the uncertainty principle.
[2] Except the vacuum state $|0\rangle$.

Using s-parameterised quasiprobability distributions [123], properties of quantum states can be described in phase space. If the Glauber-Sudarshan P representation [11, 124] can be expressed as a classical probability density, the state is classical. Nevertheless, the P representation is not necessarily a regular function and therefore the Wigner function [125] or Q function [126] are commonly used. Especially for illustrations in phase space, the Wigner function is used as it can be directly related to measured quadrature distributions.

5.2 Quadrature operators and coherent states

Quadrature operators are Hermitian operators that can be defined using the creation $\left(\hat{a}^\dagger\right)$ and annihilation $(\hat{a})$ operators of the corresponding mode with their commutator $\left[\hat{a},\hat{a}^\dagger\right]=1$:

$$\hat{X}_1=\frac{1}{C_N}\left(\hat{a}^\dagger+\hat{a}\right)\qquad \hat{X}_2=\frac{i}{C_N}\left(\hat{a}^\dagger-\hat{a}\right)\qquad \left[\hat{X}_1,\hat{X}_2\right]=2i\cdot C_N^2 \tag{5.1}$$

Coherent states are the quantum analogy to a classical laser [121]. They are displaced vacuum states $(|0\rangle)$ and described by a corresponding complex amplitude α:

$$|\alpha\rangle=e^{-\frac{1}{2}|\alpha|^2}\sum_{n=0}^{\infty}\frac{\alpha^n}{n!}\left(\hat{a}^\dagger\right)^n|0\rangle=\hat{D}(\alpha)\,|0\rangle \tag{5.2}$$

Coherent states are eigenstates of the annihilation operator $(\hat{a}\,|\alpha\rangle=\alpha\,|\alpha\rangle)$ and have Poissonian photon statistics as the expectation value of its photon number $(N=\langle\hat{n}\rangle)$ is equal to its variance $\left(\mathrm{Var}\,(\hat{n})=\langle\hat{n}^2\rangle-\langle\hat{n}\rangle^2\right)$:

$$\langle\alpha|\hat{n}|\alpha\rangle=\langle\alpha|\,\hat{a}^\dagger\hat{a}\,|\alpha\rangle=|\alpha|^2\qquad \langle\alpha|\hat{n}^2|\alpha\rangle=|\alpha|^4+|\alpha|^2 \tag{5.3}$$

For the quadrature operators, the variance of a coherent state is given by:

$$\langle\alpha|\hat{X}_1|\alpha\rangle=\frac{\alpha^*+\alpha}{C_N}\qquad \langle\alpha|\hat{X}_1^2|\alpha\rangle=\left(\frac{\alpha^*+\alpha}{C_N}\right)^2+\frac{1}{C_N^2} \tag{5.4}$$

Depending on the context, different values for C_N are commonly chosen as $\sqrt{2}$ in [118, 121], 2 in [120] or 1 in [101, 119]. From equation (5.4), it can be seen that the expectation value of $\hat{X}_1$ is the real part of the coherent amplitude[3] if $C_N=2$ is used. For $C_N=1$, the variance is given by $\mathrm{Var}\left(\hat{X}_1\right)=1$ which is beneficial for the normalisation in the experiment.

[3] For $\hat{X}_2$, it would be the imaginary part.

By rotation, the quadrature operator can be defined for arbitrary phases:

$$\hat{X}_\varphi = \hat{a}e^{-i\varphi} + \hat{a}^\dagger e^{i\varphi} \tag{5.5}$$

From equation (5.5), $\varphi = 0$ results in $\hat{X}_1$ and $\varphi = \pi/2$ results in $\hat{X}_2$. For coherent states,[4] $\mathrm{Var}\left(\hat{X}_\varphi\right)^2 = 1$ holds true for all angles. From the uncertainty relation [127, 128], the variance of two operators $\left(\hat{A}, \hat{B}\right)$ has to satisfy the following equation:

$$\mathrm{Var}\left(\hat{A}\right)\mathrm{Var}\left(\hat{B}\right) \geq \left|\frac{1}{2}\left[\hat{A}, \hat{B}\right]\right|^2 \tag{5.6}$$

Coherent states have minimum uncertainty, as for two quadratures measuring complementary observables, *e.g.* $\hat{X}_1$ and $\hat{X}_2$ or $\hat{X}_\varphi$ and $\hat{X}_{\varphi+\pi/2}$, both sides of equation (5.6) are equal.

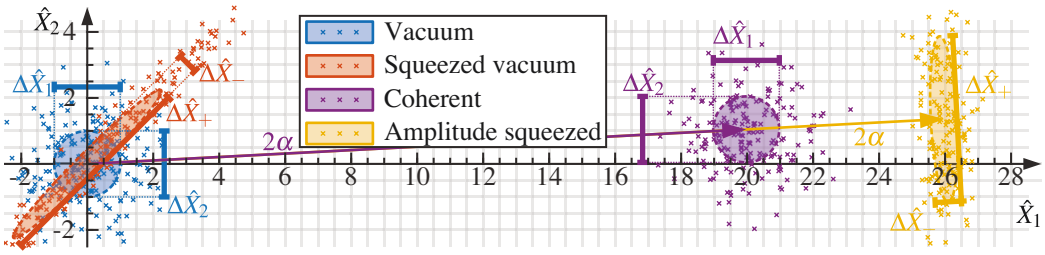

Figure 5.1 Examples of squeezed and coherent states in phase space
For each state, the area of one standard deviation $\Delta\hat{X}$ is illustrated. The minimum and maximum variances are highlighted.

5.3 Properties of squeezed states

For certain quadrature angles, squeezed states show a lower variance compared to the circular uncertainty of coherent states (figure 5.1). As they have to comply with the uncertainty principle, the orthogonal quadrature has a higher variance as shown in figure 5.3a[5]. Squeezed states can allow more accurate measurements than even a perfectly coherent laser can obtain [13, 15] but only if the corresponding quadrature is measured as otherwise less accuracy is achieved.

An ideal squeezed vacuum can be created by applying the squeezing operator[6], with the complex squeezing parameter $\xi = r \cdot e^{i\varphi_\xi}$, on the vacuum state [118, Ch. 2.3]. The

[4] Including the quantum vacuum $|0\rangle$ which is a coherent state with zero amplitude.

[5] Figure shows Kerr-squeezed states which are comparable to squeezed states for large coherent amplitudes as shown in figure 5.2.

[6] $\hat{S} = \exp\left(\frac{1}{2}\xi\hat{a}^{\dagger 2} + \frac{1}{2}\xi^*\hat{a}^2\right)$

corresponding quadrature variances (using $C_N = 1$) can be calculated accordingly:

$$\mathrm{Var}\left(\hat{X}_\varphi\right) = \cosh(2r) + \sinh(2r) \cdot \cos\left(2\varphi - \varphi_\xi\right) \tag{5.7}$$

$$= V_- \cdot \cos^2(\varphi - \theta_{\mathrm{sq}}) + V_+ \cdot \sin^2(\varphi - \theta_{\mathrm{sq}}) \tag{5.8}$$

Only for the angle $\frac{\varphi_\xi}{2}$ and $\frac{\varphi_\xi}{2} + \frac{\pi}{2}$, the product of the variances of equation (5.7) is equal to 1. For all other orthogonal quadratures, the product is above 1. To describe these variances in equation (5.8), V_- for the lower variance (for the ideal case e^{-2r}) and V_+ (ideally e^{2r}) for the higher variance were used in combination with one angle $\left(\theta_{\mathrm{sq}} = \varphi_\xi/2\right)$.

By using V_- and V_+, additional losses[7] and additional noise such as noise in the phase quadrature $\hat{X}_2$ (chapter 6) can be included. With additional uncorrelated Gaussian noise, the state can still be described in the same way, using increased quadrature variances and the according angle if the initial state was Gaussian, such as an ideal squeezed state.

A commonly used method to create squeezed states is the optical parametric amplifier [129] which can be used to obtain a squeezed vacuum with no significant coherent amplitude [130, 131] or a bright squeezed state [39, 132].

5.4 Kerr squeezing

Another method to create squeezed light is Kerr squeezing where the phase is modulated by the intensity fluctuations via the nonlinear refractive index of a media creating quantum correlations resulting in squeezing as shown in figure 5.2. Within this chapter, only an illustrative overview for the single-mode CW case is given. The discussed properties, in combination with phase noise and linear losses, are sufficient to describe most of the experimentally observed behaviour. As in the previous chapters, the properties of pulses lead to a more complex behaviour that is illustrated in appendix F.

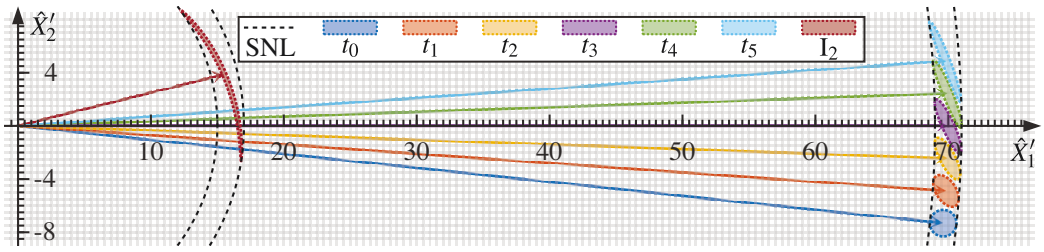

Figure 5.2 Illustration of Kerr squeezing in phase space
The initial coherent state (t_0) evolves into a squeezed state (t_{1-5}) but remains limited by shot noise. For a small amplitude or a strong interaction, the shape of the uncertainty regions rather resembles a "banana" instead of an ellipse. Angles were shifted for better visualisation. Phase-resolved variances are shown in figure 5.3.

[7] Section 5.5.2.

As described for example in [51, 101, 133], the interaction is based on the photon number operator $\hat{n}$ and therefore commutes with all direct photon number measurements. As the signal of a linear photodetector is proportional to the detected number of photons, the effect cannot be detected directly. For weak interaction, the transformation resembles squeezing and can be described like a squeezed state with two variances (V_- and V_+). The angle θ_{sq} between the quadratures of minimum and amplitude quadrature can be calculated from V_- and V_+:

$$\theta_{sq} = \operatorname{acos} \sqrt{\frac{1 - V_+}{V_- - V_+}} \tag{5.9}$$

Equation (5.9) assumes that the initial light was limited by shot noise as additional input noise would translate to the output noise [134]. For stronger interaction at low coherent amplitudes, the shape starts to resemble a "banana" as shown in figure 5.2 or even superpositions of two or four discrete coherent states [135]. As shown in figure 5.3b, the probability distributions for the quadratures of Kerr-squeezed states is well approximated by Gaussian distributions for weak interaction, *e.g.* when the coherent amplitude is large compared to the effect. Significant deviations from this behaviour, as the shown "banana", are not expected as each pulse has close to 10^9 at an average optical power of 10 mW.

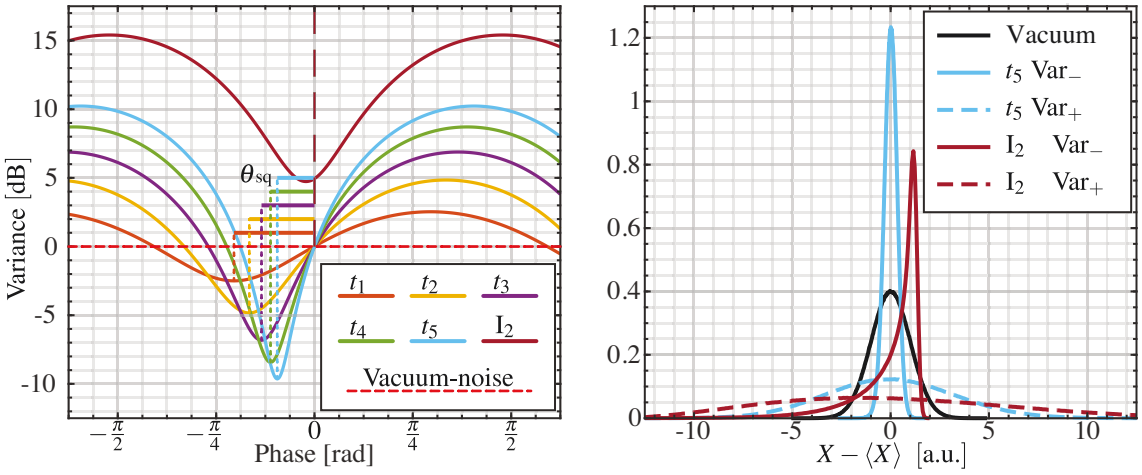

(5.3a) Phase-resolved variances

(5.3b) Probability distribution of values

Figure 5.3 Illustration of phase-resolved variances with squeezing angle **(5.3a)** and distribution of measurement values **(5.3b)**
For the illustration in phase space see figure 5.2. Squeezing angle is stated relative to amplitude quadrature ($\varphi = 0$) as in equation (5.9).

5.5 Signals in balanced homodyne detection

5.5.1 Direct detection

The signal of a linear photodiode is proportional to the number incident of photons as they create electron-hole pairs which are translated to a current as reviewed in more detail in [136, 137]. By substituting $\hat{a}^\dagger$ and $\hat{a}$ with a classical coherent amplitude α with small quantum fluctuations $\delta\hat{a}^\dagger$ and $\delta\hat{a}$, the photon number operator can be written as:

$$\hat{a}^\dagger = \alpha^* + \delta\hat{a}^\dagger \qquad \hat{a} = \alpha + \delta\hat{a} \tag{5.10}$$

$$\hat{n} = \hat{a}^\dagger\hat{a} = |\alpha|^2 + |\alpha|\left(e^{-i\varphi_\alpha}\delta\hat{a} + e^{i\varphi_\alpha}\delta\hat{a}^\dagger\right) + \delta\hat{a}^\dagger\delta\hat{a} \tag{5.11}$$

$$= |\alpha|^2 + |\alpha|\delta\hat{X}_{\varphi_\alpha} + \delta\hat{a}^\dagger\delta\hat{a} \tag{5.12}$$

From equation (5.12), it can be seen that the coherent amplitude and the fluctuations in its direction are measured if $\delta\hat{a}^\dagger\delta\hat{a}$ can be neglected compared to $|\alpha|$. Generally, the reference frame is chosen to set $\varphi_\alpha = 0$ and it measures $\hat{X}_1$ which is usually referred to as amplitude quadrature. If multiple coherent amplitudes, labelled j, have to be considered, only one can be freely chosen by an appropriate global phase and hence, the corresponding amplitude quadratures will be referred to as $\hat{X}_{\mathrm{j,A}}$. The largest contribution $|\alpha|^2$ is constant and can be subtracted. To measure other quadratures in direct detection, the coherent amplitude has to be altered in phase relative to its sidebands before the detection [138, 139].

5.5.2 Quantum beamsplitter

To change the coherent amplitude prior to detection, interference with a matched coherent state on a BS can be used. Compared to a classical BS, which can simply split the beam, a quantum BS always has to have the same number of input and output states.

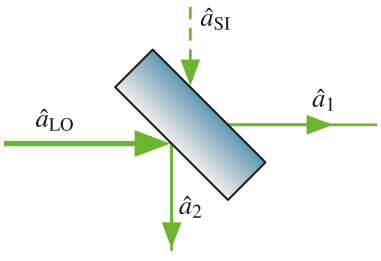

$$\begin{pmatrix}\hat{a}_1\\ \hat{a}_2\end{pmatrix} = \begin{pmatrix}\cos\phi & \sin\phi\\ -\sin\phi & \cos\phi\end{pmatrix}\cdot\begin{pmatrix}\hat{a}_{\mathrm{LO}}\\ \hat{a}_{\mathrm{SI}}\end{pmatrix} \tag{5.13}$$

Figure 5.4 Quantum BS with operator labelling for BHD and transformation
The value of ϕ gives the intensity transmissivity $(\cos\phi)^2$ and reflectivity $(\sin\phi)^2$ of the BS. For BHD, a symmetric BS, *i.e.* $\cos\phi = \sin\phi = \frac{1}{\sqrt{2}}$ is required.

This mechanism can also be used to describe the effect of linear losses (see [101, Ch. 7.4]) in the path to the detection, *e.g.* the efficiency of the detection. From equation (5.13)

with an intensity transmission equal to the quantum efficiency η_{QE}, the measured variance can be corrected for known linear losses as the reflected vacuum adds the variance of the vacuum, here simply written as $\mathrm{Var}_{\mathrm{vac}}$, to the measurement:

$$\mathrm{Var}\left(\hat{X}\right)_{\mathrm{true}} = \frac{1}{\eta_{\mathrm{QE}}}\mathrm{Var}\left(\hat{X}\right)_{\mathrm{meas}} + \frac{\eta_{\mathrm{QE}}-1}{\eta_{\mathrm{QE}}}\mathrm{Var}_{\mathrm{vac}} \tag{5.14}$$

5.5.3 Detector currents

For BHD, a splitting ration of 50 : 50 is used where the state under investigation, the SI, is interfered with a coherent state, the LO as shown in the experimental setup in figure 5.5. Using equation (5.10), the operators $(\hat{a}_{1,2})$ of the BS and the corresponding $\hat{n}_{1,2}$ can be derived:

$$\hat{a}^{\dagger}_{1,2} = \frac{1}{\sqrt{2}}\left(\alpha^{*}_{\mathrm{LO}} + \delta\hat{a}^{\dagger}_{\mathrm{LO}} \pm \alpha^{*}_{\mathrm{SI}} \pm \delta\hat{a}^{\dagger}_{\mathrm{SI}}\right) \tag{5.15}$$

$$\begin{aligned}\hat{n}_{1,2} = \frac{1}{2}\Bigg(& \overbrace{|\alpha_{\mathrm{LO}}|^2 + |\alpha_{\mathrm{SI}}|^2}^{\text{I: mean value}} \pm \overbrace{(\alpha^{*}_{\mathrm{LO}}\alpha_{\mathrm{SI}} + \alpha_{\mathrm{LO}}\alpha^{*}_{\mathrm{SI}})}^{\text{II: interference pattern}} \ldots \\ & \cdots + |\alpha_{\mathrm{LO}}|\cdot\hat{X}_{\mathrm{LO,A}} + |\alpha_{\mathrm{SI}}|\cdot\hat{X}_{\mathrm{SI,A}} \ldots \Big\}\text{III: amplitude noise} \\ & \cdots \pm \underbrace{|\alpha_{\mathrm{LO}}|\cdot\hat{X}_{\mathrm{SI},\varphi_{\mathrm{LO}}}}_{\text{IV: } \hat{X}_{\mathrm{SI}} \text{ selected by LO}} \pm \underbrace{|\alpha_{\mathrm{SI}}|\cdot\hat{X}_{\mathrm{LO},\varphi_{\mathrm{SI}}}}_{\text{V: } \hat{X}_{\mathrm{LO}} \text{ selected by SI}} + \underbrace{\delta\hat{a}^{\dagger}_{\mathrm{LO}}\delta\hat{a}_{\mathrm{LO}} + \ldots}_{\text{VI: } \ll|\alpha|\cdot\hat{X}}\Bigg)\end{aligned} \tag{5.16}$$

In equation (5.16), the terms I are the constant mean values proportional to the optical power of LO and SI while terms II describe the interference pattern observed scanning the phase. Generally, they are removed using a high-pass filter prior to the evaluation. The terms in VI contain only products of small fluctuations which can be neglected compared to the terms proportional to the coherent amplitudes if those are much larger in comparison. This reduces the complexity to the amplitude noise terms III and the quadrature variances selected by the phase of the LO in terms IV and V. The fluctuations $\Delta\hat{n}$ of the photon number can then be written as:

$$\Delta\hat{n}_{1,2} \propto |\alpha_{\mathrm{LO}}|\cdot\left(\hat{X}_{\mathrm{LO,A}} \pm \hat{X}_{\mathrm{SI},\varphi_{\mathrm{LO}}}\right) + |\alpha_{\mathrm{SI}}|\cdot\left(\hat{X}_{\mathrm{SI,A}} \pm \hat{X}_{\mathrm{LO},\varphi_{\mathrm{SI}}}\right) \tag{5.17}$$

Equation (5.17) is an approximation for the measured number of photons detected in the outputs of the BS for strong coherent amplitudes. The resulting filtered photocurrents $\mathcal{I}_{1,2}$ are then directly proportional to the fluctuations in the number of detected photons. Subtraction and addition allow to further separate the terms:

$$\mathrm{add} = \mathcal{I}_1 + \mathcal{I}_2 \quad \propto |\alpha_{\mathrm{LO}}|\cdot\hat{X}_{\mathrm{LO,A}} + |\alpha_{\mathrm{SI}}|\cdot\hat{X}_{\mathrm{SI,A}} \tag{5.18}$$

$$\mathrm{sub} = \mathcal{I}_1 - \mathcal{I}_2 \quad \propto |\alpha_{\mathrm{LO}}|\cdot\hat{X}_{\mathrm{SI},\varphi_{\mathrm{LO}}} + |\alpha_{\mathrm{SI}}|\cdot\hat{X}_{\mathrm{LO},\varphi_{\mathrm{SI}}} \tag{5.19}$$

The add-signal measures the amplitude fluctuations of both LO and SI. By a global phase, either φ_{LO} or φ_{SI} can be chosen to be 0 and only one effective phase φ is important and hence only one phase has to be varied in the experimental setup. Both equation (5.18) and equation (5.19) contain a factor of 2 that is neglected[8] here.

Balanced detection

Balanced detection is a quite useful scheme as one of the input beams is blocked and hence only vacuum fluctuations are present in all modes of this port. In this case the add-signal measures the amplitude fluctuations of the input state and the sub-signal yields the vacuum fluctuations as a reference. Amplitude fluctuations can be measured relative to the vacuum noise by division:

$$\frac{\mathrm{Var}_{\mathrm{add}}}{\mathrm{Var}_{\mathrm{sub}}} = \frac{|\alpha_{\mathrm{SI}}|^2 \cdot \mathrm{Var}\left(\hat{X}_{\mathrm{SI,A}}\right)}{|\alpha_{\mathrm{SI}}|^2 \cdot \mathrm{Var}\left(\hat{X}_{\mathrm{vac,A}}\right)} = \frac{\mathrm{Var}\left(\hat{X}_{\mathrm{SI,A}}\right)}{\mathrm{Var}_{\mathrm{vac}}} \tag{5.20}$$

The choice of C_N in equation (5.1) becomes meaningful as no further normalisation is required if $C_N = 1$ is chosen. An important property of these measurements is their use of the vacuum fluctuation in the second port and hence, as for a blocked beam all spatial modes are essentially in a vacuum state, the mode matching is not important.

5.5.4 Conventional strong LO approximation

Conventionally, the LO is much stronger than its fluctuations and the coherent amplitude of the SI and both contributions can be neglected. The variance measured in BHD with LO and SI interfering (called $\mathrm{sub}_{\mathrm{BHD}}$) is then proportional to the fluctuations of the SI in the selected phase φ. Blocking the SI allows to measure a vacuum reference for the specific LO intensity in a separate measurement (called $\mathrm{sub}_{\mathrm{LO}}$) prior to or after the actual one. Assuming the LO intensity remains constant, the fluctuations of the SI can be extracted:

$$\frac{\mathrm{Var}\left(\mathrm{sub}_{\mathrm{BHD}}\right)}{\mathrm{Var}\left(\mathrm{sub}_{\mathrm{LO}}\right)} = \frac{|\alpha_{\mathrm{LO}}|^2 \cdot \mathrm{Var}\left(\hat{X}_{\mathrm{SI},\varphi}\right)}{|\alpha_{\mathrm{LO}}|^2 \cdot \mathrm{Var}\left(\hat{X}_{\mathrm{vac},\varphi}\right)} = \frac{\mathrm{Var}\left(\hat{X}_{\mathrm{SI},\varphi}\right)}{\mathrm{Var}_{\mathrm{vac}}} \tag{5.21}$$

BHD requires the spatial modes of both beams to be matched as close to perfect as possible as otherwise the part from the coherent amplitude of the LO that interferes with the SI is significantly lower than the coherent amplitude that records the vacuum noise reference. Within the experimental setup, this is ensured as both beams are in the TEM_{00} mode of the resonator and the BS has the same distance relative to the beamwaist for both beams[9].

[8] Or moved to the gain of the detector electronics. As mostly ratios between two measurements are evaluated and this factor is cancelled out.

[9] Interference is only observed if the pulses overlap in time. For 200 fs, the corresponding distance is less than 1 mm and well below the Rayleigh length of the resonator calculated in section 4.2.1.

A first correction to these measurements is the correction for uncorrelated electronic dark noise contained in every single measurement. As uncorrelated variances add up, it can be measured by one additional measurement $\mathrm{sub}_{\mathrm{dark}}$ and then be subtracted from the other measurements. As for measured squeezing, the influence of dark noise in the numerator is greater than in the denominator and the assumed squeezing is increased by this correction.

5.5.5 Corrections to conventional evaluation

First, an estimate for the influence of the non-vanishing coherent amplitude of the SI in the experimental setup will be derived. The neglected term of equation (5.19) introduces a φ-dependent measurement of the LO noise proportional to α_{SI}. Knowledge of the complete quantum state of the LO is required to correct for this noise.

A coherent LO is assumed[10] which has a known phase-independent magnitude uncorrelated with any other contribution. Hence, it can be measured separately with only the SI and a blocked LO in measurement $\mathrm{sub}_{\mathrm{SI}}$.

$$\frac{\mathrm{Var}\left(\mathrm{sub}_{\mathrm{BHD}}\right) - \mathrm{Var}\left(\mathrm{sub}_{\mathrm{SI}}\right)}{\mathrm{Var}\left(\mathrm{sub}_{\mathrm{LO}}\right)} = \frac{\left[|\alpha_{\mathrm{LO}}|^2 \cdot \mathrm{Var}\left(\hat{X}_{\mathrm{SI},\varphi}\right) + |\alpha_{\mathrm{SI}}|^2 \cdot \mathrm{Var}_{\mathrm{vac}}\right] - |\alpha_{\mathrm{SI}}|^2 \cdot \mathrm{Var}_{\mathrm{vac}}}{|\alpha_{\mathrm{LO}}|^2 \cdot \mathrm{Var}_{\mathrm{vac}}} \tag{5.22}$$

Clearly, the corrected equation (5.22) increases the measured squeezing compared to equation (5.21) that has neglected the small contributions from $|\alpha_{\mathrm{SI}}|^2$ term. Increasing the measured squeezing is not the actual intention for this correction. More importantly, the phase and amplitude quadrature of the Kerr-squeezed state can be identified as its amplitude quadrature variance is given precisely by the shot noise (figure 5.6). This information about the orientation of the squeezing ellipse is required for the later analysis of the influences by GAWBS phase noise in chapter 6.

5.5.6 Extended evaluation methods

Conventional evaluation (section 5.5.4) requires three measurements for which the experimental setup has to be physically changed to block different beam paths, *i.e.* both beams, only LO and additionally one dark measurement. If the correction for the coherent amplitude of the SI is intended, an additional fourth measurement is required. Only the dark measurement is constant and all three other measurements have to be repeated with the corresponding physical changes for every single parameter change. Especially for multiple measurements, this and the required blocking and unblocking of beam paths

[10] Which is accurate as the laser is specified (appendix C) to be limited by shot noise above 100 kHz. This was verified for the measurement frequencies (figure 5.6). Additionally, these frequency are well above the linewidth of the separation resonator and replaced by the reflected vacuum (figure 3.1).

increases the overall required measurement time. This can be overcome by using more information than contained in only the sub-signal.

One possibility is the additional analysis of the add-signal combined with the sub-signal, assuming perfect mode matching and the LO in a perfect coherent state:

$$\frac{\mathrm{Var}\left(\mathrm{sub}_{\mathrm{BHD}}\right)}{\mathrm{Var}\left(\mathrm{add}_{\mathrm{BHD}}\right)} = \frac{|\alpha_{\mathrm{LO}}|^2 \cdot \mathrm{Var}\left(\hat{X}_{\mathrm{SI},\varphi}\right) + |\alpha_{\mathrm{SI}}|^2 \cdot \mathrm{Var}_{\mathrm{vac}}}{|\alpha_{\mathrm{LO}}|^2 \cdot \mathrm{Var}_{\mathrm{vac}} + |\alpha_{\mathrm{SI}}|^2 \mathrm{Var}\left(\hat{X}_{\mathrm{SI,A}}\right)} \tag{5.23}$$

Under the approximation of a much stronger LO, equation (5.23) reduces to the result of the conventional evaluation with one key difference as the second measurement with only LO is not required. The correction for the coherent amplitude of the SI requires $|\alpha_{\mathrm{SI}}|^2 \cdot \mathrm{Var}_{\mathrm{vac}}$ and $|\alpha_{\mathrm{SI}}|^2 \cdot \mathrm{Var}\left(\hat{X}_{\mathrm{SI,A}}\right)$ which can be obtained from the only SI measurement. Nevertheless, this evaluation strictly requires a perfect[11] coherent state for the LO[12] as additional LO noise will lead to an increased vacuum variance[13] and the evaluation claims squeezing even if no squeezing is present. Aside from one less measurement, this method does not require a long-term stable optical power for the LO as the reference is recorded implicitly at the same time.

Another simplification can be used if the amplitude quadrature of the SI is additionally limited by shot noise. This is true for the Kerr-squeezed pulse (figure 5.6) and equation (5.23) can be further analysed:

$$\frac{\mathrm{Var}\left(\mathrm{sub}_{\mathrm{BHD}}\right)}{\mathrm{Var}\left(\mathrm{add}_{\mathrm{BHD}}\right)} = \frac{|\alpha_{\mathrm{LO}}|^2 \cdot \mathrm{Var}\left(\hat{X}_{\mathrm{SI},\varphi}\right) + |\alpha_{\mathrm{SI}}|^2 \cdot \mathrm{Var}_{\mathrm{vac}}}{|\alpha_{\mathrm{LO}}|^2 \cdot \mathrm{Var}_{\mathrm{vac}} + |\alpha_{\mathrm{SI}}|^2 \mathrm{Var}_{\mathrm{vac}}} \tag{5.24}$$

This can be seen as $\mathrm{Var}\left(\hat{X}_{\mathrm{SI},\varphi}\right)$ and $\mathrm{Var}_{\mathrm{vac}}$ normalized to $\mathrm{Var}_{\mathrm{vac}}$:

$$\ldots = \left(1 + \left|\frac{\alpha_{\mathrm{SI}}}{\alpha_{\mathrm{LO}}}\right|^2\right)^{-1} \frac{\mathrm{Var}\left(\hat{X}_{\mathrm{SI},\varphi}\right)}{\mathrm{Var}_{\mathrm{vac}}} + \left(1 + \left|\frac{\alpha_{\mathrm{LO}}{}^2}{\alpha_{\mathrm{SI}}}\right|\right)^{-1} \frac{\mathrm{Var}_{\mathrm{vac}}}{\mathrm{Var}_{\mathrm{vac}}} \tag{5.25}$$

$$= \left(\eta_{\mathrm{P}} \mathrm{Var}\left(\hat{X}_{\mathrm{SI},\varphi}\right) + (1 - \eta_{\mathrm{P}})\, \mathrm{Var}_{\mathrm{vac}}\right) \frac{1}{\mathrm{Var}_{\mathrm{vac}}} \tag{5.26}$$

For the last step to equation (5.26), $\left(1 + \left|\frac{\alpha_{\mathrm{SI}}}{\alpha_{\mathrm{LO}}}\right|^2\right)^{-1}$ was written as η_{P} as it has the same effect as a limited quantum efficiency (equation (5.14)). Correction for this loss can be done based upon the average intensities of LO and SI. These quantities can, in principle, be measured simultaneously, reducing the initially required three measurements (plus dark measurement) to one measurement (plus dark measurement).

[11] At least for the sideband frequencies used for BHD.

[12] In theory, a portion of the LO can be measured separately to monitor its amplitude noise in a balanced detection.

[13] See appendix H, where this scheme is applied to experimental data from a single-mode CW-squeezed state and compared with the earlier methods.

Nevertheless, this procedure has strong requirements as not the LO has to be coherent but also the SI needs to be limited by shot noise. Furthermore, the mode matching has to be sufficient as the term $|\alpha_{\mathrm{LO}}|^2 \cdot \mathrm{Var}\left(\hat{X}_{\mathrm{SI},\varphi}\right)$ is scaled by the overlap between LO and SI. All other terms proportional to vacuum fluctuations are scaled by the full intensity.

Correlations in BHD

Previously mentioned methods are based on the sum and difference of both detector currents and the analysis of their variances within a certain time or amount of samples. Additional to the required filtering (appendix A), computational effort is required. Another approach can be made by correlating both detector currents[14] as in [140, 141]. If the LO is in a coherent state, it is not correlated with the SI.

$$\langle \mathcal{I}_1 \cdot \mathcal{I}_2 \rangle - \langle \mathcal{I}_1 \rangle \langle \mathcal{I}_2 \rangle = |\alpha_{\mathrm{LO}}|^2 \left[\mathrm{Var}_{\mathrm{vac}} - \mathrm{Var}\left(\hat{X}_{\mathrm{SI},\varphi}\right) \right] + |\alpha_{\mathrm{SI}}|^2 \left[\mathrm{Var}\left(\hat{X}_{\mathrm{SI,A}}\right) - \mathrm{Var}_{\mathrm{vac}} \right] \quad (5.27)$$

The first term (proportional to $|\alpha_{\mathrm{LO}}|^2$) of equation (5.27) is only positive if the SI is squeezed in the chosen quadrature. The second term vanishes under the assumption of the SI being limited by shot noise which was already made for equation (5.24). Without the proper normalisation, the amount of squeezing cannot be extracted solely from the correlation but its existence can be easily verified. By the combination with the variances of either the data from add or sub, the normalisation can be obtained. The earlier neglected factor of 2 has to be considered for this.

This processing requires only multiplication of two simultaneously recorded samples after the filtering process and an averaging process. It can be used to directly check the alignment of the BHD and is less demanding on the limited resources (appendix G).

5.6 Experimental setup and measurements

The experimental setup for the BHD is shown in figure 5.5. The SI port of the BHD is aligned to the reflection on the separation resonator and can be changed to the fibre output by blocking the beam inside the resonator. The LO can be switched using the FM between the transmitted beam from the separation resonator and the pulse shaped by the SLM (figure 7.3), represented by four combinations for a two-mode measurement.

All beams are interferometrically aligned on the BS in BHD and one output port can be coupled into a fibre connected to the OSA. The used ND[15] filter suppresses nonlinear propagation in this fibre and allows the measurement of the individual spectra, enabling

[14] Electronic dark noise has to be uncorrelated.
[15] neutral density

characterisation as shown in figure 5.7a or section 4.5, or the interference between the individual pulses as in figure 4.20.

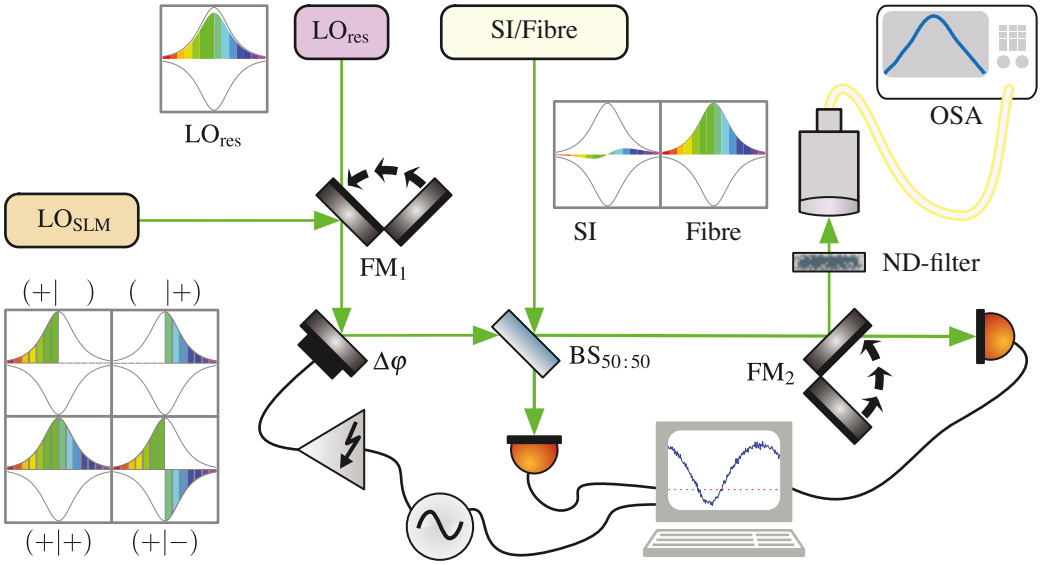

Figure 5.5 Schematic overview of the experimental BHD setup
Additional steering mirrors and delay lines for temporal and spatial overlap are not shown.

5.6.1 Shot-noise-limited LO and fibre output

After propagation through the fibre, the amplitude quadrature fluctuations of the the pulse should not be affected and hence be limited by shot noise. The LO, transmitted by the separation resonator, should be in a coherent state for the sidebands around 5.6 MHz.

To observe the amplitude quadrature, a balanced detection (equation (5.20)) is used and evaluated. Demonstrated in figure 5.6, both paths are indeed limited by shot noise. Details on the detector parameters and used filters can be found in appendix A.

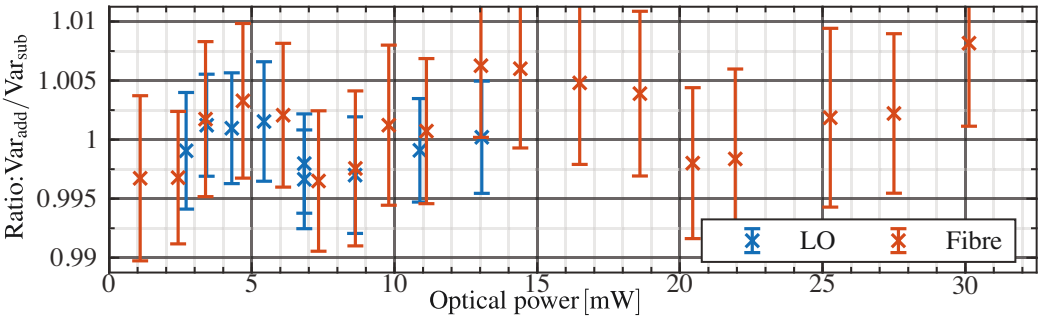

Figure 5.6 Shot noise level of LO and fibre output compared with vacuum noise at multiple optical powers. Two representative measurements were chosen. Data for fibre was recorded prior to the integration of the SLM which limits the available optical power. Optical power was measured directly in front of the BHD. Error bars give the 95 % confidence interval.

5.6.2 Alignment procedure

The mode matching between the optical fibre was discussed in section 4.2.2 and all involved paths are either in the TEM_{00} mode of the separation resonator or the highly matched fibre mode. For a coarse alignment, SFL is used and the achievable visibility is mainly limited by the orthogonal polarisation and the other spatial modes (figure 4.14). After coarse alignment, the PDH locking scheme (section 4.3.1) is used to stabilise the separation resonator. As soon as the resonator is locked, the interference pattern changes as the coherent carrier is transmitted. The resulting interference pattern cannot be used to fully adjust the temporal overlap of SI and LO (figure 4.23a). Instead, the signal of both detectors is subtracted and fed into a spectrum analyser. Blocking the SI path, a vacuum reference is recorded before the observed (anti-)squeezing is maximised while scanning the delay of the LO (procedure described in section 5.5.4 and shown in figure 5.7b). After alignment, the electric signals are connected to the digitising hardware controlled by a computer. Within the limitations of the digitising hardware (appendix G), the recording length and resolution are chosen.

In figure 5.7a, the ratio between LO and SI intensity was spectrally resolved after all modes were matched to the fibre for the OSA. Measured at 5 mW average power propagating through the optical fibre, 92.7 % of all optical power is contained within a region where the LO is 20 dB stronger than the SI and for above 99.7 % the LO is still more than 10 dB stronger.

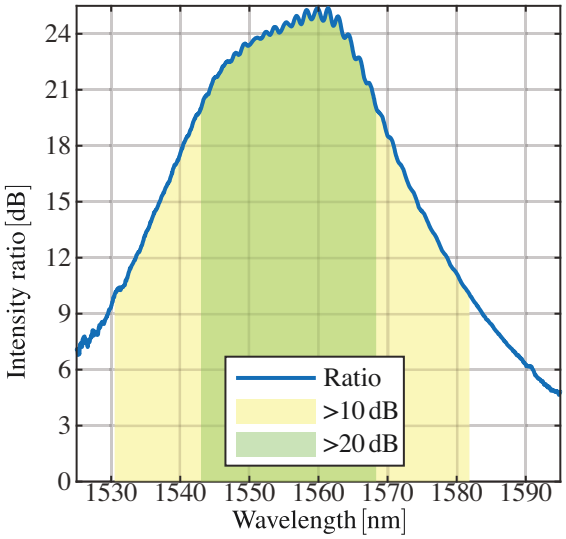

(5.7a) Spectrally-resolved intensity ratio between LO and SI

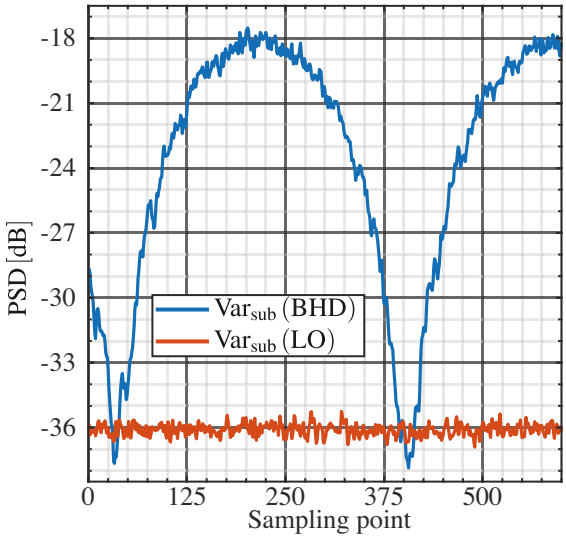

(5.7b) Zero-span RF-spectrum at 5.6 MHz with an RBW of 1 MHz

Figure 5.7 Experimental data recorded during alignment
The OSA was used to spectrally resolve alignment in BHD **(5.7a)**.
(5.7b) shows the power spectral density of zero-span RF-spectra of the subtracted signal measured with a spectrum analyser.

Visibility and quantum efficiency

The mode matching was above 97 % and limited only by a few weak spatial modes and the orthogonal polarisation as analysed in section 4.5.1. The measured interference between SI and LO, using SFL, was also limited by the same remaining spatial modes and the orthogonal polarisation leading to the conclusion that the TEM_{00} modes are as close to a perfect overlap as the measurement can resolve.

To estimate an upper bound for the overall quantum efficiency in the reflected SI path, the average optical power directly after the optical fibre (5.6 mW) is measured. Afterwards, the optical power in the SI path is measured directly in front of the BS (5.12 mW) while the separation resonator is locked off-resonance[16]. Accounting for the Fresnel losses on the end of the fibre, an upper bound of 88.5 % is calculated without considering the quantum efficiency of the detectors[17] (85 ± 5) % (section A.2.1). Overall the upper bound for the quantum efficiency is (75 ± 5) % which may be lowered by up to 2 % due to the mode matching as the surface of the power detector also measures all spatial modes as well as the orthogonal polarisation.

5.6.3 Experimental data

As displayed in figure 5.8a, the piezo control voltage for the detuning and the intensity on both detectors are recorded with a rate of usually 100 kS/s. The fluctuations are measured with a bandwidth of 1 MHz around 5.6 MHz (appendix A.2.3) and recorded with a synchronised digitiser at a rate of 25 MS/s or 50 MS/s[18] depicted in figure 5.8b.

The phase in BHD is not stabilised and, as examined earlier in section 4.5.5, not necessarily linear to the phase of the interference pattern and multiple measurements cannot be combined easily with sufficient accuracy. Furthermore, the ramp of the piezo cannot be used directly to trigger the recording due to the synchronous recording and continuous data readout. It can be driven by the used computer but this hinders the alignment process where multiple discrete devices (oscilloscopes and spectrum analyser) are used consecutively.

5.6.4 Data evaluation

From the overall recorded data, rising and falling ramps of the homodyne measurements are extracted and a phase is fitted to these interference patterns (figure 5.8a). The current fluctuations are filtered and then evaluated by calculating the variance of a number of con-

[16] By inverting the error signal, the lock is stabilised to upper or lower sideband of the phase modulation applied by the EOM.

[17] Measurements on quantum efficiency are limited by the available *S122B* [142], a germanium-based optical power meter head with an uncertainty of ±5 %.

[18] Depending on the intended measurement duration fluctuations, an analogue subtractor was used to reduce the amount of data due to hardware limitations.

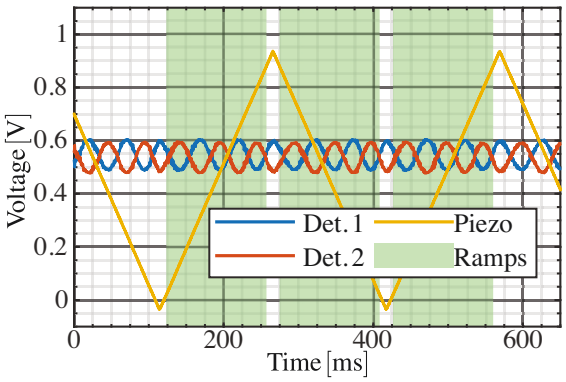

(5.8a) Monitoring voltages during measurement

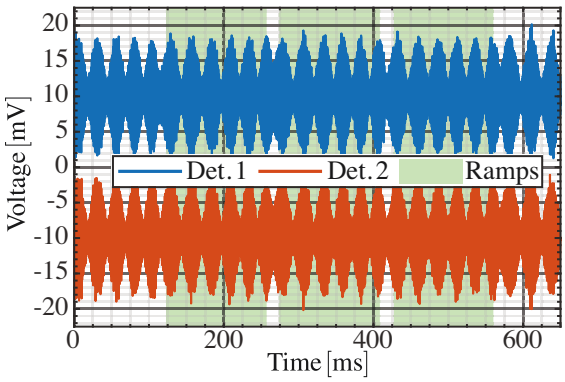

(5.8b) Fast fluctuations during measurement (Vertically shifted for visibility.)

Figure 5.8 Exemplary experimentally measured data
Monitor data from photodetectors and piezo voltage are shown in **(5.8a)** while **(5.8b)** illustrates the fast fluctuations. Data was recorded for 12 mW (or a pulse energy of 150 pJ) after 5 m of *PM1550-XP*.

secutive samples (figure 5.9a). The squeezing can be extracted from the data (figure 5.9b) and related to the phase (figure 5.10b).

In principle, the data points can be assigned to a specific phase in the range of $-\pi$ rad to π rad (compare [131]) but as figure 5.10b illustrates, the phase extracted from the interference pattern does not completely match the phase measured in BHD and hence the squeezing is averaged out by sorting the data.

To extract a useful squeezing parameter, the variances of a squeezed state (equation (5.8)) are fitted to the extracted phase within a range of π using an additional polynomial fit for the actual phase to account for the behaviour estimated in figure 4.23. By moving the π interval, several estimations for Var_- and Var_+ are extracted as depicted in figures 5.10c and 5.10d.

Essential portions of the used MATLAB code can be found in appendix I.

5.6.5 Data interpretation

For the measured experimental data, squeezing was measured and the methods discussed in sections 5.5.4 to 5.5.6 are applied in figure 5.9b and yield very similar results[19]. The influence of the coherent amplitude of the SI clearly reduces the squeezing estimated by the conventional approach (M_1). Corrections for the coherent amplitude of the SI in the BHD (M_2) and its missing in the recorded LO (M_3) increase the estimated squeezing but require three measurements BHD, LO and additionally SI. By using only one measurement (equation (5.26)) in (M_4), the squeezing is slightly overestimated as the reflected SI is

[19] The same section was analysed with different methods as by evaluating different datasets the fluctuations between the different datasets would mask the differences due to the evaluation methods.

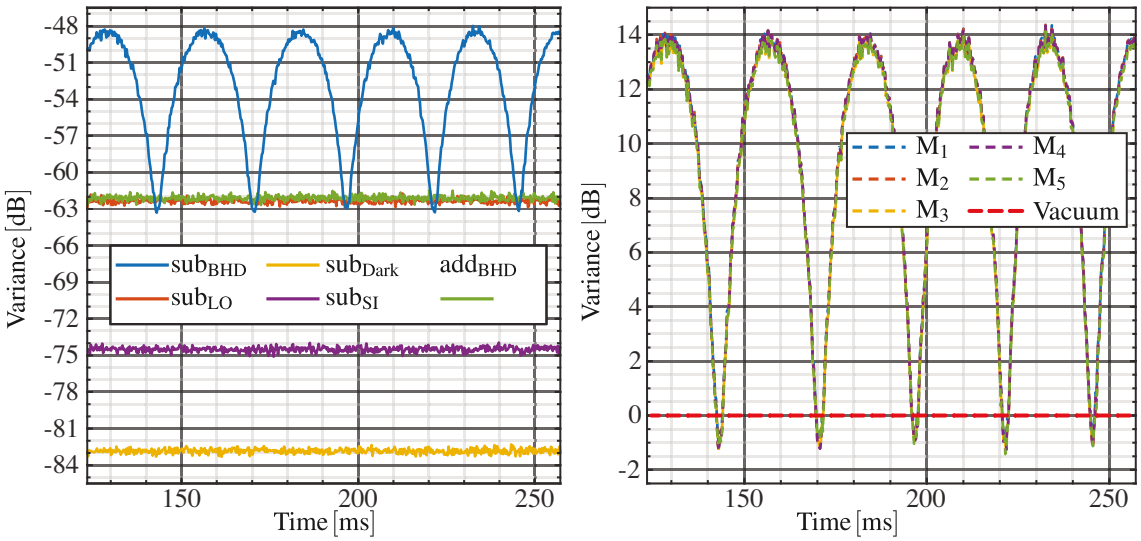

(5.9a) Variances of add- and sub-signal for one ramp for different beam configurations

(5.9b) Different methods used to extract the phase quadrature variance of the SI.

Figure 5.9 Evaluated data from figure 5.8
In **(5.9a)** subtracted signal is shown. In **(5.9b)** data is analysed according to methods discussed. M_1 is conventionally evaluated (equation (5.21)). M_2 is corrected for the coherent amplitude of SI (equation (5.22)). A correction for the vacuum level (equation (5.23)) is added for M_3. M_4 only contains one measurement instead of 3 (equation (5.26)) and M_5 used correlation (equation (5.27)) and add-signal. Differences discussed in section 5.6.5.

not limited by shot noise. The squeezing is overestimated by 0.02 dB as the SI is 0.15 dB above shot noise. While the direct fibre output is limited by shot noise, the carrier pulse of the reflected SI is altered by the separation resonator which changes its intensity noise.

This contribution can be neglected due to the low intensity of the SI compared to the LO. But its influence may increase due to changes in either LO intensity, mode matching, impedance matching, dispersion or CEO. Nevertheless, the extended evaluation reduces the amount of measurement configurations from three to one and requires less data. Additionally, the required processing can be done directly and allows for more time-efficient measurement as well as a reduction of the required storage space.

Using the correlation approach of equation (5.27) combined with the add-signal of both detectors yields similar results. Measured variances vary compared to the other methods as these are based on sub-signal of both detectors.

Presented in figure 5.10b, all three highlighted ramps are analysed individually and the estimated phases show a good overlap. The phase mismatch between the interference pattern, between LO pulse and depleted SI pulse, and the phase for the sidebands measured in BHD causes the squeezing in the phase-sorted data to smear out if the phases are wrapped to a single interval of π. The deviation from the π-periodicity matches the expectations indicated in section 4.5.5.

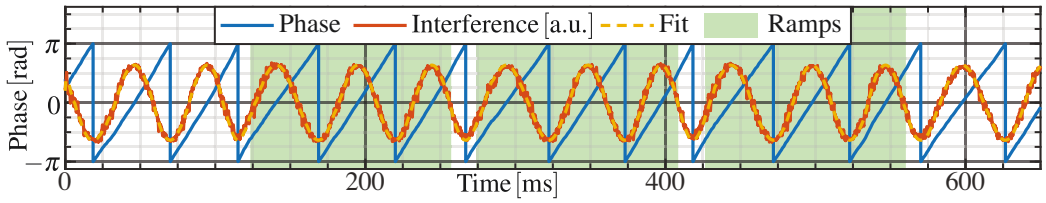

(5.10a) Interference pattern and extracted phase

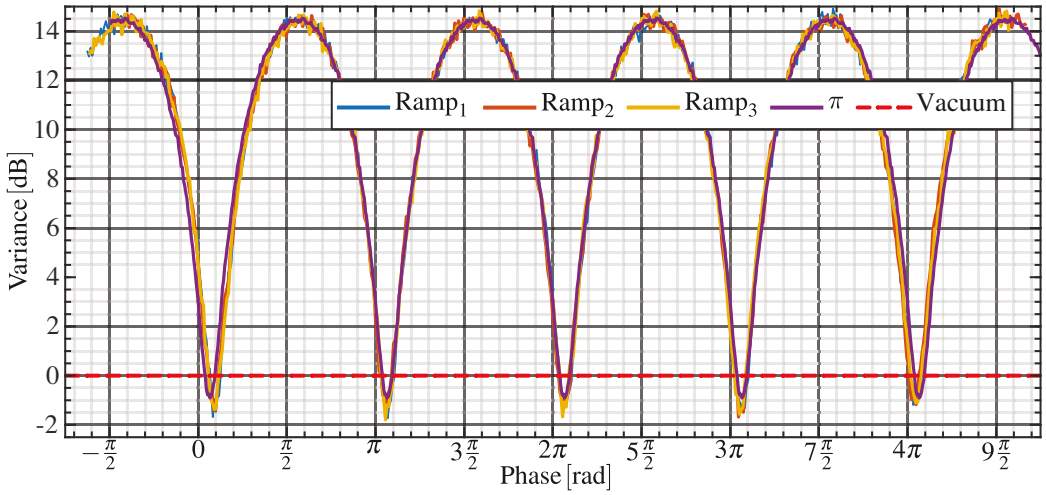

(5.10b) Unwrapped phase-resolved variances for all three ramp sections (10 kS per point) and all data mapped to a single interval of π (100 kS per point)

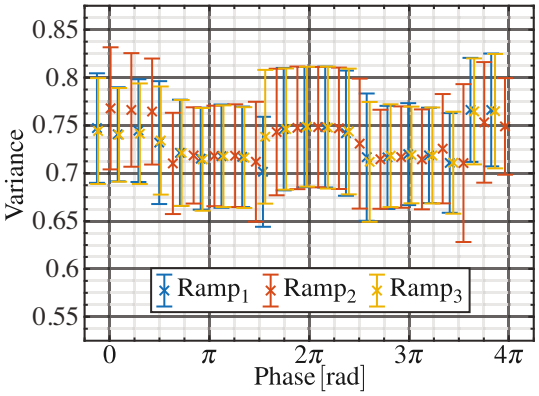

(5.10c) Fitted Var_- for all ramps ($\varnothing = 0.733$)

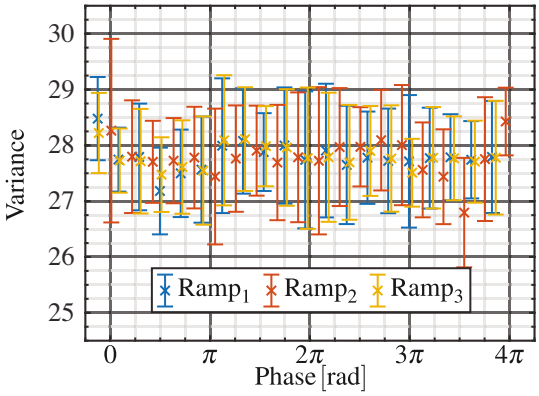

(5.10d) Fitted Var_+ for all ramps ($\varnothing = 27.8$)

Figure 5.10 Phase-resolved BHD evaluation for 12 mW after 5 m of *PM1550-XP* **(5.10a)** shows the extracted phase from the interference pattern wrapped from $-\pi$ to π. **(5.10b)** shows the evaluated variance for all three full ramps and all data combined. In **(5.10c)** and **(5.10d)**, equation (5.8) is fitted to a π-interval which is moved over each ramp.

A window of π is moved over the measured data to overcome this limitation. Within this window, values and uncertainties for Var_- and Var_+ (figures 5.10c and 5.10d) are obtained by additional fitting[20]. The average values correspond to a squeezing of 1.35 dB, anti-squeezing of 14.4 dB and a squeezing angle (equation (5.9)) of $\theta_{\mathrm{sq}} = 5.7\,^\circ$. Further evaluating the statistics of the fitted results yields $\mathrm{Var}_- = 0.73 \pm 0.05$ and $\mathrm{Var}_+ = 27.8 \pm 0.5$ which differs from the $\mathrm{Var}_- = 0.8 \pm 0.01$ and $\mathrm{Var}_+ = 28.0 \pm 0.2$ acquired from phase-sorted data (Line π in figure 5.10b)

All subsequent measurements are not provided in such detail and are mostly reduced to these fitted variances.

5.6.6 Temporal pulse overlap

From the analysis of the resonator in section 4.5.5, not only the phase of the interference pattern differs from the BHD phase but also the maximum of the envelope of the interference pattern does not coincide with optimal temporal overlap in BHD. As a result, the measured RF spectra (figure 5.7b) were used to align the spatial and temporal overlap in the BHD setup. By altering the temporal overlap, additional information can be obtained and the previously estimated influence can be checked for validity.

Experimental approach

While a piezo is used to shift the temporal overlap to scan the phase[21] in BHD, a manual linear translation stage was used for coarse µm alignment. This stage can be used to change the temporal overlap in the experiment and measure the according interference pattern and quadrature variances. An average optical power of 17 mW (213 pJ pulse energy) and the same 5 m *PM1550-XP* fibre were used. The translation stage was shifted by approximately 20 µm between measurements which relates to detuning steps of 40 µm.

Simulated reference values

Pulse propagation in the fibre is simulated using an SSFM[22] [143–146] (further presented in section 7.3 and appendix I.2) and for the resulting pulse, the transmitted LO pulse and depleted carrier pulse in the SI path are calculated according to measured dispersive properties of the separation resonator. The estimated interference pattern is compared to the experimentally obtained one. Additionally, a Monte Carlo simulation is used to simulate the quantum properties of the pulses and obtain the quadrature variances. This simulation already includes GAWBS, which is later investigated in chapter 6, as otherwise the simulated squeezing exceeds the measured by far.

[20] A polynomial fit is used to correct the phase, estimated from the interference pattern.
[21] The small changes in length by the piezo can be approximated as a phase shift.
[22] split-step Fourier method

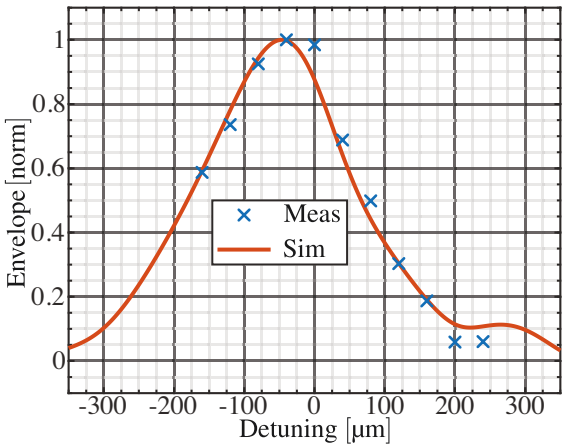

(5.11a) Envelope of interference pattern

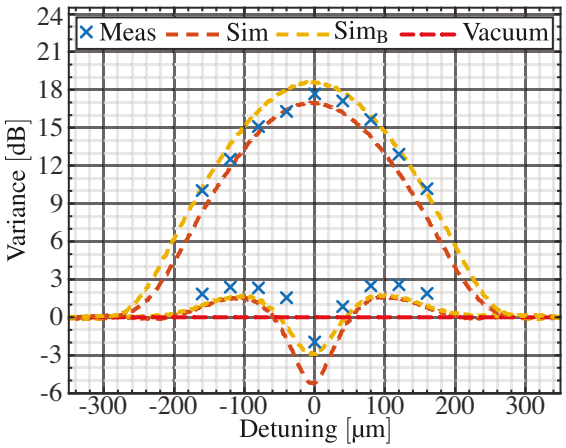

(5.11b) Var_+ and Var_- for each detuning

Figure 5.11 Effects of temporal pulse overlap in BHD
The measured envelope of the interference pattern **(5.11a)** as well as V_+ and V_- **(5.11b)** are compared to simulated data. For comparison, quantum efficiency is considered for the simulated data. $\mathrm{Sim_B}$ indicates the influence of GAWBS (chapter 6).

Measurement and analysis

Measured data is evaluated as described in the previous section and the interference pattern is normalised to its maximum value for a direct comparison to the simulation.

For the simulation, a pulse duration of 200 fs prior to the fibre is used and the dispersive properties (section 4.5) of the separation resonator are considered. The resulting match in figure 5.11a is remarkable, especially as neither the actual experimental parameters are fully known nor are the simulation parameters tweaked to match the experiment.

The measured pattern for temporal detuning (figure 5.11b) is symmetric, indicating that the remaining intensity in the reflected pulse (figure 4.22) and the dispersion of the separation resonator on the measured sidebands have no observable influence. For the experimental quantum efficiency and under the influence of GAWBS, this is also seen in the simulation. For no GAWBS and perfect efficiency, a minor influence in the simulation was observed (figure 7.2).

Aside from less squeezing, also less anti-squeezing is observed compared to the simulated data. The measured envelope of Var_+ is broader than for the simulated data. This may originate from a mismatch of the initial pulse duration or the estimated fibre properties in the simulation. Nevertheless, the overall agreement between simulated measurements and actual experimental measurements is good enough to estimate the influence of the separation resonator and temporal detuning and hence likely further measurements in chapter 7.

6. Influence of GAWBS

GAWBS is scattering on usually thermally excited acoustic modes originating from the cylindrical structure of the fibre. Relevant modes are found between 20 MHz and 800 MHz with linewidths down to 50 kHz [147]. As light propagates through the fibre, these vibrational modes of the optical fibre cause both phase and polarisation modulation or rather noise as they are mostly driven by thermal fluctuations. The first fibre-squeezing experiment [21] used CW light and GAWBS had to be suppressed by using liquid helium as a coolant. Later in fibre squeezing, the influence of GAWBS was reduced by using short pulses in the regime of 100 ps [148, 149]. Within the duration of such short pulses, the acoustic vibrations in the MHz regime barely move and all photons, within the same pulse, experience the same phase shift. For all experiments using single pulses, this leads to an almost complete reduction of GAWBS [23, 24, 30, 150].

As shown in the previous chapter, more phase noise than expected is measured in the used experimental setup. Measured squeezing was not limited by the stability of the separation resonator[1] and the stability of the laser system on short timescales cannot be characterised further using the available experimental resources as discussed in chapter 4. With the aim to exclude limitations from GAWBS, the optical fibre was submerged in LN_2. However, the measurements improved and hence the influence of GAWBS was further analysed.

First, the approximate amount of GAWBS is estimated in section 6.1 from other recent publications prior to the discussion of its influence on the measurement at the separation resonator. Following in section 6.2, expected scaling and influence on bright Kerr-squeezed states is discussed. Recorded experimental data is presented, analysed and related to the previously discussed properties. At the end of the chapter, additional open questions and an experimental outlook regarding GAWBS is given.

6.1 Coupling to GAWBS and its estimation

Detailed information on GAWBS coefficients and the properties of specific optical fibres is not available and cannot be measured easily. In data transmission, GAWBS may become

[1] As a decreased stability of the locking scheme (with a bandwidth in the kHz regime) did not significantly influence the measurement.

relevant at longer distances and can, in principle, be compensated [151]. Error-free digital coherent optical transmission is limited by GAWBS to 4600 km using a 64 QAM [152]. Current fibre-optic transmission schemes, using 16 QAM, can transmit 26.2 Tbps per pair of fibres over 6644 km [9]. As a result, the influence of GAWBS is currently not relevant for most technical applications, even if it is currently researched. Hence, it is not characterised for every fibre. In the used measurement scheme, the influence of GAWBS has to be estimated more generally.

The frequencies of the individual GAWBS resonances depend on the fibre geometry, doping and MFD [153, 154] while their linewidths are influenced by mechanical properties of the coating[2] [147]. By interferometric measurements using CW light and fast detectors, GAWBS spectra can be observed and compared even for shorter fibres [155] but cannot easily provide an absolute reference. Furthermore, its influence on pulsed experiments is different as the repetition rate, in the experiment 80 MHz, is low compared to the occurring frequencies of GAWBS. Hence, a chaotic broad spectrum is expected as the full CW spectra is observed with each harmonic of the repetition rate, resulting in a complex aliasing-like effect [156].

In [152], vector analysis is performed for different fibre lengths ranging from 80 km to 400 km. Their observations provide a linear dependence of the variance of optical carrier phase on fibre length (L) for commercial SM[3] fibres:

$$\mathrm{Var}\left(\varphi_{\mathrm{GAWBS}}\right) = 8.76 \cdot 10^{-10} \frac{\mathrm{rad}^2}{\mathrm{m}} \cdot L \tag{6.1}$$

For other fibre geometries, additionally $5.56 \cdot 10^{-10} \frac{\mathrm{rad}^2}{\mathrm{m}}$ (for a fibre with a large MFD) and $1.21 \cdot 10^{-9} \frac{\mathrm{rad}^2}{\mathrm{m}}$ (for a dispersion-shifted fibre with small MFD) are stated.

Using the dependence of equation (6.1) and the used experimental fibre length of 5 m, a variance of $4.4 \cdot 10^{-9}\,\mathrm{rad}^2$ or $3 \cdot 10^{-3}\,\mathrm{as}^2$ in time[4] is expected.

For the timing jitter between pulses, this translates to 55 zs, a value which is well below the already very low advertised values (down to 67.2 as) by the manufacturer ([60, 157]) but these measurements usually refer to the value between 1 kHz or 10 kHz and 1 MHz.

For the light reflected by the separation resonator, only frequencies above ≈ 500 kHz are relevant as fluctuations within its linewidth are mostly transmitted. At these frequencies, the jitter of stable optical oscillators [59, 158] is below the noise floor of even advanced measurement techniques [92, 117, 159] and should in theory approach the quantum limit. For frequencies around 5.6 MHz, this was verified in BHD by measuring the attenuated

[2] The soft acrylic coating dampens the vibrations and couples the glass to the surrounding.
[3] single-mode
[4] At 1550 nm, one optical cycle is 5.2 fs and one mrad hence translates to about 0.9 as.

pulse from the laser with the LO transmitted by the resonator. Indeed, no significant difference to the vacuum noise was observed for any quadratures.

While the absolute value for the phase variance seems almost insignificant, it has to be related to the fluctuations in phase space and hence the coherent amplitude $\left(\alpha \approx 3.1 \cdot 10^4\right)$ of a single pulse[5]. Related to the quantum noise (section 5.2), the expected phase variance from GAWBS, between individual pulses, is approximately 16.9 times larger compared to the vacuum variance. In the BHD setup, only one pulse is measured by one LO pulse and squeezing is observed over far more than a few mrad (figure 5.9) and hence the minuscule influence from GAWBS has to have an influence within the separation resonator setup. The following section presents a mechanism by which the small random GAWBS phase fluctuation of each single pulse, compared to the averaged pulse, influences the measurement.

6.2 Influence of GAWBS on measured squeezing and its scaling

Within the BHD setup, significantly more phase noise than initially estimated from GAWBS is observed. The random phase noise would not have a significant influence on a BHD with a strong LO as depicted in figure 6.2b. At the separation resonator, the coherent amplitude in reflection is highly attenuated by destructive interference with the pulse circulating within the resonator as illustrated in figure 6.1. Ideally, the real value of the coherent amplitude vanishes but the imaginary component remains. Instead of the small (1 ° in the illustration) phase noise between SI and LO, that has no significant influence in a BHD, the phase quadrature $\hat{X}_2$ fluctuations are measured as illustrated in figure 6.2b. The projection of this noise in phase quadrature reduces the observed amount of squeezing.

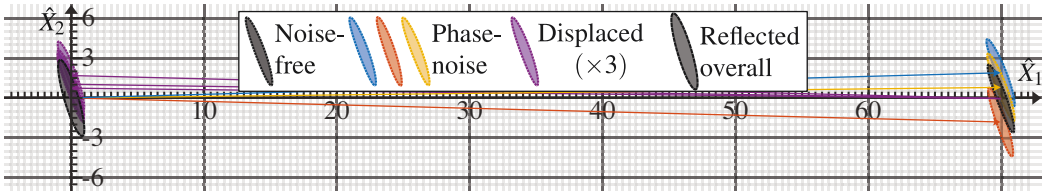

Figure 6.1 GAWBS influence in resonator reflection
Representation of Kerr-squeezed pulses with 1 ° phase noise. For the individual pulse, the phase noise has no effect (figure 6.2b). Displacing the state close to the origin, by interfering with the pulse circulating inside the resonator, leads to fluctuations in $\hat{X}_2$ close to the origin.

Of course the overall coherent amplitude in figure 6.1 is not even close to actual scale but illustrates the effect for a Kerr-squeezed pulse as adequately as possible. For imperfect

[5] For 10 mW average optical power at a wavelength of 1560 nm and 80 MHz pulse repetition rate, each pulse has 12.5 pJ or $9.82 \cdot 10^8$ photons.

impedance matching or an off-resonant separation resonator, which is actually the case for wavelengths off-centre (section 4.5), the influence is less pronounced due to the remaining coherent amplitude. This results in a nonlinear influence which for the sake of simplicity is not discussed here as it cannot be easily altered in the experiment and did not show significant influence if included in numerical simulations discussed in the later section 7.3.

6.2.1 Assumptions and simplifications for the influence

While the previous discussion indicated both the mechanism and magnitude of GAWBS in the experimental setup, further assumptions and simplifications provide a simplified model for thermally driven GAWBS that can be applied to experimental data.

I. GAWBS is classical and only affects the phase quadrature for very small angles:

$$\text{a)} \quad \sin\left(\varphi_{\mathrm{GAWBS}}\right) = \varphi_{\mathrm{GAWBS}} \qquad \text{b)} \quad \cos\left(\varphi_{\mathrm{GAWBS}}\right) = 1 \tag{6.2}$$

$$\mathrm{Var}\left(\hat{X}_{2,\mathrm{GAWBS}}\right) = 4|\alpha|^2 \cdot \mathrm{Var}\left(\varphi_{\mathrm{GAWBS}}\right) \qquad \mathrm{Var}\left(\hat{X}_{1,\mathrm{GAWBS}}\right) = 0 \tag{6.3}$$

II. Kerr squeezing and GAWBS are not correlated.

   a) GAWBS has no influence on the single pulse.

   b) Excited vibrational phonons decay before the subsequent pulse.

III. The physical properties of the fibre do not change significantly with temperature.

Based on these assumptions, the temperature dependence of GAWBS can be used to measure its influence and subtract it from the measurement. To estimate the temperature influence, two or more clearly discriminable temperatures are required. While assumptions I.a) and II.a) are quite solid, with sub-km long fibres and sub-ps pulses, assumption I.b) may break down at some point, but $\varphi^2_{\mathrm{GAWBS}}$ is orders of magnitude smaller than φ_{GAWBS} in the expected range.

Assumption III. is a vast simplification as even small temperature changes shift the frequencies of vibrational modes [160]. Furthermore, a significant and stable change in temperature is required. As room temperature is stabilised around $T_{\mathrm{RT}} = 293\,\mathrm{K}$, controlled direct heating and cooling would be limited by $\pm 30\,\mathrm{K}$[6] or $\pm 10\,\%$ and would not necessarily provide sufficient change (figure 6.2a) for an experimental verification. LN_2[7] can provide a stable temperature around $T_{\mathrm{LN_2}} = 77\,\mathrm{K}$ by submerging the optical fibre.

In an optical laboratory, placing a bowl of LN_2 directly next to an approximately 2 m long interferometric setup, which is stabilised in the nm regime, is a drastic and desperate

[6] At least for moderate and easy to implement efforts.
[7] liquid nitrogen

measure. But the measured phase noise was reduced and after improved thermal shielding (appendix J), longer measurements were possible.

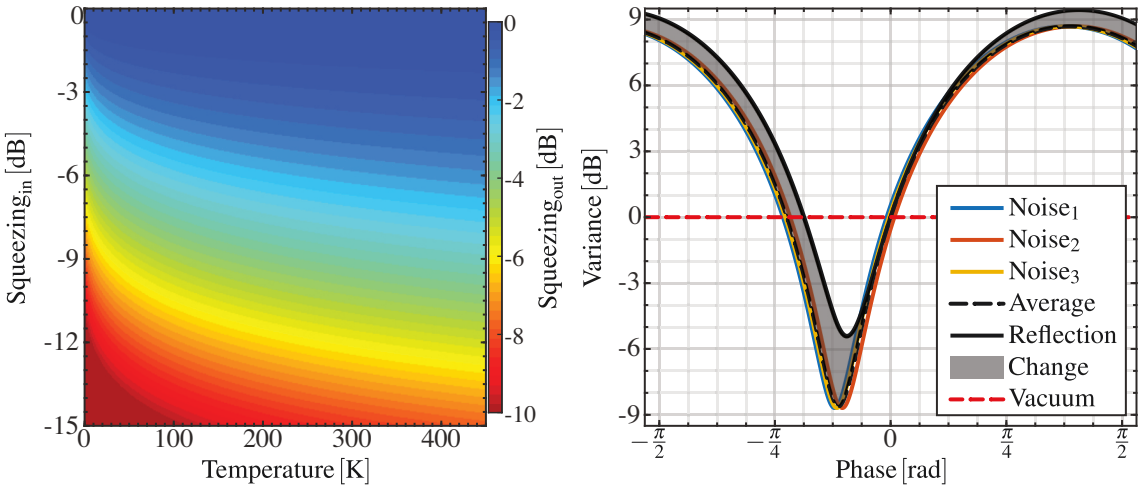

(6.2a) Remaining squeezing in reflection

(6.2b) Corresponding variances for figure 6.1

Figure 6.2 Expected measured squeezing depending on initial squeezing and temperature is shown in **(6.2a)**. The estimation is based on 5 m fibre and $9.82 \cdot 10^8$ photons per pulse with temperature-depended phase noise estimated from equations (6.1) and (6.5) under the assumption of perfect Kerr squeezing. Vastly simplified as for illustration purposes the Kerr coefficient of the fibre is changed. Expected squeezing is limited to −10 dB. In **(6.2b)** variances for the illustration figure 6.1 are shown.

This radical method has further influences on assumption III. as the surrounding LN_2 has an influence on the spectrum [161] and the above mentioned frequency shift becomes nonlinear [162, 163]. At least for stimulated Brillouin scattering, the increase in internal friction leads to an increase of the linewidths which are maximal in the range of 110 K to 130 K [162, 163]. Below these temperatures the internal friction decreases and as a result the linewidths also decrease by more than an order of magnitude [163]. For GAWBS, no reliable data was found but it may behave more linearly as the major dampening occurs at the interface between fibre and coating. Hence, the nonlinear changes in internal friction may be less influential than for the stimulated Brillouin scattering in direction of propagation. Nevertheless, a nonlinearity is still expected as due to the change in temperature also the properties of the coating are believed to change and influence the linewidths. This behaviour depends on the fibre itself and no data for the used *PM1550-XP* fibre is available.

6.2.2 Model for the temperature-dependent influence of GAWBS

Under the previously stated assumptions (section 6.2.1), the individual modes can be treated as individual, thermally driven and uncorrelated harmonic oscillators with frequencies f_j. The expected variance for the corresponding harmonic oscillator (see [118, Ch. 1.5]) is

proportional to the number of thermally excited phonons:

$$\mathrm{Var}\left(\hat{X}_{\mathrm{th},j}\right) \propto \langle n \rangle_j + \frac{1}{2} = \frac{1}{\exp\left(\frac{h \cdot f_j}{k_\mathrm{B} T}\right) - 1} + \frac{1}{2} \underbrace{\approx \frac{k_\mathrm{B}}{h \cdot f_j} T}_{h \cdot f_j \ll k_\mathrm{B} \cdot T} \tag{6.4}$$

As the important frequencies are below 1 GHz, the linear approximation in equation (6.4) holds even below 1 K. Additionally, the constant vacuum fluctuations (the $\frac{1}{2}$-term) can be dropped at LN_2 temperature, treating GAWBS as classical thermal noise.

Assuming that the thermal fluctuations between all modes are uncorrelated, the variances of the corresponding GAWBS-induced phase noise can be summed up and written effectively as a single linear coefficient:

$$\mathrm{Var}\left(\varphi_\mathrm{GAWBS}\right) = \mathrm{C}_\mathrm{GAWBS} \cdot T \tag{6.5}$$

The measured variances are the sum of the Kerr-squeezed state and the uncorrelated GAWBS phase noise. As neither GAWBS nor Kerr squeezing affect the amplitude quadrature, the squeezing angle (equation (5.9)) can be extracted to determine the phase quadrature. Hence the measured phase quadrature noise $\mathrm{Var}_{\varphi_\mathrm{M}}(T)$ can be written depending on temperature as:

$$\mathrm{Var}_{\varphi_\mathrm{M}}(T) = \mathrm{Var}\left(\varphi_{KERR}\right) + \mathrm{C}_\mathrm{GAWBS} \cdot T \tag{6.6}$$

Equation (6.6) allows to determine and subtract $\mathrm{C}_\mathrm{GAWBS}$ from a temperature-dependent measurement to estimate the actual Kerr squeezing.

This evaluation assumes that additional to the linear temperature dependence of GAWBS neither the dispersion nor the nonlinear Kerr coefficient of the fibre change. A fact that has to be kept in mind as none of these conditions or their temperature dependence can be experimentally verified within the current setup using only two discrete temperatures.

In figure 6.2a, the estimated measured squeezing and anti-squeezing are shown for different GAWBS phase noise and initial Kerr squeezing. As with higher initial squeezing, the squeezed quadrature approaches amplitude quadrature and the influence of GAWBS phase noise decreases. Within the model, phase noise from GAWBS is directly proportional to the electric field and consecutively its variance with the intensity compared to Kerr anti-squeezing variance that ideally increases quadratically with intensity. Using higher intensities (or shorter pulses) may limit the influence of GAWBS on the measured squeezing but the detected Kerr squeezing may behave differently due to the nonlinear pulse propagation (discussed in section 7.3). Additionally, squeezing would be observed for a narrower range of phases and hence more susceptible to additional phase noise in the BHD.

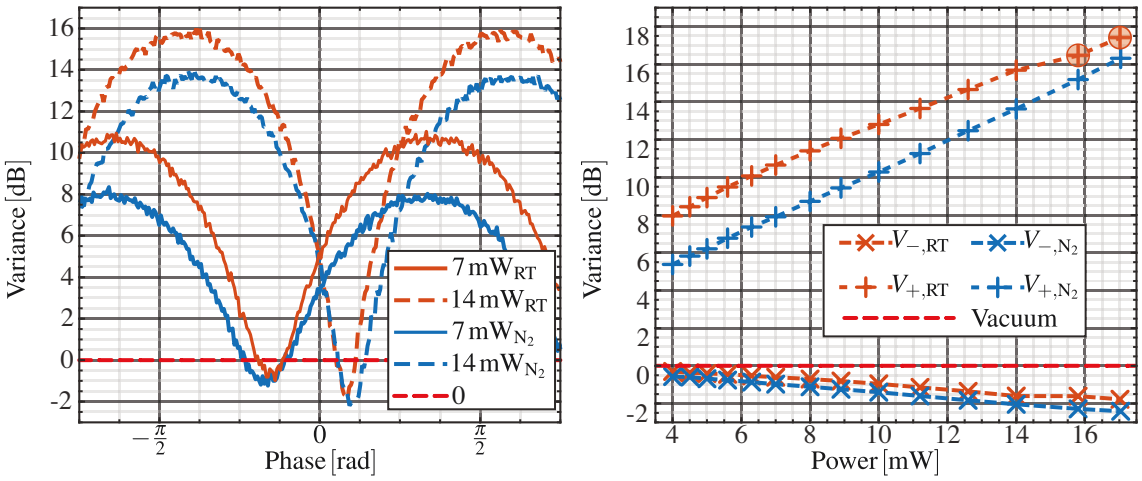

(6.3a) Comparison 7 mW and 14 mW

(6.3b) Fitted overall results

Figure 6.3 Temperature and power dependence of the measured squeezing (5 m *PM1550-XP* fibre at room temperature (RT) and submerged in LN_2 (N_2). In **(6.3b)**, the last two measurements are marked as they fell out of line.

6.3 GAWBS measurement procedure

As for the previous measurements, the separation resonator setup and BHD is aligned at room temperature. To investigate the temperature dependence as well as the intensity scaling, multiple fixed average optical powers are adjusted using a detachable measurement diode on a magnetic fixture, allowing quick and repeatable measurements.

Different optical powers are measured consecutively without realignment of the optical setup. Nevertheless, the gain of the locking loop required adjustments due to the increasing signal every few increases in optical power.

For measurements at LN_2 temperature, the fibre was submerged in LN_2. During the cooling process, the evaporated cold nitrogen affects the optical alignment. As the separation resonator and the BHD are not in close proximity to the cooled fibre, their (time-consuming) alignment is not immediately required. The shielded fibre couplers (appendix J) are affected by initial drifts. These are corrected using the corresponding mirror pair after the LN_2 is filled up. Most of the cold air is guided off the optical table but nevertheless, all optical components and path lengths are slowly misaligned due to the occurring temperature gradient. The measurement was performed at room temperature and then repeated with the fibre submerged in LN_2. Within 20 min to 30 min, the LN_2 evaporates limiting the overall measurement time as refilling would pour more cold air on the components leading to an increased time effort for realignment.

6.4 GAWBS measurement evaluation

Each individual measurement is processed individually as described in chapter 5 resulting in the data (figure 6.3 and appendix K). The anti-squeezing difference between cooled fibre and room temperature narrows for measurements above 14 mW (15.6 mW and 17 mW marked in figure 6.3b). This is an unexpected behaviour and may be caused by misalignment. Aside from a misalignment of an actual optical component, the redshift of the pulse due to Raman scattering and the corresponding change of the error signal (section 4.3.3) may lead to a detuning of the separation resonator. Due to the temperature dependence of the Raman gain [164–166] this effect may be reduced at LN_2 temperatures. Without further investigation, the origin of this deviation in the measured data is unknown. For the desired analysis, these measurements are excluded as it cannot be accounted for neither an actual physical cause nor a misalignment.

Before analysing the data according to section 6.2.2, data is corrected for the estimated quantum efficiency of 75 % (section 5.6.2). The orientation of the squeezing ellipse is calculated from Var_- and Var_+ using equation (5.9). Another approach would be to use the phase modulation of the EOM but due to used analogue filters, this signal at a frequency of 17.25 MHz is close to the electronic noise floor. Hence its recovery requires many sampling points and becomes unreliable[8].

77 K are used for the evaluation as the actual fibre temperature is well defined by LN_2. In figure 6.4, the estimated Kerr squeezing and GAWBS phase noise are shown on a linear (figure 6.4b) and logarithmic scale (figure 6.4a). The area above 14 mW is highlighted in red as those points are calculated from the excluded data.

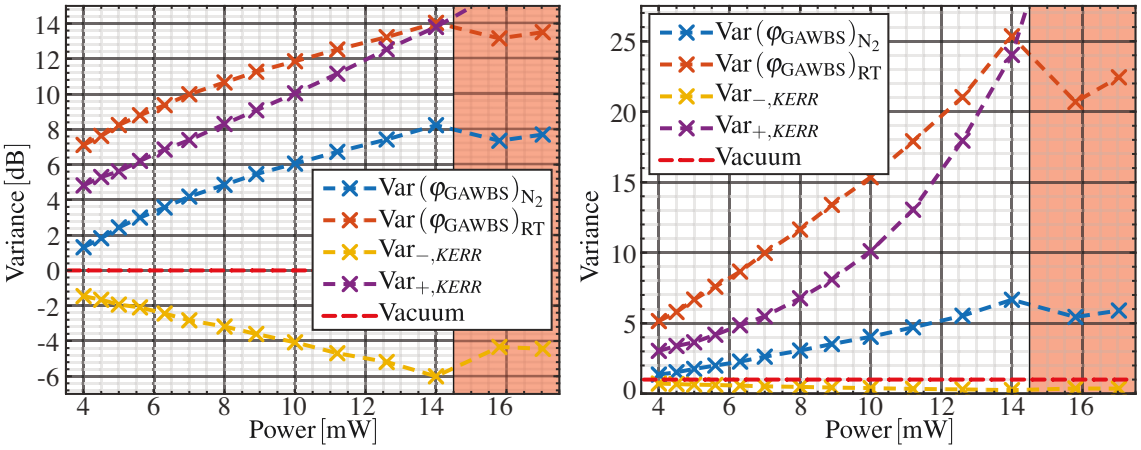

(6.4a) Evaluated variances (logarithmic)

(6.4b) Evaluated variances (linear)

Figure 6.4 Evaluation of GAWBS for the data in figure 6.3
Shown are estimated variances of GAWBS phase noise as well as $V_\pm$ for the Kerr squeezed pulse and their scaling with average optical power.

[8] However, future measurements may utilise it if analogue signal processing and data acquisition are adapted.

Figure 6.5a considers different overall quantum efficiencies between 50 % and 80 %, evaluated for $T = 77\,\mathrm{K}$. As debated in section 6.2.1, the physical properties of the fibre may not be constant and hence evaluation for different effective temperatures from 50 K to 150 K is depicted in figure 6.5b. Above a certain assumed temperature (112 K) or below a certain quantum efficiency (52 %), the evaluation results in states that violate the uncertainty principle which can be seen as a limit for actual quantum efficiency and temperature scaling.

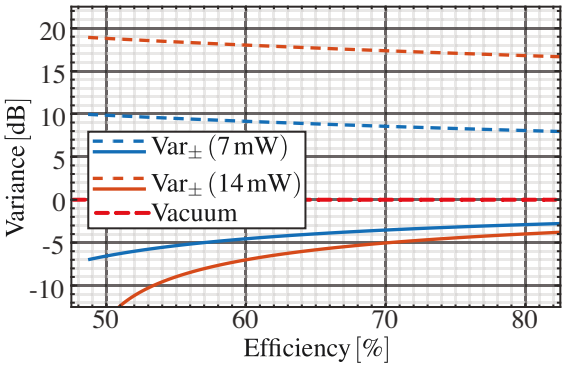

(6.5a) Changes in quantum efficiency for 77 K effective fibre temperature

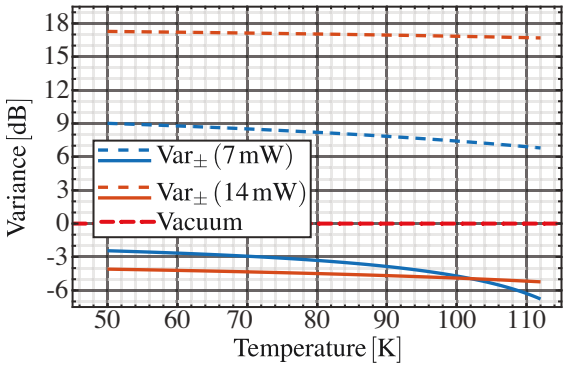

(6.5b) Changes of effective temperature at 75 % quantum efficiency

Figure 6.5 Quantum efficiency and temperature influences on GAWBS evaluation

6.5 GAWBS measurement discussion

The direct experimental observation is that the measured squeezing is increased and the observed anti-squeezing is simultaneously reduced as the fibre is cooled down.

A phase variance of 15.4 times the vacuum variance is extracted for the GAWBS contribution at room temperature from the measurement at 10 mW. This value is close to the value of 16.9 estimated in section 6.1 from [152].

The derived simplified model of GAWBS-induced phase noise coincides well with the measured data (figure 6.4b) as, up to 14 mW, the assumed variance of GAWBS scales linear with intensity. The remaining anti-squeezing scales almost with the square of the intensity.

Assuming the complex nonlinear changes of fibre properties [162, 163] at cryogenic temperatures, the model fits almost too well and certainly the discussed additional effects should be further characterised. Aside from the phase noise due to GAWBS, the intrinsic phase noise from the laser may have an additional contribution but it is assumed that the phase noise of the laser is limited by quantum noise for frequencies outside the linewidth of the separation resonator.

Corrected for GAWBS and quantum efficiency, the estimated squeezing of 6 dB approaches other experiments [30, 167]. Measured squeezing can definitely be further improved by increasing the intensity and stabilising the BHD.

By using only two discrete temperatures, no deviations from a linear behaviour can possibly be observed. For a more sophisticated analysis, multiple temperatures from 10 K to 300 K and fibre lengths have to be measured. Such measurements require a well controlled stabilised fibre temperature, and reliable isolation of the separation resonator and the beam paths from the occurring thermal gradient. The phase noise from GAWBS is expected to drop further and at temperatures below 20 K may already become insignificant for the experimental setup. It may be possible to use a setup similar to the current one and submerge the fibre in liquid helium but due to its lower heat capacity, a larger volume is required and the thermal drift of the setup is expected to limit the measurement time. Hence, it will likely be not successful. One could feed the fibres into a helium-filled tank and place the couplers under normal atmosphere but at least 50 cm of the fibre will be close to room temperature. The effective average temperature in such a setup, using an overall fibre length of 5 m, will not be much lower than already achieved with LN_2. To observe the temperature behaviour with proper isolation, both the couplers and the fibre have to be placed in a cryostat with optical access.

Another application of the setup could be measurement and characterisation of phase noise for well stabilised frequency combs outside the linewidth of the resonator. This frequency range is not well accessible by other current measurement schemes. Furthermore, this scheme would be directly referenced to the fundamental quantum vacuum and allow an absolute measurement.

7. Local oscillator shaping and correlations

In the experimental setup, the separation resonator provides the quantum state and a depleted carrier pulse (chapter 4) in reflection which can be analysed by the transmitted carrier pulse in a BHD setup (chapter 5). This setup allows a full BHD measurement of the Kerr-squeezed pulse but is severely affected and limited by GAWBS scattering (chapter 6).

It is limited to the measurement of a single-mode squeezed state in the mode chosen by the LO. Replacing the LO by a shapable pulse provides experimental access to correlations within the spectral and temporal structure of the pulse. In chapter 5, a temporal detuning between SI and LO was used to measure different combinations of spectral modes (figure 5.11) which altered the measured squeezing. Nevertheless, the phase shift between different spectral modes caused by temporal detuning allows only limited conclusions on the correlations within the spectrum of the pulse. Ideally, spectral components in the LO can be adjusted in both amplitude and phase to allow analysis of arbitrary modes and correlations. In extension of the previously built experimental setup, an SLM was implemented to allow for these adjustments for the LO pulse. This extension is presented after a brief introduction to multimode measurements and the limitations of previous measurements. A numerical simulation is used to discuss the expected behaviour of Kerr squeezing caused by the nonlinear propagation in the optical fibre.

Function and limitations of the used setup are discussed before data from multiple different measurements is presented and discussed showing the capability of the experimental method and its current technical constraints.

7.1 Beyond single-mode measurements

The non-classical properties of a single-mode state can already be used to improve measurements [13, 15]. Entanglement between multiple modes provides a resource for quantum applications [168–170]. Famously known is the Einstein-Podolsky-Rosen paradox, or short EPR paradox [171] and consecutively, violations of Bell-type inequalities [172–177].

Such quantum correlations were experimentally observed and are used for example in quantum communication [26, 178], computation [179] and new measurement schemes [180].

As discussed in appendix F.3, the Kerr effect creates correlated photons throughout the broad spectrum of the pulse and the long propagation in an optical fibre changes the pulse shape. While each individual spectral component observed alone does not show significant non-classicality, the combination of several spectral components does and the amount of squeezing depends on the chosen combination as emphasised for simulated data (figures 7.1 and 7.2).

Such complex quantum states [181] can be used as quantum resources [36].

7.1.1 Criteria for separability

By shaping the pulse, the SLM allows to measure complex modes but it also allows to define two (or more) orthogonal modes and measure these modes and the correlations between them. To distinguish whether the state is separable, *i.e.* it can be written as a mixture of product states, a more general necessary and sufficient criterion is the Peres-Horodecki separability criterion [182]. Optimised criteria for the verification of inseparability can also be found [183, 184] but two similar and particularly useful criteria were introduced by Simon [185] and Duan [186]. Both base on the Peres-Horodecki separability criterion. They consider the second order moments and provide a sufficient condition for inseparability in continuous variable systems. For Gaussian states, which are fully described by the second order moments and a mean value, they are even necessary. The criteria of Simon is formulated for the covariance matrix which has to be extracted from experimental data while the separability criteria of Duan [186] can be applied directly to the measured variances, assuming the correct phases can be assigned. It states a lower bound for the overall variance of separable states:

$$\mathrm{Var}\left(\hat{U}\right) + \mathrm{Var}\left(\hat{V}\right) \geq a^2 + \frac{1}{a^2} \tag{7.1}$$

Therein, a is a real number and $\hat{U}$ and $\hat{V}$ are related to any local operators $\hat{x}_j, \hat{p}_j$ of two modes $(j = 1,2)$ that satisfy $\left[\hat{x}_j, \hat{p}_{j'}\right] = i\delta_{jj'}$

$$\hat{U} = |a|\hat{x}_1 + \frac{1}{a}\hat{x}_2 \qquad \hat{V} = |a|\hat{p}_1 - \frac{1}{a}\hat{p}_2 \tag{7.2}$$

First, $\hat{x}_j$ and $\hat{p}_j$ are replaced by two quadrature operator separated by $\pi/2$ in the respective mode as formulated in section 5.2:

$$\hat{x}_j = \frac{1}{\sqrt{2}}\hat{X}_j\left(\varphi_j\right) \qquad \hat{p}_j = \frac{1}{\sqrt{2}}\hat{X}_j\left(\varphi_j + \pi/2\right) \tag{7.3}$$

Furthermore, the parameter a has to be considered as it is used to weight the contributions from each mode. Ideally, two BHD setups with proper normalisation would be used setting a to 1 yielding the lower bound 2 for separable states. Clearly, $a^2 + \frac{1}{a^2}$ can never be smaller than 2. The used experimental setup measures both modes on the same setup and normalises to the overall vacuum level. Hence the measured variances ($\mathrm{Var_M}$) need to be analysed:

$$\mathrm{Var_M}(\varphi_1, \varphi_2) = \frac{I_1 \cdot \mathrm{Var}\left(\hat{X}_1\right)(\varphi_1) + I_2 \cdot \mathrm{Var}\left(\hat{X}_2\right)(\varphi_2)}{I_1 + I_2} \tag{7.4}$$

$$= \frac{\sqrt{I_1 \cdot I_2}}{I_1 + I_2} \cdot \left(\underbrace{\sqrt{\frac{I_1}{I_2}}}_{a} \mathrm{Var}\left(\hat{X}_1\right) + \underbrace{\sqrt{\frac{I_2}{I_1}}}_{1/a} \mathrm{Var}\left(\hat{X}_2\right) \right) \tag{7.5}$$

Using equations (7.3) and (7.5), equation (7.1) can be rewritten as:

$$\mathrm{Var_M}(\varphi_1, \varphi_2) + \mathrm{Var_M}(\varphi_1 + \pi/2, \varphi_2 - \pi/2) \geq 2 \cdot \frac{\sqrt{I_1 \cdot I_2}}{I_1 + I_2} \left(\frac{I_1}{I_2} + \frac{I_2}{I_1} \right) \tag{7.6}$$

If for any combination of φ_1 and φ_2 the inequality equation (7.6) is violated, both modes are inseparable.

Assuming the SLM provides equally powered modes ($I_1 = I_2$), the bound of equation (7.6) is 2. If one mode has double the intensity of the other, the bound would increase to 2.357. To avoid such arbitrary boundaries, if I_1 and I_2 are precisely known, it can be written as:

$$\frac{\mathrm{Var_M}(\varphi_1, \varphi_2) + \mathrm{Var_M}(\varphi_1 + \pi/2, \varphi_2 - \pi/2)}{\sqrt{I_1 \cdot I_2}\,(I_1/I_2 + I_2/I_1)/(I_1 + I_2)} \geq 2 \tag{7.7}$$

7.2 Previous work on Kerr-squeezed pulses

Previous experiments used interference, *e.g.* in a Sagnac interferometer [23, 24], between two pulses to show the Kerr squeezing. By using two nearly identical co-propagating pulses, a tomographic measurement for polarisation squeezing was also realised [30]. Nevertheless, these measurements could not access the correlations between different spectral components. Using only spectral filtering, Kerr squeezing was also revealed [28] as well as correlations between the amplitude fluctuations of its spectral components [29, 187].

Numerical simulations indicate that the carrier pulse itself is not the most squeezed temporal mode and that additional squeezed temporal modes exist [144, 188]. By separation of the carrier pulse and the implementation of a pulse shaper, described in this chapter, the experimental setup provides access to tomographic measurements between multiple spectral components.

7.3 Numerical simulation

While in the experiment GAWBS (chapter 6) and resonator properties (section 4.5) always have an influence on the measurement, they can be turned off or altered in a numerical simulation. As already demonstrated in figure 5.11, the used numerical simulation can reproduce experimentally observed behaviour. Within the complex experimental setup, it would be a tremendous effort to precisely characterise each pulse and the relative delays. For the available experimental resources, this cannot be performed within the measurement time which is limited by the overall stability. The used numerical simulation allows to analyse well defined modes, understand experimental findings and suggest future experimental parameters.

7.3.1 Simulation principle

The classical pulse propagation through the optical fibre is simulated using an SSFM [143–146]. It includes the Kerr nonlinearity and linear dispersion but further effects can be included[1]. Quantum fluctuations are introduced by using a Monte Carlo method as random noise is added to the pulse and 10 000 individual pulses are simulated.

These 10 000 pulses can be used for statistical analysis on squeezing and anti-squeezing in several modes. Corresponding MATLAB code is given in appendix I.2 and I.3.

7.3.2 Exemplary simulation results

This section focusses on simulated data for a fibre[2] length of 5 m and 17 mW according to the experimental setup used in chapters 5 and 6.

In figure 7.1a, the intensities and phases of the spectral components of the pulses are shown. The initial pulse also enters the SLM setup and can be altered prior to the use as LO. The output pulse of the fibre cannot be used directly as the LO but the changes in the experiment due to the transmission by the separation resonator are minimal. This is particularly relevant as the linear part of the phase mainly changes the CEO which can be compensated well for by a temporal detuning. Furthermore from the fluctuation of the 10 000 simulated pulses, two eigenmodes of the resulting covariance matrix are shown in figure 7.1b.

The calculated eigenmodes do neither match the transmitted output pulse nor the input pulse but are expected to show significantly increased squeezing, at least in the absence of

[1] For the comparison with experimental data, these effects were sufficient and hence higher order dispersion and nonlinear Raman scattering were excluded for simplicity.

[2] Relevant parameters for pulse propagation in the used *PM 1550-XP* fibre are based on the measurements in [189].

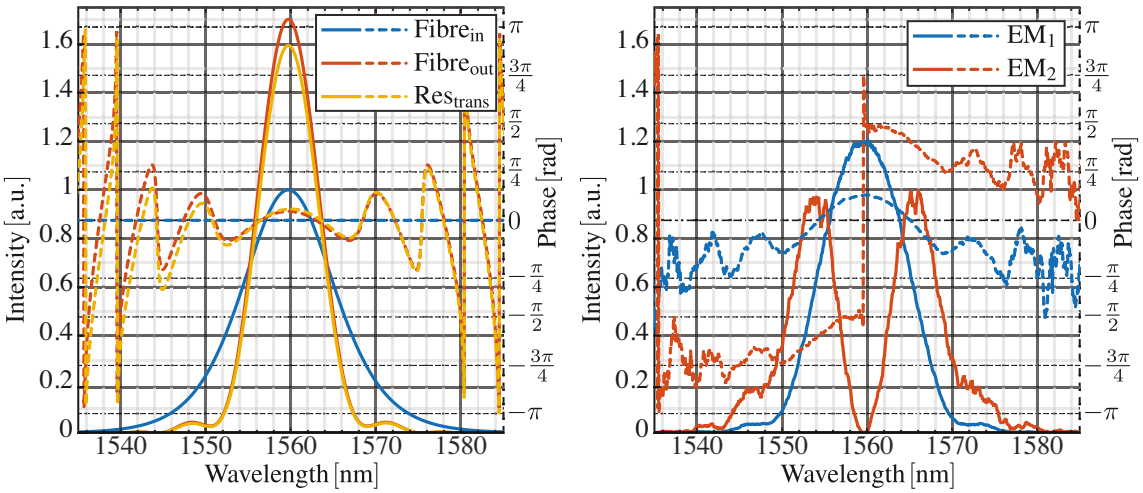

(7.1a) Phase and intensity

(7.1b) Phase and intensity of eigenmodes

Figure 7.1 Simulated pulse shapes for 5 m fibre and 17 mW
(7.1a) shows the intensity and phase of input and output pulse (prior and after the separation resonator). **(7.1b)** shows two calculated eigenmodes.

GAWBS. In figure 7.2, the squeezing analysed with an LO, derived from this pulse with equal power to the transmitted pulse, is shown for different configurations (figure 7.2). For figure 7.2a, the coherent amplitude was removed while a dispersive resonator close to the experimental setup was simulated for the other configurations. Both figures 7.2c and 7.2d assumed GAWBS. In three of these cases, the phase between LO and SI was altered without a temporal detuning. In figure 7.2d, GAWBS and the resonator dispersion were simulated and the length was detuned instead of the actual phase. For short detuning distances, no significant difference was found between a shifted phase and a length detuning. For larger detuning as in figure 5.11, the simulation matches the experimental findings. Generally, the phase was used as it is numerically more efficient to calculate variances with 1 ° resolution instead of using a comparable resolution of 5 nm for a detuning range of 100 µm.

The influence of GAWBS is generally much stronger than the expected influence of the dispersive resonator which can merely be seen in the simulation. For the second eigenmode, two spectral regions with close to equal optical power have a phase shift of π which drastically reduces the influence of GAWBS for this mode. As GAWBS equally affects all spectral components of a single pulse, the phase shift of π for one half of the spectral intensity leads to an annihilation of the GAWBS as ideally $I_1 \cdot \varphi_{\mathrm{GAWBS}} - I_2 \cdot \varphi_{\mathrm{GAWBS}} = 0$ if $I_1 = I_2$. The mode EM$_2$ (figure 7.1b) has these properties and in the simulation it is not significantly affected by GAWBS (figure 7.2c).

Depending on the pulse parameters and fibre length, drastic changes in the spectral intensity of the transmitted carrier pulse may occur which further reduce the expected squeezing. This could also be beneficial if the pulse prior to the SLM is altered in an optical fibre to increase the overlap with an intended LO pulse to reduce the losses that the SLM has to introduce. To obtain the ideal LO for the second eigenmode with the SLM between

1545 nm and 1575 nm, an additional loss of 64 % would be required, leading to a much weaker LO.

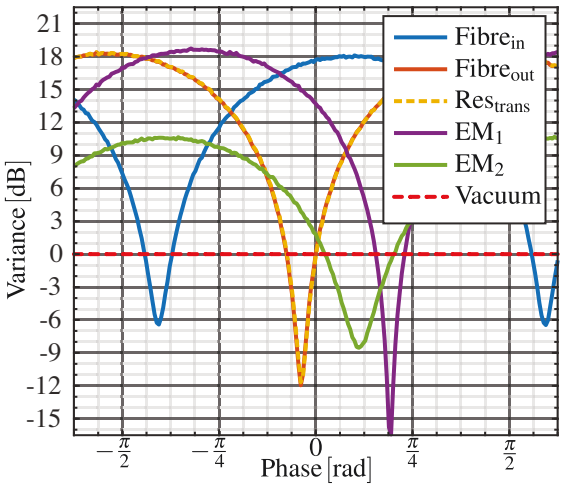

(7.2a) Zero amplitude for SI

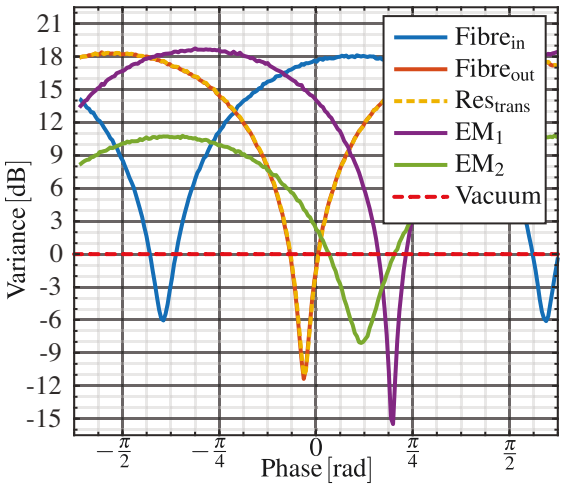

(7.2b) Reflected amplitude

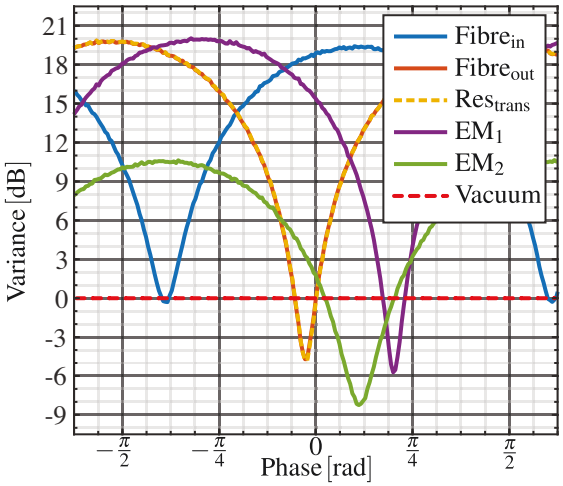

(7.2c) GAWBS and reflected amplitude

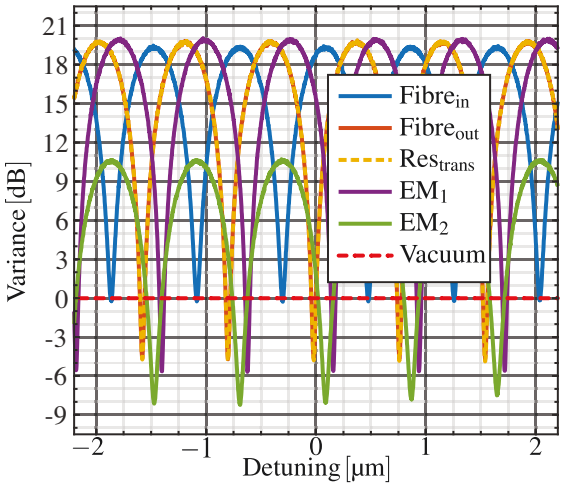

(7.2d) Delay instead of phase for (7.2c)

Figure 7.2 Simulated influence of GAWBS and resonator in BHD
Data is based on 200 fs pulses with average optical power of 17 mW after 5 m *PM1550-XP*. Further details in text.

7.4 Experimental setup

The experimental setup for the pulse shaping and mode matching is illustrated in figure 7.3. By its design [190], the $4f$ setup of the SLM requires at least a path length of 1 m as well as additional steering mirrors and adjustments in beam height (from 5 cm to 12.5 cm and back). The spatial mode is affected by the shaping process and additional mode matching is required for BHD. Due to the pulse shape, the measured visibility cannot be used to sufficiently match the beam waist and its position. Their matching is ensured by an additional filter resonator which is built using a curved mirror from the same batch also used for the separation resonator. Its length is given by f_{rep} and hence the spatial

mode in transmission is close to identical to the separation resonator. Only two coupling mirrors for the separation resonator were ordered and as no high finesse is required for the spatial filtering, two 70 : 30 BS[3] are used for the filter resonator. Distance from beam waist to BHD is matched to the separation resonator within a few cm (sufficient regarding the Rayleigh range of 1.45 m).

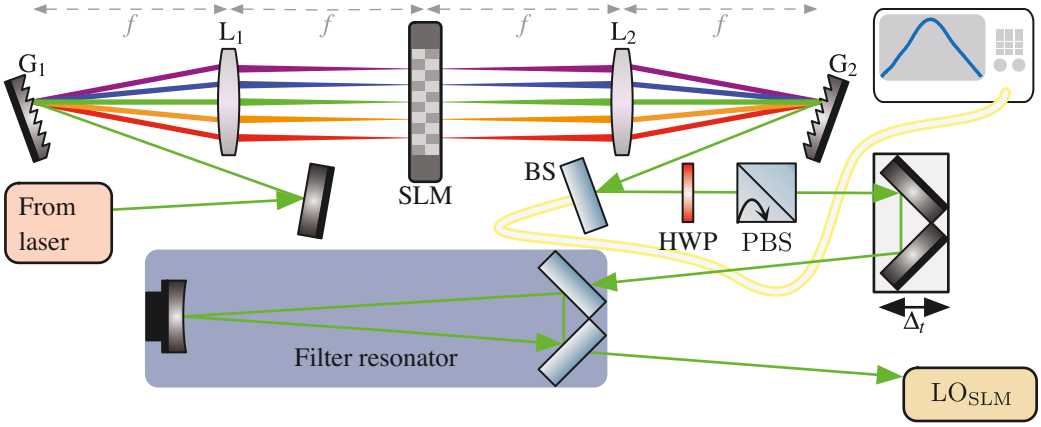

Figure 7.3 SLM setup
The SLM manipulates the spectrum in a $4f$ setup. For BHD, polarisation is rotated to s-polarisation and a filter resonator is used for spatial mode matching.

7.5 SLM operational principle

P-polarised light is required for the SLM setup to obtain maximum efficiency ($\approx 80\,\%$) of each grating. The SLM itself is build by two consecutive masks of 128 pixels each. The masks are rotated by $\pm 45\,^\circ$ to the incident p-polarised light. By assigning a 12 bit integer value, each pixel can apply a wavelength-dependent phase shift (figure L.2). If both consecutive pixels apply the same phase shift, the overall phase is shifted while different phases alter the polarisation, leading to an amplitude modulation by the following polarisation filter [190, 191].

7.5.1 Pulse shape variation

In order to fully control the actual pulse shape in BHD, the required mask depends on the pulse shape entering the SLM setup and would require pulse shape measurements [190, 109, 192, 193] prior to the SLM setup as well as for SI and LO at the BHD setup. This would require not only more measurement time but also additional complexity for the experimental setup as access to the pulse at different locations is required. Furthermore, the required LO pulse shapes are not directly related to neither the input pulse nor to the

[3] *BST12* from Thorlabs (86 : 14 for s-polarisation at 1559 nm and unknown dispersion).

output pulse of the optical fibre as the complex nonlinear pulse propagation in the optical fibre and its resulting fluctuations have to be considered. For optimal results, a numerical simulation of the pulse propagation is required to estimate a pulse shape for the LO. Only for a perfect simulation, this estimation can be perfect. Otherwise the pulse has to be varied to find a better or optimal LO for an intended measurement.

Due to the complexity, this was not implemented for the first experiments carried out for this PhD thesis. Instead, variations of the pulse shape were done by applying a chirp (section 7.8). Multimode measurements were based on different spectral components instead of defined variations of the temporal pulse shape (section 7.9).

7.5.2 Setup and power transmission

For this setup, the path lengths have to be either precisely matched or differ by a multiple of the distance between two pulses. By choosing a 2 m long *PM1550-XP* fibre, the path has an optical length of roughly 3 m plus steering mirrors. By its design, the SLM requires at least 1.2 m plus additional mirrors, mode matching and adjustable delay. The length of this path was chosen to exactly match the fibre path. By matching both paths, a drift in repetition rate does not affect the delay.

Additionally, a shorter fibre length of 2 m and optical power of 12 mW reduces changes in pulse shape and squeezing which lead to a less complex pulse and correlations. This also reduces the susceptibility to variations in length detuning and the pulse shape. Furthermore, it simplifies the initial observation of squeezing which is required to optimise the optical alignment. The experimentally realised changes of the LO pulse were intended to verify the principle and hence the optical power was not altered. As the laser pulse is limited by the TBWP, the SLM was aligned by observing the intensity autocorrelation [194] and minimising its width.

Overall power transmission is limited by the transmission of the SLM (roughly 50 % [190]) and the achieved transmission of the filter resonator (≈ 75 %). Combined with additional losses from 15 mirrors and the rotation of the polarisation, an overall power transmission close to 25 % was achieved. For the applied simple masks, this is sufficient as the roughly 90 mW of optical power used for this arm resulted in up to 25 mW for the LO, close to the saturation limit of the used detectors.

The combination of HWP and PBS is required to rotate the polarisation for BHD. It can also be used, as the SLM, to attenuate the LO. For practical reasons[4], optical power in the optical fibre was set to 12 mW. Due to the the fixed splitting ratio to the SLM path, the interference of SI and LO did not fully saturate the detectors at this optical power close

[4] Alternating optical power with the SLM requires an additional program to calculate the mask in the laboratory and limits the achievable phase shift. Rotating the waveplate would alter the spectrum as it is not perfectly $\lambda/2$ for all wavelengths.

to 20 mW. This optical power would be reduced to about 7 mW if the SLM was used to shape the squeezed mode (EM_2) which is unaffected by GAWBS. This additional loss in optical power was another reason for the masks to be kept as simple as possible for the reviewed first measurements.

By reducing losses and improving the overall alignment, a power transmission from 50 % to 70 % may be achieved, increasing the available power by a factor of three which was not required for the measurements performed during this thesis.

Using the factory calibration curves (figure L.2 in the appendix) of the SLM and the measured relation between wavelength and pixel number (figure L.1), masks can be calculated to influence or shape the pulse.

7.6 Data recording

For the previous measurements, data was sampled continuously and stored for detailed analysis after the measurement (section 5.6.4). Measurements involving the SLM require the loading of a previously prepared mask before the corresponding data can be recorded. Recording data for both configurations, only LO and BHD, requires blocking and unblocking the SI for each measurement and for 160 consecutive measurements, close to 20 GB[5] of data was gathered. This would take multiple hours within which stabilisation loops are not allowed to fail. Additionally, air turbulences from the active presence of a person disturb the optical paths. To avoid these long measurement times and amounts of data, the measurement scheme described in section 5.5.6 was directly implemented on the laboratory computer. Adapted to the limited resources, a measurement time of 0.4 s was used. Variances were calculated from 10 000 points in time, measured with 25 MS/s, and 40 000 points were recorded for the monitoring traces. A fixed ramp pattern for the phase-shifting piezo was used to streamline the evaluation of consecutive measurements. This allowed for both efficient recording and evaluation but the post-processing was limited compared to storing and accessing the full obtainable data. For the alignment, adjustable default masks were used and directly evaluated during the alignment.

7.7 Experimental alignment

By blocking the beam inside the separation resonator, it becomes a mirror. As the pulse from the fibre matches the fundamental mode of the resonator and is well aligned, it is used for the initial alignment. The pulse from the filter resonator in the SLM path is

[5] In difference to chapter 5, the ramp was provided by the acquisition, allowing the recording of one asymmetric ramp and hence reducing the recording time. Without this optimisation, 300 MB per measurement would produce roughly 96 GB.

aligned to the TEM_{00} mode, reflected by the separation resonator, using two mirrors and an additional delay line. Optical power, measured after the fibre, is increased to 12 mW and the separation resonator is locked upon resonance. At this point, no squeezing was measured and the SLM was used to limit the spectral width of the LO. By additionally tuning the spatial alignment and delay, squeezing was observed and optimised. From this alignment, the applied masks were loaded to the SLM and measured. Neither the fibre pulse nor the pulse after the filter resonator nor its dispersive properties were measured or monitored due to limited time and resources. Hence, no definitive statement on the actual measurements can be made aside from the relative differences between the used masks. This significantly limits the comparison of experimental data to the numerical simulations.

7.8 Chirped local oscillator masks

Using the SLM, an additional chirp can be added to the LO altering the measured mode. Within the parameters of the SLM (appendix L), 201 masks were created to provide an additional GDD of up to $\pm 0.13\,\mathrm{ps}^2$. For a bandwidth-limited 200 fs pulse, the applied chirps would stretch the pulse to up to 300 fs.

12 mW of average optical power was measured after the fibre. For each mask, V_- and V_+ (see equation (5.8)) were extracted as shown in figure 7.4.

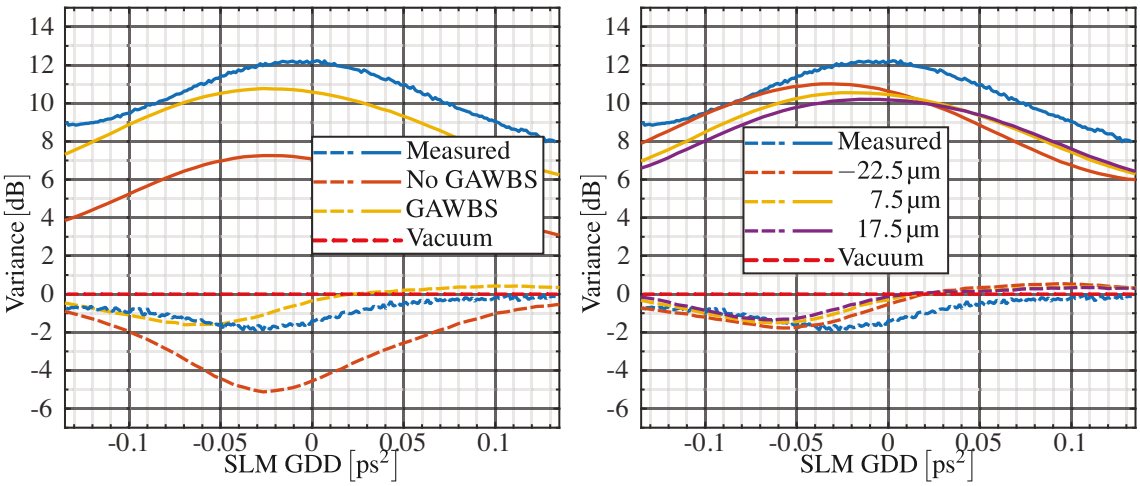

(7.4a) Influence of GAWBS (no detuning)

(7.4b) Influence of detuning (with GAWBS)

Figure 7.4 Chirped LO measurement compared to simulation with chirp centred at 1558 nm
Influence of different parameters on the simulation is illustrated.

The observed V_- was improved by adding GDD but V_+ obtained its maximum value at a different GDD. This indicates that indeed the LO can be used to experimentally optimise the observed squeezing. Compared to the experimental results, the simulation is similar but shows reduced phase noise. This may be the result of discrepancies between the

parameters in the simulation and the experimental parameters. In figure 7.4b, the simulated delay between both pulses is varied as its precise value in the experiment is unknown. An offset in dispersion between simulation and experiment is observed which is likely due to unknown dispersion of the optical components in the LO path. Initial pulse properties, fibre properties, detuning as well as dispersion of the filter resonator can likely further reproduce the experimental data. This was not yet implemented as the precise experimental parameters are unknown. Experimental bounds for those are needed to reduce the required time for their variation in the simulation.

7.9 Multimode measurements

For measurements between multiple modes, the spectrum of the LO was split in areas of close to equal optical power as show in figure 7.5. This is the most straightforward way to define multiple modes and it has significant advantages. These modes are independent of the actual pulse shape, do not interfere with each other and their phases can be shifted easily. Obtaining and shifting other modes requires complex masks, depending on the actual pulse shape.

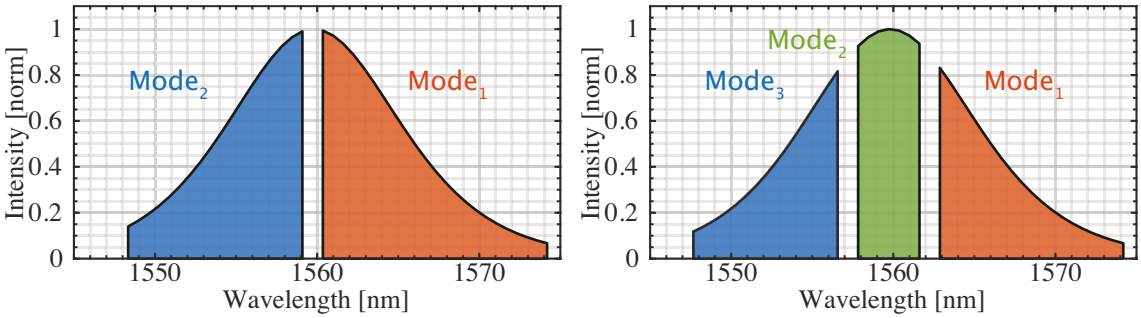

(7.5a) Divided into two modes

(7.5b) Divided into three modes

Figure 7.5 Separation and spectral division in multiple modes for the intensity of the laser pulse

7.9.1 Phase estimation

For CW measurements with multiple modes, commonly multiple BHD setups are used [195, 196]. Here the multiple modes are defined spectrally but the BHD cannot resolve different spectral components as done in [197].

All spectral components interfere individually on the BS in BHD. For each defined mode, a separate interference pattern for phase estimation can only be recorded for spectrally resolved detection. As all spectral components are detected by the same photodiode, only

the sum of all individual patterns can be recorded. In the following, the scheme to estimate the phases of both modes from a single interference pattern is described.

The SLM can be used to vary the phase difference (φ_M) between the two used modes in a well defined manner (appendix chapter L). For each phase difference, the phase in BHD (φ) is scanned and an interference pattern ($I_{1+2}(\varphi, \varphi_M)$) is recorded. This interference pattern is given by the sum of I_1 and I_2 and assuming that for the length detuning by the piezo these modes have approximately the same period[6], it can be written as:

$$I_{1+2}(\varphi, \varphi_M) = I_1(\varphi) + I_2(\varphi, \varphi_1, \varphi_M) \tag{7.8}$$

Each interference pattern can be approximated, at least locally, by a cosine function:

$$A_{1+2}(\varphi_M) \cdot \cos(\varphi + \varphi_M + \Delta\varphi) = A_1 \cdot \cos(\varphi) + A_2 \cdot \cos(\varphi + \varphi_1 + \varphi_M) \tag{7.9}$$

The phase φ_1 is the initial offset between the interference patterns of both modes, $\Delta\varphi$ is the offset of the overall interference pattern and the initial phase of I_1 is chosen to be zero. A_1 and A_2 are known from measurements on the single modes. A_{1+2} is observed for each measurement and $\varphi_1 + \varphi_M$ can be linked to the amplitudes using equation (7.9):

$$A_{1+2}(\varphi_M) = \sqrt{A_1^2 + A_2^2 + 2 \cdot A_1 A_2 \cos(\varphi_1 + \varphi_M)} \tag{7.10}$$

Knowing $\varphi_1 + \varphi_M$, the angle $\varphi_M + \Delta\varphi$ can also be determined from equation (7.9).

$$\cos(\varphi_M + \Delta\varphi) = \frac{A_1 + A_2 \cos(\varphi_1 + \varphi_M)}{A_{1+2}(\varphi_M)} \qquad \sin(\varphi_M + \Delta\varphi) = \frac{A_2 \sin(\varphi_1 + \varphi_M)}{A_{1+2}(\varphi_M)} \tag{7.11}$$

The relations in equations (7.10) and (7.11) can be derived from equation (7.9) easily if complex numbers are used. Due to measurement errors, the right sides of equation (7.11) may be greater than 1. This may be caused by drifts in the overall power of the LO due to the long optical path or the interference pattern being concealed by GAWBS. To avoid this behaviour, a fit is used to extract $\Delta\varphi$ for each measurement as well as φ_1, the phase offset between both interference patterns.

7.9.2 Two-mode measurement

For the measurement, two modes (figure 7.5a) were defined to contain almost equal optical intensity. The phase between the two modes was altered in 160 steps of 2.5 ° by adjusting the phase of only one mode. As a result, the overall interference pattern (figure 7.6a) shows a diagonal structure. Both paths are close to 5 m long and the phase in detection

[6] As the overall spectrum has a width below 15 nm and a central wavelength close to 1559 nm, both carrier wavelengths are close and so are the periods of their interference pattern.

drifts without stabilisation[7]. As a certain time is required for loading a new mask and transferring the data[8], the phase appears to jump between measurements.

Depending on the phase between both modes, the effect of GAWBS can bee seen as it is annihilated by subtraction (figures 7.6b and 7.7b).

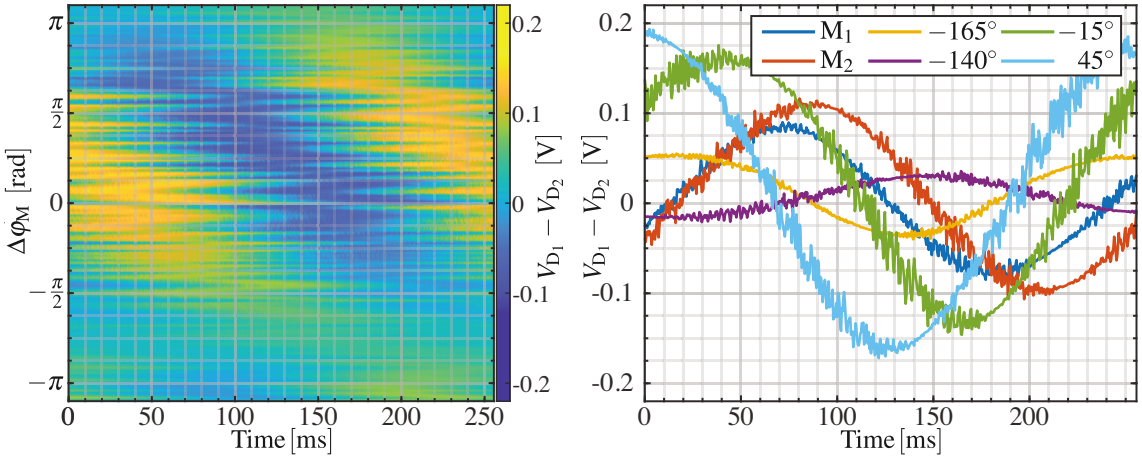

(7.6a) Two-mode interference measured

(7.6b) Example interference patterns

Figure 7.6 Measured interference patterns for two-mode measurement
Data is reduced to the voltage difference between both detectors corrected for offsets. Applied voltage to ramp is fixed to time as indicated in **(7.6b)**.

From each measurement, V_- and V_+ are extracted. A relative angle between the measured variances and the observed interference pattern can be estimated and the amplitudes of the individual interference patterns allow for the deduction of individual quadrature angles for both modes according to equations (7.10) and (7.11).

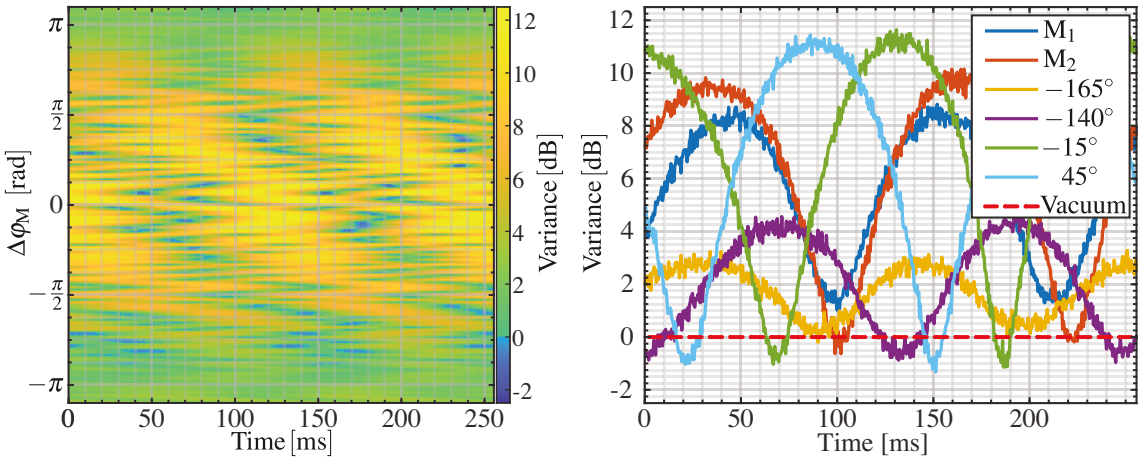

(7.7a) Two-mode variances measured

(7.7b) Example variances

Figure 7.7 Measured variances for two-mode measurement

[7]Optical patch length is equal and hence frequency drifts of the laser do not affect the length difference. Nevertheless, atmosphere and the thermal stability of the 2 m long fibre still result in drifts.

[8]Approximately every three seconds, one of the shown 250 ms segments of data was recorded during the automated measurement.

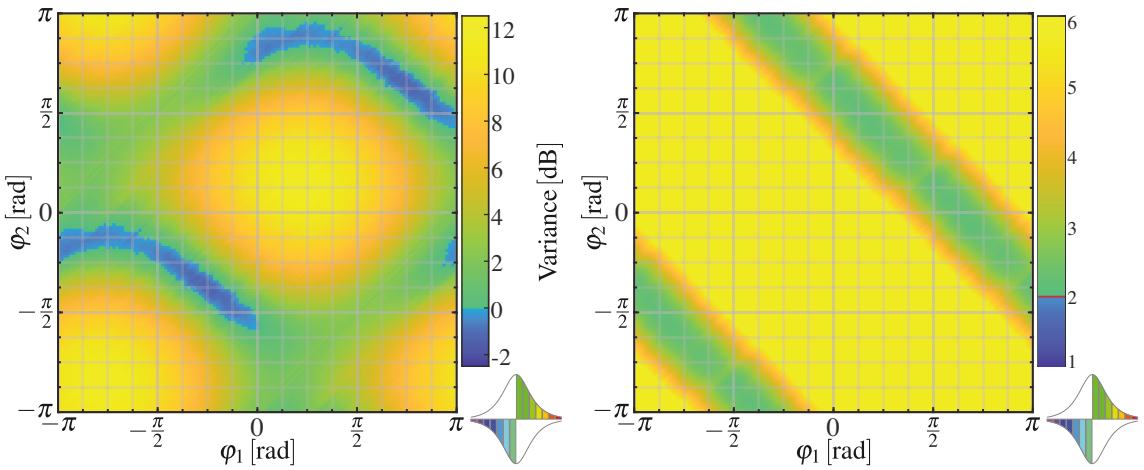

(7.8a) Fitted variances sorted **(7.8b)** Comparison with Duan limit

Figure 7.8 Fitted variances and estimated phases between both modes and comparison to the classical Duan limit of 2 for separability

From the calculated variances, equation (7.7) can be evaluated and while the overall structure strongly resembles simulated data in figures M.1 and M.2, the criteria for separability is violated only for the simulated data and not in the measurement (table 7.1).

A value of 2.29 is obtained which is above the minimum value of 2. The intensities of both modes are not perfectly equal leading to an increased minimum value of 2.06 (equation (7.6)) which is also not surpassed by the measured values. Nevertheless, correlations between both modes are clearly visible as the noise from GAWBS can be cancelled out.

Additionally, Simon's criterion was applied to the experimentally estimated covariance matrix without indicating inseparability of the chosen modes.

The amplitude of the interference pattern changes and the pattern itself is also affected by GAWBS (figure 7.6b). Furthermore, the periodicity of the observed interference pattern is not necessarily identical to the one for the variances, measured for the off-resonant sidebands, as already reviewed for previous measurements. This cannot explain that the measurements do not show the inseparability as the values for V_- range between 0.76 and 1.48. For no phase difference, any other obtained variance can be added to 1.48 to remain below 2 for the proof of inseparability.

	Temperature [K]						
Limit	0	150	225	300	375	450	measurement
2	**1.16**	**1.65**	**1.77**	**1.85**	**1.92**	**1.97**	2.29

Table 7.1 Inseparability criterion for two-mode measurement and simulated data Quantum efficiency is not considered.

One possible reason would be additional noise or the preprocessing of the data but likely, the chosen modes were not a particular good choice. Tuning the simulation by adding a chirp, a delay and using a slightly asymmetric power splitting between both modes, the estimated violation of the separability limit vanishes (at least for the GAWBS at room temperature). These changes were made within a reasonable estimate for the misalignment of the experimental setup. Fibre parameters were not tuned to better reproduce the measurements nor was the Raman effect considered. Also, neither dispersive properties nor spectral intensity changes in the SLM path were analysed or modelled. This can only be done after narrowing down the actual experimental parameters.

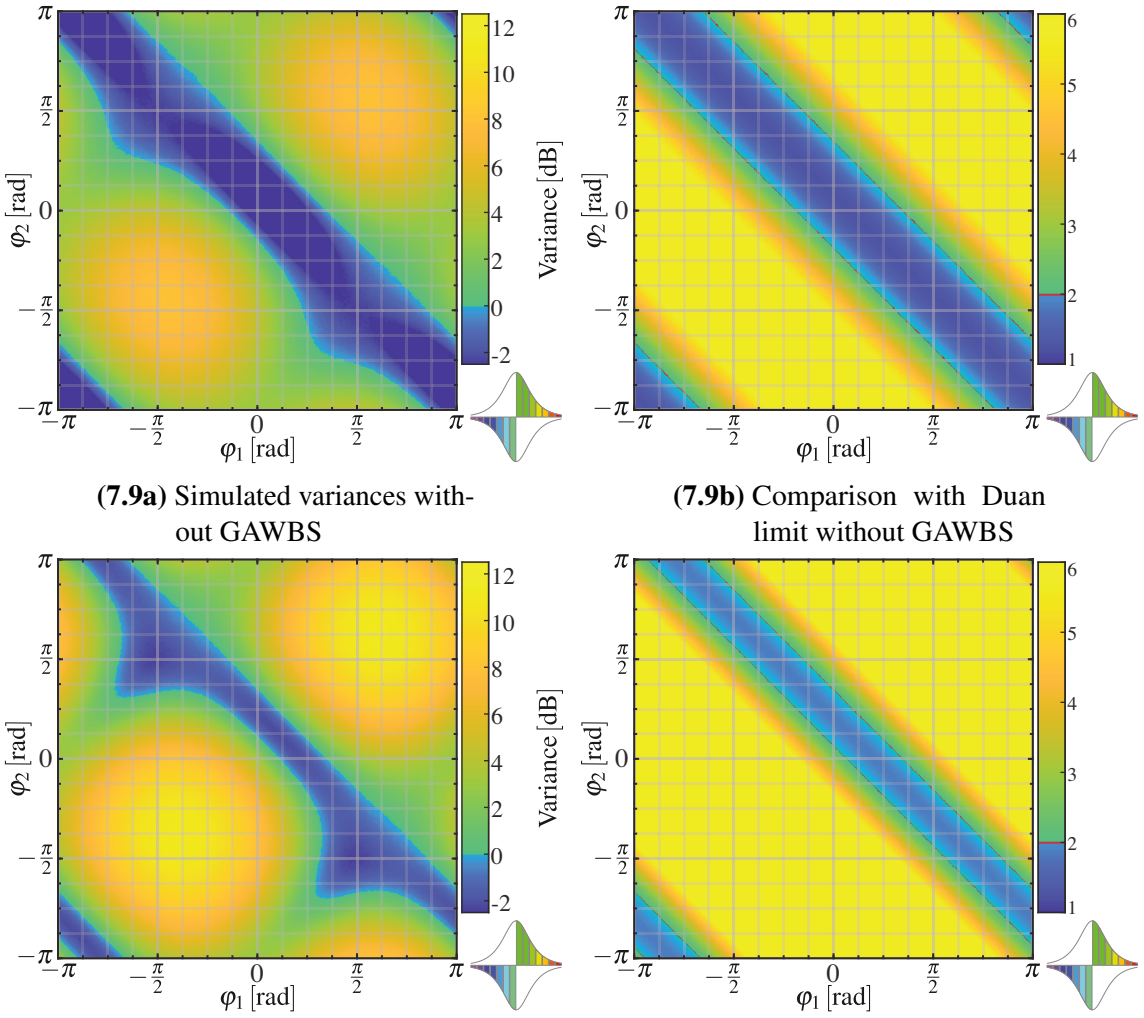

(7.9a) Simulated variances without GAWBS

(7.9b) Comparison with Duan limit without GAWBS

(7.9c) Simulated variances with GAWBS

(7.9d) Comparison with Duan limit with GAWBS

Figure 7.9 Simulated two-mode measurements for 12 mW and 2 m fibre length Used modes were derived by splitting the estimated eigenmode in two equal intense modes.

In figure 7.9, the simulated data is analysed with respect to two modes created by equally splitting the calculated squeezed eigenmode. Without GAWBS, a value of 0.77 is expected and with GAWBS, still a value of 1.36 is expected at 300 K. In principle, these modes can be accessed with the experimental setup but this requires the SLM to find and match the

mode by altering phase and amplitude of the spectral components and afterwards splitting it into two equally powered modes with variable phases.

7.9.3 Three-mode measurement

To measure the correlations between three modes, each mode is measured with each other mode and additionally two modes are added without phase difference and measured with the third one, yielding six two-mode measurements. Each measurement was carried out like previous two-mode measurements (section 7.9.2). The evaluated experimental data (variances and comparison to the boundary for separability) as well as simulations for GAWBS from different temperatures are presented in appendix M due to the number of figures. After sorting the phases, the measured data in figure M.3 resembles the simulated data in figure M.11. In the simulation, all combinations violate the classical boundary discussed in section 7.1.1 if no GAWBS is present. At room temperature in presence of GAWBS, only the combination 6 (blue and red in figure 7.5b) is expected to violate the classical boundary.

Within the experimental measurement, only combination 5 (blue and green) violates the limit of 2 for separability with an average value of 1.99. Based on the almost equal intensities of the involved modes, the limit for separability is estimated to be 2.01. For this combination, the structure of figure M.4e is clearly diagonal but for other combinations, especially 4 and 6, the effect of the imprecise phase estimate is clearly visible. Results are summarised in table M.1. While the overall images of the measured variances resemble the simulated data, the resulting numerical values for the separability criterion do not match the experimental findings. For combinations 1, 3, 4 and 6, the measured values exceed the simulated value and for combinations 2 and 5, it is below the expected value from the simulation. As for two modes, the simulation does not account for additional experimental parameters.

As in other measurements, the operational principle is proven and experimental data and the overlap with the simulation is as good as it can be expected, regarding the relative simplicity of the simulated pulse propagation in the optical fibre as well as the lack of precise experimental characterisation and long-term stabilisation. Nevertheless, the violation of a separability criteria depends strongly on the chosen modes and the experimental alignment. It is expected that by optimising the measured modes, reducing GAWBS and improving data recording, the experiment could reveal significant inseparability. By evaluating the complete data from BHD, criteria beyond those based on second order moments can be investigated for future measurements.

8. Homodyne cross-correlation measurement

During this thesis, the research was focussed on the experimental approach based on the separation resonator and its properties as well as capabilities which were discussed within the major part of this thesis. During its experimental alignment and improvement, the squeezing was either significantly lower than expected or completely hidden for a long time. Squeezing can easily be masked by classical noise but some detection schemes are more susceptible to this than others. Hence, supervised students implemented different methods to verify the non-classicality of the pulses after their propagation through the fibre. One successful approach [193] was using the available adjustable SLM setup to spectrally filter the pulse in order to reveal squeezing with balanced detection, similar to previous works [29, 150, 198]. Another interesting approach was the implementation of a HCCM scheme [56] for the Kerr-squeezed pulses that can verify non-classicality based on LO and SI pulses with comparable intensities. In contrast, BHD is based on a strong LO and weak SI. Compared to the separation resonator–based measurements, the two used pulses directly interfere without significant GAWBS phase noise.

Previously, this approach was applied only once to a squeezed state in the CW regime and revealed non-classicality over a wider range of phases than in BHD [39].

To present this different approach, first the experimental setup is presented prior to the measurement procedure and the corresponding condition for classicality. The results from the HCCM [199] are shown and related to other measurement setups.

8.1 Principle of HCCM

Compared to a BHD, where a balanced BS is used (chapter 5), the HCCM relies on an unbalanced BS. The intensity noise correlation of both detectors has different contributions that can be separated by their periodicity with respect to the phase or their dependence on LO intensity [200].

From the field transmission (τ) and reflection (r) coefficients of the BS, four parameters are derived to simplify the occurring terms in the intensity correlation.

$$\mathcal{T} = |\tau|^2|r|^2 \qquad \mathcal{T}_0 = 1 \qquad \mathcal{T}_1 = \frac{|r|}{|\tau|} - \frac{|\tau|}{|r|} \qquad \mathcal{T}_2 = -1 \tag{8.1}$$

This allows to write the phase-dependent correlation of the intensity fluctuations $\Delta G^{(2,2)}(\phi)$ as:

$$\Delta G^{(2,2)}(\phi) = \underbrace{\mathcal{T}\mathcal{T}_0 \left\langle (\Delta I)^2 \right\rangle}_{\Delta G_0^{(2,2)}} + \underbrace{\mathcal{T}\mathcal{T}_1 E_{\mathrm{LO}} \left\langle \Delta E_\phi \Delta I \right\rangle}_{\Delta G_1^{(2,2)}(\phi)} + \underbrace{\mathcal{T}\mathcal{T}_2 E_{\mathrm{LO}}^2 \left\langle \left(\Delta E_\phi\right)^2 \right\rangle}_{\Delta G_2^{(2,2)}(\phi)} \tag{8.2}$$

While $\Delta G_0^{(2,2)}$ is phase-independent, the second term $\Delta G_1^{(2,2)}(\phi)$ is π-periodic and only accessible with an unbalanced BS as in the balanced case $\mathcal{T}_1 = 0$. It is proportional to the fluctuations of two non-commuting observables ΔE_ϕ and ΔI. The last term $\Delta G_2^{(2,2)}(\phi)$ is proportional to the variance of the field fluctuations at the chosen quadrature angle.

Detectors absorb photons with a certain efficiency, and the electronics afterwards further amplify the signal. Hence, the measured correlation $C(\phi)$ additionally contains a pre-factor ($\zeta_{1,2}$) for each detector:

$$C(\phi) = \zeta_1 \zeta_2 \Delta G^{(2,2)}(\phi) \tag{8.3}$$

$$= C_0 + C_1(\phi) + C_2(\phi) \tag{8.4}$$

$$= a_0 + \sum_{k=1}^{2} \left[a_k \cos(k\phi) + b_k \sin(k\phi)\right] \tag{8.5}$$

Equation (8.4) splits the measured correlation according to equation (8.2) and equation (8.5) provides an analytic expression based on the periodicity of C_1 and C_2. As C_0 is phase-independent and $\Delta E_\phi = -\Delta E_{\phi+\pi}$, the C_1 term cannot have a constant offset. The C_0 term can be measured directly with a blocked LO beam (C_{block}). The other contributions can be written as:

$$C_1(\phi) = a_1 \cos(\phi) + b_1 \sin(\phi) \tag{8.6}$$

$$C_2(\phi) = a_2 \cos(2\phi) + b_2 \sin(2\phi) + a_0 - C_{\mathrm{block}} \tag{8.7}$$

For classical states with classical correlations between ΔE_ϕ and ΔI, the following Cauchy-Schwarz inequality has to hold true:

$$\left\langle \Delta E_\phi \Delta I \right\rangle^2 \leq \left\langle (\Delta I)^2 \right\rangle \left\langle \left(\Delta E_\phi\right)^2 \right\rangle \tag{8.8}$$

Using equation (8.2), this inequality can be written as:

$$\frac{\Delta G_0^{(2,2)}}{\mathcal{T}\mathcal{T}_0} \cdot \frac{\Delta G_2^{(2,2)}}{\mathcal{T}\mathcal{T}_2 E_{\mathrm{LO}}^2} - \left(\frac{\Delta G_1^{(2,2)}}{\mathcal{T}\mathcal{T}_1 E_{\mathrm{LO}}} \right)^2 \geq 0 \tag{8.9}$$

Multiplying with the positive factor $\zeta_1^2 \zeta_2^2 \mathcal{T}^2 E_{\mathrm{LO}}^2$ and using equation (8.3), the inequality can be written in term of $C_{0,1,2}$ which can be extracted from experimentally data:

$$L(\phi) = \frac{C_0}{\mathcal{T}_0} \cdot \frac{C_2(\phi)}{\mathcal{T}_2} - \left(\frac{C_1(\phi)}{\mathcal{T}_1} \right)^2 \geq 0 \tag{8.10}$$

Classical states cannot violate equation (8.10).

8.2 HCCM setup

Implementing a HCCM for Kerr-squeezed pulses from an optical fibre requires propagation through the optical fibre. Instead of using a free-space BS, requiring additional mode matching, a PM fibre-based BS is used, ensuring a stable mode matching to the LO path. The overall power to the experimental setup (figure 8.1) can be adjusted. Additional apertures in both arms allow for individual adjustments in coupling efficiency. The distance Δs is used to optimise the temporal overlap with the LO pulse. By using a 5 m long optical fibre, the delay to the LO pulse is known to be the time between two pulses or about 25 ns. To adjust the phase in the detection, the repetition rate of the laser is altered by up to 200 Hz, altering the time between two pulses by about 30 fs. By the additional factor of two, this corresponds to more than 10 times the period of one optical cycle[1] which is more than sufficient.

The BS was ordered with a splitting ration of 90 : 10 at 1550 nm, which was sufficiently close to the optimal value of 86 : 14. Prior to the HCCM, the splitting ratio of the used BS [201] was measured using the OSA. The characterisation is depicted in figure 8.2b. At 1550 nm, splitting ratios of 89 : 11 and 11.5 : 88.5 are measured for the ports of SI and LO. During this, the 5 m fibre was connected to the input and the OSA to the corresponding output. Prior to and after the measurement of the BS, the direct spectrum from the fibre was measured. These two measurements differed by 1.3 %, either due to instability of the coupling or reproducibility of the connection. Hence, the measured deviation between the two splitting ratios is insignificant and overlaps with the measured splitting ratio of 89.7 : 11.3 provided by the manufacturer at 1550 nm.

A balanced detection (chapter 5) in the transmitting port was performed for various pulse energies in both arms (figure 8.2b) to verify that the interference is stable enough to show

[1] For 1560 nm, one period corresponds to 5.2 fs.

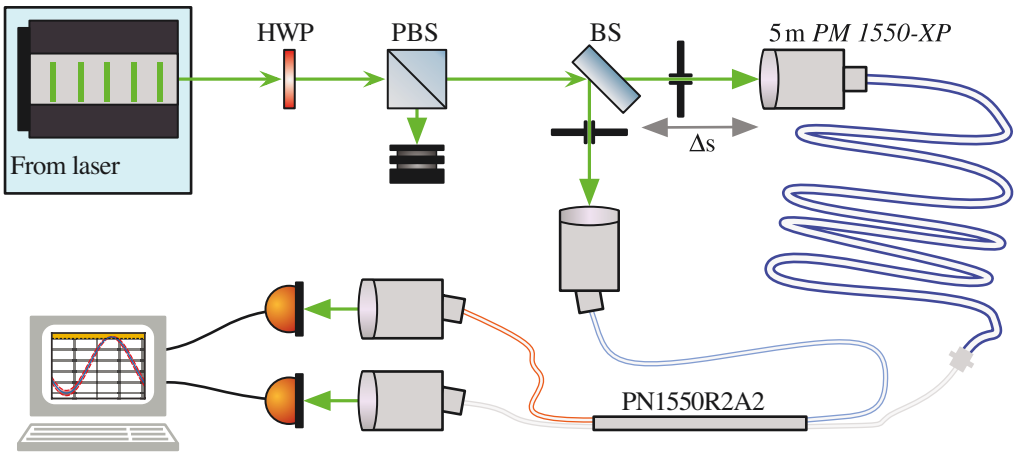

Figure 8.1 HCCM setup reduced to its essential components
The incident light from the laser distribution (figure 3.2) is adjusted in optical power (HWP+PBS) and split by a BS before being coupled into both fibre arms. Additional apertures allow for individual adjustments in optical power and a variation of the splitting ratio. Pulse overlap is adjusted using a delay in one arm and scanned using the modulation of the laser repetition rate (figure 3.2)

squeezing. This configuration is similar to previous experiments [24, 202, 203] with the crucial difference that the pulses propagate through different fibres and hence experience different GAWBS as well as drifts in fibre length which reduces the overall stability. Squeezing can be observed in this setup as the interference of both pulses displaces the squeezing ellipse (see [144, Ch. 5]). In this port, the optical power of the used second pulse was 11.8 times weaker than the pulse from the 5 m fibre. The 50 : 50 BS, used for the balanced detection, is removed and one detector per output port of the fibre BS is used for HCCM[2]. All optical powers are measured after the fibre BS to avoid frequent reconnections for the 5 m fibre.

[2]In principle, a balanced detection can be performed for each output port simultaneously to the HCCM but two sets of detectors and four recording channels are required.

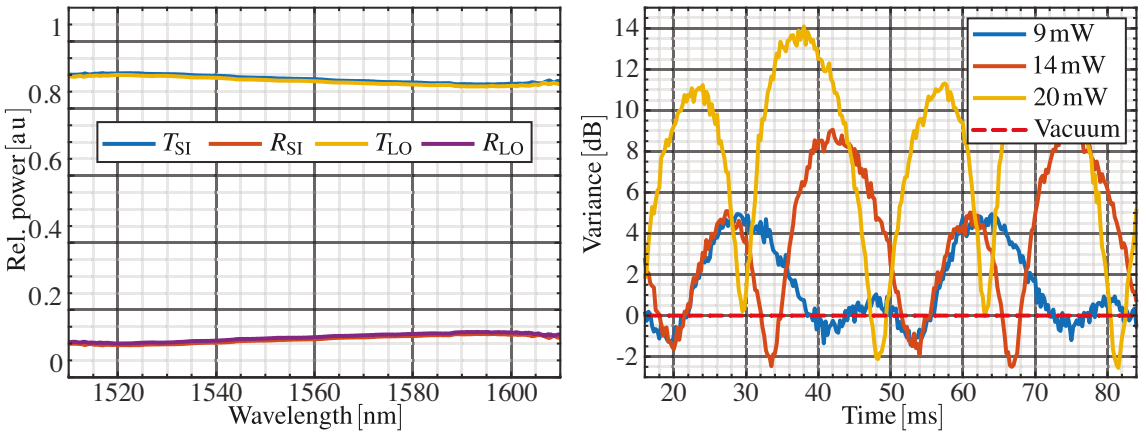

(8.2a) Fibre BS characterisation

(8.2b) Squeezing in balanced detection

Figure 8.2 (8.2a) shows the wavelength dependence of power splitting for the fibre BS. In (8.2b), the measured variances in balanced detection are provided for three different average optical powers propagating through the 5 m fibre after interference with a second pulse. Phase is almost linear in time.

8.3 HCCM results

The average intensities of SI and LO were adjusted individually. For each output, the power of the stronger port is adjusted to receive an average optical power of 10 mW. As the expected non-classicality increases with intensity, these values were chosen as the occurring interference patterns did not yet saturate the detectors. The measured splitting ratio for the overall spectrum was 88.4 : 11.6 .

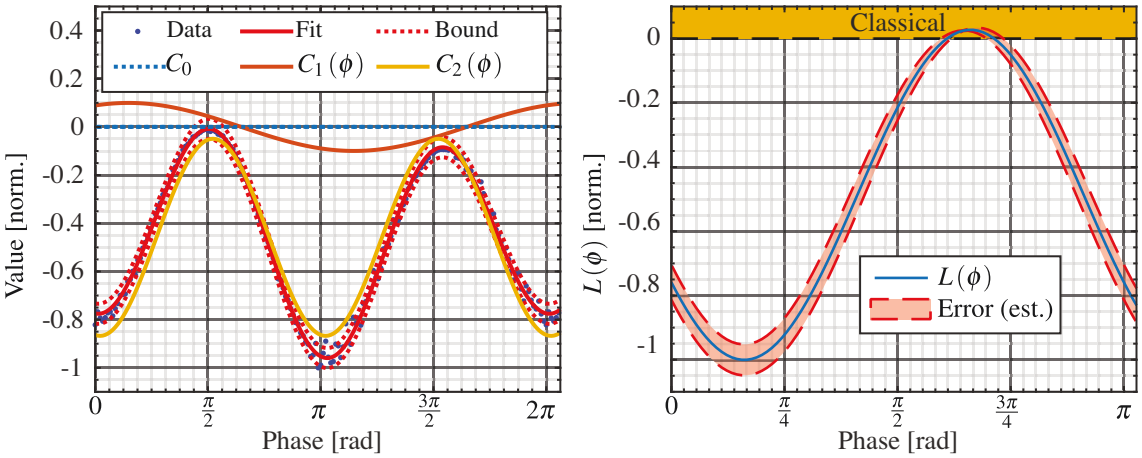

(8.3a) Phase-resolved measured correlation and its decomposition normalised to its maximum absolute value

(8.3b) Phase-resolved non-classicality criteria for HCCM normalised to its maximum absolute value

Figure 8.3 (8.3a) shows the measured data and the fitted decomposition in C_0, C_1 and C_2. 88 720 data points were used per phase interval of 2 °.
(8.3b) depicts one period of the π-periodic $L(\phi)$ (equation (8.10)) and an estimation of its error.

In figure 8.3, the measured correlations from 12 periods of 2π are shown with the decomposition in C_0, C_1 and C_2. In figure 8.3b, the resulting clear violation of equation (8.10) is shown for almost all phases.

At this point, the used criterion for non-classicality has to be further analysed. For any state, $C_0 \geq 0$ and $C_2 \leq 0$ are already indicators for non-classicality. With $\mathcal{T}_0 = 1$ and $\mathcal{T}_2 = -1$, the first term $(K_1 = C_0 C_2(\phi)/(\mathcal{T}_0\mathcal{T}_2))$ in equation (8.10) has to be zero or positive for a classical state. The subtracted second term $\left(K_2 = (C_1(\phi)/\mathcal{T}_1)^2\right)$ is also positive. For any classical state, the remainder $(K_1 - K_2)$ has to be greater than or equal to zero.

For an ideal coherent state, the intensity correlation between both detectors would vanish as the BS splits the coherent state in two coherent states and hence C_0 and K_1 would be zero and any non-zero value for K_2 would directly imply a non-classical state. To create the Kerr-squeezed pulse, a coherent state propagates through the optical fibre and neither linear losses nor the Kerr effect[3] alter its intensity correlations. As a result, any intensity based measurement[4] such as the intensity correlation yields the same result as without the propagation. Hence only where C_1 is near zero, the criteria cannot verify the non-classicality.

Like the CW implementation [39], the HCCM is able to resolve the non-classicality over a broader range of phases than previously applied BHD or balanced correlation schemes with Kerr-squeezed pulses [140]. However, these results only verify the non-classicality and do not yet provide intuitive additional information that can be obtained in BHD.

[3] See [204, (Ch.22.6)] and section 5.4.

[4] That measures the number of photons within a single pulse without any spectral filtering or further interference.

9. Summary and Outlook

9.1 Summary of experimental results

In this thesis, an experimental setup to spectrally separate the carrier pulse from a non-classical Kerr-squeezed fs pulse was successfully developed and implemented. The experimental setup provides a spectrally broad (well above 10 nm) non-classical state with significantly lowered coherent amplitude on which BHD measurements with both a fixed and a shapeable LO pulse can be performed.

The required frequency comb structure of the laser system and its stability were pointed out. Due to limited resources, it was not possible to resolve the extraordinary stability on short timescales. Long-term stability (over days) was found to be limited by atmospheric pressure changes which should equally affect both laser and separation resonator. Additionally, the dispersive characteristics of the resonator were measured by implementing a spectrally resolved scan of the resonator transmission using a stabilised detuning from resonance in the nm regime. The measured dispersion drastically altered the shape of the depleted carrier pulse in reflection leading to a reduced visibility and a mismatch of the observable interference pattern between carrier pulses and the nearly fully reflected sidebands.

Based upon the above mentioned experimental setup, a BHD was set up and characterised. Spatial modes of both LO and SI were given by the separation resonator which resulted in excellent spatial mode matching. For the evaluation of the recorded data, methods were derived and implemented that exceed the commonly used approximations. These methods provided a simultaneously recorded vacuum reference and reduced the number of required separate measurements. The previously expected mismatch between the interference pattern and the sidebands, analysed in BHD, was verified experimentally.

These conducted BHD measurements showed significantly less squeezing and more anti-squeezing than expected. The hypothesis that GAWBS, caused by thermally excited vibrations of the fibre structure, introduce phase noise between consecutive pulses was tested by submerging the fibre in LN_2. While a simple model explains the observed reduction in anti-squeezing and increase in squeezing quite well, it is expected that a more complex model is required.

As GAWBS was found to be the limiting factor, an SLM was used to shape the LO pulse and access different temporal modes to extend the experimental setup. Spatial mode matching was ensured by a second resonator. The acquired data shows that an optimised LO can increase the observed squeezing. Measurements on different modes can be used to analyse their correlations and possibly reveal inseparability. These measurements are limited by the determination of the phase and the used modes which can both be improved upon. Additionally, the influence of Brillouin noise can be reduced significantly by the shape of the LO.

Overall, the built experimental setup enables temporal-mode selective tomographic measurements of the quantum state for bright pulses based on their frequency comb structure. Performance is limited by several identified parameters which can be overcome by future experimental improvements. With such improvements, the experimental setup could provide enormous potential for the analysis of quantum correlations within one pulse and between pulses.

9.2 Outlook

For the outlook, two different categories will be discussed. One category is based on the technical limitations observed and identified during this thesis. Methods for their optimisation are discussed as they may be needed for future measurements and extensions. The other category discussed possible future extensions of the actual quantum measurements and applications of the presented measurement scheme.

9.2.1 Technical limitations improvements

Brillouin scattering is the most dominant influence and limitation in the current experimental setup, especially for low pulse energies. LN_2 reaches a temperature of 77 K which is still a quarter of the room temperature and hence does not sufficiently suppress the effect of GAWBS. Additionally, the cold air leads to constant drifts in the alignment limiting the measurement time to a few minutes if not a constant and stable cooling is implemented for future measurements. A possible solution could be moving the optical fibre and its coupling into a cryostat with optical access. This could achieve temperatures near 4 K which is 75 times lower than room temperature and GAWBS influence could be greatly reduced.

Improving the quantum efficiency as well as the data acquisition could reduce the time required to obtain enough data in the laboratory. The bandwidth of the detectors could be improved by a factor of 3. This could be achieved by shifting the resonance frequency closer to 10 MHz and increasing the bandwidth from 1 MHz to 3 MHz. Combined with

an upgrade in data transfer rate to the computer, required time for each measurement could likely be reduced by an order of magnitude. Additional automatisation of power adjustment, beam blocks and length detuning could further reduce the time required for measurements and shaping the LO.

Furthermore, a tailored nonlinear propagation for the LO pulse can be used to change its spectrum, *i.e.* spectral broadening, to decrease the losses within the SLM. If properly characterised and stabilised, this would allow to access an even larger number of pulse shapes.

The phase and detuning readout from the interference pattern is not accurate enough to be used as an absolute reference as the dispersion inside the separation resonator affects the interference pattern. Additionally, the detuning in length is not a true phase detuning as the spectral components are affected slightly different. In principle, the path length difference could be read using a second laser but an enormous stability would be required due to lengths of several meter. A far more elegant solution could be realised using a separate pulsed laser system for the LO with identical repetition rate but a CEO differing by a few Hz, leading to a quasi-continuous scan of solely the phase. Furthermore, the second laser could provide a broader spectrum with shorter pulses which could allow the SLM to access such modes with fewer losses.

To achieve such a stability, complex stabilisation loops and a stable reference would be required for the used lasers. Generally long-term relative stabilities in the regime of 10^{-21} are possible [205, 206] but substantial effort would be required. Furthermore, this would alter the pulse shape and energy as the CEO would be stabilised to atmospheric fluctuations by using the pump diode current. Therefore, atmospheric fluctuations would alter the CEO of the used resonators relative to a stabilised laser. To avoid this, a stabilised atmosphere for the setup may be compulsory.

9.2.2 Future extensions and applications

Subsequent to the initial SLM-based measurements, a follow-up approach could be to experimentally shape the LO to find and match the most squeezed modes. Due to the almost endless number of possible masks and/or detuning, this most certainly would require an automated implementation. Parallel evaluation of the pulse shape may be beneficial for this approach.

One objective could be the optimisation of the experimental parameters, such as pulse shape, pulse energy, fibre length and fibre parameters. During this process, their influence on both the quantum state and classical noise could be analysed. Especially in combination with the SLM, even more measurements may be possible or even required. By improving the experimental readout, additional improvements on the simulation could be made. An

improved simulation could provide additional experimental insight and give inspiration for new experimental configurations and measurements.

More complex pulse propagation, like interacting soliton pulses [190] or the output of a Sagnac interferometer [24], could also be investigated with this setup. Additionally, the setup could be extended to two interacting pulses that differ in polarisation or wavelength. Changing for example the delay between both pulses, the interaction between both pulses could be altered and the resulting correlations can be studied. For this analysis, two separation resonators and LO pulses may be needed.

The separation resonator setup could also be applied, in principle, on bright squeezed pulses from a $\chi^{(2)}$ nonlinearity. Such measurements and their evaluation could be used to further stabilise and to improve the obtained squeezing by optimising for example the pump pulse. This may further improve the abilities of quantum enhanced microscopes [13] or it could be used to tailor the quantum correlations for specific interactions with a sample.

The developed and implemented experimental setup provides vast potential to characterise quantum correlations in bright pulses. Major technical difficulties have been identified and can likely be overcome as the above suggestions imply.

List of Figures

List of Tables

Bibliography

[1] Planck, M. Ueber das Gesetz der Energieverteilung im Normalspectrum. *Annalen der Physik* **309**, 553–563 (1901). URL https://doi.org/10.1002/andp.19013090310.

[2] Einstein, A. Über einen die Erzeugung und Verwandlung des Lichtes betreffenden heuristischen Gesichtspunkt. *Annalen der Physik* **322**, 132–148 (1905). URL https://doi.org/10.1002/andp.19053220607.

[3] BIPM. *Le Système international d'unités / The International System of Units ('The SI Brochure')* (Bureau international des poids et mesures, 2019), ninth edn.

[4] Maiman, T. H. Optical and microwave-optical experiments in ruby. *Phys. Rev. Lett.* **4**, 564–566 (1960). URL https://doi.org/10.1103/PhysRevLett.4.564.

[5] Jang, Y.-S. *et al.* Comb-referenced laser distance interferometer for industrial nanotechnology. *Scientific Reports* **6**, 31770 (2016). URL https://doi.org/10.1038/srep31770.

[6] Giunta, M. *et al.* 20 years and 20 decimal digits: A journey with optical frequency combs. *IEEE Photonics Technology Letters* **31**, 1898–1901 (2019). URL https://doi.org/10.1109/LPT.2019.2955096.

[7] Ferrari, F. *et al.* High-energy isolated attosecond pulses generated by above-saturation few-cycle fields. *Nature Photonics* **4**, 875–879 (2010). URL https://doi.org/10.1038/nphoton.2010.250.

[8] Yoon, J. W. *et al.* Realisation if laser intensity over 10^{23} W/cm^2. *Optica* **8**, 630–635 (2021). URL https://doi.org/10.1364/OPTICA.420520.

[9] Grubb, S. *et al.* Real-time 16QAM transatlantic record spectral efficiency of 6.21 b/s/hz enabling 26.2 tbps capacity. In *Optical Fiber Communication Conference (OFC) 2019*, M2E.6 (Optical Society of America, 2019). URL https://doi.org/10.1364/OFC.2019.M2E.6.

[10] Rademacher, G. *et al.* Peta-bit-per-second optical communications system using a standard cladding diameter 15-mode fiber. *Nature Communications* **12**, 4238 (2021). URL https://doi.org/10.1038/s41467-021-24409-w.

[11] Glauber, R. J. Coherent and incoherent states of the radiation field. *Phys. Rev.* **131**, 2766–2788 (1963). URL https://doi.org/10.1103/PhysRev.131.2766.

[12] Andersen, U. L., Gehring, T., Marquardt, C. & Leuchs, G. 30 years of squeezed light generation. *Physica Scripta* **91**, 053001 (2016). URL https://doi.org/10.1088/0031-8949/91/5/053001.

[13] Casacio, C. A. *et al.* Quantum-enhanced nonlinear microscopy. *Nature* **594**, 201–206 (2021). URL https://doi.org/10.1038/s41586-021-03528-w.

[14] de Andrade, R. B. *et al.* Quantum-enhanced continuous-wave stimulated Raman scattering spectroscopy. *Optica* **7**, 470 (2020). URL https://doi.org/10.1364/OPTICA.386584. 2002.04674.

[15] Acernese, F. *et al.* Increasing the Astrophysical Reach of the Advanced Virgo Detector via the Application of Squeezed Vacuum States of Light. *Phys. Rev. Lett.* **123**, 231108 (2019). URL https://doi.org/10.1103/PhysRevLett.123.231108.

[16] Lemos, G. B. *et al.* Quantum imaging with undetected photons. *Nature* **512**, 409–412 (2014). URL https://doi.org/10.1038/nature13586.

[17] Joshi, S. K. *et al.* A trusted node–free eight-user metropolitan quantum communication network. *Science Advances* **6** (2020). URL https://doi.org/10.1126/sciadv.aba0959.

[18] Pirandola, S. *et al.* Advances in quantum cryptography. *Adv. Opt. Photon.* **12**, 1012–1236 (2020). URL https://doi.org/10.1364/AOP.361502.

[19] Lloyd, S. & Braunstein, S. L. Quantum Computation over Continuous Variables. *Phys. Rev. Lett.* **82**, 1784–1787 (1999). URL https://doi.org/10.1103/PhysRevLett.82.1784.

[20] Huang, H.-L., Wu, D., Fan, D. & Zhu, X. Superconducting quantum computing: a review. *Science China Information Sciences* **63** (2020). URL https://doi.org/10.1007/s11432-020-2881-9.

[21] Milburn, G. J. *et al.* Optical-fiber media for squeezed-state generation. *J. Opt. Soc. Am. B* **4**, 1476–1489 (1987). URL https://doi.org/10.1364/JOSAB.4.001476.

[22] Imoto, N., Haus, H. A. & Yamamoto, Y. Quantum nondemolition measurement of the photon number via the optical kerr effect. *Phys. Rev. A* **32**, 2287–2292 (1985). URL https://link.aps.org/doi/10.1103/PhysRevA.32.2287.

[23] Rosenbluh, M. & Shelby, R. M. Squeezed optical solitons. *Phys. Rev. Lett.* **66**, 153–156 (1991). URL https://link.aps.org/doi/10.1103/PhysRevLett.66.153.

[24] Meissner, M. *et al.* All-fibre source of amplitude squeezed light pulses. *Journal of Optics B* **6**, 652–657 (2004). URL https://doi.org/10.1088/1464-4266/6/8/005.

[25] Semmler, M. *et al.* Single-mode squeezing in arbitrary spatial modes. *Opt. Express* **24**, 7633–7642 (2016). URL https://doi.org/10.1364/OE.24.007633.

[26] Silberhorn, C. *et al.* Generation of Continuous Variable Einstein-Podolsky-Rosen Entanglement via the Kerr Nonlinearity in an Optical Fiber. *Phys. Rev. Lett.* **86**, 4267–4270 (2001). URL https://doi.org/10.1088/1464-4266/6/8/005.

[27] Peuntinger, C. *et al.* Distribution of Squeezed States through an Atmospheric Channel. *Phys. Rev. Lett.* **113**, 060502 (2014). URL https://doi.org/10.1103/PhysRevLett.113.060502.

[28] Friberg, S. R., Machida, S., Werner, M. J., Levanon, A. & Mukai, T. Observation of Optical Soliton Photon-Number Squeezing. *Phys. Rev. Lett.* **77**, 3775–3778 (1996). URL https://doi.org/10.1103/PhysRevLett.77.3775.

[29] Spälter, S., Korolkova, N., König, F., Sizmann, A. & Leuchs, G. Observation of Multimode Quantum Correlations in Fiber Optical Solitons. *Phys. Rev. Lett.* **81**, 786–789 (1998). URL https://doi.org/10.1103/PhysRevLett.81.786.

[30] Heersink, J., Josse, V., Leuchs, G. & Andersen, U. L. Efficient polarization squeezing in optical fibers. *Opt. Lett.* **30**, 1192–1194 (2005). URL https://doi.org/10.1364/OL.30.001192.

[31] Müller, C. R. *et al.* Quantum polarization tomography of bright squeezed light. *New Journal of Physics* **14**, 085002 (2012). URL https://doi.org/10.1088/1367-2630/14/8/085002. 1203.0166.

[32] Breitenbach, G., Schiller, S. & Mlynek, J. Measurement of the quantum states of squeezed light. *Nature* **387**, 471–475 (1997). URL https://doi.org/10.1038/387471a0.

[33] Collett, M., Loudon, R. & Gardiner, C. Quantum Theory of Optical Homodyne and Heterodyne Detection. *Journal of Modern Optics* **34**, 881–902 (1987). URL https://doi.org/10.1080/09500348714550811.

[34] Juodawlkis, P. W. *et al.* Absorption saturation nonlinearity in InGaAs/InP p-i-n photodiodes. In *The 15th Annual Meeting of the IEEE Lasers and Electro-Optics Society*, vol. 2, 426–427 vol.2 (2002). URL https://doi.org/10.1109/LEOS.2002.1159361.

[35] Ye, J., Schnatz, H. & Hollberg, L. Optical frequency combs: From frequency metrology to optical phase control. *Selected Topics in Quantum Electronics, IEEE Journal of* **9**, 1041 – 1058 (2003). URL https://doi.org/10.1109/JSTQE.2003.819109.

[36] Roslund, J., de Araújo, R., Jiang, S., Fabre, C. & Treps, N. Wavelength-multiplexed quantum networks with ultrafast frequency combs. *Nature Photonics* **8**, 109–112 (2014). URL https://doi.org/10.1038/nphoton.2013.340.

[37] Chen, M., Menicucci, N. C. & Pfister, O. Experimental Realization of Multipartite Entanglement of 60 Modes of a Quantum Optical Frequency Comb. *Phys. Rev. Lett.* **112**, 120505 (2014). URL https://doi.org/10.1103/PhysRevLett.112.120505.

[38] Ra, Y.-S. *et al.* Non-Gaussian quantum states of a multimode light field. *Nature Physics* **16**, 144–147 (2020). URL https://doi.org/10.1038/s41567-019-0726-y.

[39] Kühn, B., Vogel, W., Mraz, M., Köhnke, S. & Hage, B. Anomalous Quantum Correlations of Squeezed Light. *Phys. Rev. Lett.* **118**, 153601 (2017). URL https://doi.org/10.1103/PhysRevLett.118.153601.

[40] Casacio, C. A. *Quantum enhanced microscopy*. Ph.D. thesis, The university of Queensland (2021). URL https://doi.org/10.14264/3e54d4d.

[41] Taylor, M. A. *et al.* Biological measurement beyond the quantum limit. *Nature Photonics* **7**, 229–233 (2013). URL https://doi.org/10.1038/nphoton.2012.346.

[42] RAMAN, C. V. & KRISHNAN, K. S. The Optical Analogue of the Compton Effect. *Nature* **121**, 711–711 (1928). URL https://doi.org/10.1038/121711a0.

[43] Turrell, G., Delhaye, M. & Dhamelincourt, P. 2 - Characteristics of Raman Microscopy. In Turrell, G. & Corset, J. (eds.) *Raman Microscopy*, 27–49 (Academic Press, London, 1996). URL https://doi.org/10.1016/B978-012189690-4/50022-3.

[44] Cheng, J.-X. & Xie, X. S. Vibrational spectroscopic imaging of living systems: An emerging platform for biology and medicine. *Science* **350**, aaa8870 (2015). URL https://doi.org/10.1126/science.aaa8870.

[45] Camp Jr, C. H. & Cicerone, M. T. Chemically sensitive bioimaging with coherent raman scattering. *Nature Photonics* **9**, 295–305 (2015). URL https://doi.org/10.1038/nphoton.2015.60.

[46] Freudiger, C. W. *et al.* Label-Free Biomedical Imaging with High Sensitivity by Stimulated Raman Scattering Microscopy. *Science* **322**, 1857–1861 (2008). URL https://doi.org/10.1126/science.1165758s.

[47] Caves, C. M. Quantum-mechanical noise in an interferometer. *Phys. Rev. D* **23**, 1693–1708 (1981). URL https://doi.org/10.1103/PhysRevD.23.1693.

[48] Giovannetti, V., Lloyd, S. & Maccone, L. Quantum-Enhanced Measurements: Beating the Standard Quantum Limit. *Science* **306**, 1330–1336 (2004). URL https://doi.org/10.1126/science.1104149.

[49] Moester, M., Ariese, F. & de Boer, J. Optimized signal-to-noise ratio with shot noise limited detection in Stimulated Raman Scattering microscopy. *Journal of the European Optical Society - Rapid publications* **10** (2015). URL http://dx.doi.org/10.2971/jeos.2015.15022.

[50] Walls, D. F. Squeezed states of light. *Nature* **306**, 141–146 (1983). URL https://doi.org/10.1038/306141a0.

[51] Kitagawa, M. & Yamamoto, Y. Number-phase minimum-uncertainty state with reduced number uncertainty in a kerr nonlinear interferometer. *Phys. Rev. A* **34**, 3974–3988 (1986). URL https://doi.org/10.1103/PhysRevA.34.3974.

[52] White, A. G. *et al.* Experimental test of modular noise propagation theory for quantum optics. *Phys. Rev. A* **54**, 3400–3404 (1996). URL https://link.aps.org/doi/10.1103/PhysRevA.54.3400.

[53] Willke, B. *et al.* Spatial and temporal filtering of a 10-W Nd:YAG laser with a Fabry–Perot ring-cavity premode cleaner. *Opt. Lett.* **23**, 1704–1706 (1998). URL https://doi.org/10.1364/OL.23.001704.

[54] Hage, B., Samblowski, A. & Schnabel, R. Towards Einstein-Podolsky-Rosen quantum channel multiplexing. *Phys. Rev. A* **81**, 062301 (2010). URL https://doi.org/10.1103/PhysRevA.81.062301s.

[55] Ou, Z. Y., Hong, C. K. & Mandel, L. Detection of squeezed states by cross correlation. *Phys. Rev. A* **36**, 192–196 (1987). URL https://doi.org/10.1103/PhysRevA.36.192.

[56] Vogel, W. Homodyne correlation measurements with weak local oscillators. *Phys. Rev. A* **51**, 4160–4171 (1995). URL https://link.aps.org/doi/10.1103/PhysRevA.51.4160.

[57] Kühn, B. & Vogel, W. Unbalanced Homodyne Correlation Measurements. *Phys. Rev. Lett.* **116**, 163603 (2016). URL https://doi.org/10.1103/PhysRevLett.116.163603.

[58] Instruments, N. PXI-5404 Specifications (2018). URL https://www.ni.com/pdf/manuals/373315h.pdf. Accessed 2022-02-11.

[59] Kwon, D. *et al.* Reference-free, high-resolution measurement method of timing jitter spectra of optical frequency combs. *Scientific Reports* **7**, 40917 (2017). URL https://doi.org/10.1038/srep40917.

[60] Peng, M. Y. *et al.* Long-term stable, sub-femtosecond timing distribution via a 1.2-km polarization-maintaining fiber link: approaching 10^{-21} link stability. *Opt. Express* **21**, 19982–19989 (2013). URL https://doi.org/10.1364/OE.21.019982.

[61] Pupeza, I. *et al.* Highly sensitive dispersion measurement of a high-power passive optical resonator using spatial-spectral interferometry. *Opt. Express* **18**, 26184–26195 (2010). URL https://doi.org/10.1364/OE.18.026184s.

[62] Lilienfein, N. *et al.* Enhancement cavities for few-cycle pulses. *Opt. Lett.* **42**, 271–274 (2017). URL https://doi.org/10.1364/OL.42.000271.

[63] Fortier, T. & Baumann, E. 20 years of developments in optical frequency comb technology and applications. *Communications Physics* **2**, 153 (2019). URL https://doi.org/10.1038/s42005-019-0249-y.

[64] Riehle, F. *Frequency Standards: Basics and Applications* (Wiley-VCH, Weinheim, 2004). URL https://doi.org/10.1002/3527605991.

[65] Weiner, A. M. *Ultrafast optics*. Wiley series in pure and applied optics (John Wiley & Sons, Inc., Hoboken, New Jersey, 2009). URL https://doi.org/10.1002/9780470473467.

[66] Hasegawa, A. & Tappert, F. Transmission of stationary nonlinear optical pulses in dispersive dielectric fibers. I. Anomalous dispersion. *Applied Physics Letters* **23**, 142–144 (1973). URL https://doi.org/10.1063/1.1654836.

[67] Haus, H. Optical fiber solitons, their properties and uses. *Proceedings of the IEEE* **81**, 970–983 (1993). URL https://doi.org/10.1109/5.231336.

[68] Mollenauer, L. F. & Stolen, R. H. The soliton laser. *Opt. Lett.* **9**, 13–15 (1984). URL https://doi.org/10.1364/OL.9.000013s.

[69] Mitschke, F. M. & Mollenauer, L. F. Ultrashort pulses from the soliton laser. *Opt. Lett.* **12**, 407–409 (1987). URL https://doi.org/10.1364/OL.12.000407.

[70] Kärtner, F., Franz X.tner, Jung, I. & Keller, U. Soliton mode-locking with saturable absorbers. *IEEE Journal of Selected Topics in Quantum Electronics* **2**, 540–556 (1996). URL https://doi.org/10.1109/2944.571754.

[71] de Bohan, A., Antoine, P., Milošević, D. B. & Piraux, B. Phase-Dependent Harmonic Emission with Ultrashort Laser Pulses. *Phys. Rev. Lett.* **81**, 1837–1840 (1998). URL https://doi.org/10.1103/PhysRevLett.81.1837.

[72] McCracken, R. A., Charsley, J. M. & Reid, D. T. A decade of astrocombs: recent advances in frequency combs for astronomy [invited]. *Opt. Express* **25**, 15058–15078 (2017). URL https://doi.org/10.1364/OE.25.015058.

[73] Baumann, E. *et al.* Comb-calibrated frequency-modulated continuous-wave ladar for absolute distance measurements. *Opt. Lett.* **38**, 2026–2028 (2013). URL https://doi.org/10.1364/OL.38.002026.

[74] Baumann, E. *et al.* Comb-calibrated laser ranging for three-dimensional surface profiling with micrometer-level precision at a distance. *Opt. Express* **22**, 24914–24928 (2014). URL https://doi.org/10.1364/OE.22.024914.

[75] Coddington, I., Newbury, N. & Swann, W. Dual-comb spectroscopy. *Optica* **3**, 414–426 (2016). URL https://doi.org/10.1364/OPTICA.3.000414.

[76] Telle, H. R. *et al.* Carrier-envelope offset phase control: A novel concept for absolute optical frequency measurement and ultrashort pulse generation. *Applied Physics B* **69**, 327–332 (1999). URL https://doi.org/10.1007/s003400050813.

[77] Keller, U. Ultrafast solid-state lasers. In Herziger, G., Weber, H. & Poprawe, R. (eds.) *Landolt-Börnstein - Group VIII Advanced Materials and Technologies* (Springer-Verlag, 2007). URL https://doi.org/10.1007/978-3-540-44821-1_2.

[78] Kärtner, F. X. & Keller, U. Stabilization of solitonlike pulses with a slow saturable absorber. *Opt. Lett.* **20**, 16–18 (1995). URL https://doi.org/10.1364/OL.20.000016.

[79] Kärtner, F. X., der Au, J. A. & Keller, U. Mode-locking with slow and fast saturable absorbers-what's the difference? *IEEE Journal of Selected Topics in Quantum Electronics* **4**, 159–168 (1998). URL https://doi.org/10.1109/2944.686719.

[80] Paschotta, R. & Keller, U. Passive mode locking with slow saturable absorbers. *Applied Physics B* **73**, 653–662 (2001). URL https://doi.org/10.1007/s003400100726.

[81] Schilt, S. *et al.* Noise properties of an optical frequency comb from a SESAM-mode-locked 1.5-µm solid-state laser stabilized to the 10^{-13} level. *Applied Physics B* **109**, 391–402 (2012). URL https://doi.org/10.1007/s00340-012-5072-z.

[82] Hoffmann, M., Schilt, S. & Südmeyer, T. Ceo stabilization of a femtosecond laser using a sesam as fast opto-optical modulator. *Opt. Express* **21**, 30054–30064 (2013). URL https://doi.org/10.1364/OE.21.030054.

[83] Spühler, G. J., Reffert, S., Haiml, M., Moser, M. & Keller, U. Output-coupling semiconductor saturable absorber mirror. *Applied Physics Letters* **78**, 2733–2735 (2001). URL https://doi.org/10.1063/1.1370122. https://doi.org/10.1063/1.1370122.

[84] Schawlow, A. L. & Townes, C. H. Infrared and Optical Masers. *Phys. Rev.* **112**, 1940–1949 (1958). URL https://doi.org/10.1103/PhysRev.112.1940.

[85] Wiseman, H. M. Light amplification without stimulated emission: Beyond the standard quantum limit to the laser linewidth. *Phys. Rev. A* **60**, 4083–4093 (1999). URL https://doi.org/10.1103/PhysRevA.60.4083.

[86] Henry, C. Theory of the linewidth of semiconductor lasers. *IEEE Journal of Quantum Electronics* **18**, 259–264 (1982). URL https://doi.org/10.1109/JQE.1982.1071522.

[87] Schilt, S. *et al.* Fully stabilized optical frequency comb with sub-radian CEO phase noise from a SESAM-modelocked 1.5-µm solid-state laser. *Opt. Express* **19**, 24171–24181 (2011). URL https://doi.org/10.1364/OE.19.024171.

[88] Kim, Y., Kim, S., Kim, Y.-J., Hussein, H. & Kim, S.-W. Er-doped fiber frequency comb with mHz relative linewidth. *Opt. Express* **17**, 11972–11977 (2009). URL https://doi.org/10.1364/OE.17.011972.

[89] Gordon, J. P. & Haus, H. A. Random walk of coherently amplified solitons in optical fiber transmission. *Opt. Lett.* **11**, 665–667 (1986). URL https://doi.org/10.1364/OL.11.000665.

[90] Haus, H. A. & Mecozzi, A. Noise of mode-locked lasers. *IEEE Journal of Quantum Electronics* **29**, 983–996 (1993). URL https://doi.org/10.1109/3.206583.

[91] Stumpf, M. C. *et al.* Self-referencable frequency comb from a 170-fs, 1.5-µm solid-state laser oscillator. *Applied Physics B* **99**, 401–408 (2010). URL https://doi.org/10.1007/s00340-009-3854-8.

[92] Schibli, T. R. *et al.* Attosecond active synchronization of passively mode-locked lasers by balanced cross correlation. *Opt. Lett.* **28**, 947–949 (2003). URL https://doi.org/10.1364/OL.28.000947.

[93] Ciddor, P. E. Refractive index of air: new equations for the visible and near infrared. *Appl. Opt.* **35**, 1566–1573 (1996). URL https://doi.org/10.1364/AO.35.001566.

[94] Wetterdienst, D. Cdc - climate data center. Online. URL https://opendata.dwd.de/climate_environment/CDC/. Accessed 2021-11-30.

[95] Siglent. *SDG2000X Series*, datasheet-2017.05 edn.

[96] Saleh, B. E. A. & Teich, M. C. *Fundamentals of Photonics*. Wiley series in pure and applied optics (Wiley-Interscience, Hoboken, New Jersey, 2007), 2 edn. URL https://doi.org/10.1002/0471213748.

[97] Mitschke, F. *Fiber Optics* (Springer, Berlin, 2016), 2 edn. URL https://doi.org/10.1007/978-3-662-52764-1.

[98] Marcuse, D. Loss analysis of single-mode fiber splices. *The Bell System Technical Journal* **56**, 703–718 (1977). URL https://doi.org/10.1002/j.1538-7305.1977.tb00534.x.

[99] Drever, R. W. P. *et al.* Laser phase and frequency stabilization using an optical resonator. *Applied Physics B* **31**, 97–105 (1983). URL https://doi.org/10.1007/BF00702605.

[100] Black, E. D. An introduction to Pound–Drever–Hall laser frequency stabilization. *American Journal of Physics* **69**, 79–87 (2001). URL https://doi.org/10.1119/1.1286663.

[101] Bachor, H.-A. & Ralph, T. C. *A Guide to Experiments in Quantum Optics* (Wiley-VCH, Weinheim, 2019), 3 edn. URL https://doi.org/10.1002/9783527695805.

[102] Darwazeh, I. *Microwave Active Circuit Analysis and Design* (Academic Press is an imprint of Elsevier, Amsterdam, 2016). URL https://doi.org/10.1016/B978-0-12-407823-9.00017-2. Online-Ausg.

[103] Polyanskiy, M. Refractiveindex.info (2021). URL https://refractiveindex.info/. Accessed 2021-09-01.

[104] Diddams, S. & Diels, J.-C. Dispersion measurements with white-light interferometry. *J. Opt. Soc. Am. B* **13**, 1120–1129 (1996). URL https://doi.org/10.1364/JOSAB.13.001120.

[105] Carstens, H. *et al.* High-harmonic generation at 250 MHz with photon energies exceeding 100 eV. *Optica* **3**, 366–369 (2016). URL https://doi.org/10.1364/OPTICA.3.000366.

[106] Trubetskov, M. *et al.* Design, Production and Characterization of Mirrors for Ultra-Broadband, High-Finesse Enhancement Cavities. In *Optical Interference Coatings 2016*, ThA.2 (Optical Society of America, 2016). URL https://doi.org/10.1364/OIC.2016.ThA.2.

[107] Holzberger, S. *et al.* Enhancement cavities for zero-offset-frequency pulse trains. *Opt. Lett.* **40**, 2165–2168 (2015). URL https://doi.org/10.1364/OL.40.002165.

[108] Holzberger, S. *Enhancement cavities for attosecond physics*. Ph.D. thesis, Ludwig–Maximilians–Universität München (2015). URL https://doi.org/10.5282/edoc.19010.

[109] Trebino, R. *Frequency-Resolved Optical Gating: The Measurement of Ultrashort Laser Pulses* (Springer, Boston, MA, Boston, 2002). URL https://doi.org/10.1007/978-1-4615-1181-6.

[110] Gordon, I. *et al.* The HITRAN2016 molecular spectroscopic database. *Journal of Quantitative Spectroscopy and Radiative Transfer* **203**, 3–69 (2017). URL https://doi.org/10.1016/j.jqsrt.2017.06.038.

[111] Rieker, G. B. *et al.* Frequency-comb-based remote sensing of greenhouse gases over kilometer air paths. *Optica* **1**, 290–298 (2014). URL https://doi.org/10.1364/OPTICA.1.000290.

[112] Waxman, E. M. *et al.* Intercomparison of open-path trace gas measurements with two dual-frequency-comb spectrometers. *Atmospheric Measurement Techniques* **10**, 3295–3311 (2017). URL https://doi.org/10.5194/amt-10-3295-2017.

[113] Voronin, A. A. & Zheltikov, A. M. The generalized sellmeier equation for air. *Scientific Reports* **7**, 46111 (2017). URL https://doi.org/10.1038/srep46111.

[114] Yang, H. *et al.* 10-fs-level synchronization of photocathode laser with RF-oscillator for ultrafast electron and x-ray sources. *Scientific Reports* **7**, 39966 (2017). URL https://doi.org/10.1038/srep39966.

[115] Bouchand, R. *et al.* Compact Low-Noise Photonic Microwave Generation From Commercial Low-Noise Lasers. *IEEE Photonics Technology Letters* **29**, 1403–1406 (2017). URL https://doi.org/10.1109/LPT.2017.2723821.

[116] Zobel, J. W. *et al.* Comparison of Optical Frequency Comb and Sapphire Loaded Cavity Microwave Oscillators. *IEEE Photonics Technology Letters* **31**, 1323–1326 (2019). URL https://doi.org/10.1109/LPT.2019.2926190.

[117] Hou, D., Lee, C.-C., Yang, Z. & Schibli, T. R. Timing jitter characterization of mode-locked lasers with $< 1\text{zs}/\sqrt{\text{Hz}}$ resolution using a simple optical heterodyne technique. *Opt. Lett.* **40**, 2985–2988 (2015). URL https://doi.org/10.1364/OL.40.002985.

[118] Agarwal, G. S. *Quantum Optics* (Cambridge University Press, Cambridge, 2013). URL https://doi.org/10.1017/CBO9781139035170.

[119] Vogel, W. & Welsch, D.-G. *Quantum Optics* (Wiley-VCH Verlag GmbH & Co. KGaG, Weinheim, 2006), 3 edn. URL https://doi.org/10.1002/3527608524.

[120] Gerry, C. C. & Knight, P. L. *Introductory Quantum Optics* (Cambridge University Press, Cambridge, 2005). URL https://doi.org/10.1017/CBO9780511791239.

[121] Leonhardt, U. *Essential Quantum Optics* (Cambridge University Press, Cambridge, 2010), first published edn. URL https://doi.org/10.1017/CBO9780511806117.

[122] Garrison, J. C. & Chiao, R. Y. *Quantum Optics*. Oxford graduate texts (Oxford University Press, Oxford, 2014), first published in paperback edn. URL https://doi.org/DOI:10.1093/acprof:oso/9780198508861.001.0001.

[123] Cahill, K. E. & Glauber, R. J. Ordered Expansions in Boson Amplitude Operators. *Phys. Rev.* **177**, 1857–1881 (1969). URL https://doi.org/10.1103/PhysRev.177.1857.

[124] Sudarshan, E. C. G. Equivalence of Semiclassical and Quantum Mechanical Descriptions of Statistical Light Beams. *Phys. Rev. Lett.* **10**, 277–279 (1963). URL https://doi.org/10.1103/PhysRevLett.10.277.

[125] Wigner, E. On the Quantum Correction For Thermodynamic Equilibrium. *Phys. Rev.* **40**, 749–759 (1932). URL https://doi.org/10.1103/PhysRev.40.749.

[126] HUSIMI, K. Some Formal Properties of the Density Matrix. *Proceedings of the Physico-Mathematical Society of Japan. 3rd Series* **22**, 264–314 (1940). URL https://doi.org/10.11429/ppmsj1919.22.4_264.

[127] Heisenberg, W. Über den anschaulichen Inhalt der quantentheoretischen Kinematik und Mechanik. *Zeitschrift für Physik* **43**, 172–198 (1927). URL https://doi.org/10.1007/BF01397280.

[128] Robertson, H. P. The Uncertainty Principle. *Phys. Rev.* **34**, 163–164 (1929). URL https://doi.org/10.1103/PhysRev.34.163.

[129] Wu, L.-A., Xiao, M. & Kimble, H. J. Squeezed states of light from an optical parametric oscillator. *J. Opt. Soc. Am. B* **4**, 1465–1475 (1987). URL https://doi.org/10.1364/JOSAB.4.001465.

[130] Vahlbruch, H., Mehmet, M., Danzmann, K. & Schnabel, R. Detection of 15 dB Squeezed States of Light and their Application for the Absolute Calibration of Photoelectric Quantum Efficiency. *Phys. Rev. Lett.* **117**, 110801 (2016). URL https://doi.org/10.1103/PhysRevLett.117.110801.

[131] Agudelo, E. *et al.* Continuous sampling of the squeezed-state nonclassicality. *Phys. Rev. A* **92**, 033837 (2015). URL https://doi.org/10.1103/PhysRevA.92.033837.

[132] Slusher, R. E., Grangier, P., LaPorta, A., Yurke, B. & Potasek, M. J. Pulsed Squeezed Light. *Phys. Rev. Lett.* **59**, 2566–2569 (1987). URL https://doi.org/10.1103/PhysRevLett.59.2566.

[133] Bajer, J., Miranowicz, A. & Tanaś, R. Limits of Noise Squeezing in Kerr Effect. *Czechoslovak Journal of Physics* **52**, 1313–1319 (2002). URL https://doi.org/10.1023/A:1021867510898.

[134] White, A. G., Lam, P. K., McClelland, D. E., Bachor, H.-A. & Munro, W. J. Kerr noise reduction and squeezing. *Journal of Optics B: Quantum and Semiclassical Optics* **2**, 553–561 (2000). URL https://doi.org/10.1088/1464-4266/2/4/315.

[135] Sanders, B. C. & Milburn, G. J. Quantum limits to all-optical phase shifts in a Kerr nonlinear medium. *Phys. Rev. A* **45**, 1919–1923 (1992). URL https://doi.org/10.1103/PhysRevA.45.1919.

[136] Silberhorn, C. Detecting quantum light. *Contemporary Physics* **48**, 143–156 (2007). URL https://doi.org/10.1080/00107510701662538.

[137] Hage, B. *Purification and Distillation of Continuous Variable Entanglement*. Ph.D. thesis, Gottfried Wilhelm Leibniz Universität Hannover (2010). URL https://doi.org/10.15488/7410.

[138] Chelkowski, S. *et al.* Experimental characterization of frequency-dependent squeezed light. *Phys. Rev. A* **71**, 013806 (2005). URL https://doi.org/10.1103/PhysRevA.71.013806.

[139] Zhao, Y. *et al.* Frequency-dependent squeezed vacuum source for broadband quantum noise reduction in advanced gravitational-wave detectors. *Phys. Rev. Lett.* **124**, 171101 (2020). URL https://doi.org/10.1103/PhysRevLett.124.171101.

[140] Krivitsky, L. A. *et al.* Electronic noise-free measurements of squeezed light. *Opt. Lett.* **33**, 2395–2397 (2008). URL https://doi.org/10.1364/OL.33.002395.

[141] Krivitsky, L. A. *et al.* Correlation measurement of squeezed light. *Phys. Rev. A* **79**, 033828 (2009). URL https://link.aps.org/doi/10.1103/PhysRevA.79.033828.

[142] Thorlabs. Spec Sheet: S122B Germanium Power Meter Optical Head (2006). URL https://www.thorlabs.com/_sd.cfm?fileName=13337-S01.pdf&partNumber=S122B. Accessed 2022-02-11.

[143] Studer, J. Spektrale Zerlegung und Analyse Kerr-gequetschter Femtosekunden-Pulse. Bachelor thesis Universität Rostock(2015).

[144] Schlettwein, O. *Experimentelle und numerische Analyse der Quantenrauschdynamik optischer Pulse in Glasfasern*. Ph.D. thesis, Universität Rostock (2018). URL https://doi.org/10.18453/rosdok_id00002412.

[145] Agrawal, G. P. *Nonlinear Fiber Optics*. Optics and photonics (Academic Press, San Diego, 2019), 6 edn. URL https://doi.org/10.1016/C2018-0-01168-8.

[146] Washburn, B. R. *Dispersion and nonlinearities associated with supercontinuum generation in microstructure fibers*. Ph.D. thesis, Georgia Institute of Technology (2002).

[147] Shelby, R. M., Levenson, M. D. & Bayer, P. W. Guided acoustic-wave Brillouin scattering. *Phys. Rev. B* **31**, 5244–5252 (1985). URL https://doi.org/10.1103/PhysRevB.31.5244.

[148] Bergman, K. & Haus, H. A. Squeezing in fibers with optical pulses. *Opt. Lett.* **16**, 663–665 (1991). URL https://doi.org/10.1364/OL.16.000663.

[149] Bergman, K., Haus, H. A. & Shirasaki, M. Analysis and measurement of GAWBS spectrum in a nonlinear fiber ring. *Applied Physics B* **55**, 242–249 (1992). URL https://doi.org/10.1007/BF00325012.

[150] Spaelter, S., Sizmann, A., Stroessner, U., Burk, M. & Leuchs, G. Photon number squeezing of spectrally filtered solitons. In *Quantum Electronics and Laser Science Conference*, QThB4 (Optical Society of America, 1997). URL http://www.osapublishing.org/abstract.cfm?URI=QELS-1997-QThB4.

[151] Nakazawa, M. *et al.* Observation of guided acoustic-wave Brillouin scattering noise and its compensation in digital coherent optical fiber transmission. *Opt. Express* **26**, 9165–9181 (2018). URL https://doi.org/10.1364/OE.26.009165.

[152] Takefushi, N., Yoshida, M., Kasai, K., Hirooka, T. & Nakazawa, M. Theoretical and experimental analyses of GAWBS phase noise in various optical fibers for digital coherent transmission. *Opt. Express* **28**, 2873–2883 (2020). URL https://doi.org/10.1364/OE.384505.

[153] Nishizawa, N., Kume, S., Mori, M., Goto, T. & Miyauchi, A. Experimental analysis of guided acoustic wave Brillouin scattering in PANDA fibers. *J. Opt. Soc. Am. B* **12**, 1651–1655 (1995). URL https://doi.org/10.1364/JOSAB.12.001651.

[154] Yoshida, M., Takefushi, N., Kasai, K., Hirooka, T. & Nakazawa, M. Precise measurements and their analysis of gawbs-induced depolarization noise in various optical fibers for digital coherent transmission. *Opt. Express* **28**, 34422–34433 (2020). URL http://www.osapublishing.org/oe/abstract.cfm?URI=oe-28-23-34422.

[155] Elser, D. *et al.* Reduction of Guided Acoustic Wave Brillouin Scattering in Photonic Crystal Fibers. *Phys. Rev. Lett.* **97**, 133901 (2006). URL https://doi.org/10.1103/PhysRevLett.97.133901.

[156] Poustie, A. J. Guided acoustic-wave Brillouin scattering with optical pulses. *Opt. Lett.* **17**, 574–576 (1992). URL https://doi.org/10.1364/OL.17.000574.

[157] Peng, M. Y. *et al.* Long-term stable, large-scale, optical timing distribution systems with sub-femtosecond timing stability. In *FEL2013: Proceedings of the 35th International Free-Electron Laser Conference* (International Free-Electron Laser conference, Manhattan (USA), 26 Aug 2013 - 30 Aug 2013, 2013). URL https://bib-pubdb1.desy.de/record/167720.

[158] Benedick, A. J., Fujimoto, J. G. & Kärtner, F. X. Optical flywheels with attosecond jitter. *Nature Photonics* **6**, 97–100 (2012). URL https://doi.org/10.1038/nphoton.2011.326.

[159] Casanova, A., Courjaud, A., Trophème, B. & Santarelli, G. Measurement of absolute timing jitter of SESAM mode-locked lasers with yoctosecond sensitivity. *Opt. Lett.* **45**, 6098–6101 (2020). URL https://doi.org/10.1364/OL.405761.

[160] Hayshi, N., Suzuki, K., Set, S. Y. & Yamashita, S. Temperature dependence of polarized GAWBS spectrum in high nonlinear fibers. In *Conference on Lasers and Electro-Optics*, STh1K.1 (Optical Society of America, 2017). URL https://doi.org/10.1364/CLEO_SI.2017.STh1K.1.

[161] Hayashi, N., Mizuno, Y., Nakamura, K., Set, S. Y. & Yamashita, S. Experimental study on depolarized GAWBS spectrum for optomechanical sensing of liquids outside standard fibers. *Opt. Express* **25**, 2239–2244 (2017). URL https://doi.org/10.1364/OE.25.002239.

[162] Floch, S. L., Riou, F. & Cambon, P. Experimental and theoretical study of the Brillouin linewidth and frequency at low temperature in standard single-mode optical fibres. *Journal of Optics A: Pure and Applied Optics* **3**, L12–L15 (2001). URL https://doi.org/10.1088/1464-4258/3/3/102.

[163] Thevenaz, L. *et al.* Brillouin optical fiber sensor for cryogenic thermometry. In Inaudi, D. & Udd, E. (eds.) *Smart Structures and Materials 2002: Smart Sensor Technology and Measurement Systems*, vol. 4694, 22 – 27. International Society for Optics and Photonics (SPIE, 2002). URL https://doi.org/10.1117/12.472623.

[164] Lewis, S. A. E., Chernikov, S. V. & Taylor, J. R. Temperature-dependent gain and noise in fiber Raman amplifiers. *Opt. Lett.* **24**, 1823–1825 (1999). URL https://doi.org/10.1364/OL.24.001823.

[165] Rogers, A. Distributed optical-fibre sensors for the measurement of pressure, strain and temperature. *Physics Reports* **169**, 99–143 (1988). URL https://doi.org/10.1016/0370-1573(88)90110-X.

[166] Saxena, M. K. *et al.* Raman optical fiber distributed temperature sensor using wavelet transform based simplified signal processing of Raman backscattered signals. *Optics & Laser Technology* **65**, 14–24 (2015). URL https://doi.org/10.1016/j.optlastec.2014.06.012.

[167] Dong, R. *et al.* Experimental evidence for Raman-induced limits to efficient squeezing in optical fibers. *Opt. Lett.* **33**, 116–118 (2008). URL https://doi.org/10.1364/OL.33.000116.

[168] Jozsa, R. & Linden, N. On the role of entanglement in quantum-computational speed-up. *Proceedings: Mathematical, Physical and Engineering Sciences* **459**, 2011–2032 (2003). URL https://doi.org/10.1098/rspa.2002.1097.

[169] Żukowski, M., Zeilinger, A., Horne, M. A. & Ekert, A. K. "Event-ready-detectors" Bell experiment via entanglement swapping. *Phys. Rev. Lett.* **71**, 4287–4290 (1993). URL https://doi.org/10.1103/PhysRevLett.71.4287.

[170] Bennett, C. H. *et al.* Teleporting an unknown quantum state via dual classical and Einstein-Podolsky-Rosen channels. *Phys. Rev. Lett.* **70**, 1895–1899 (1993). URL https://doi.org/10.1103/PhysRevLett.70.1895.

[171] Einstein, A., Podolsky, B. & Rosen, N. Can Quantum-Mechanical Description of Physical Reality Be Considered Complete? *Phys. Rev.* **47**, 777–780 (1935). URL https://doi.org/10.1103/PhysRev.47.777.

[172] Bell, J. S. On the Einstein Podolsky Rosen paradox. *Physics Physique Fizika* **1**, 195–200 (1964). URL https://doi.org/10.1103/PhysicsPhysiqueFizika.1.195.

[173] Freedman, S. J. & Clauser, J. F. Experimental Test of Local Hidden-Variable Theories. *Phys. Rev. Lett.* **28**, 938–941 (1972). URL https://doi.org/10.1103/PhysRevLett.28.938.

[174] Hensen, B. *et al.* Loophole-free Bell inequality violation using electron spins separated by 1.3 kilometres. *Nature* **526**, 682–686 (2015). URL https://doi.org/10.1038/nature15759.

[175] Thearle, O. *et al.* Violation of Bell's Inequality Using Continuous Variable Measurement. *Phys. Rev. Lett.* **120**, 040406 (2018). URL https://doi.org/10.1103/PhysRevLett.120.040406.

[176] Ekert, A. K. Quantum cryptography based on Bell's theorem. *Phys. Rev. Lett.* **67**, 661–663 (1991). URL https://doi.org/10.1103/PhysRevLett.67.661.

[177] Menicucci, N. C. *et al.* Universal Quantum Computation with Continuous-Variable Cluster States. *Phys. Rev. Lett.* **97**, 110501 (2006). URL https://doi.org/10.1103/PhysRevLett.97.110501.

[178] Dixon, A. R., Yuan, Z. L., Dynes, J. F., Sharpe, A. W. & Shields, A. J. Gigahertz decoy quantum key distribution with 1 Mbit/s secure key rate. *Opt. Express* **16**, 18790–18797 (2008). URL https://doi.org/10.1364/OE.16.018790.

[179] Menicucci, N. C., Flammia, S. T. & Pfister, O. One-way quantum computing in the optical frequency comb. *Phys. Rev. Lett.* **101**, 130501 (2008). URL https://link.aps.org/doi/10.1103/PhysRevLett.101.130501.

[180] Kviatkovsky, I., Chrzanowski, H. M., Avery, E. G., Bartolomaeus, H. & Ramelow, S. Microscopy with undetected photons in the mid-infrared. *Science Advances* **6**, eabd0264 (2020). URL https://doi.org/10.1126/sciadv.abd0264.

[181] Medeiros de Araújo, R. *et al.* Full characterization of a highly multimode entangled state embedded in an optical frequency comb using pulse shaping. *Phys. Rev. A* **89**, 053828 (2014). URL https://doi.org/10.1103/PhysRevA.89.053828.

[182] Horodecki, M., Horodecki, P. & Horodecki, R. Separability of mixed states: necessary and sufficient conditions. *Physics Letters A* **223**, 1–8 (1996). URL https://doi.org/10.1016/S0375-9601(96)00706-2.

[183] Gerke, S. *et al.* Full Multipartite Entanglement of Frequency-Comb Gaussian States. *Phys. Rev. Lett.* **114**, 050501 (2015). URL https://doi.org/10.1103/PhysRevLett.114.050501.

[184] Gerke, S., Vogel, W. & Sperling, J. Numerical Construction of Multipartite Entanglement Witnesses. *Phys. Rev. X* **8**, 031047 (2018). URL https://doi.org/10.1103/PhysRevX.8.031047.

[185] Simon, R. Peres-Horodecki Separability Criterion for Continuous Variable Systems. *Phys. Rev. Lett.* **84**, 2726–2729 (2000). URL https://doi.org/10.1103/PhysRevLett.84.2726.

[186] Duan, L.-M., Giedke, G., Cirac, J. I. & Zoller, P. Inseparability Criterion for Continuous Variable Systems. *Phys. Rev. Lett.* **84**, 2722–2725 (2000). URL https://doi.org/10.1103/PhysRevLett.84.2722.

[187] Spälter, S., Burk, M., Strößner, U., Sizmann, A. & Leuchs, G. Propagation of quantum properties of sub-picosecond solitons in a fiber. *Opt. Express* **2**, 77–83 (1998). URL https://doi.org/10.1364/OE.2.000077.

[188] Hosaka, A., Kawamori, T. & Kannari, F. Multimode quantum theory of nonlinear propagation in optical fibers. *Phys. Rev. A* **94**, 053833 (2016). URL https://doi.org/10.1103/PhysRevA.94.053833.

[189] Castelló-Lurbe, D. *et al.* Measurement of the soliton number in guiding media through continuum generation. *Opt. Lett.* **45**, 4432–4435 (2020). URL https://doi.org/10.1364/OL.399382.

[190] Rohrmann, P. *Experimentelle Charakterisierung von Bindungszuständen aus drei Solitonen in dispersionsalternierenden Glasfasern*. Ph.D. thesis, Universität Rostock (2014). URL https://doi.org/10.18453/rosdok_id00001333.

[191] Wefers, M. M. & Nelson, K. A. Analysis of programmable ultrashort waveform generation using liquid-crystal spatial light modulators. *J. Opt. Soc. Am. B* **12**, 1343–1362 (1995). URL https://doi.org/10.1364/JOSAB.12.001343.

[192] Kraft, S. *Realisierung und Charakterisierung eines modifizierten Aufbaus zur Vermessung ultrakurzer Lichtpulse*. Master's thesis, Universität Rostock (2013).

[193] Studer, J. *Spectral Mode Analysis of Quantum Properties in Optical Fibres*. Master's thesis, Universität Rostock (2019).

[194] Armstrong, J. A. MEASUREMENT OF PICOSECOND LASER PULSE WIDTHS. *Applied Physics Letters* **10**, 16–18 (1967). URL https://doi.org/10.1063/1.1754787.

[195] Hage, B. *et al.* Demonstrating various quantum effects with two entangled laser beams. *The European Physical Journal D* **63**, 457–461 (2011). URL https://doi.org/10.1140/epjd/e2011-20153-9.

[196] Köhnke, S. *et al.* Quantum Correlations beyond Entanglement and Discord. *Phys. Rev. Lett.* **126**, 170404 (2021). URL https://doi.org/10.1103/PhysRevLett.126.170404.

[197] Cai, Y., Roslund, J., Thiel, V., Fabre, C. & Treps, N. Quantum enhanced measurement of an optical frequency comb. *npj Quantum Information* **7**, 82 (2021). URL https://doi.org/10.1038/s41534-021-00419-w.

[198] Opatrný, T., Korolkova, N. & Leuchs, G. Mode structure and photon number correlations in squeezed quantum pulses. *Phys. Rev. A* **66**, 053813 (2002). URL https://doi.org/10.1103/PhysRevA.66.053813.

[199] Kraeft, T. *Proof of Nonclassical Properties of Kerr-Squeezed Laser Pulses via Homodyne Cross-Correlation Measurement*. Master's thesis, Universität Rostock (2020).

[200] Schünemann, M. *Characterization of Nonclassical Properties of Quantum States Generated in an Optical Parametric Amplifier*. Ph.D. thesis, Universität Rostock (2017). URL https://doi.org/10.18453/rosdok_id00002070.

[201] Thorlabs. FINAL INSPECTION REPORT 2x2 90:10 PM Narrowband Coupler PN1550R2A2 SN: T060920 (2020).

[202] Krylov, D. & Bergman, K. Amplitude-squeezed solitons from an asymmetric fiber interferometer. *Opt. Lett.* **23**, 1390–1392 (1998). URL https://doi.org/10.1364/OL.23.001390.

[203] Schmitt, S. *et al.* Photon-Number Squeezed Solitons from an Asymmetric Fiber-Optic Sagnac Interferometer. *Phys. Rev. Lett.* **81**, 2446–2449 (1998). URL https://doi.org/10.1103/PhysRevLett.81.2446.

[204] Mandel, L. & Wolf, E. *Optical Coherence and Quantum Optics* (Cambridge Univ. Press, Cambridge University Press, 1995), 1. publ. edn. URL https://doi.org/10.1017/CBO9781139644105.

[205] Bercy, A. *et al.* Two-way optical frequency comparisons at 5×10^{-21} relative stability over 100-km telecommunication network fibers. *Phys. Rev. A* **90**, 061802 (2014). URL https://doi.org/10.1103/PhysRevA.90.061802.

[206] Benkler, E. *et al.* End-to-end topology for fiber comb based optical frequency transfer at the 10^{-21} level. *Opt. Express* **27**, 36886–36902 (2019). URL https://doi.org/10.1364/OE.27.036886.

[207] Serikawa, T. & Furusawa, A. 500 MHz resonant photodetector for high-quantum-efficiency, low-noise homodyne measurement. *Review of Scientific Instruments* **89**, 063120 (2018). URL https://doi.org/10.1063/1.5029859.

[208] Schlettwein, O. *Detektion der Quanteneigenschaften gepulster Laserstrahlung*. Master's thesis, Universität Rostock (2013).

[209] Park, J. Quote for resonator mirrors. Mail (2017). (Theorethical specifications as stated prior to order).

[210] Uprety, S. & Cao, C. Radiometric Comparison of 1.6-µm CO_2 Absorption Band of Greenhouse Gases Observing Satellite (GOSAT) TANSO-FTS with Suomi-NPP VIIRS SWIR Band. *Journal of Atmospheric and Oceanic Technology* **33**, 1443 – 1453 (2016). URL https://doi.org/10.1175/JTECH-D-15-0157.1.

[211] Drummond, P. D. & Hillery, M. S. *The Quantum Theory of Nonlinear Optics* (Cambridge University Press, 2014). URL https://doi.org/10.1017/CBO9780511783616.

List of publications

1. Catxere A. Casacio, Lars S. Madsen, Alex Terrasson, Muhammad Waleed, Kai Barnscheidt, Boris Hage, Michael A. Taylor and Warwick P. Bowen. Quantum-enhanced nonlinear microscopy. Nature **594**, 201–206, June 2021. URL https://doi.org/10.1038/s41586-021-03528-w

2. Melanie Schünemann, Karsten Sperlich, Kai Barnscheidt, Samuel Schöpa, Johannes Wenzel, Stefan Kalies, Alexander Heisterkamp, Heinrich Stolz, Oliver Stachs and Boris Hage. Balanced Heterodyne Brillouin Spectroscopy Towards Tissue Characterization. IEEE Access **10**, 24340-24348, February 2022. URL https://doi.org/10.1109/ACCESS.2022.3154424

Appendices

A. Detector design and characteristics

This chapter of the appendix gives additional information about the general challenges in efficiently detecting high optical powers with short pulses lasers (section A.1) as well as problems occurring in more conventional designs. Properties and design parameters of the implemented design are discussed afterwards in section A.1.2 before characteristics of used detectors and additionally applied digital filters are demonstrated.

A.1 Photodetection with short pulses

The contribution to [13] was not related to the optical setup and measurement scheme briefly discussed in chapter 2, however it is the foundation of the final stage of the microscope: the detection of the light. Within this section, the occurring additional difficulties for photodiode and electronic circuit are elaborated which arise from the use of short light pulses.

A.1.1 Photodiode capacitance

For the electronic circuit, the absorption of a ps pulse is almost instantaneous and the used photodiode is essentially isolated from all other components during this time. During one ps, light travels only 300 µm and even the closest electrical components are placed several mm away from the photodiode.

The photodiode requires a reverse-bias voltage to operate in photoconductive mode. This voltage must not break down during the absorption of the pulse. If the voltage breaks down, the photodiode operates in photovoltaic mode which is not beneficial for the intended fast and efficient detection. For 1560 nm at 80 MHz and 10 mW average optical power, one pulse consists of about 10^9 photons. Such a pulse can deposit a charge of up to 160 pC on the photodiode, depending on the actual efficiency. As the depletion region of a photodiode widens with increased reverse-bias voltage, its capacitance is not constant. Typical values for InGaAs photodiodes[1] with a diameter of 500 µm are 30 pF to 60 pF at 0 V and 5 pF to

[1] These are the typical choice for high efficiencies in the NIR for 1064 nm as well as 1560 nm.

15 pF for reverse-bias voltages of 5 V to 10 V[2]. For a reverse-bias voltage of 10 V, such a 500 µm photodiode can be charged with approximately 200 pC by a single pulse and still remain in photoconductive mode afterwards, at least if the full reverse-bias voltage is restored within the 12.5 ns prior to the next pulse.

Depending on the incident number of photons per pulse, the capacitance is increased upon absorption as the reverse-bias voltage is reduced. As the reverse-bias voltage is restored within a certain time afterwards, the capacitance is decreased again. Both the increase in capacitance and the time required to restore the bias voltage depend on the number of absorbed photons. As a result, the time average of the capacitance of the photodiode depends on the incident optical power. For CW light, a nearly constant flow of photons creates charges that are transported by a nearly constant current and hence the voltage across the diode and its capacitance are constant[3].

For pulsed light, the capacitance can only be close to constant if the applied bias voltage is large enough to maintain its terminal capacitance after the absorption of a pulse. To give an numeric example:

A capacitance of 5 pF is reached at 10 V. Therefore, a total bias voltage of 42 V is required to be able to absorb the 160 pC from a single pulse and still maintain a bias voltage of 10 V or above after the absorption.

Such voltages do not only exceed the specifications of most InGaAs photodiodes but can also be harmful to most low-noise operational amplifiers.

Usually, smaller photodiodes are the preferred choice as they are faster and have a lower dark current. For pulsed light however, the required reverse-bias voltage and its technical limitations require larger areas and capacitances. Hence, the choice of photodiode size has to be as large as needed to store one pulse but at the same time as small (or fast) as possible to provide low electronic background noise.

A.1.2 Electronic circuit for the photodiode

Assuming that a proper photodiode is chosen, it provides a current proportional to the flow of incident photons which has to be processed. The most simple way to process this current is by directly using a load resistor and measuring the voltage as depicted in figure A.1a. The bandwidth is then limited by the capacitance of the diode and the chosen resistor $\left((2\pi RC)^{-1}\right)$. As a result, a small resistor has to be used, resulting in a small signal that generally requires a very low-noise amplifier. This limitation can be overcome by using a resonant design. In this, an additional inductor is added prior to the resistor as depicted in

[2]These values vary not only between different models *e.g.* ETX-500, FD500 and IG17X500S4i, but also between production charges and within the same charge.

[3]At least as long as the supply voltage does not change due to the required overall current.

figure A.1b. The resonant structure of its load impedance provides a stronger signal close to its resonance frequency of ω_{res}.

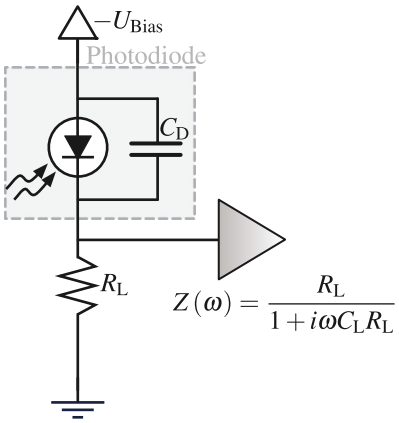

(A.1a) Load resistor circuit

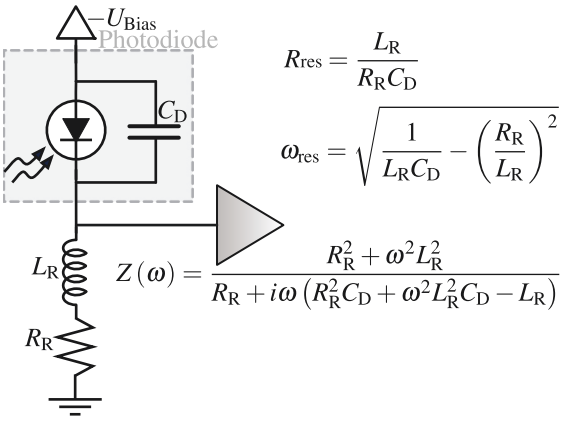

(A.1b) Resonant photodiode circuit

Figure A.1 Simple photodiode circuits and their impedances
The resonance frequency and its resistance are given for **(A.1b)**.

Even if the resonant circuit has a good SNR, it has one significant problem for pulsed light as its resonance frequency depends on the capacitance of the photodiode and hence the number of photons per pulse. Aside from the earlier discussed large bias voltage, a large parallel capacitance can be used to compensate for this. Such a capacitance would reduce the load impedance and lower the SNR and hence this design is not used. A more detailed discussion on these circuits for high frequencies can be found in [207].

Another design is based on a transimpedance amplifier (figure A.2a) and allows to convert the current fluctuations to voltage fluctuations using a resistor and an operational amplifier. Such designs are used in many optical experiments but even for low-noise operational amplifiers, like the *LMH-6624*, at least a feedback impedance of 3 kΩ is required to be limited by the thermal noise of the feedback impedance instead of the voltage noise from the operational amplifier. For higher impedances, the SNR does not improve as the thermal noise is also amplified. The optimal value depends on the noise characteristics of the used amplifier but a value of 5 kΩ has proven to be a good choice[4] for currently available low-noise amplifiers in the regime of several MHz. For further gain, it is actually beneficial to use a second amplifier stage.

Using such a transimpedance amplifier (figure A.2a), the conversion from current to voltage is determined by the feedback impedance and not significantly influenced by the capacitance of the photodiode. An average intensity of 10 mW at 1560 nm with perfect quantum efficiency would result in an average current of 12.5 mA and hence an output voltage above 60 V. This is far beyond the capabilities of many operational amplifiers, even without considering any contribution from the repetitive pulse pattern.

[4] If every single dB of SNR is key, it should be checked whether this choice is appropriate.

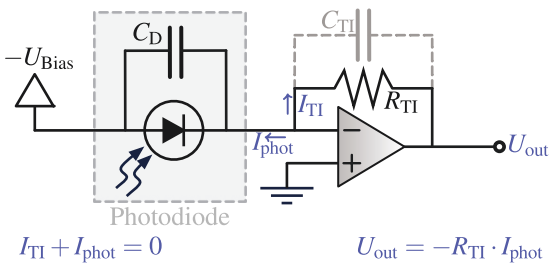

(A.2a) Schematic circuit for a detector based on a transimpedance amplifier.

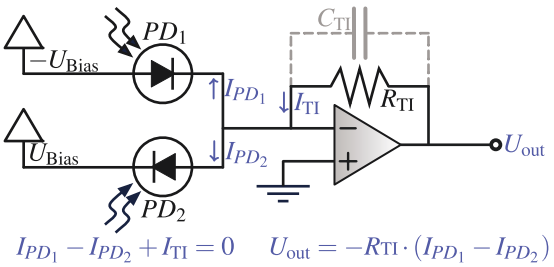

(A.2b) Transimpedance amplifier with balanced photodiodes

Figure A.2 Schematic transimpedance amplifier circuits with single and balanced photodiodes

One possible solution to this problem is a balanced detector (figure A.2b) where the current from a second photodiode is subtracted. If both photodiodes are illuminated by equally strong pulses at the same time, the average currents as well as contributions at the pulse repetition rate and its harmonics cancel out, and only the subtracted fluctuations remain. This can be used where the subtracted signal is of a particular interest, *e.g.* as in a BHD. If the signal of one photodiode is required or of interest, this scheme is not ideal since the second photodiode contributes at least the corresponding shot noise. Assuming the optical powers are not well balanced, the same limits as for the single photodiode design apply. In the used experimental setup this may be caused by the remaining coherent amplitude of the SI and the resulting interference pattern.

To avoid large output voltages due to the average current, another modification in the circuit (figure A.3) was used to reduce the impedance at low frequencies. The value of the resistor is lowered and an inductance is placed in series with the resistor. This leads to an impedance which increases with frequency. For high frequencies, the capacitor[5] in parallel lowers the impedance and hence the amplification of the pulse pattern.

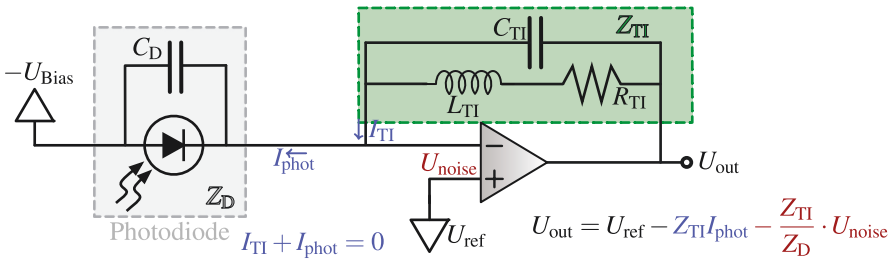

Figure A.3 Resonant transimpedance amplifier design with input voltage noise and reference voltage

[5] This capacitor is also required for the stability of the circuit and to reduce the noise floor as discussed later.

At this point, the feedback network consists of three components and at least two design parameters are predetermined: The maximum impedance $|Z_{\max}| \approx 5\,\mathrm{k\Omega}$ and f_{res} which was fixed to 20 MHz for the detector built for [13] due to the required moduluation.

The resonance frequency ω_0 of the feedback network and its maximum impedance $Z_{\max}$ are given by:

$$\omega_0 = \sqrt{\frac{1}{L_{\mathrm{TI}} C_{\mathrm{TI}}} - \left(\frac{R_{\mathrm{TI}}}{L_{\mathrm{TI}}}\right)^2} \qquad |Z_{\max}| = \frac{L_{\mathrm{TI}}}{R_{\mathrm{TI}} C_{\mathrm{TI}}} \tag{A.1}$$

This allows to calculate L_{TI} and C_{TI}:

$$L_{\mathrm{TI}} = C_{\mathrm{TI}} \cdot R_{\mathrm{TI}} \cdot |Z_{\max}| \qquad C_{\mathrm{TI}} = \frac{1}{\omega_0 \cdot |Z_{\max}|} \sqrt{\frac{|Z_{\max}|}{R_{\mathrm{TI}}} - 1} \tag{A.2}$$

Given these dependencies, R_{TI} remains the only independent parameter in the circuit and has to be chosen wisely. By increasing the value of R_{TI}, the detection bandwidth increases which is desired to obtain data over a large bandwidth. Simultaneously, the required capacitance decreases which leads to a higher amplification for the pulse repetition rate and its harmonics. The amplifier cannot deliver voltages above the provided supply voltages. By approaching its maximum output swing, the signal is clipped and it becomes unusable. This posts an upper limit for R_{TI} depending on the maximum supply rail voltages and the initial offset voltage of the detector.

In the used design (figure A.5), the offset voltage of the detector is $-300\,\mathrm{mV}$ due to an input buffer transistor and hence R_{TI} was set to $100\,\Omega$. A new design (figure A.4) allows an additional offset voltage and hence higher resistances without impeding the headroom available for the output swing.

The amount of required output swing is determined by the bandwidth of the photodiode and the impedance of the transimpedance amplifier at the repetition rate of the laser and its harmonics. To limit the contribution of the laser repetition rate, the capacitance C_{TI} has to be as high as possible and therefore R_{TI} as low as possible (equation (A.2)). This contradicts the intended large bandwidth and all parameters have to be balanced depending on the actual experimental parameters for the best performance. The capacitance has further implications on the stability and electronic noise of the detector that are discussed within the next section.

Stability and noise considerations

For stability and dark noise of the detector, another effective circuit has to be considered. The operational amplifier outputs a voltage to counter the current from the diode to bring both its input pins to equal potential (blue part of the equation in figure A.3). Aside

from the output noise of the amplifier, the output signal also contains contributions from the thermal noise of the feedback impedance, voltage fluctuations between both input pins of the amplifier, the current caused by the incident photons and dark current of the photodiode[6].

For the voltage noise on the input pins of the amplifier, the circuit is an inverting amplifier (red part of the equation in figure A.3). The gain of its amplification is determined by the ratio of Z_D and Z_{TI} as illustrated in figure A.3. The shunt resistance of the photodiode is in the region of 100 MΩ and hence the gain for the voltage noise is close to zero at low frequencies. For high frequencies, the capacitance of the photodiode dominates and the resulting noise floor rises with frequency. The gain is mainly limited by the used feedback capacitance as well as the bandwidth of the used amplifier. A higher capacitance in the feedback network reduces the gain for this voltage noise. Nevertheless, most operational amplifiers are not stable for low gains. For examples, the *LMH-6624* requires a minimum gain of 10 which essentially limits the feedback capacitance to $1/10$ of the photodiode capacitance[7]. For this reason and its higher output current, the resonant design used the unity-gain stable *OPA690*. Additionally, the larger capacitance of larger photodiodes, required to absorb all photons in a single pulse without breakdown of the bias voltage, increases the gain for the input voltage noise.

Additional signal amplification

After the photocurrent is converted into a voltage, the signal could be analysed. The signal consists of an average voltage, proportional to the average optical power, and small fluctuations. To reduce the requirements on the further transmission of the signal and its processing, the signal is further processed directly after the transimpedance amplifier. A low-pass filter with a simple buffer amplifier is used to provide a signal proportional to the average of the incident optical power. For the fast fluctuation at the measurement frequency, an additional bandpass filter is used to block both the pulse repetition rate and the average voltage prior to the amplification of the signal. The resulting signal can be accessed for the analysis with a spectrum analyser, the digitising hardware or other methods. Usually a gain above 10 is required for the amplifier to be stable. Again, this may result in the exceeding of the maximum output voltage swing for the fundamental pulse repetition rate if the bandpass filter is too broad or the measurement frequency is too close to the laser repetition rate. This can be avoided by using an inductance that itself has a resonance frequency very close to the repetition rate to block this frequency component.

[6] Dark current is essentially proportional to the area of the photodiode. The dark current itself depends on the temperature of the photodiode and will not be discussed here. Additional ambient light can be shielded if observed but due to the small area of the used photodiodes, its contribution is small compared to the intense laser light.

[7] Additional capacitances from other components, such as the used transistors, increase this limit.

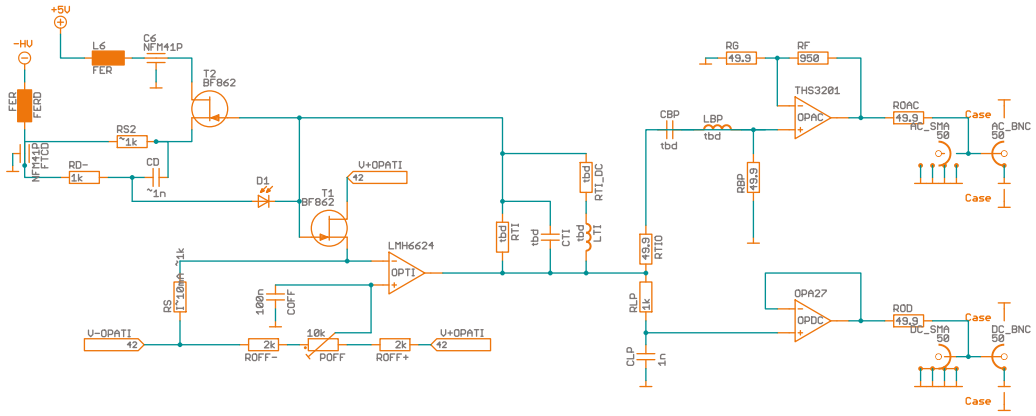

Figure A.4 Updated detector circuit
In the circuit diagram all essential components and those for additional adjustments are shown. Supply voltages are not included.

Bottom line of detector design

The general idea of the detector design and its most important limitations were presented. Depending on the intended detection frequency and maximum optical power, all parameters have to be considered to obtain optimal performance. Nevertheless, this design has a lower SNR and bandwidth compared to a linear transimpedance amplifier with balanced photodiodes. A well designed resonant photodiode circuit for CW light can obtain a higher bandwidth and also a better SNR. For lower optical powers in the regime of a few hundredth µW, a single broadband photodetector will also perform better. Only for average optical powers in the mW regime and short pulses at repetition rates of several MHz, this design performs better than the other mentioned designs. To achieve this better performance, the design parameters have to be chosen within a small window and this design relies on inductances that usually do not have tight tolerances.

Aside from the above mentioned components, additional components can be used to provide more freedom for the used parameters. For the used detectors, an additional resistor parallel to the discussed feedback network was used (figure A.5). This resistor limits the impedance on resonance and broadens the bandwidth even if a smaller resistor is used as R_{TI}.

A.2 Used detectors and their characterisation

The detectors used within the BHD setup were built by Oskar Schlettwein during his master's thesis in 2013 [208]. The overall circuit is provided in figure A.5 and their parameters differ from the above discussed design guidelines. During the design process, circuit simulation software is used to improve the chosen parameters. This software can account for the contributions from additional components as well as parasitic inductances and capacitances. Furthermore, these detectors were designed for a lower laser repetition

rate of around 57 MHz and most importantly they fulfil the designated task within the setup. While a new detector board with improved design and housing was designed during this PhD thesis by the author, it was not yet used for the BHD detectors. However, it was used in several detectors to obtain monitoring and locking signals at various locations within the separation resonator–based experimental setup. Furthermore, it was used in the detectors for the actual homodyne measurements in chapter 8.

Based on the new detector board and the detector provided for [13], a second iteration was built that can detect five times more light. This improved design is currently being implemented in the quantum-enhanced microscope to further increase imaging speed and usable light intensity.

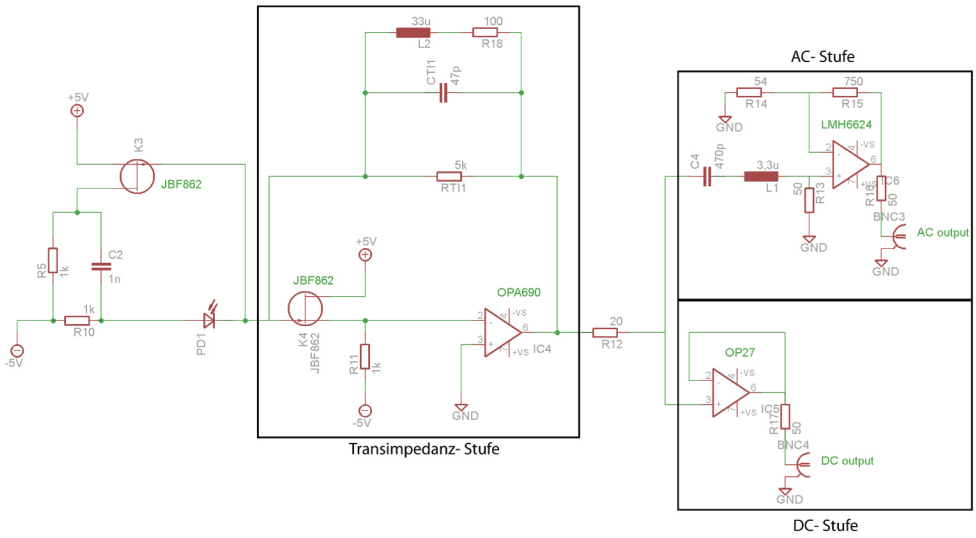

Figure A.5 Schematics of detectors used for BHD. (From [208])

For the BHD detection scheme in the experimental setup, a redesigned detector (based on figure A.4) could likely provide three times more usable data as well as a better SNR by shifting the detection frequency and improving the bandwidth. Due to limited time and financial resources, this was not yet done as the data recording is also limited by the used digitiser and computer.

A.2.1 Measurement setup

Using a HWP and a PBS, the optical power was varied. The optical light was focussed on the photodiode using an AR-coated 50 mm lens. Power was measured using a germanium-based optical power meter head (*S122B* [142]) with an uncertainty of $\pm 5\,\%$. Reproducible sensor placement was ensured by a magnetic mounting mechanism.

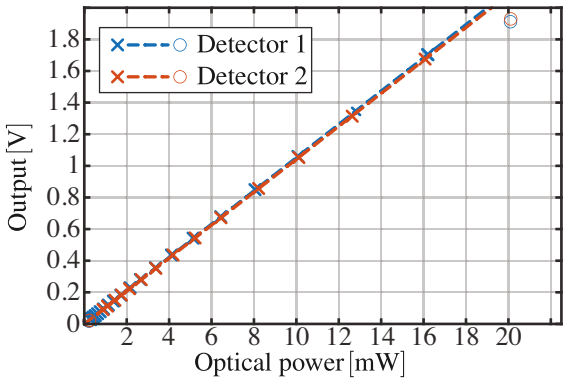

Figure A.6 Output voltages of the detectors used in BHD depending on incident optical power (1558.5 nm) corrected for voltage offset
The crosses mark the data points used for the linear fit while the rings mark excluded data points.

A.2.2 Quantum efficiency

From the recorded data in figure A.6, slopes of 0.105 V/mW for Detector 1 and 0.104 V/mW for Detector 2 are derived. These slopes result in quantum efficiencies of 85 % ± 5 % and 84 % ± 5 %. The given error is mainly dominated by the used sensor of ±5 % [142]. For high optical powers, the photodiodes are saturated and those points were omitted as well as those at very low optical powers.

A.2.3 Filtering

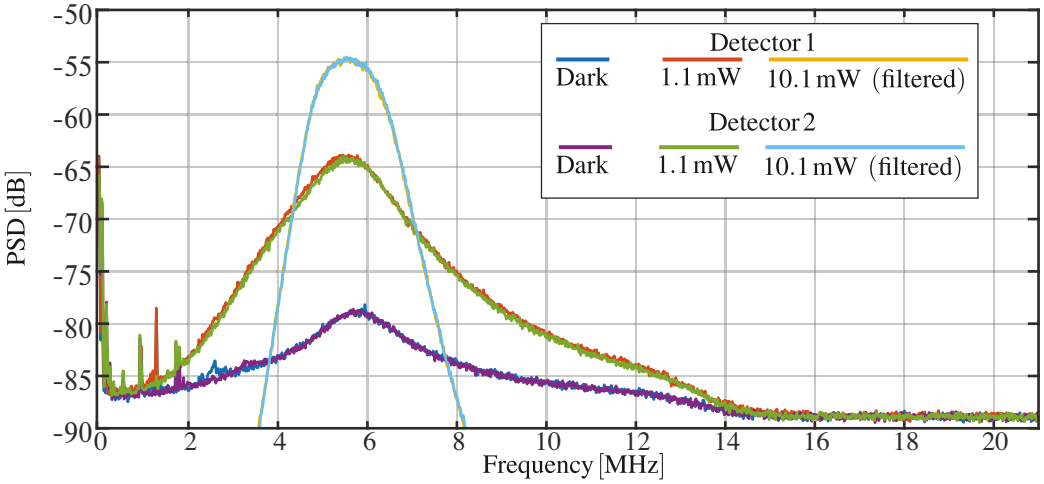

Figure A.7 Example RF spectra of detectors used in BHD
Detector dark noise and measured spectra close to 1 mW and 10 mW are shown.

Electronic circuits inside the detector (figure A.5) yield a good SNR around 5.6 MHz. Below 4 MHz, significant electronic noise contributions can be found. Due to an additional

higher order low-pass filter and an input filter of the digitiser, the measured spectrum quickly approaches the constant digitiser noise floor.
For processing, the data is filtered within a 1 MHz window around 5.6 MHz using two 6^{th} order Chebyshev filters with 0.1 dB ripple.

B. Specification sheet
Origami 15 SN 3369

NKT Photonics Switzerland GmbH
Althardstrasse 70
8105 Regensdorf
Switzerland
www.nktphotonics.com

Origami 15

Part Number	**OR/SM/80/15550/150/130/FS**
Serial Number	**3369**

Date of test	**23.12.2019**
Ambient temperature	22.6 °C

Performance		
Average output power	135	mW
Pulse repetition rate	80.001	MHz
Pulse duration	192	fs
Center wavelength	1558.8	nm
Spectral width (FWHM)	13.1	nm
Time-bandwidth product	0.31	
Polarization extinction ratio	24.9	dB
Freq out, peak-to-peak	1.9	V
RF output power	10.5	dBm @ fundamental

Options		
External modulation	yes	
Trigger output	yes	
Amplitude stabilization	no	
Isolator inside	yes	*new: linear polarization is oriented at 45° with respect to baseplate*
Sync	no	
Piezo	yes	
Coarse tuning	yes	

NKT Photonics Switzerland GmbH
Althardstrasse 70
8105 Regensdorf
Switzerland
www.nktphotonics.com

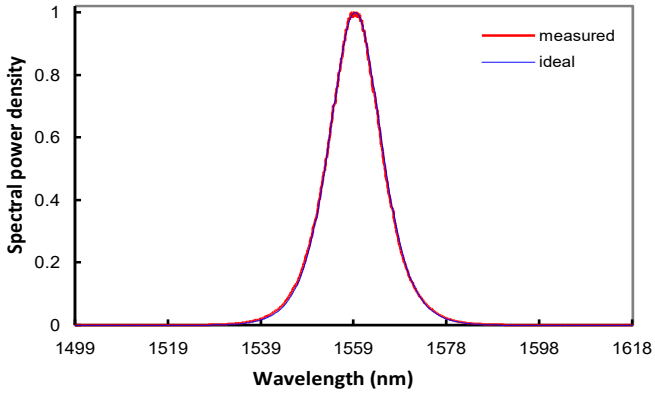

Ideal sech^2 FWHM: 13.1 nm Wavelength: 1558.8 nm

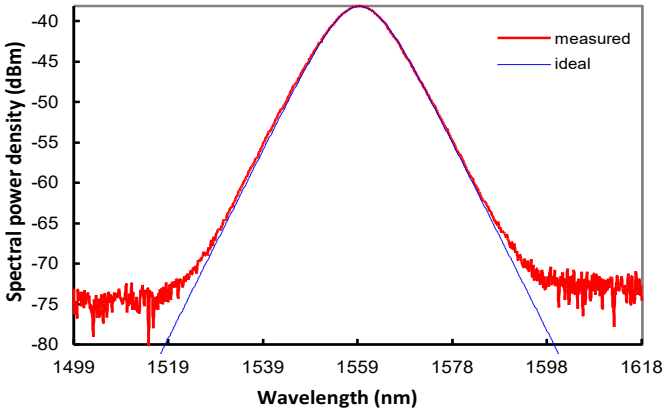

Ideal sech^2 FWHM: 13.1 nm Wavelength: 1558.8 nm

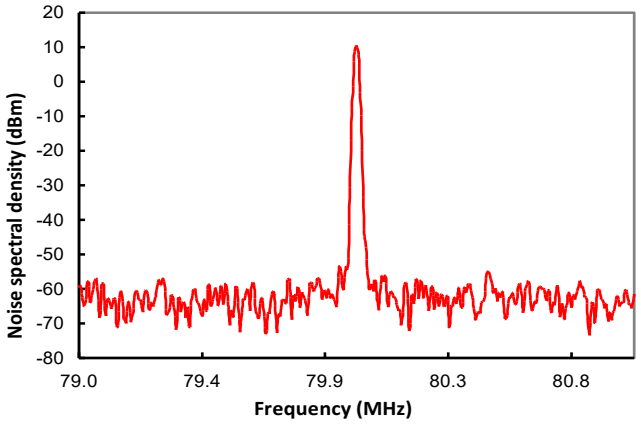

Span: 2.0 MHz Resolution: 10.0 KHz

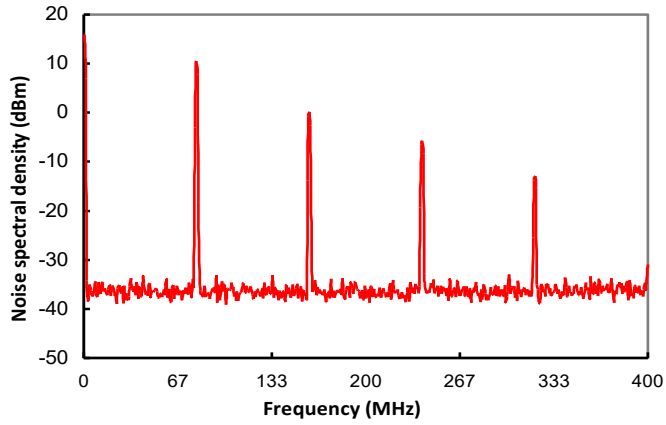

Span: 400.0 MHz Resolution: 1.0 MHz

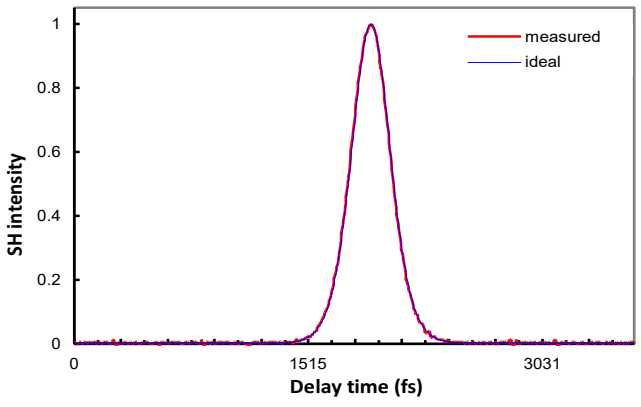

Ideal soliton: 192 fs

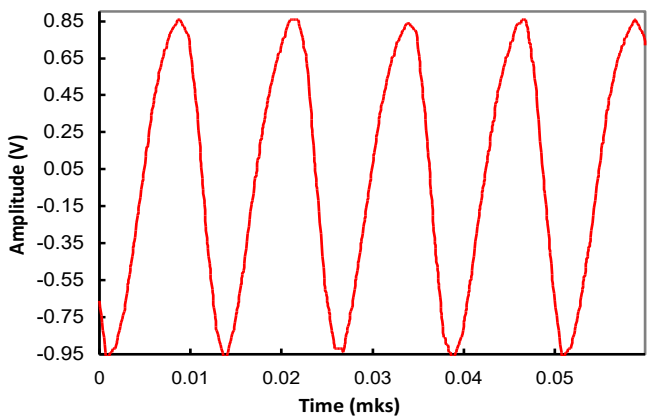

Peak-to-peak: 1.86 V

NKT Photonics Switzerland GmbH
Althardstrasse 70
8105 Regensdorf
Switzerland
www.nktphotonics.com

Ext Mod option

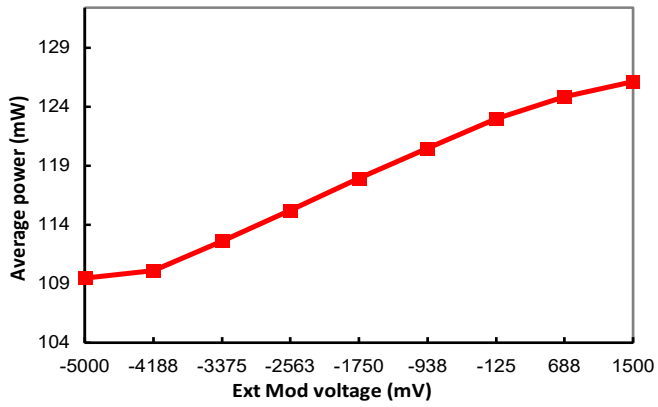

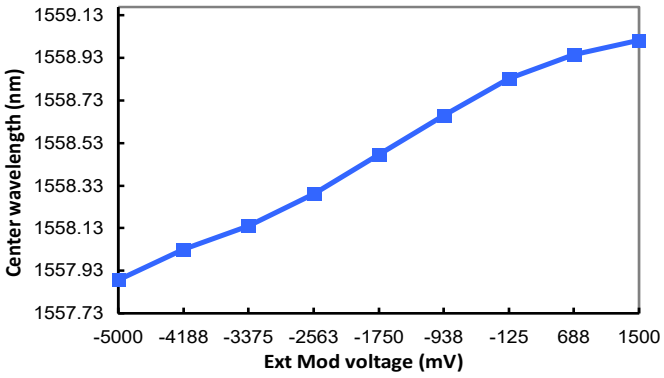

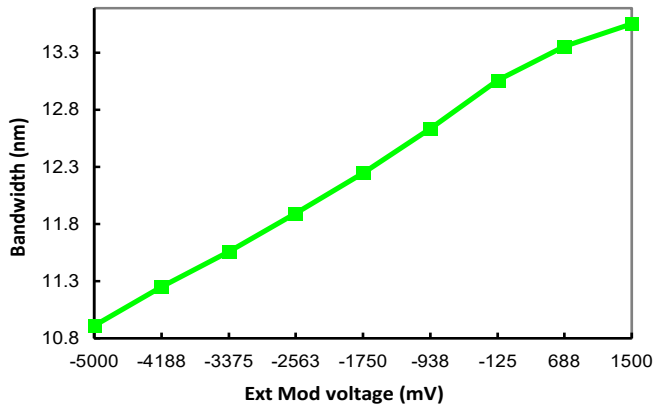

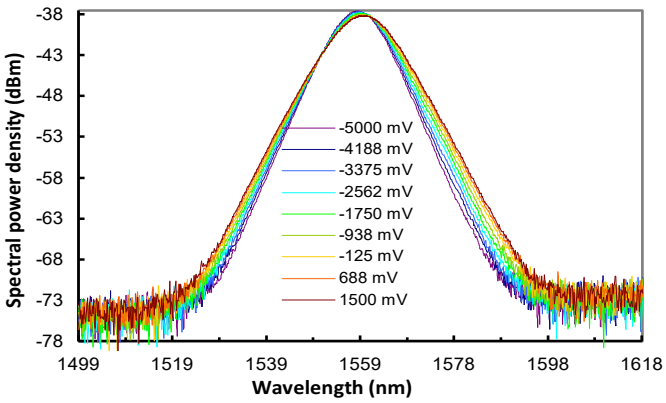

NKT Photonics Switzerland GmbH
Althardstrasse 70
8105 Regensdorf
Switzerland
www.nktphotonics.com

Piezo option

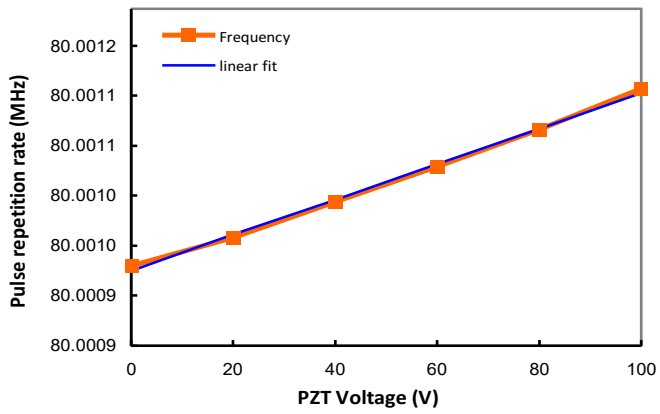

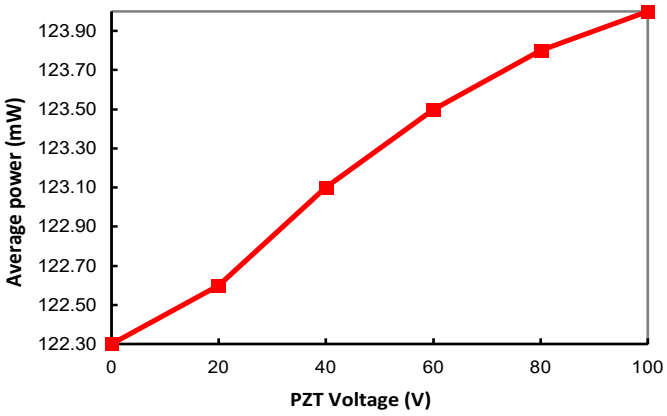

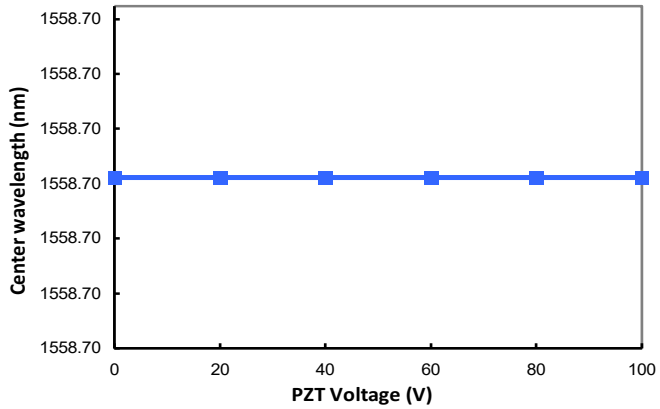

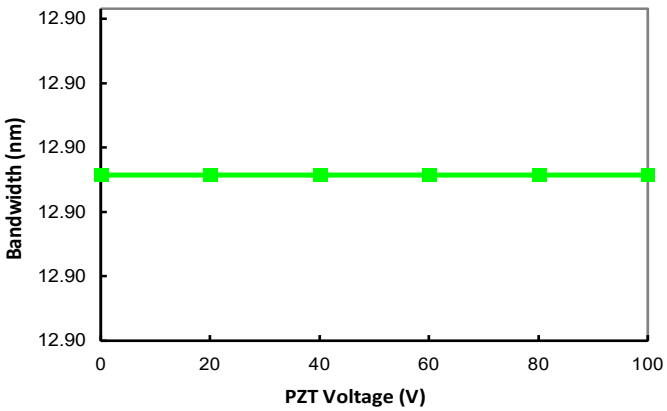

PZT slope: 1.8 Hz/V

80.001 MHz at: -529 V

NKT Photonics Switzerland GmbH
Althardstrasse 70
8105 Regensdorf
Switzerland
www.nktphotonics.com

Coarse tuning option

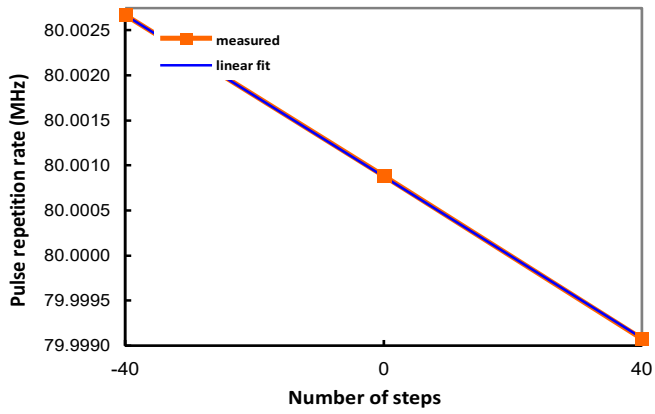

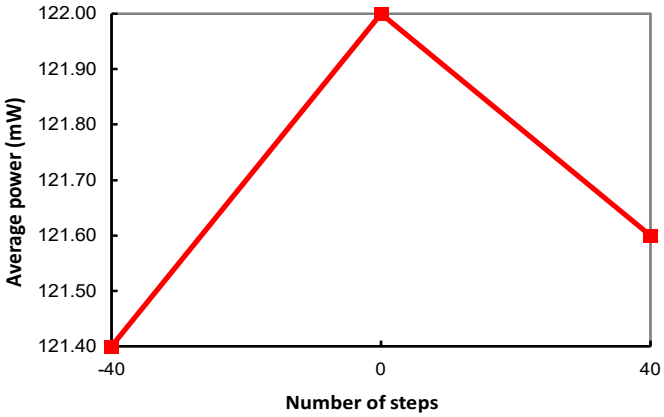

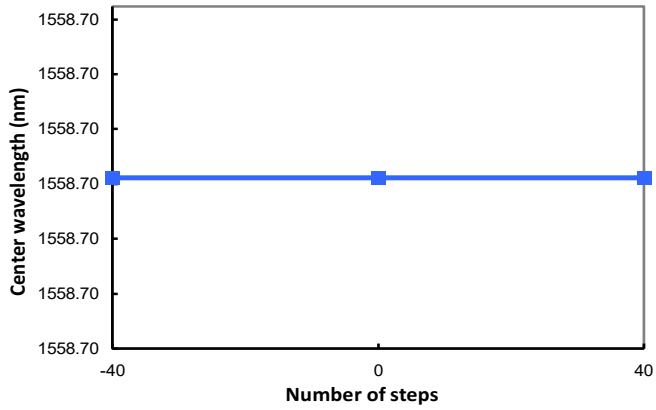

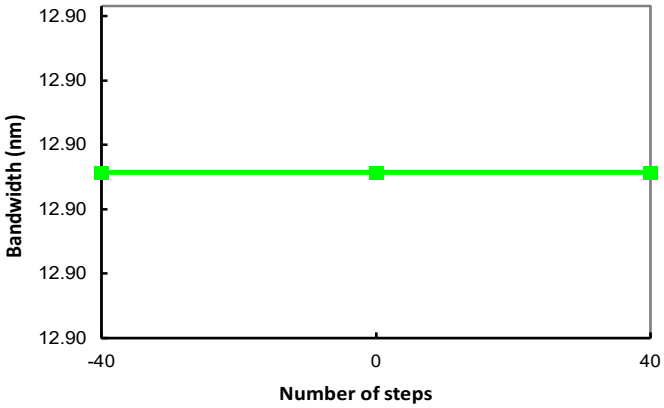

Coarse tuning slope: -44.8 Hz/Step
Tuning range: 3.585 kHz

C. Quote Origami 15

Quote

Onefive GmbH
Althardstrasse 70
CH-8105 Regensdorf
Switzerland

Phone: +41 43538 3657
Fax: +41 43538 3686
Bank: [redacted]
VAT Reg. No:

OneFive GmbH is a subsidiary of
NKT Photonics A/S

Universität Rostock
AG Experimentelle Quantenoptik

Kai Barnscheidt
Albert Einstein Straße 23
Rostock 18059
DE - Germany

Customer number:
Customer VAT no.:

Quote No: [redacted]
Date: April 12, 2018
Salesperson: [redacted]

Dear Kai Barnscheidt,

Thank you for your enquiry. We are pleased to offer you the following:

Line No.	Item No.	Description	Qty.	Price/unit	Discount	Amount
1		Onefive ORIGAMI-15 custom configuration (*)	1	[redacted]	[redacted]	[redacted]
2	OF300-000-005	Low noise driver Onefive ORIGAMI	1	[redacted]	[redacted]	[redacted]
3	OF300-000-001	Trigger output Onefive ORIGAMI	1	[redacted]	[redacted]	[redacted]
4	OF300-000-003	Fine Repetition Rate Tuning	1	[redacted]	[redacted]	[redacted]
5	OF300-000-004	Coarse Repetition Rate Tuning	1	[redacted]	[redacted]	[redacted]
6	OF300-000-002	External Modulation Input	1	[redacted]	[redacted]	[redacted]
	Total Excl. VAT					[redacted]

All prices in Euro

(*) Custom Onefive ORIGAMI-15:

Pulse repetition rate frequency 80 MHz ± 2 MHz fixed
Average optical output power >120 mW
Pulse energy >1 .5nJ
Pulse duration 200 fs +/- XX fs
Spectral bandwidth XX nm
Pulses have no pedestals, no satellite pulses, no background, soliton shape
Center wavelength out of laser 1550 ± 5nm (standard is 1560 ± 5nm)
Spectral bandwidth transform limited, soliton shape, no ripples, no pedestals
Spectral bandwidth (FWHM) >10 nm
Time-bandwidth product <0.35
Free space output M^2 <1.1
Polarization extinction ratio >23 dB
Timing jitter <30 fs rms [1 kHz – 10 MHz] (without low noise driver)
No ASE background
RIN performance shot-noise limited [100 kHz – 100 MHz]
Cooling: Air
Polarization state: s (to be confirmed)

Low Noise Driver:

Timing jitter <1 fs rms [1 kHz – 10 MHz]
Size 19” rack mount, passively air-cooled

Trigger Output

Built-in temperature controlled internal fast monitor photodiode

Bandwidth	>300 MHz, SMA connector on laser head
RF level	>-10 dBm

External modulation input

Pump power control by external voltage
Bandwidth DC - 500 Hz, BNC connector
Modulation depth ± 5%
Timing jitter will be affected by input voltage noise

Fine Repetition Rate Tuning

Repetition rate tuning via built-in PZT (for Onefive ORIGAMI lasers)

Stroke	>1 µm, corresponds to tuning range of >25 Hz for 40 MHz laser >40 Hz for 50 MHz laser >100 Hz for 80 MHz laser >150 Hz for 100 MHz laser
Resonance frequency	>30 kHz
Input requirements: Voltage	0 – 100 V

BNC connector on laser head

Coarse Repetition Rate Tuning

Repetition rate tuning by	+/-0.8 kHz for 40 MHz laser +/-1 kHz for 50 MHz laser +/-1.7 kHz for 80 MHz laser +/-2 kHz for 100 MHz laser

Tuning speed on minute scale
TTL input for repetition rate up or down
Digital read out of tuning steps

Delivery time is approximately 12 weeks ARO. If you need further information, please don't hesitate to contact us.

Best regards

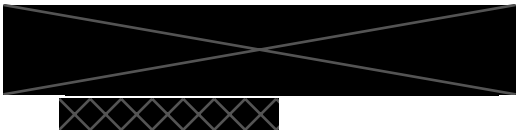

Sales Engineer

Payment Terms: Net 30 days
Incoterms 2010: FCA, Zürich CH

Warranty: 24 months

Country of origin: Switzerland

This offer is valid 30 days from today and is subject to NKT Photonics’ General Terms & Conditions (attached)
Manuals and other documentation for the products are written in English.

D. Specifications of the coupling mirrors

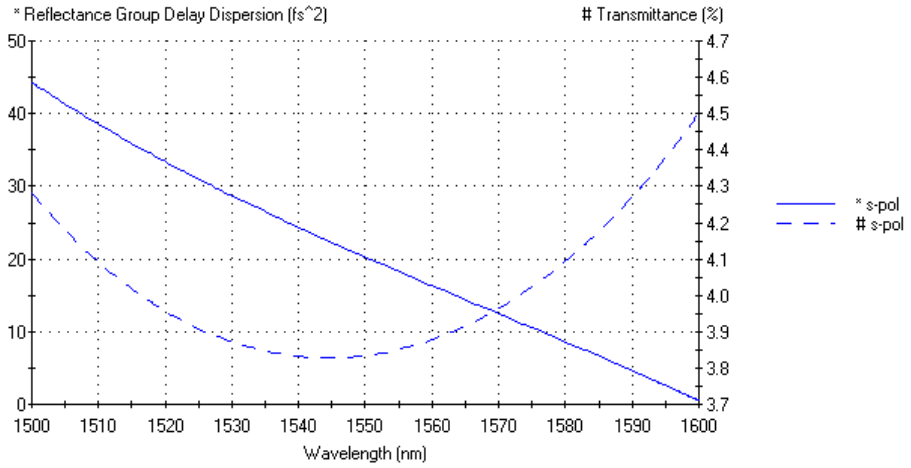

Figure D.1 Calculated coating of coupling mirrors as ordered (given prior to the production). Tolerance of reflectivity is ± 1 % [209].

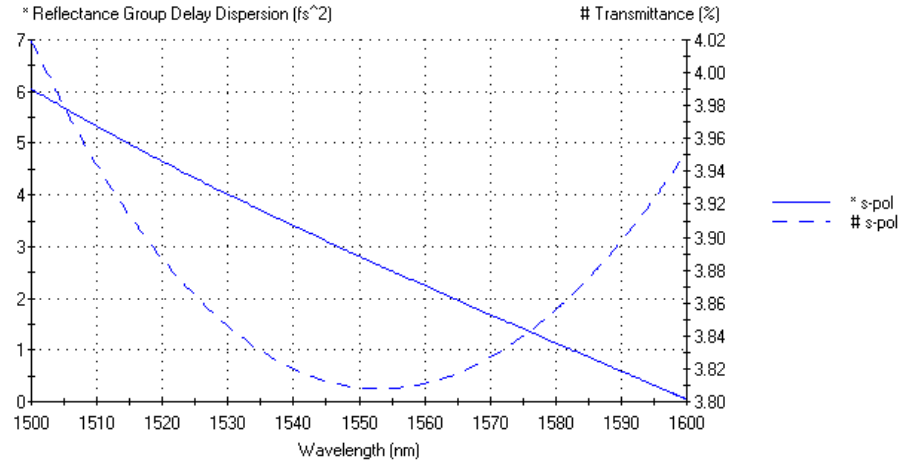

Figure D.2 Calculated coating for coupling mirrors, enhanced for fs pulses [209]. Not ordered due to cost and as dispersion was not considered to be a problem at time of ordering.

E. Influence of atmospheric gases on the separation resonator

This chapter of the appendix briefly presents measurements with different gases injected into the separation resonator. As within the dispersion measurements for the separation resonator (section 4.5), its dispersive properties in the red part of the spectrum above 1560 nm did not match initial expectations. These initial expectations were that a linear detuning due to the CEO is visible and that other dispersive effects should either be invisible or well described by second order approximations (GVD of air and GDD of he three dielectric mirrors). But neither the second nor the third order yielded sophisticating results.

Searching the HITRAN database [110] for molecular absorptions of major atmospheric gases, it was found that only CO_2 has some transitions in this specific region. In figure E.3, the spectral line intensities of 12 814 transitions are illustrated with the resolution provided by the MATLAB vector graphic export. A further analysis on the spectral lines was not performed as the pulse itself consists of roughly 100 000 lines with linewidths in the low kHz regime. These are equally spaced by 80 MHz with an unknown offset frequency that drifts $\approx$ 10 MHz. Due to the resonator, the change in phase and amplitude could in theory be observed but as the available OSA only has a resolution in the regime of 10 GHz, depending on the used settings, this is not possible with the current setup. Without a reference from a second frequency comb, as used in [75, 111, 112], there is little hope to properly resolve the actual CO_2 spectrum and its influence. Nevertheless, the relative measurements in figure E.1 show similarities to satellite observations of CO_2 concentration based on these transitions [210]. Above 1590 nm, the measurement is limited by the optical bandwidth of the pulse as well as the sensitivity of the OSA.

For a first investigation, the increased CO_2 concentration in exhaled air was used. The locking loop of the resonator remained stable as the transmitted spectrum changed.

To improve the setup, a tube was used to guide the gases into the casing that shields the resonator from air turbulences. The temperature gradient due to the gases was minimised by guiding them through a CPU water cooling block which was held at room temperature.

Furthermore, foam was placed at the end of the tube to minimise the resulting turbulences inside the resonator.

Using a CO_2 cartridge and an inflator for a bicycle tyre, pure CO_2 was guided into the casing which was sealed, exempting holes for the laser beams. Due to changes in refractive index, the length had to be readjusted. Furthermore, the most visible effect was a change in CEO and a constant drift as CO_2 slowly escaped the casing. Another observed effect was that a layered structure built inside the casing as CO_2 has a higher density than the normal air. This layered structure affects the beam propagation and hence the spatial mode of the resonator changes making realignment neccesary. As a result, the recorded data does not allow a precise measurement of the molecular transitions without further improvements.

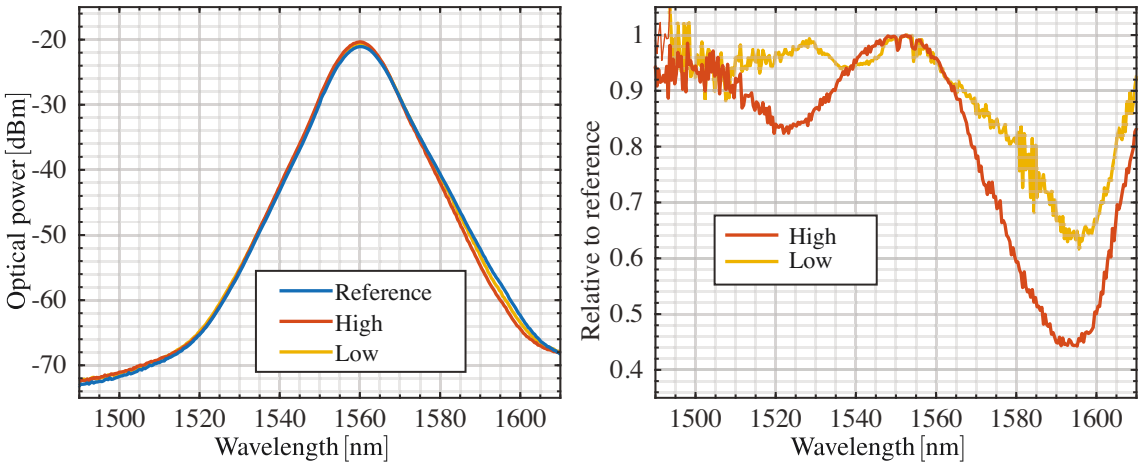

(E.1a) Measured spectra with increased CO_2 concentration

(E.1b) Data of **(E.1a)** relative to reference spectrum

Figure E.1 Increased CO_2 concentration in resonator
CO_2 was injected once, creating a higher CO_2 concentration that afterwards dropped over time. For **(E.1b)**, data was normalised to power measured at the central wavelength due to alignment drifts.

The same setup was used to constantly flush the separation resonator with pure nitrogen in order to eliminate any effects of the molecular transitions from CO_2. While squeezing was still observed, the overall stability suffered due to the turbulences created by the constant flow of nitrogen which is unavoidable without further efforts, especially as the gas has to flow through the holes for the laser beams. Compared to air, nitrogen has a higher density, it fills the casing from the bottom and escapes mainly through the lowest hole. A hole placed below the holes for the laser beams would allow the nitrogen to flow out of the resonator without effectively flushing the normal air at the level of the laser beam. A hole above would also have no significant influence as the nitrogen already flows trough the holes needed for the laser beam. The only effective way would be to completely encapsulate the three mirrors of the resonator and use either Brewster windows or AR-coated windows. Additionally, the nitrogen cooled the resonator which lead to a constant drift in resonator length over several minutes.

Due to the decreased stability, no successful dispersion measurements or other longer measurements were possible. Nevertheless, squeezing was observed with the nitrogen-flushed resonator. At first glance, these effects did neither improve nor degrade the amount of observable squeezing and anti-squeezing. Only the decreased stability and a relative change in CEO between resonator and laser was observed and hence it was decided not to spend further time on these effects.

For further analysis, it would be beneficial to take the additional effort to place the overall resonator setup in a chamber to gain complete control of its atmosphere. This would allow to control the pressure and composition of the atmosphere. Combined with a second comb [75, 111, 112], this would allow to study these influence in detail. The atmosphere could be used to compensate for the CEO or the GDD of the mirrors. 162 1662

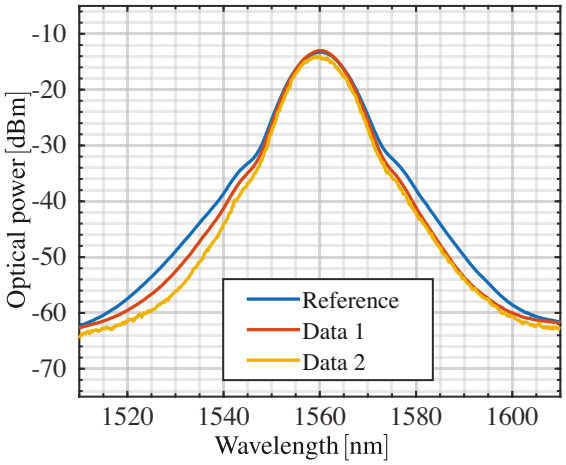

(E.2a) Measured spectra during flushing with nitrogen

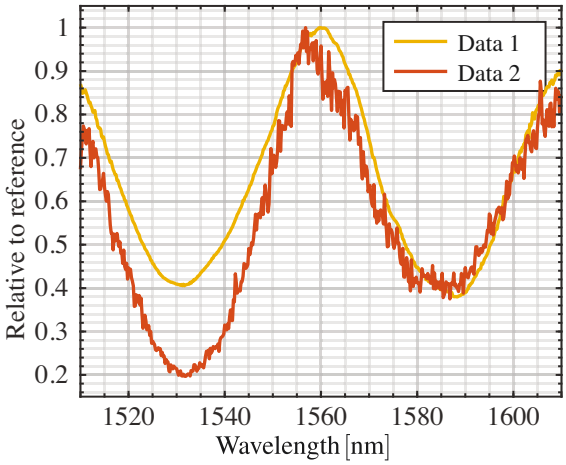

(E.2b) Data of **(E.2a)** relative to reference spectrum

Figure E.2 Resonator flushed with nitrogen
Depending on the flow rate, the transmitted power gets noisy. Deviation looks quite symmetric due to the change in CEO. For **(E.2b)**, data was normalised to the optical power measured at the central wavelength to compensate for drifts in alignment.

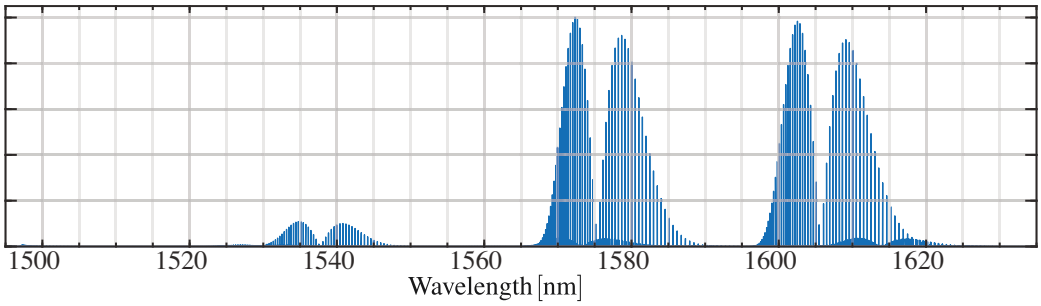

Figure E.3 CO_2 absorption from the HITRAN database [110]
Spectral line intensities of 12 814 transitions are shown. The resolution limited by the graphic export.

F. Illustrative introduction to Kerr-squeezed fs pulses

Within the main part of this thesis, the Kerr squeezing was motivated by the visual representation of the intensity-dependent refractive index that shapes the circular minimum uncertainty region of a coherent state into close to perfectly squeezed state. Due to the photon number conservation of the Kerr effect, this squeezed state has to be shot noise-limited if the initial state is limited by shot noise. Even for large coherent amplitudes, its amplitude quadrature fluctuations remain at the shot noise-limit. For any measured combination of squeezing below the vacuum reference and anti-squeezing, this allows to calculate an angle according to equation (5.9). These two variances and the rotation angle can describe the resulting squeezed state quite well. Using this simplified model, any measurement within this thesis that does not involve specifically selected modes by temporal detuning or the used SLM can be explained.

It was indicated that for stronger Kerr interactions, the assumption may break down as the uncertainty regions would rather resemble a banana than an ellipse. Within the first section of this appendix, the Kerr interaction for a single mode of light is discussed in more detail as the Kerr interaction itself can give rise to more complex quantum states if strong enough. Additionally, the limit for weaker Kerr interactions, a squeezed state, is motivated and related to the creation of a squeezed state in an optical parametric amplifier.

The second section of this appendix will discuss what changes compared to the CW case when a pulse, built by multiple frequency components, is squeezed. The last section of this appendix highlights the complexity of Kerr-squeezed pulses as the pulse itself affects its own shape and squeezing upon propagation.

This chapter is meant to provide an illustrative image to the observed experimental findings that helps further understanding of the involved phenomenons. For a more complete theoretical review of quantum optical phenomena in nonlinear optics, [211] can be used and [97, 145] for fibre optics.

F.1 Single-mode Kerr squeezing

In section 5.3, the properties of Kerr-squeezed states were compared to those of squeezed states created by the squeezing operator $\hat{S} = \exp\left(\frac{1}{2}\xi\hat{a}^{\dagger 2} + \frac{1}{2}\xi^{*}\hat{a}^{2}\right)$ and its complex squeezing parameter $\xi = r \cdot e^{i\varphi_\xi}$. For squeezed states, the amount of squeezing (r) and the orientation of the ellipse can in principle be chosen freely. For the Kerr-squeezing, the squeezing angle, with respect to the amplitude quadrature, is directly linked to the amount of observed squeezing. To further investigate its properties and the used simplification, both Hamiltonians can be compared.

$$\hat{H}_{\mathrm{SQ}} = \hbar\left(G\hat{c}\hat{a}^{\dagger 2} + \mathrm{H.c.}\right) \tag{F.1}$$

$$\hat{H}_{\mathrm{Kerr}} = \frac{\hbar}{2}g\hat{a}^{\dagger 2}\hat{a}^{2} = \frac{\hbar}{2}g\hat{n}\left(\hat{n}-1\right) \tag{F.2}$$

G and g are given by experimental parameters from the corresponding $\chi^{(2)}$ and $\chi^{(3)}$ nonlinearities. The corresponding interaction time is given by the length and refractive index of the media. For the squeezing Hamiltonian, $\hat{c}$ is the annihilation operator of a pump mode with twice the energy per photon. Assuming the pump can be treated classically, *i.e.* it has a strong coherent amplitude and is not significantly depleted, it can be replaced by the corresponding complex amplitude. With this assumption, the Hamiltonian results in the squeezing operator. For Kerr squeezing, the Hermitian conjugate is not required as the interaction can be written using only the already Hermitian photon number operator. Instead of the annihilation of one photon in another mode to create a pair of photons in the mode, as for the squeezing Hamiltonian, two photons in the mode itself are annihilated to create a pair of photons. While this process conserves the overall number of photons and the photon number statistics, it still creates a squeezed state. In [133], the resulting squeezing and its limitations for the evolution of an initially coherent state are discussed.

The strength of the interaction depends on the nonlinear media (g) as well as the coherent amplitude of the state. For the same interaction time, the combination of strong coherent amplitude α with weak g can result in more squeezing than the same overall interaction $\left(\alpha^2 \cdot g\right)$ with a smaller coherent amplitude. By approximating a simple squeezed state, it is assumed that the initial Wigner function evolves into a squeezed ellipse. This approximation is good if the resulting ellipse is small compared to the coherent amplitude. For an ideal single-mode Kerr interaction, the achievable squeezing and the corresponding coherent amplitude can be calculated in dependence of the media [133].

In principle, optical fibres allow for a fine tuning of the interaction by adjusting the length of the fibre. Due to the required high optical power for CW light, other nonlinear effects

have to be considered as well as linear effects such as GAWBS and losses based on the length of the fibre.

Using short intense pulses, more squeezing can be obtained with the same average optical power while simultaneously reducing the effects of GAWBS and stimulated Brillouin scattering. Such short pulses have a broad spectrum. This broad spectrum gives rise to differences to the single-frequency-mode squeezed state as discussed within the next section.

F.2 Squeezed pulses

Within the last section, the Kerr-squeezed state was discussed and related to a normal squeezed state. Within the experiment the pulse behaves like a squeezed state, at least when squeezing was observable. Unlike an ideal squeezed state however, it is not a minimum uncertainty state. Even a perfect squeezed state is only a minimum uncertainty state if no losses occur but comparing a Kerr-squeezed fs pulse to an ideal CW squeezed state may be too optimistic. Hence, the properties of a squeezed pulse are considered first.

As discussed in section 4.1.1, a mode-locked laser emits (many) equally spaced CW laser lines which are locked with respect to each other. Very regularly, all of these CW laser modes interfere constructively forming the pulse pattern. To form a squeezed pulse, it is possible to use many phase-stable individually squeezed modes with corresponding coherent amplitudes as indicated in figure F.1.

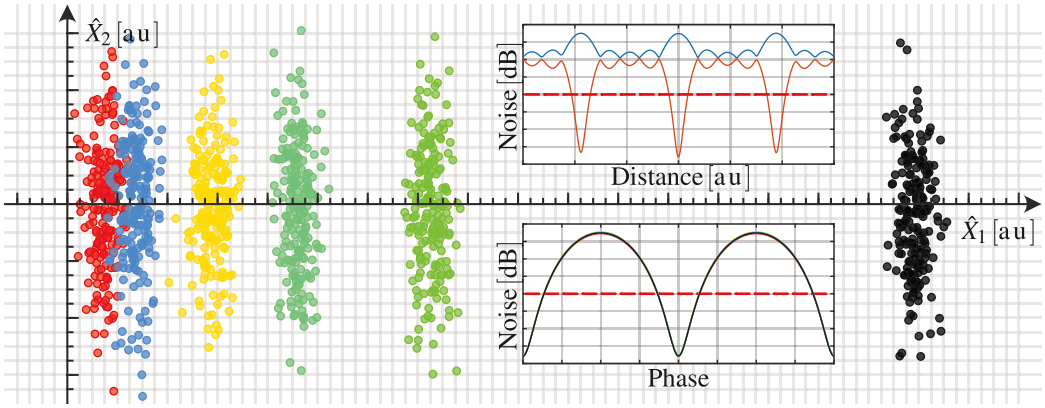

Figure F.1 Squeezed pulse formed by multiple individually squeezed states. Multiple amplitude-squeezed states (coloured) are used to form an overall squeezed pulse (black). For each mode, the phase-depending variances are shown. The dependence on distance detuning is indicated of observable squeezing and anti-squeezing is indicated as well.

Assuming such a state is analysed with a strong LO in the identical pulse shape, squeezing is observed for perfect pulse overlap. However, if the pulses do not overlap at all, the LO measures each mode of the squeezed pulse under a more or less random quadrature

angle and the resulting variance is well above the vacuum variance as illustrated in figure F.1. Furthermore, every single mode analysed separately will show the same amount of squeezing. A structure like this is not a squeezed pulse but rather an ensemble of individually squeezed modes.

For a squeezed pulse, the creation and annihilation operators of the specific pulse have to be considered. For $2N+1$ modes around a centre frequency, this can be written as a sum of the corresponding annihilation operators for the modes with angular frequencies ω_j:

$$\hat{a}_\mathrm{P} = \sum_{j=-N}^{N} A_j \cdot \hat{a}_j \qquad \omega_j = \omega_\mathrm{c} + j \cdot 2\pi \cdot f_\mathrm{reP} \qquad \sum_{j=-N}^{N} |A_j|^2 = 1 \tag{F.3}$$

By writing down the squeezing operator for such a mode, it can be seen that a squared operator for a single modes appears only in very few terms. Most terms consist of two different modes and hence indicate correlated photons between these modes. This is illustrated in figure F.3. In figure F.2, the data points for each individual mode resemble more a coherent state than those in figure F.1. As only five modes are used for the illustration, individual modes still show some squeezing. For the correct combination of modes, the state is clearly squeezed. A Kerr-squeezed pulse from a mode-locked laser consists of more than ten thousand individual modes of which each individually appears to be classical but if investigated in the correct superposition, they form a squeezed state with almost minimum uncertainty.

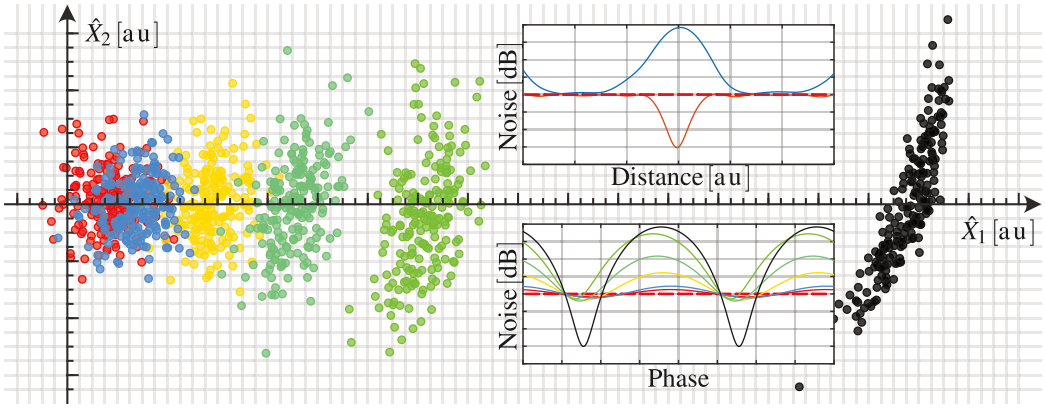

Figure F.2 Simplified Kerr-squeezed pulse rotated to amplitude quadrature. Multiple modes form overall squeezed pulse (black). For each mode, the phase-depending variances are shown. The dependence on distance detuning is indicated of observable squeezing and anti-squeezing is indicated as well.

For any other superposition (chirp, delay and any other phase or intensity modulation), less squeezing or even only anti-squeezing can be observed. This was intentionally measured for figures 5.11 and 7.4a.

F.3 Squeezed Kerr pulses

In optical fibres, short pulses are affected by linear effects such as dispersion as well as nonlinear effects like the Kerr nonlinearity. These effects change the shape of the pulse and its spectrum as it propagates (figure F.4). Therefore, Kerr squeezing is special as the pulse itself provides the pump for the squeezing process and this pulse-shape-dependent process acts back on the pulse shape. Two photons from arbitrary modes in the pulse are annihilated and two photons can be created in one mode or in two separate modes of the pulse if energy is conserved as represented in figure F.3. The likelihood of creating two photons within the same frequency modes is low due to the amount of other possibilities, especially when considering that the pulse consists of several thousand modes. All in all, the outcome of the process depends on the overall phase and amplitudes of the involved modes.

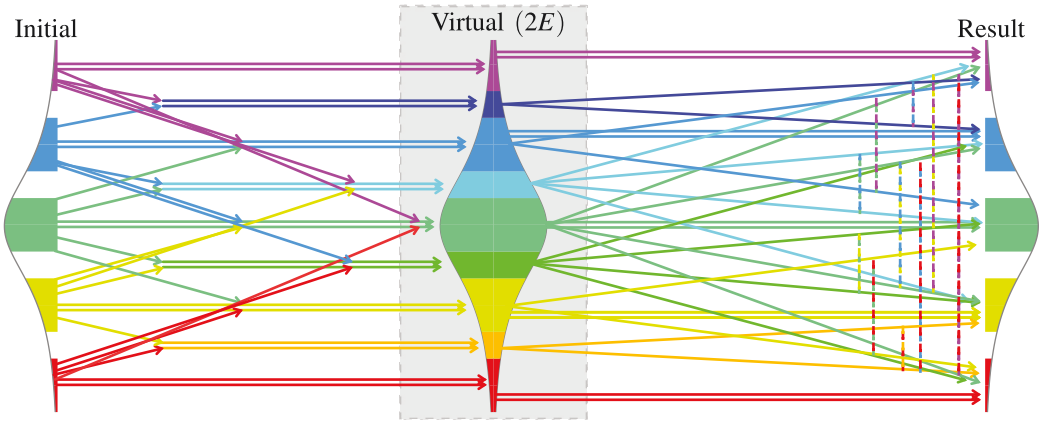

Figure F.3 Representation of photon correlations due to Kerr interaction
The left part of the illustration shows how much energy is available upon annihilation of two photons from a pulse with five frequency modes. On the right side, it illustrates which photon pairs can be created within the five modes based on the available energy. Pairwise created photons in different modes are linked by a corresponding dashed line.
Changes in intensity or the creation of photons in additional modes of the comb are not considered.

These involved modes change as the pulse propagates through the optical fibre as the Kerr-squeezed state constantly evolves. For example, some modes that initially contained a significant intensity loose their complete intensity during the propagation. All photons that are measured in these modes after the propagation where created as part of a pair. The other photon of this pair is somewhere in the comb. This is a significant difference to the usual squeezing process where a strong classical beam pumps photons into a weak single- or two-mode squeezed state. As a result, the Kerr-squeezed pulses contain complex correlations between its different modes that can be measured in several combinations [144, 188]. Therefore, the carrier pulse at the end of the fibre is not necessarily the optimal

LO to measure maximum squeezing on the resulting state with complex correlations between all of its frequency modes.

In figure F.4, the evolution of the pulse is simulated, using only dispersion and Kerr-nonlinearity, for the mostly used average powers of 12 mW and 17 mW. To improve measured squeezing, the optical power and fibre parameters could be altered to a point where the resulting LO well approximates a squeezed mode. As an alternative, it could be optimised to a squeezed mode that can be accessed with reasonable effort by the pulse-shaping capabilities of SLM.

Within the experiment, only weak squeezing was observed compared to the strong anti-squeezing. But this does not necessarily mean that this was solely due to used LO pulse. It can also be caused by the limited quantum efficiency or be masked by the influence of GAWBS. Simultaneously, measured squeezing is mainly limited by GAWBS at the moment which does not mean that the LO shape is good or even optimal. Nevertheless, the improved observed squeezing from a better LO is likely hard to resolve as GAWBS is the main limiting factor.

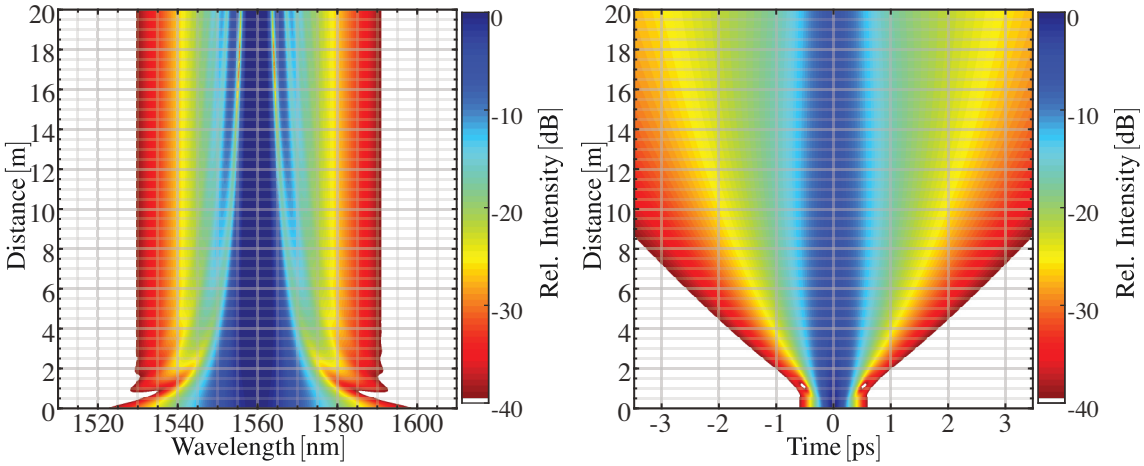

(F.4a) Evolution of the spectrum for 12 mW.

(F.4b) Evolution in time for 12 mW.

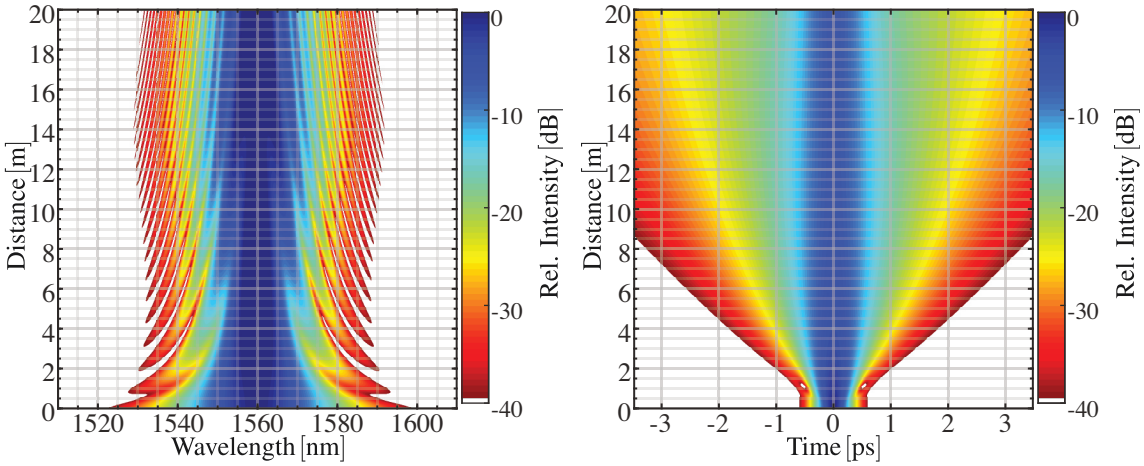

(F.4c) Evolution of the spectrum for 17 mW.

(F.4d) Evolution in time for 17 mW.

Figure F.4 Exemplary pulse propagation for the most commonly used average optical powers in the experiment. Intensities are shown in the time as well as the spectral domain as the pulse propagates a 20 m long fibre.

G. Data acquisition resources and methods

G.1 Data acquisition resources

Central component of the data acquisition is a PXI[1]-based system from NI™[2]. The PXI system allows to control and synchronise data acquisition, data transfer as well as data processing of installed modules. Using LabVIEW[3], this allowed the implementation of several automated measurement routines and sequences which were used for measurements throughout this thesis.

PXIe-1062Q
A chassis that houses the other modules and provides a common clock source as well as a backplane with a bandwidth of up to 3 GB/s to the controller and 1 GB/s for individual modules. It uses 4 lanes per module of first generation PCIe, each supporting 250 MB/s .

NI PXIe-8115
Embedded controller and computer that provides computing resources. It can communicate with the chassis and all installed modules. Instead of the 4 lanes per link provided by the chassis, only one lane (250 MB/s) is used which limits the bandwidth.

Due to the 32-bit operating system, the system memory is limited to ≈ 3.2 GB. Processing resources (*Core i5-2510E*) are shared with the operating system (Windows) and all other active programmes. Data storage was upgraded from HDD to SSD to provide faster write speeds and lower latency.

NI PXI-5124
A high-resolution (12-bit) two-channel digitiser that has a maximum sampling rate of 200 MS/s and 32 MB of memory per channel.

[1] PCI eXtensions for Instrumentation
[2] National Instruments
[3] Laboratory Virtual Instrumentation Engineering Workbench

Communication with this card is based upon a PXI link instead of PCI, limiting the maximum data transfer rate to 132 MB/s. As each 12-bit sample is transferred using a 16-bit block, this relates to a theoretical limit ≈ 33 MS/s if both channels are used and no further information is transferred. As the sampling rate is derived by dividing the maximum rate by an integer number, only discrete sampling rates are available. Furthermore the impedance as well as the coupling of the inputs can be changed and analogue filters can be used to limit its bandwidth. This is necessary to avoid aliasing from higher frequencies, such as the laser repetition rate, modulation frequency and their combinations.

NI PXIe-6124

This module is a multifunctional module which can sample 4 channels with a resolution of 16 bit and a maximum sampling rate of 4 MS/s. Two analogue outputs can be used to generate arbitrary waveforms on demand. Multiple digital inputs and outputs are available as well and can be used to control other instruments and components. This can be done with more precise timing than via a USB controller which adds an unknown latency. Communication with this card is based upon PCI and has a theoretical bandwidth of 250 MB/s that exceeds the requirements for continuous operation if the computer can handle the amount of data.

NI PXI-5404

A frequency generator used to provide a sine for the EOM and the corresponding reference for demodulation in the PDH locking scheme. Using a PLL, the generated signals can be referenced to the same clock source used for data acquisition. As a result, the used modulation has a well defined and known frequency as well as a stable phase to all acquired data.

G.2 Data acquisition methods

Within all schemes, the sampling rates of both cards are derived from their internal clock. Each internal clock uses a PLL to synchronise with the backplane clock of the chassis. For all schemes, LabVIEW programs are written that store the most important settings as well as the data in a structured folder using a binary format. This data structure can be accessed both easily and efficiently by multiple MATLAB functions written for this purpose.

Single recording

Both cards are initialised and start recording a given amount of samples upon the same trigger. After recording, data is transferred to the computer and can either be stored or evaluated directly. Maximum recording length is determined by the available memory on

both cards. For the fast digitiser *PXI-5124*, this allows 16 MS per channel, for example 0.4 s at 40 MS/s.

Continuous sampling

Fast and slow digitiser are initialised with corresponding sampling rates, meaning that for each block of N samples by the *PXIe-6124*, the faster digitiser samples an integer number times more samples. Continuous sampling is started upon the same trigger. Both cards store the data temporally in their respective onboard memory. If the onboard memory is filled, the data is overwritten and further acquisition fails. To avoid this, the data has to be transferred to the computer simultaneously. On the computer, two loops handle the data. One loop receives the data from both cards simultaneously and stores it in the computer's memory, as it is the fastest available storage. The other loop accesses the data in memory and either processes[4] it or writes it to permanent storage.

As both cards have to be read simultaneously, onboard memory size, transfer speed as well as the available computing resources limit the maximum achievable performance. Aside from evaluation and storing, the data can also be discarded. If all components keep up with the acquisition, the measurement can run continuously for days. Practically, due to limited resources and background tasks, the existing system cannot operate reliable in this way with a meaningful sampling rate.

Limited continuous sampling

This scheme is closely related to the continuous sampling. It is initialised in the same way but sampling stops after a predetermined number of samples. This allows to record more successive samples than the onboard memory of the cards can store as data is already transferred to the computer during the further acquisition. It is checked whether the required number of samples has already been acquired after each transferred block of data. If the number is reached, the running acquisition is stopped and the remaining data is transferred from the cards to the computer. This allows to record more than 40 MS on both channels with a sampling rate of 40 MS/s if no background tasks disturb the process. Longer measurement times are possible with a reduction in sampling rate.

Due to limited system memory, long measurements have to be stored and evaluated afterwards. For processing, the recorded samples of 16-bit are converted to the double-precision floating-point format which requires 64-bit per sample. To process large amounts of data directly in the laboratory, either more memory or more efficient processing is required. Measurements evaluated on the computer were recorded with single recordings instead of continuous sampling to reduce the amount of stored data.

[4] If processing one block of data takes more time than recording the next block of data, the data stored in memory will grow. This can be avoided by simply deleting all data blocks in memory except the most recent, prior to each processing step.

H. Analysis of CW data from a different setup

Within this chapter, the extended methods described in chapter 5 are applied to older data recorded on a squeezed state in the CW regime. Compared to the Kerr-squeezed pulses from the fibre, the CW state has more squeezing and less anti-squeezing leading to a better visualisation. Furthermore, the used LO is not limited by shot noise at all frequencies (figure H.1b) which leads to the overestimation of the measured squeezing as expected in section 5.5.6. Close to 12 MHz, the modulation by the EOM inside the laser is visible.

The used data was recorded on 11.11.2017 with a neutral density filter in the signal arm to attenuated it from 161 µW to 21 µW. The used detectors have a flat frequency response and the range from 4 MHz to 8 MHz is used in the normal evaluation shown in figure H.1.

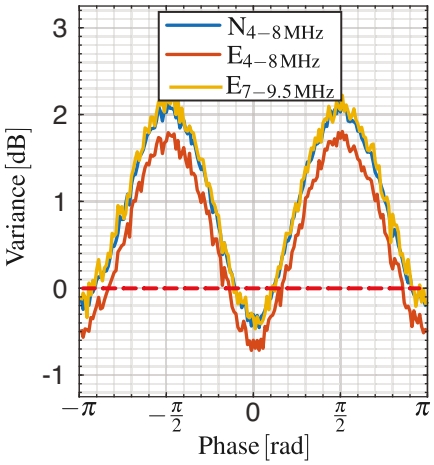

(H.1a) Variances relative to dark measurement

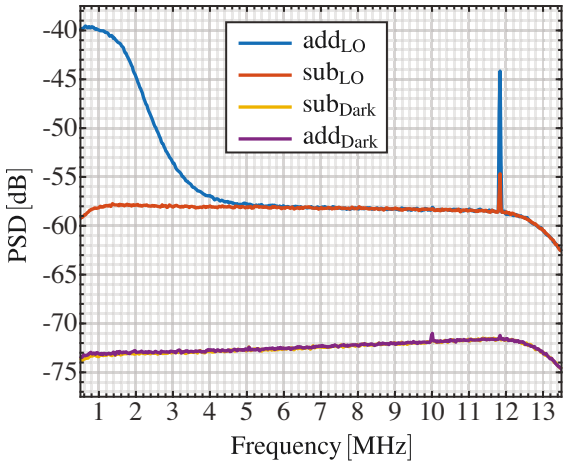

(H.1b) Unfiltered power spectral density for various signals

Figure H.1 Sample data for CW evaluation
(H.1a) shows the variances calculated from 20 000 consecutive samples relative to the variance of the dark measurement. Data is bandpass (4 MHz to 8 MHz) filtered while **(H.1b)** shows the power spectral density of the unfiltered data.

In figure H.2, the calculated variances from different methods are compared. To avoid the influence of the amplitude noise present on the laser, the extended method has to use a narrower frequency window from 7 MHz to 9.5 MHz.

Even within the used narrower bandwidth, the results from both methods are comparable as illustrated in figure H.2. The advantage of the extended method is clear as no separate vacuum reference has to be recorded, even if the average optical power of the laser drifts or is adjusted during longer measurements. Nevertheless, the LO has to be limited by shot noise within the used frequency range, as otherwise squeezing is overestimated. This is a strong prerequisite that can in principle be monitored by a separate balanced detection of the LO. Even if the used laser is just 1 dB above shot noise at 4 MHz, estimated squeezing is increased by 0.3 dB. The corresponding minimum quantum efficiency for a measurement with 1.7 dB anti-squeezing and 0.6 dB squeezing is 17.7 % which is above the transmission of the used attenuator.

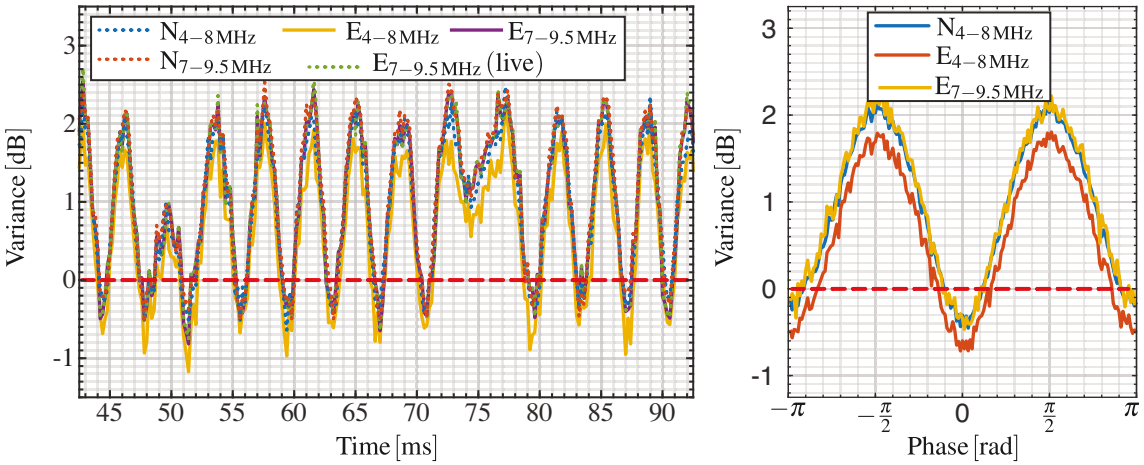

(H.2a) Variances of 20 000 data points referenced to vacuum noise
Green doted trace (live) is referenced to the vacuum level calculated from the same data points while the other are referenced to the overall reference.

(H.2b) Phase-sorted data with a resolution of 2 ° and 60 500 data points per interval for different methods

Figure H.2 Exemplary data evaluated with normal (N) and extended (E) methods within the state bandwidth. **(H.2a)** shows the same time interval of the data as figure H.1a while **(H.2b)** shows the phase-sorted data.

The used LO was already transmitted by a mode-cleaning resonator. This can be seen in figure H.1b as for frequencies below 4 MHz the noise level increases as these frequencies are transmitted by the mode-cleaning resonator. To obtain a true shot-noise-limited LO in the 4 MHz to 8 MHz range, either the finesse or the length of the used mode-cleaning resonator have to be increased.

I. MATLAB code

Within this section of the appendix, exemplary MATLAB code segments are presented to give the reader an understanding of the used methods. Due to the amount of measurements, not every single written line of code can be given. Instead, commented and reduced segments of the most important or repetitive code fragments are given.

I.1 Data evaluation

Different segments for the evaluation and processing of a typical BHD measurement are presented here.

I.1.1 Data reading

This section shows the typical code used to read the data from the measurement folder. It is shown how the different measurement files within the folder are assigned to different variables in the workspace. Additional functions were used to access the binary data in the file structure created by the written LabVIEW program. Aside from the required data, additional information is stored in these binary files and can be accessed by these functions. This information is given by additional return values from 'ScopeSet' and 'DaqSet'. The functions 'readScope' and 'readDaq' allow, if required, more than the reading of the data from a single measurement. They can read either the direct 8 to 24-bit integer values, as recorded by the cards, or the assigned -voltages[1]. Furthermore, a subset of the data or a subset of channels can be chosen, which is beneficial for large files as a 2 GB file of 8-bit integers would require 16 GB of memory stored in the 'double' format. These functions are specifically tailored to the used LabVIEW program and its structure. Instead of reading the whole binary file and reducing it to the needed amount afterwards, they know prior to reading the data how much storage in memory is required and where this data is stored in the file. This avoids reading large amounts of data from the disk to the memory and copying it within the memory. As a result, those functions are quite complex and abstract but of no specific interest for the actual evaluation.

[1] Based on the calibration equation for each channel of each card.

```
%Path of the measurement folder
DF = '[insert path here]';
%Read used sampling rate for both cards
ACrate  = ScopeSet(DF); %Read used sampling rate of the
   fast card
DCrate = DaqSet(DF); %Read used sampling rate of the slow
    card
%Read number of measurement files and their names with a
   subscript (FileRead)
[Nmeas, ~, Names] = FileRead(DF);
% Automatically filter given measurement names (only if
   properly named during measurement)
fileN = 1:Nmeas; %Array from 1 to number of measurements
SIs = fileN(strcmp('Si',Names)); %SI only measurements
LOs = fileN(strcmp('Lo',Names));  %LO only measurements
BHDs = fileN(strcmp('Homo',Names));  %Full BHD
   measurements
Ds = fileN(strcmp('Dark',Names));  %Dark measurements
   without light
clearvars fileN %Array not used anymore
%Create the bandpass filter for the fast fluctuations
[baa,aaa]=cheby1(6,0.1,2*6.1e6/ACrate); %Low-pass filter
[blf,alf]=cheby1(6,0.1,2*5.1e6/ACrate,'high'); %High-pass
    filter
resampbo=@(data)filter(baa,aaa,filter(blf,alf,data)); %
   Bandpass filter
%Read the data from one measuremnet
dataAC = resampbo(readScope(DF,BHDs(4))); %Read and
   filter data from forth BHD measurement
Offsets = mean(readDaq(DF,Ds(end))); %Read monitor
   voltages from last dark measurement and average for
   detector offset
Offsets(3:end) = 0; %Only channels 1 and 2 have an offset
dataDC = readDaq(DF,BHDs(4))-Offsets; %Read monitor
   voltages of actual measurement
```

I.1.2 Data processing

Within this section, it is shown how the data is processed to obtain the variances of consecutive samples normalised to the vacuum according to the different methods.

```
%Quick evaluation of fluctuations only
avAC = 1e4;% use 10.000 samples
VacVar = var(diff(resampbo(readScope(DF,LOs(2))),1,2)); %
    Variance of Vacuum from LO only measurement 2
Add = sum(dataAC,2); %Sum of both channels
Sub = diff(dataAC,1,2); %Difference of both channels
Corr = prod(dataAC,2); %Product of both channels
clearvars dataAC; %No longer needed
Vcl = var(reshape(Sub,[],avAC))/VacVar; %Variance of
   subtracted signal normalised to reference measurement
Vext = (var(reshape(Add,[],avAC))-4*mean(reshape(Corr,[],
   avAC)))./var(reshape(Add,[],avAC)); %Extented
   evaluation normalised to simultaneously measured
   vacuum reference
```

I.1.3 Phase fitting

The previous section analysed the data in time as it was recorded. Ideally, phase and time are perfectly linear, and the according phase in BHD can be directly assigned to each point in time. But due to atmospheric turbulences, thermal drifts and nonlinearities of the used piezo-mounted mirrors, this is more difficult and requires a nonlinear fit.

```
%Isolate the piezo voltage for analysis with some
   averaging
ramp = movmean(dataDC(:,3),1e3); %Ramp data with
   averaging
temp =[min(ramp) max(ramp)]; %Find minimum and maximum to
    correct for offset and amplitude
ramp = 2*(ramp-sum(temp)/2)/diff(temp); %Ramp normalised
   and shifted to 0
cover = 0.9; %Defines how much of a single ramp is used
ramprange = find(abs(ramp)<=cover);%Indices of ramp
   within cover
rampedges = find(diff(ramprange)>10);%At the edge of a
   ramp the next few samples are not within the cover
```

```
8  rampidx = [ramprange(rampedges(1:end-1)+1) ramprange(
       rampedges(2:end))]; %Start and end of full ramps
9  rampdir = sign(ramp(rampidx(:,2))); %Direction of each
       ramp rising ramp is positive at end and falling
       negative
10 %Analyse the interference pattern of either one or two
       detectors
11 ipat = diff(dataDC(:,1:2),1,2);
12 temp =[min(movmean(ipat,2e2)) max(movmean(ipat,2e2))]; %
       Minimum and maximum for shifting and stretching
13 ipat =  2*(ipat-sum(temp)/2)/diff(temp); %Interference
       pattern centred aroudn 0 and stretched to amplitude 1
14 AngleHilbert = angle(hilbert(ipat)); %Numercially
       efficent way to estimate angle if ipat is good enough
15 %Analyse the phase for each ramp
16 itR = 1; %Index of ramp under investigation for loop
17 ipatR = ipat(rampidx(itR,1):rampidx(itR,2)); %Full
       interference pattern for the ramp region
18 AHR = unwrap(AngleHilbert(rampidx(itR,1):rampidx(itR,2)))
       ; %Unwraped angle of Hilbert transform within the ramp
        region
19 Tfit = (1:size(ipatR,1))/DCrate; Tfit=Tfit'-mean(Tfit);%
       Some time axis for plotting or fitting a function
20 PHR = polyfit(Tfit,rampdir(itR)*AHR,5); %Polynomial fit
       of the unwrapped angle considering the slope
21 %Alternative method is fitting a sine with nonlinear
       phase of some order the interference pattern
22 PhaseFitFunction = fittype('offset+amplitude*sin(
       phaseOffset+a*x+b*x^2+c*x^3+d*x^4)','independent','x')
       ;
23 %Long code required as initial start values and
       boundaries have to be estimated or given. Usually
       requires some manual adjustments to obtain a
       polynomial function for the phase
24 fitres = fit(Tfit,ipatR,PhaseFitFunction,'start',[70 1 0
       0 0 0 0]);
25 PHS = [fitres.d fitres.c fitres.b fitres.a fitres.
       phaseOffset]; %Polynom from fitting
```

I.1.4 Squeezing estimation

The previous code segments have shown how data is read, how variances are assigned to points in time and how each point in time is assigned a phase based upon the interference pattern. For each ramp, the slope and starting value of the phase have to be considered to avoid obvious errors in the evaluation. The MATLAB code for this requires the consideration of a few cases as well as for loops to iterate over all ramp periods. Those are usually case-specific and hence are not of particular interest here.

A nonlinear fit has to be used as the phase of the evaluated interference pattern is not linear to the phase for the analysed off-resonant sidebands. The phase dependent variance pattern itself has to be π-periodic and for a squeezed state and the following function can be fitted to the data:

$$\mathrm{Var}\left(\varphi_{\mathrm{est}}\right) = \sin^2\left(\varphi_0 + c_1 \cdot \varphi_{\mathrm{est}} + c_2 \cdot \varphi_{\mathrm{est}}^2 + \ldots\right) \cdot \mathrm{Var}_- + \ldots \tag{I.1}$$

$$\ldots \cos^2\left(\varphi_0 + c_1 \cdot \varphi_{\mathrm{est}} + c_2 \cdot \varphi_{\mathrm{est}}^2 + \ldots\right) \cdot \mathrm{Var}_+ \tag{I.2}$$

For example, this can be done for one rising or falling ramp to provide an estimation or a window of π or 2π is moved over the pattern. Whenever the variance window ends with large or small variances, *i.e.* close to the minimum or maximum value, the fit function tends to assume that the variance further increases or decreases. If the overall ramp is used, this requires a good starting point and boundaries for the parameters as otherwise the fit function converges to a wrong point. Likely for many of the several ramps per file, individual starting values have to be chosen by hand. For 28 files as shown in appendix K, this is not practical.

By moving a window over the data, the effort for fitting is increased but the results of the multiple fits can be analysed automatically by simply removing those intervals for which the fit converged to a wrong result. Hence, the moving window was usually preferred where only the values of Var_- and Var_+ were of interest.

No code is provided on this part as it would include several case specific guesses for start values of the fit, iterations over several ramps and files, as well storing the obtained information. With informative comments, this would fill several pages with trivial lines of code.

I.1.5 Phase-sorting and Wigner function

The code written for sorting the phase and using the inverse Radon transform to obtain a Wigner function is far more relevant for the processing of the data. The inverse Radon transform requires the projections for multiple phase intervals[2].

[2] Equal to the measured quadrature angles.

Depending on the required resolution, all data points (usually several million) have to be sorted to those phase intervals. For each phase interval, an equal number of points should be used. The trivial way to achieve this would be to add each data point to one array that contains all other data points of the corresponding phase interval. For each data point, this requires assigning a new array in memory. This array has to be one element larger than the previous array for the same phase interval. Then, the old array as well as the new data point have to be copied into this array. Finally, the arrays for each phase interval are cut to the size of the smallest array, or smaller depending on the requirements. For the cutting, a random selection of data points should be omitted. This process is not very efficient and can be optimised by a large factor with minor efforts.

The first step is to normalise the subtracted trace SUBARRAY to the vacuum[3] and create one array with all phases of each measurement[4].

```
SUBARRAY; %Array with normalised subtracted channel}
SF  = ACrate/DCrate; %Ratio between both sampling rates
ramprange; %Array with the absolute position of each DC-
   sample within the ramp as previously determined
PhaseDC; %All phases of each DC-sample within the ramp (
   same length as ramprange)
[PhaseDC, sortidx] = sort(wrapToPi(PhaseDC)); %Project
   all phases to the range of -pi to pi, sort them and
   store the sorting order
nPhases = 180; %Number of phases
pax = -pi:2*pi/nPhases:pi; pax(1)=[]; %Array with the end
    of all phase intervals.
StartStopIdx = ones(nPhases,2); StartStopIdx(end,2)=size(
   sortidx,1); %Array for start and stop indices of the
   intervals with first( and last value for convenience
   only)
for it = 1:nPhases-1%For loop for phase intervals
    StartStopIdx(it+1,1) = find(PhaseDC>pax(it),1); %Find
        the beginning of the next interval
    StartStopIdx(it,2) =StartStopIdx(it+1,1)-1; %Last
       interval ends directly prior to the next. Could
       also be done after the loop
end
nSamples = diff(StartStopIdx,1,2); %Available samples per
    interval
```

[3] For the correct normalisation of the Wigner function, the vacuum variance has to be $\frac{1}{2}$.

[4] Depending on the required accuracy, a nonlinear correction has to be applied to each estimated fit in order to obtain a π-periodic variance pattern. This is due to the influence of the separation resonator.

```
14 nPoints = min(nSamples)+1; %Number of points is minimum
   of samples
15 SUBsorted = zeros(nPhases,nPoints*SF); %Empty array for
   all subtracted data
16 for it = 1:nPhases
17     selected = SF*ramprange(sortidx(1+StartStopIdx(it,1)+
          randperm(nSamples(it),nPoints)))+((-SF+1):0); %
          Random selection of points for this interval.
          ramprange and sortidx are used to find the
          corresponding fast fluctuation points and adding a
           vector makes it a nPoints x SF big array;
18     SUBsorted(it,:) = SUBARRAY(selected(:)); %Write the
          data to the array
19 end
20 VarSorted = var(SUBsorted,[],2); %Calculate the variance
   of each phase if needed
21 %% Reconstruct Wigner-function
22 rangeHist = ceil(max(VarSorted(:))); %Upper limit for
   used histogram
23 wRes  = 201;%Points per axis of reconstructed Wigner
   function
24 xs = linspace(-rangeHist,rangeHist,wRes); %One axis
25 pphi = hist(SUBsorted',xs);%Histograms for the phases
26 w = iradon(pphi,4,0.55,Wigres); %Inverse radon for Wigner
    function
27 w = w./sum(w(:))/mean(diff(xs))^2; %Proper normalisation
   to one and unit area of axis
28 figure;  s = pcolor(xs,xs,w); s.EdgeColor = 'none'; axis
   equal; colorbar; %Simple plot
```

This code reduced the time required to read and write in the memory and takes less than 0.2 s to sort 20 million data points, compared to above 5 min without pre-aligned memory.

I.2 Pulse propagation

Within this code, the spectral resolution is derived from the parameters of the SLM and the time domain is created accordingly. Quantum noise is added in the spectral domain to obtain a Poissonian distribution for the average photon number of the pulses. The SSFM itself is based around the centre frequency and a shift in centre frequency does not change the pulse propagation. In the quantum world, each allowed frequency has the vacuum energy corresponding to half the energy of a single photon. This gives rise to an asymmetric noise floor in the spectrum which may influence the numerical pulse propagation. For the chosen parameters, no obvious disturbances were observed but this has to be kept in mind.

```
DF = '../exportfolder/'; %Name of basefolder for export
%% Input parameters
Pin = 12e-3; %Average output power in Watt
nP = 1e4; %Number of pulses to propagate
Lc = 1559.7e-9; %Central wavelength
Lmax =20; %Length of fibre
Lsteps = 2^11; %Number of steps
tFWHM = 200e-15;  %FWHM of pulse
frep = 80e6; %Laser rep rate required for pulse energy
   from power
dw = 2*pi*60e9/9; %Spacing of angular frequencies one SLM
    pixel has ~0.6nm or ~60GHz (@1560nm) dived of
   simulation points per pixel (here 9)
wSpan = 2*pi*100e9*250; %Minimum spectral width for
   simulation ~100GHz per nm times approx width in nm
%% Some constants
c0 = 299792458;
h_p = 662607015e-42;     %Plancks constant
h_pB = h_p/2/pi;         %Plancks constant divided by 2 pi
BWF = 2*acosh(sqrt(2)); %Numeric factor for the bandwith
   of a sech pulse
%% Fibre parameters
gk = 1.27e-3;   %Parameter for kerr nonlinearity
beta_2= -23e-27; %Dispersion parameter
Esol = abs(2*beta_2/gk/tFWHM*BWF);%Energy of fundamental
   soliton
Psol = Esol*frep; %Average power for fundamental soliton
   pulse
```

```
Lsol = tFWHM^2/abs(beta_2)/2; %Soliton period
%% Derive other essential parameters from input
wc = 2*pi*c0/Lc; %Central angular frequency
fc =c0/Lc; %Central frequency of pulse
tp = 2^ceil(log2(wSpan/dw)); %Points for simulation
wx = (-tp/2:tp/2-1)'*dw; %Create axis of frequencies
dt = 2*pi/(dw*tp);%Resolution of temporal axis
tf = 2*pi/dw; %Width of simulation time
tx = (-tp/2:tp/2-1)*dt;  %Time axis
WLax = 1e9*(c0./(wc+wx)*2*pi); %Wavelength axis
DL = Lmax/Lsteps; %Length of one interval
QNN = sqrt(h_pB/2/tf*(wc+wx))*tp; %Quantum noise level
   for each spectral component (approx)
save([DF 'NoiseLvl.mat'],'QNN');%Store this information
   for later analysis
%% Create the input pulse shape in time domain
ShapeIn = sech(tx/tFWHM*BWF).^2;
ShapeIn = sqrt(ShapeIn./sum(ShapeIn*dt)/frep); %Pulse
   amplitude for 1 W
%% Test chosen Quantum noise level
Ntest = 1e4; %Number of test pulses
TestEnergy = zeros(Ntest,1);
for it =1:Ntest
    pulse =  (ShapeIn*sqrt(Pin)).'; %Pulse with input-
       power
    pulseW = ifftshift(fft(fftshift(pulse))); % Go to
       spectral domain
    pulseW = pulseW + 1/sqrt(2)*QNN.*(randn(tp,1)+1i*
       randn(tp,1)); %Add noise
    pulse = fftshift(ifft(ifftshift(pulseW))); %Go back
       to time domain
    TestEnergy(it) = sum(abs(pulse).^2)*dt; %Calcualte
       pulse energy
end
%
Nphots = TestEnergy./h_pB/wc; %Calculated number of
   photons per pulse for each test pulse
sqrt(var(Nphots)/mean(Nphots)) %Ideally this should be
   close to 1
%% Pulse propgation functions
```

```
52 %Dispersion for one step
53 dispersion = exp(1i*DL/2*beta_2*wx.^2); dispersion =
      ifftshift(dispersion); %Dispersion for one step
54 dodisp = @(field)ifft(dispersion.*fft(field)); %Function
      to apply dispersion for one step
55 %Half dispersion for start and end (numerically efficient
      )
56 dispersion = exp(1i*DL/4*beta_2*wx.^2); dispersion =
      ifftshift(dispersion);
57 dodispstart = @(field)ifft(dispersion.*fft(field));
58 dispersion = exp(-1i*DL/4*beta_2*wx.^2); dispersion =
      ifftshift(dispersion);
59 dodispend = @(field)ifft(dispersion.*fft(field));
60 %Kerr effect in time
61 dokerr = @(field)field.*exp(1i*DL*gk*field.*conj(field));
62 %% Propagate one noise free reference pulse
63 QNC = QNN*1e1; %Clearance to quantum noise for storing (
      reduce data)
64 QNCB = zeros(Lsteps+2,length(wx)); %Array to compare with
       quantum noise
65 pulse =  (ShapeIn*sqrt(Pin)).';  %Input pulse
66 pulseW = ifftshift(fft(fftshift(pulse))); %-> spectral
67 pulseWS = pulseW; %-> store spectrum for later
68 QNCB(1,:) =abs(pulseW)>QNC;  %Store where signal is above
       QNC
69 %% One reference pulse propagation
70 tic
71 pulse = fftshift(ifft(ifftshift(pulseW))); %->spectrum
72 pulse = dodispstart(pulse); %Half disp
73 for it = 1:Lsteps %Loop over fibre intervals
74     pulse = dokerr(pulse); %Do Kerr effect
75     pulse = dodisp(pulse); %Do dispersion
76     pulseW = ifftshift(fft(fftshift(pulse))); %->spectrum
77     QNCB(it+1,:) =abs(pulseW)>QNC; %Store where signal is
          above QNC
78
79 end
80 pulse = dodispend(pulse); %Reverse half a dispersion step
81 pulseW = ifftshift(fft(fftshift(pulse))); %Spectrum
```

```
QNCB(end,:) = abs(pulseW)>QNC; %Store where signal is above QNC
toc %Time for one pulse
%% Find where signal is useful to store to reduce the amount of data
impIDXt = sum(QNCB)>0;
impIDX = (find(impIDXt==1,1,'first')):(find(impIDXt==1,1,'last'));
%% Store the reduced data
WLs = WLax(impIDX);
SpekIn = pulseWS(impIDX);
SpekOut = pulseW(impIDX);
QNNr = QNN(impIDX);
ControlD = [WLs SpekIn SpekOut];
save([DF 'Refprop.mat'],'ControlD','QNNr'); Reduced data exported
%% Do the noisy part by repeating from code above
nP = 1e4; %Number of pulses
Noisy = zeros(nP,length(impIDX)); %Array for output pulses
tic
for it2 = 1:nP
    pulse =  (ShapeIn*sqrt(Pin)).';
    pulseW = ifftshift(fft(fftshift(pulse)));
    pulseW = pulseW + 1/sqrt(2)*QNN.*(randn(tp,1)+1i*randn(tp,1));
    pulse = fftshift(ifft(ifftshift(pulseW)));
    pulse = dodispstart(pulse);
    for it = 1:Lsteps
        pulse = dokerr(pulse);
        pulse = dodisp(pulse);
    end
    pulse = dodispend(pulse);
    if mod(it2,50)==0 %Once in a while output something to see progress
        [100*it2/nP toc]
    end
    pulseW = ifftshift(fft(fftshift(pulse)));
    Noisy(it2,:) = pulseW(impIDX);
end
```

```
115 save([DF num2str(nP) '_pulses.mat'],'Noisy'); %Save
    results
```

I.3 Pulse analysis

This section provides a brief overview of the fundamental code used in the analysis of the simulated datasets. This code allows for similar analysis as in the actual experiment. It can include the dispersive effects of the separation resonator as well as GAWBS. Additionally any changes, such as a chirp, a delay or spectral attenuation, can be applied to the LO or SI pulse.

```
1  DF = '../FolderWithData/'; %Where the propagated pulse is
       stored
2  c0 = 299792458; %Useful constant
3  BNref = 8.76e-10;%Reference variance of GAWBS
4  %% Load data stuff
5  load([DF 'NoiseLvl.mat']);
6  load([DF 'Refprop.mat']);
7  load([DF '10000_pulses.mat']);
8  %% Constants and parameters
9  L = 2; %Length of fibre in simulation
10 anaP = 1e4; %Used to reduce the number of pulses if
       needed
11 BN = sqrt(L*BNref); %Brillouin noise for fibre length at
       room temperature
12 %%
13 WL = ControlD(:,1); %Wavelength axis
14 LOI = ControlD(:,2); %Input pulse
15 LO = ControlD(:,3); %Output pulse
16 Noisy = Noisy(randperm(length(Noisy),anaP),:); %Reduced
       Noisy array
17 LOn = mean(Noisy,1).';
18 oms = 2*pi*c0./WL*1e9; %Angular frequency axis
19 omc = sum((abs(LOn).^2)'*oms)/sum((abs(LOn).^2)); %
       Central angular frequency
20 omspace = oms-omc; %Shifted angular frequncy axis
21 WLC = c0/omc*2*pi; %Central wavelength
22 %% Calculate eigenmodes
23 cmoB =cov((NoisyB.'));
```

```
[eob,dob] = eig(cmoB);
EM1 = eob(:,end); %First eigenmode
EM2 = eob(:,end-1); %Second eigenmode
PNorm = sqrt(sum(abs(LOI).^2));%Factor for appropriate
   optical power
EM1 = conj(EM1)*PNorm; %Bring to same power as initial
   pulse
EM2 = conj(EM2)*PNorm;%Bring to same power as initial
   pulse
%% Include resonator
R = 0.965; %Coupling mirrors reflectivity
eta = 0.998; %End mirror reflectivity
[~,Fin] = ResTrans(0,R,R,eta); %Finesse is one return
   value of a custom function for resonator transmission;
Resdisp =  -1e-15*omspace; %Detuning of resonator due to
   dispersion (Example for linear dispersion)
Rdetu = 0; %Additional length detuning of resonator (
   usful for example if dispersion requires adjustment
   for maximum power transmission)
TransR = ResTrans(Resdisp+2*pi*Rdetu./WL ,R,R,eta); %
   Complex tranmission factor for each component
RefR = ResRefl(Resdisp+2*pi*Rdetu./WL ,R,R,eta); %Complex
    reflection factor for each component
LOt = TransR.*LOn; %Transmitted LO from Resonator
%% Create a phase detuning axis
mindetu = -pi/2;
maxdetu  = pi/2;
detstep = pi/180;
detus = mindetu:detstep:maxdetu; %Detuning in nm;
Ndetu =  length(detus);
%% Create displaced noisy fields and LOs
AMpres = (1-RefR).*LOn; %Amplitude of transmitted field
   inside the resonator
NoisyA = (Noisy-LOn.').'; %Remove average pulse to shift
   noisy array to 0 coherent amplitde
NoisyR = (Noisy-LOn.').'+RefR.*LOn; %With reflected
   carrier pulse
NoisyB = (Noisy-(AMpres.*exp(1i*BN*randn(1,size(Noisy,1))
   )).').'; %Include Brillouin noise
```

```
%For other temperatures BN need to be adjusted accordingly
LOuse = LOI; % Use the inut pulse as LO (for example);
detuLO = 1e-5;% A delay for the LO
detchirp = 1e-27;% A chirp for the LO
LOuse = LOuse.*exp(1i*2*pi*detuLO./WL); %Apply the delay
LOuse = LOuse.*exp(1i/2*detchirp*omspace.^2); %Apply the chirp
%Additional manipulations by SLM can be implemented or one simply uses the calcualted eigenmodes
NoisyAn = NoisyB; %Select which noise should be analysed;
%% Do the actual phase detuning and variance calculation
%Or instead of phase one could use delay with nm resolution
VarsEval = zeros(size(detus)); %Estimated variances
Ipat = zeros(size(detus)); %Difference in mean "photon" number.
for it = 1:length(detus)
    %%
    Lonoise =1/sqrt(2)*QNNr.*(randn(size(NoisyA))+1i*randn(size(NoisyA))); %Noise of LO for vacuum reference for each step (Alternatively just once outside the loop)
    LOit = LOuse*exp(1i*detus(it))+Lonoise; %Shift phase and add noise
    D1I = sum(abs(LOit + NoisyAn).^2); %Measured "photons" by detector 1
    D2I =sum(abs(LOit - NoisyAn).^2); %Measured "photons" by detector 2
    add = D1I+D2I; %Subtracted channel
    sub = D1I-D2I; %Added channel
    VarsEval(it) = var(sub)/var(add);
    Ipat(it) = mean(sub);
end
%By looping over different detunins/chirps or LO-modes the simulated data can be analysed similar to the experimental condition.
```

J. Thermal shielding

This chapter of the appendix gives a visual demonstration of the setup used to submerge the optical fibre in LN_2.

Figure J.1a shows one of the first implementations where a bare fibre is coiled and connected to a carrier plate. The carrier plate is placed in a plastic tray and weighted. The plastic tray itself is placed on a layer of foam inside a second tray to improve the insulation. Additional material is used to direct some of the cold air away from the optical setup. As LN_2 is poured into the tray, the fibre is cooled down to liquid nitrogen temperature and held there for several minutes.

To submerge a large portion of the optical fibre, the assembly was placed close to the used fibre couplers. As the diameter of the light-guiding core of the fibre is 10 µm and it is held in place by a metal fibre chuck, hold by an optical mount with two springs, this assembly is highly affected by the cold air. This setup required frequent realignment of both fibre couplers every few minutes. Nevertheless, the measured anti-squeezing was reduced and squeezing was not impeded. Hence, a more sophisticating solution for cooling the fibre was built.

By replacing the bare fibre with a patch cable and collimator assembly (figure J.1b), the alignment between fibre and coupler became one mechanical assembly. As a result, the amount and frequency of the required realignment were reduced. By placing these couplers in 3D-printed houses (figure J.1b), the influence of the cold air was further reduced.

Instead of using two arbitrary plastic trays, a round plastic container for the coiled fibre was obtained. An additional 3D-printed enclosure was used to place the fibre container on the optical table. The thick 3D-printed wall of the enclosure is filled with a hollow diamond structure for increased insulation. The contact surface between the round plastic container and the 3D-printed enclosure is reduced by a support structure on which the fibre container was placed inside the enclosure. A paper pipe guides cold air away from the enclosure of the optical table which is required as otherwise the cold air would escape through the feedthrough holes for the patch cable and at the top.

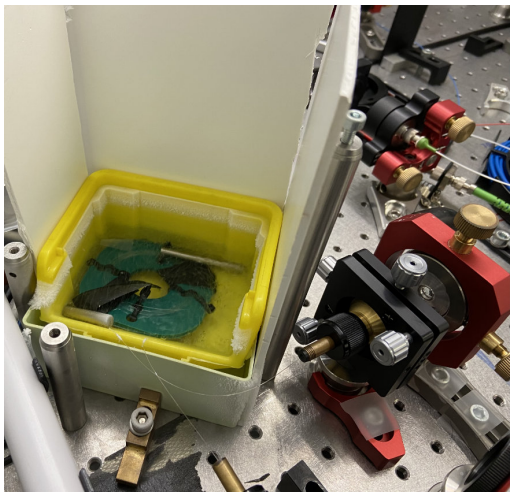

(J.1a) One of the first implementations used to submerge a bare fibre in LN_2 with additional shielding from cold air for the optical components.

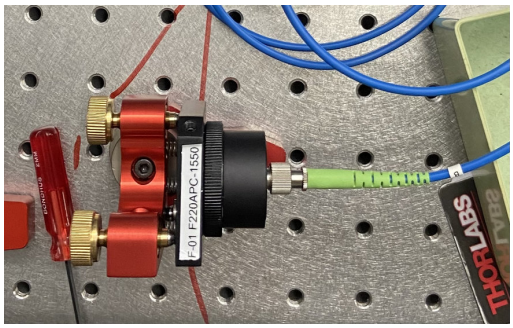

(J.1b) Fibre patch cables and sturdy mounts improve mechanical stability.

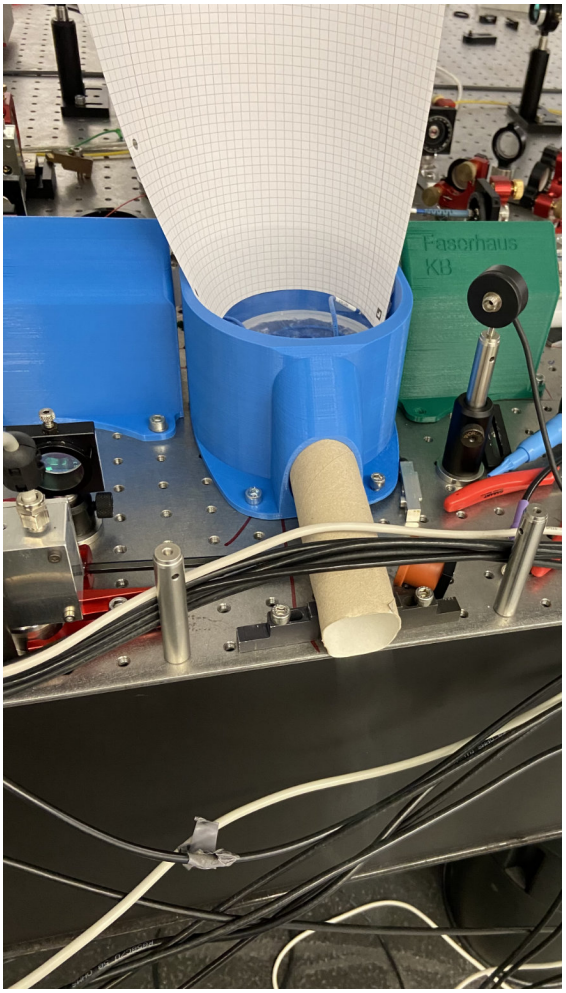

(J.1c) The container with the fibre patch cable is placed in the enclosure and cold air is guided of the optical table.

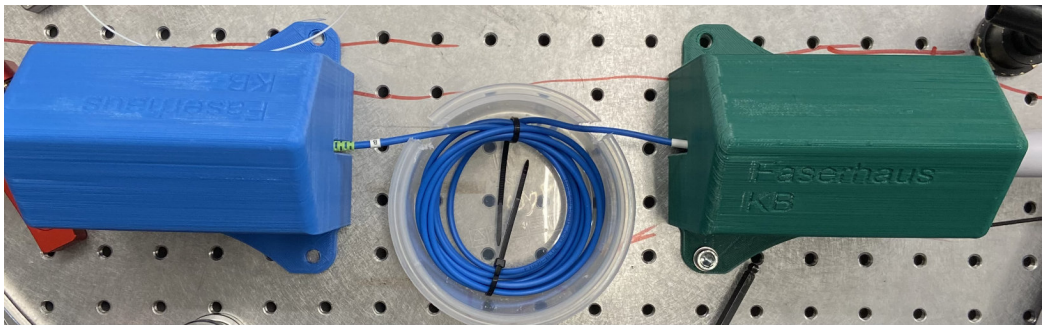

(J.1d) Fibre couples are additionally shielded from cold air.

Figure J.1 Thermal shielding for GAWBS measurements and improvements in mechanical stability

K. Results of GAWBS measurement

Within this section of the appendix, the numerical values for the estimated power-dependent squeezing and anti-squeezing from measurements at room temperature (293 K) and LN_2 temperature (77 K) are given. The graphical representation of the overall results can be seen in figure 6.3b. Exemplary graphical representation of individual measurements are illustrated in figure 6.3a. The temperature-dependent evaluation of GAWBS phase noise (figure 6.5) is based on the values stated within this section.

					$T = 77\,\mathrm{K}$		$T = 293\,\mathrm{K}$	
P_{opt} (mW)	Var_- [dB]		Var_+ [dB]		Var_-		Var_+	
4.0	−0.57	−0.30	5.38	7.95	0.88 ± 0.03	0.93 ± 0.04	3.45 ± 0.02	6.2 ± 0.2
4.5	−0.60	−0.37	5.82	8.44	0.87 ± 0.03	0.92 ± 0.04	3.82 ± 0.10	7.0 ± 0.2
5.0	−0.69	−0.41	6.21	8.93	0.85 ± 0.04	0.91 ± 0.04	4.17 ± 0.22	7.8 ± 0.3
5.6	−0.76	−0.45	6.77	9.50	0.84 ± 0.04	0.90 ± 0.05	4.75 ± 0.21	8.9 ± 0.3
6.4	−0.87	−0.54	7.36	10.1	0.82 ± 0.03	0.88 ± 0.05	5.45 ± 0.26	10.2 ± 0.4
7.0	−0.97	−0.60	7.91	10.7	0.80 ± 0.05	0.87 ± 0.06	6.2 ± 0.3	11.6 ± 0.5
8.0	−1.11	−0.70	8.72	11.3	0.77 ± 0.04	0.85 ± 0.05	7.5 ± 0.4	13.8 ± 0.6
8.9	−1.24	−0.81	9.44	12.1	0.75 ± 0.04	0.83 ± 0.05	8.8 ± 0.5	16.1 ± 0.7
10.0	−1.40	−0.96	10.3	12.8	0.72 ± 0.05	0.80 ± 0.05	10.7 ± 0.5	19.1 ± 0.9
11.2	−1.60	−1.15	11.3	13.7	0.69 ± 0.04	0.77 ± 0.07	13.4 ± 0.7	24.2 ± 1.1
12.6	−1.83	−1.35	12.5	14.7	0.66 ± 0.05	0.73 ± 0.05	17.7 ± 0.9	29.2 ± 1.4
14.0	−2.04	−1.61	13.6	15.7	0.62 ± 0.05	0.69 ± 0.06	23.1 ± 1.3	37.0 ± 2.0
15.8	−2.29	−1.61	15.2	16.5	0.59 ± 0.07	0.69 ± 0.08	33.0 ± 2.0	44 ± 3
17.0	−2.41	−1.77	16.3	17.4	0.57 ± 0.05	0.66 ± 0.07	43 ± 3	55 ± 4

Table K.1 Numerical values obtained from GAWBS measurement.

The used error estimate in table K.1 is based on the results from multiple fits. A window of π was moved across the estimated phases (figure 5.10). Due to the additionally required nonlinear fit for the phase, the individual fits for one measurement scatter, leading to the estimated error. These error intervals overlap for several consecutive optical powers as well as the hot and cold measurements. Nevertheless, obtained results can be well related with each other to obtain the results (figure 6.4). This indicates that the estimated statistical error is too large. To improve on the actual error estimate, more data for each measurement

is required. The stated error does not account for any systematic errors due to unknown separation resonator detuning, dispersive effects and mode matching.

L. SLM information

This chapter provides calibration curves for the used SLM. The used model (*SLM-128-D-NM*) was manufactured by *Cambridge Research and Instrumentation Inc.* and it was acquired several years ago during a PhD thesis [190]. Meanwhile, the website of the manufacturer is no longer available and the product seems to be continued by *Meadowlark Optics*. The curves provided here are calculated from the the calibration data which was originally provided by the manufacturer for the specific used unit.

For each pixel of both 128 pixel masks, a 12-bit integer can be handed to the driving electronics. Absolute modulation is stated for 633 nm (figure L.2a). For other wavelengths, the modulation can be calculated using the provided values for relative modulation (figure L.2b).

The resulting phase modulation is calculated and displayed in figure L.2c. For the actual relevant wavelengths used in the experimental setup, a detailed view is provided in figure L.2d. From 1530 nm to 1590 nm, all wavelengths can be shifted by a common mode phase of at least $3.8\,\pi$. Taking into account that a shift of π is needed for amplitude modulation, this phase shift is reduced to $2.8\,\pi$.

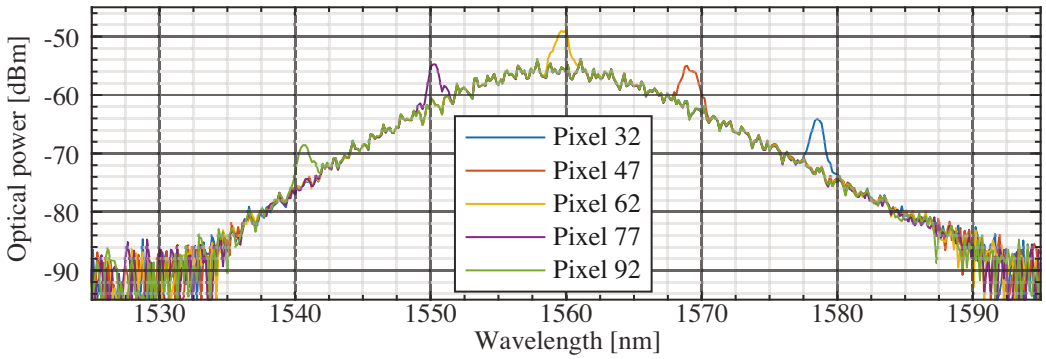

(L.1a) Spectra measured after the SLM.

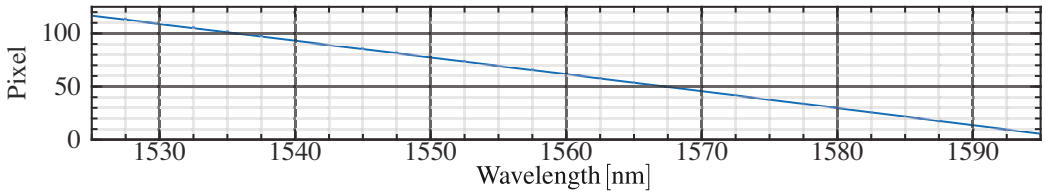

(L.1b) Relation fitted between pixel number and wavelength.

Figure L.1 Calibration measurement to assign each SLM pixel the corresponding wavelength.

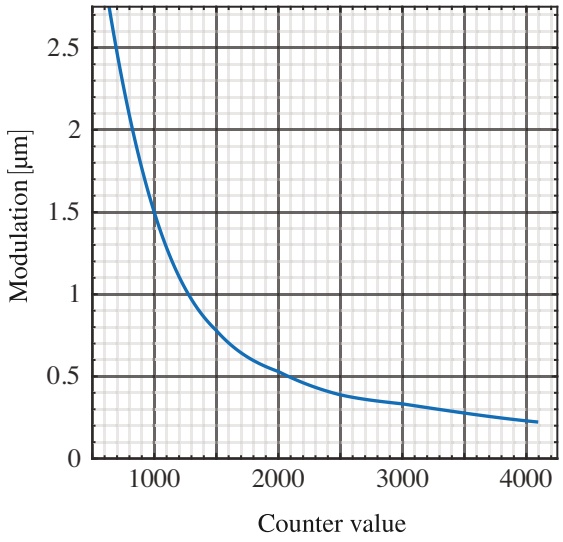

(L.2a) Modulation for 633 nm depending on drive voltage counter

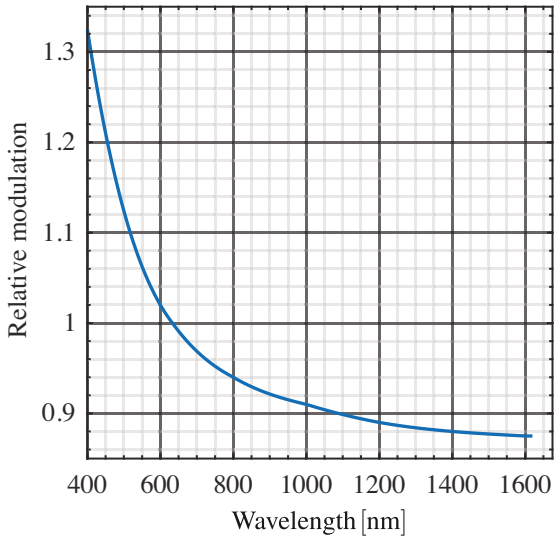

(L.2b) Wavelength-depending relative modulation

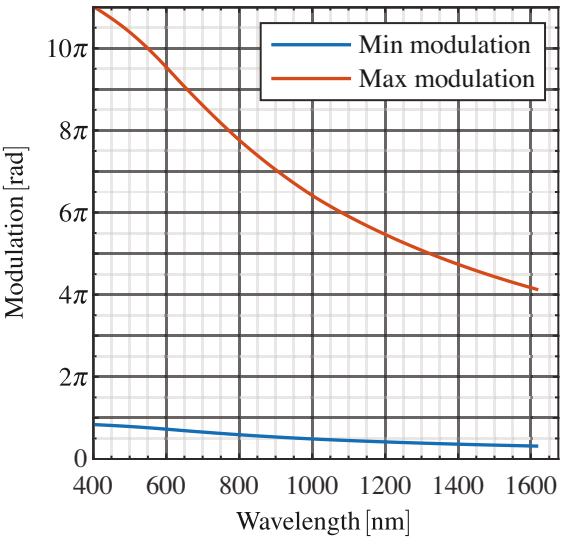

(L.2c) Wavelength-dependent phase modulation range

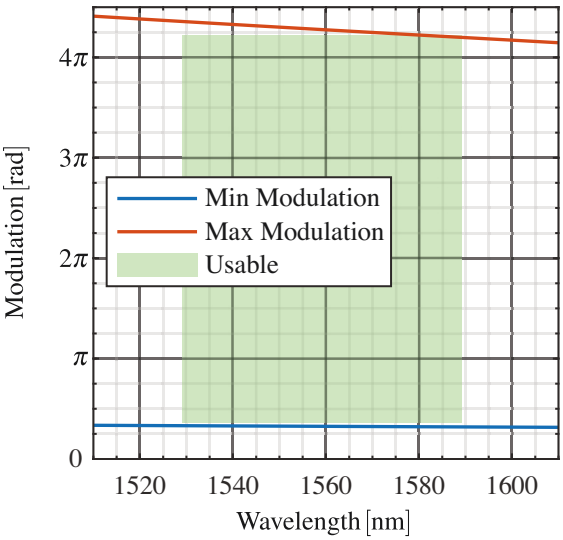

(L.2d) Relevant wavelength range of **(L.2c)**

Figure L.2 Provided calibration data is presented in **(L.2a)** and **(L.2b)**. The calculated achievable phase modulation is illustrated in **(L.2c)** and **(L.2d)**.

M. Entanglement data and simulation

Within this chapter of the appendix, a visual representation of the measured data and its evaluation for three-mode entanglement is provided. Furthermore, simulated data is evaluated with GAWBS for different temperatures for two modes as well as for all combinations of three modes. For each measurement, the phase-sorted variances are presented as well as the used inseparability criteria (section 7.1.1). The modes in the simulation were, as in the experimental setup, derived from the initial pulse. They were similarly divided and neither additional chirp nor temporal detuning were considered. The red scale, in the range from 2 to 2.35, implies a violation of the Duan limit for separability if one mode has two times the intensity of the other mode.

M.1 Summarised results for three modes

		Temperature [K]							
Modes	Limit	0	100	200	300	400	500	Measured	Limit (est.)
1 [RB] [G]	2.35	**1.99**	**2.30**	2.53	2.72	2.89	3.04	3.00	2.20
2 [R] [BG]	2.35	**1.61**	**2.10**	2.49	2.84	3.14	3.42	2.19	2.10
3 [RG] [B]	2.35	**1.51**	**2.02**	2.42	2.77	3.07	3.35	4.01	2.86
4 [R] [G]	2	**1.77**	**1.89**	**1.96**	2.02	2.05	2.07	2.31	2.12
5 [G] [B]	2	**1.71**	**1.87**	**1.95**	2.02	2.05	2.08	**1.99**	2.01
6 [R] [B]	2	**1.34**	**1.55**	**1.70**	**1.80**	**1.87**	**1.89**	2.19	2.17

Table M.1 Inseparability criteria for simulated data summarised with three modes.
For three modes, the modes are indicated by their position in the spectrum, *i.e.* [RB] is the combination of the relative **R**ed and **B**lue parts of the spectrum while centre is referred to as **G**reen.
For each configuration, the limit, depending on the power ratios of both modes, is stated. Bold font highlights where inseparability can be verified. With increasing temperature/GAWBS, the inseparability can no longer be verified for all modes with the chosen criteria.
Values estimated from measured data and the corresponding limits are stated in the last two columns.

M.2 Two-mode simulation

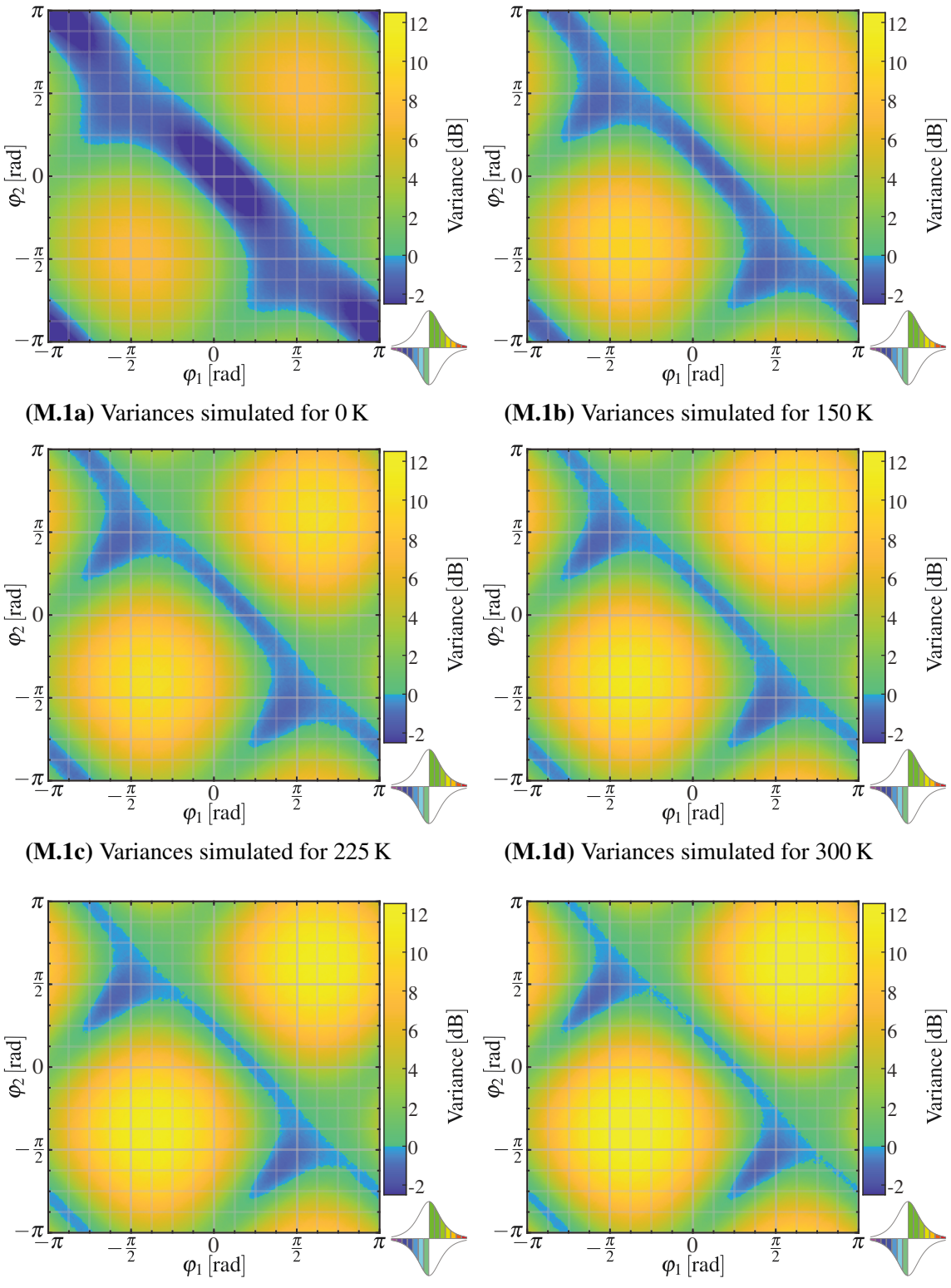

(M.1a) Variances simulated for 0 K

(M.1b) Variances simulated for 150 K

(M.1c) Variances simulated for 225 K

(M.1d) Variances simulated for 300 K

(M.1e) Variances simulated for 375 K

(M.1f) Variances simulated for 450 K

Figure M.1 Simulated variances for two modes with GAWBS for different temperatures

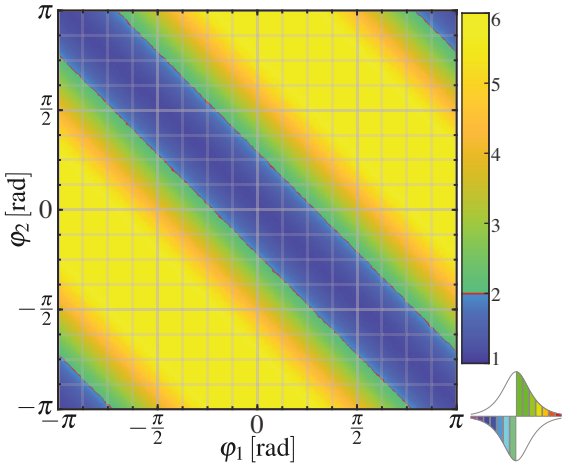

(M.2a) Comparison with Duan limit simulated for 0 K

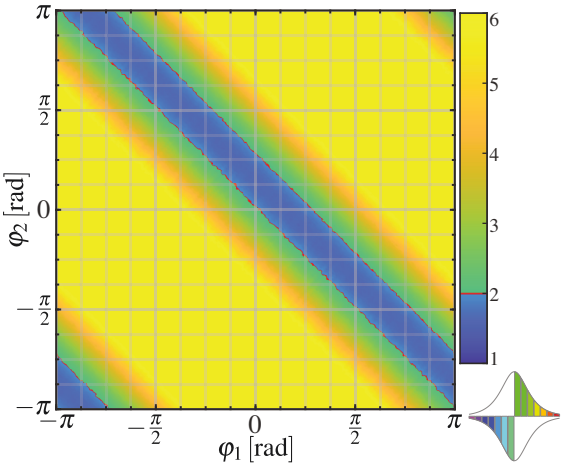

(M.2b) Comparison with Duan limit simulated for 150 K

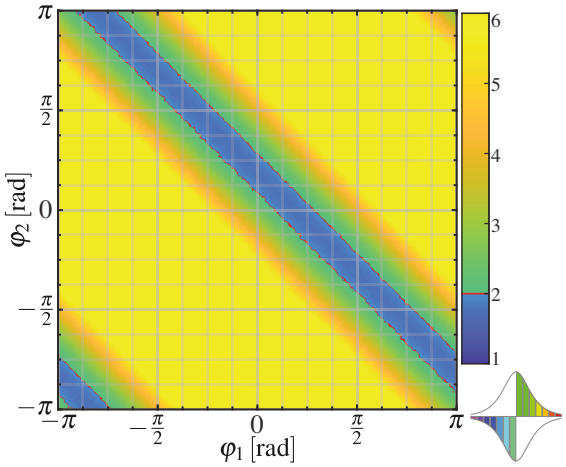

(M.2c) Comparison with Duan limit simulated for 225 K

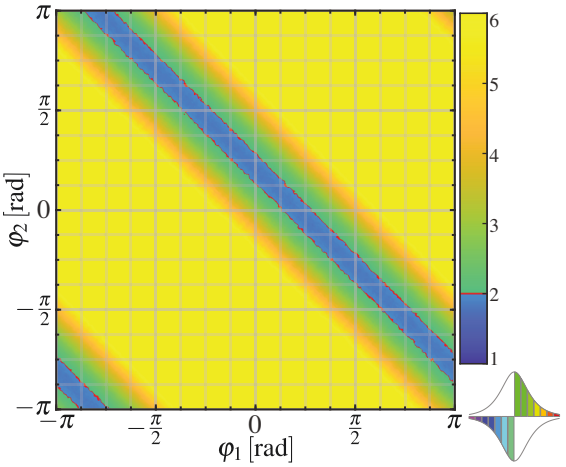

(M.2d) Comparison with Duan limit simulated for 300 K

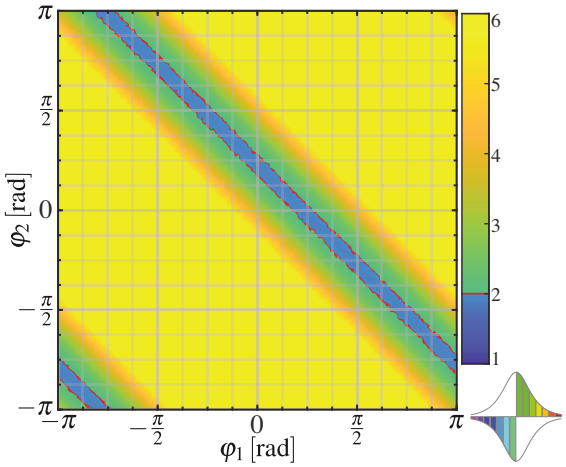

(M.2e) Comparison with Duan limit simulated for 375 K

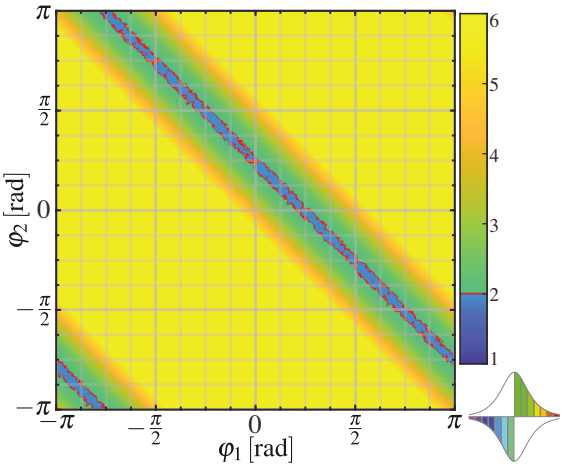

(M.2f) Comparison with Duan limit simulated for 450 K

Figure M.2 Comparison to the Duan limit for inseparability for simulated data using two modes including GAWBS for different temperatures

M.3 Three-mode measurement

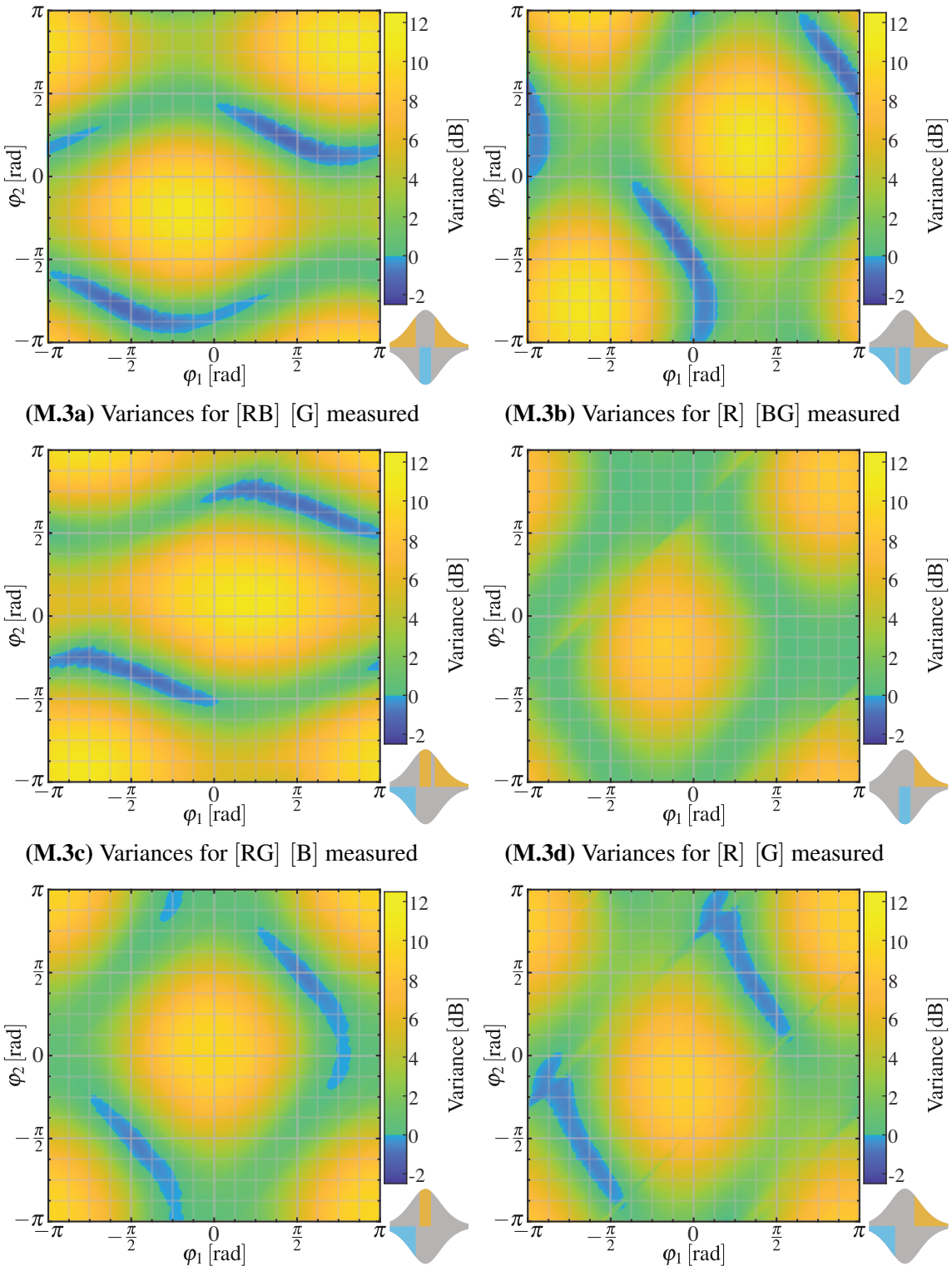

(M.3a) Variances for [RB] [G] measured

(M.3b) Variances for [R] [BG] measured

(M.3c) Variances for [RG] [B] measured

(M.3d) Variances for [R] [G] measured

(M.3e) Variances for [G] [B] measured

(M.3f) Variances for [R] [B] measured

Figure M.3 Measured variances for three-mode measurement at room temperature

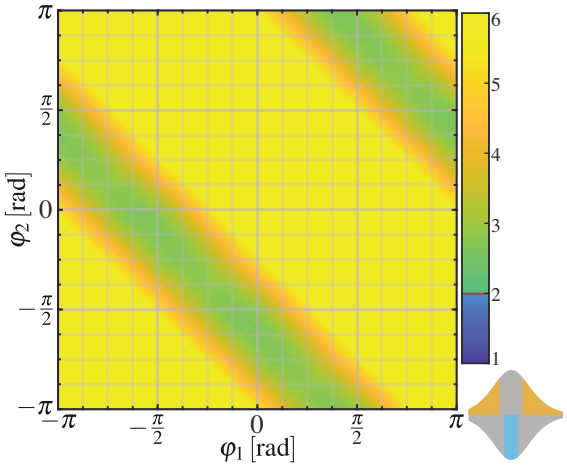

(M.4a) Comparison with Duan limit for [RB] [G] measured

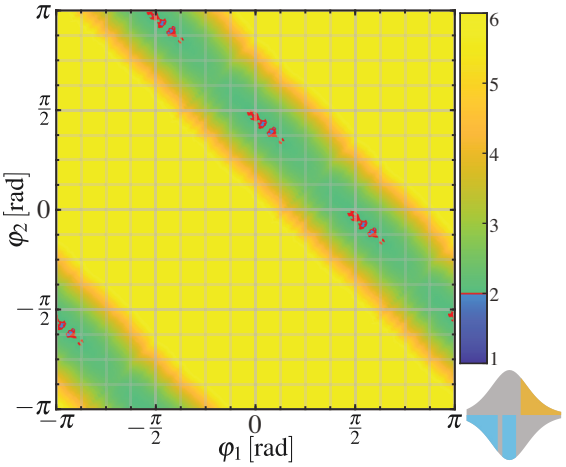

(M.4b) Comparison with Duan limit for [R] [BG] measured

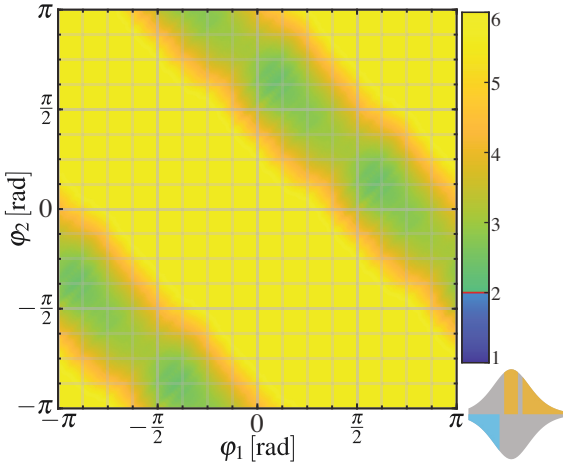

(M.4c) Comparison with Duan limit for [RG] [B] measured

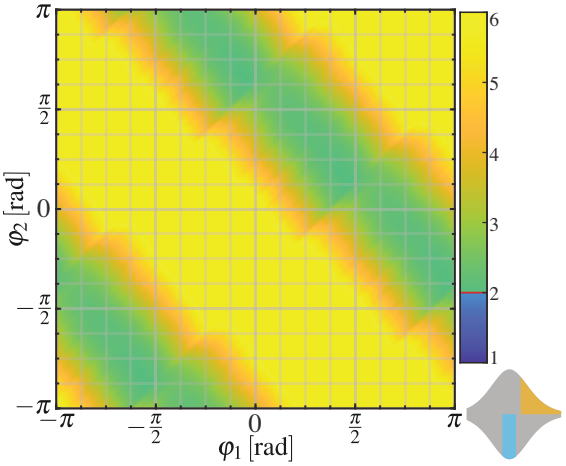

(M.4d) Comparison with Duan limit for [R] [G] measured

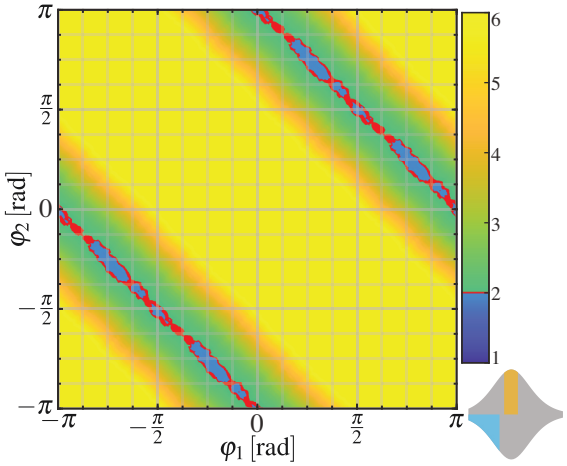

(M.4e) Comparison with Duan limit for [G] [B] measured

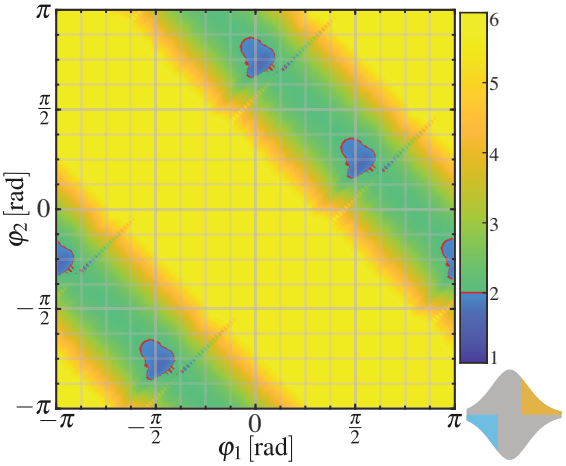

(M.4f) Comparison with Duan limit for [R] [B] measured

Figure M.4 Comparison to the Duan limit (estimated from the measured mode intensities) for inseparability for the performed three-mode measurement

M.4 Three-mode simulation

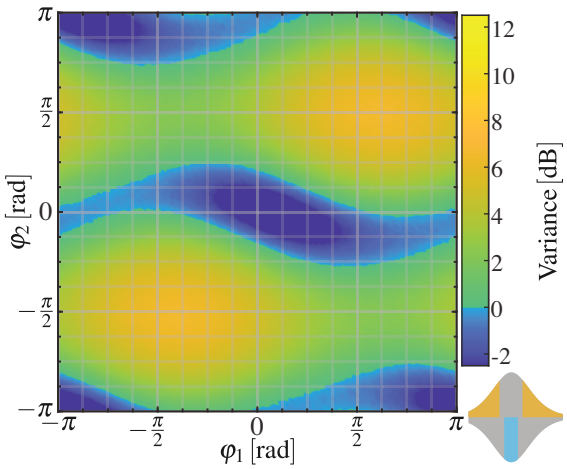

(M.5a) Variances for [RB] [G] at 0 K

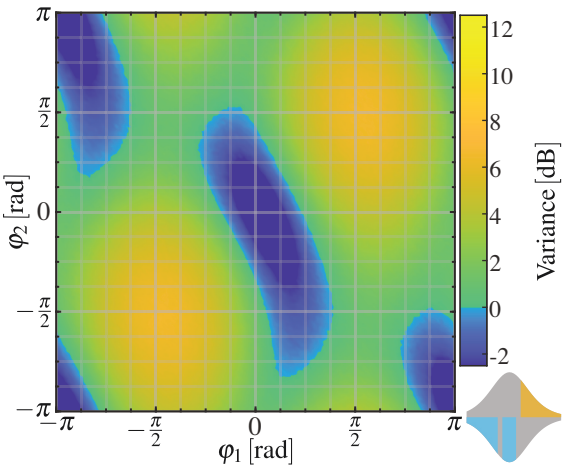

(M.5b) Variances for [R] [BG] at 0 K

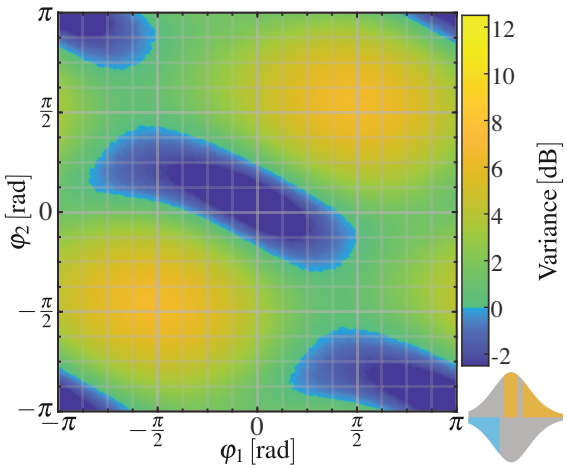

(M.5c) Variances for [RG] [B] at 0 K

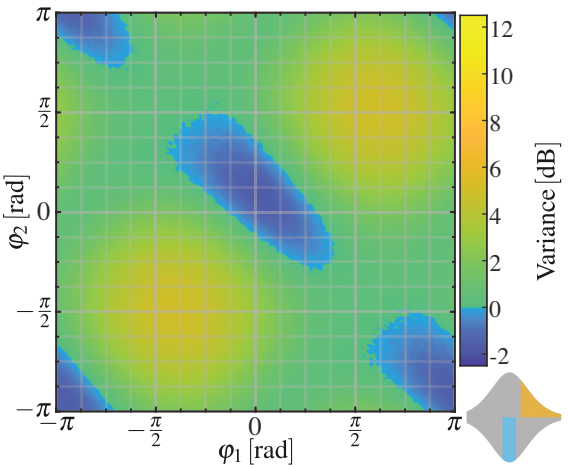

(M.5d) Variances for [R] [G] at 0 K

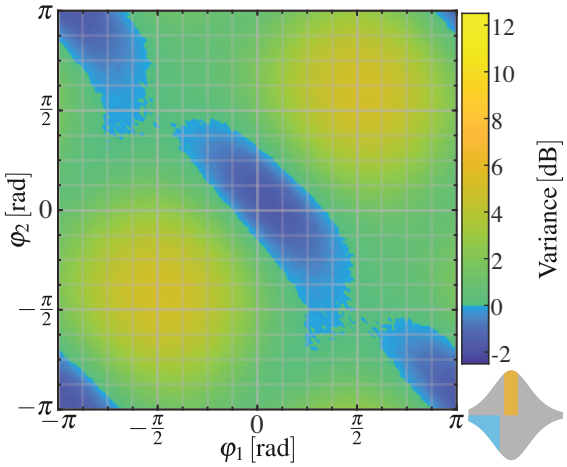

(M.5e) Variances for [G] [B] at 0 K

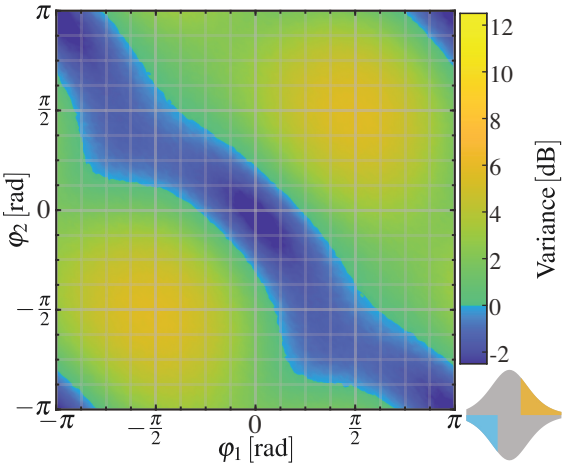

(M.5f) Variances for [R] [B] at 0 K

Figure M.5 Simulated variances for three-mode measurement at 0 K

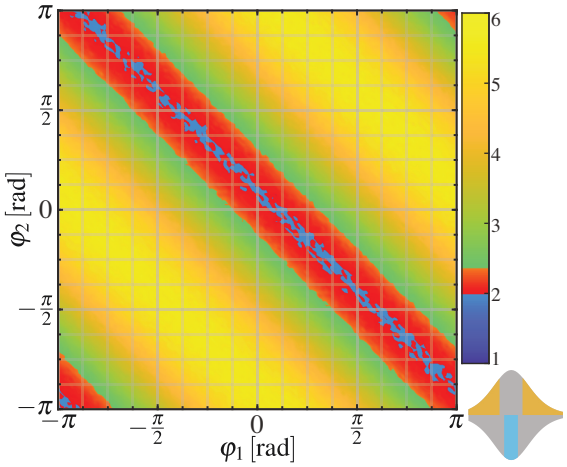

(M.6a) Comparison with Duan limit for [RB] [G] at 0 K

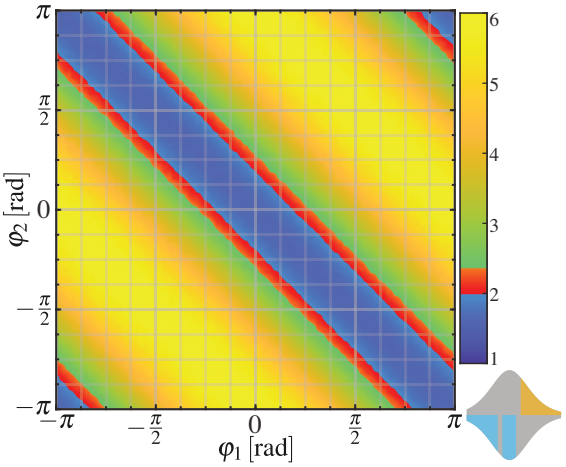

(M.6b) Comparison with Duan limit for [R] [BG] at 0 K

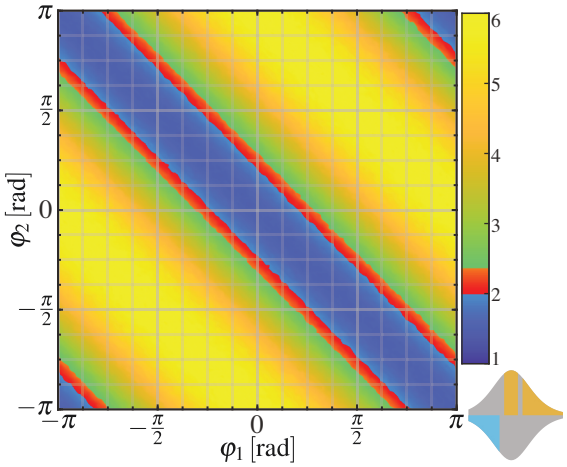

(M.6c) Comparison with Duan limit for [RG] [B] at 0 K

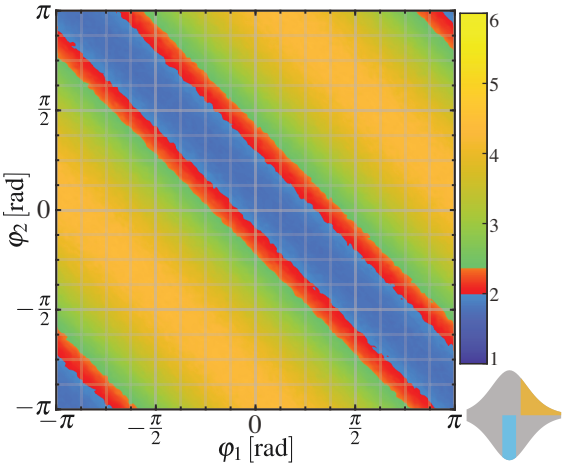

(M.6d) Comparison with Duan limit for[R] [G] at 0 K

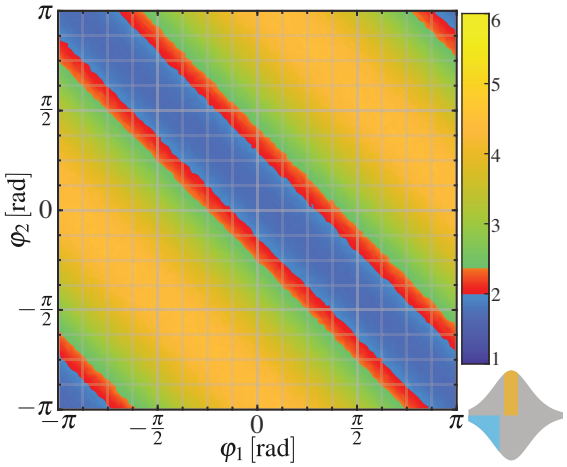

(M.6e) Comparison with Duan limit for [G] [B] at 0 K

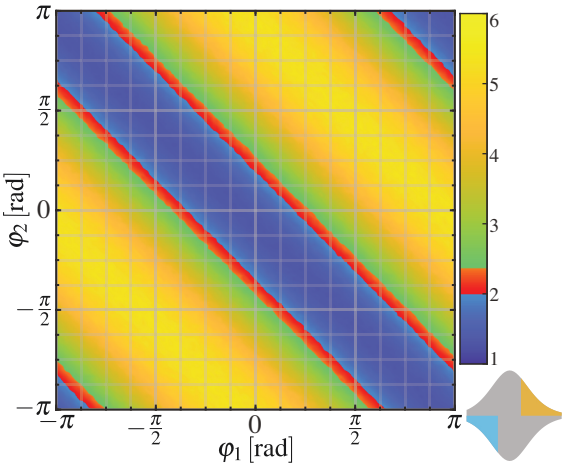

(M.6f) Comparison with Duan limit for [R] [B] at 0 K

Figure M.6 Comparison to the Duan limit for inseparability for simulated data with three modes at 0 K

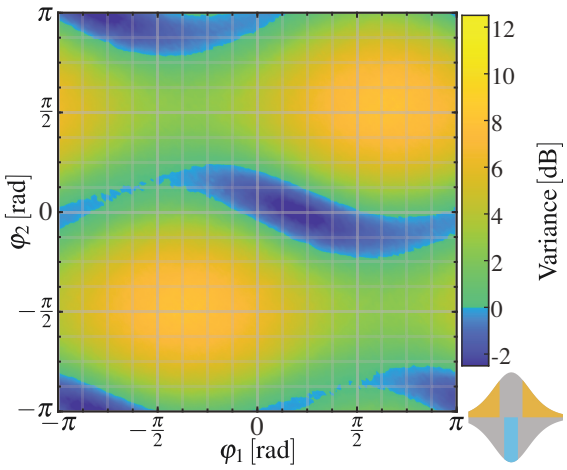

(M.7a) Variances for [RB] [G] at 100 K

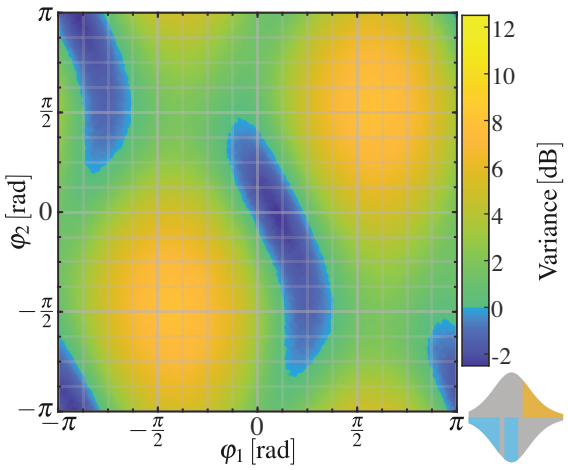

(M.7b) Variances for [R] [BG] at 100 K

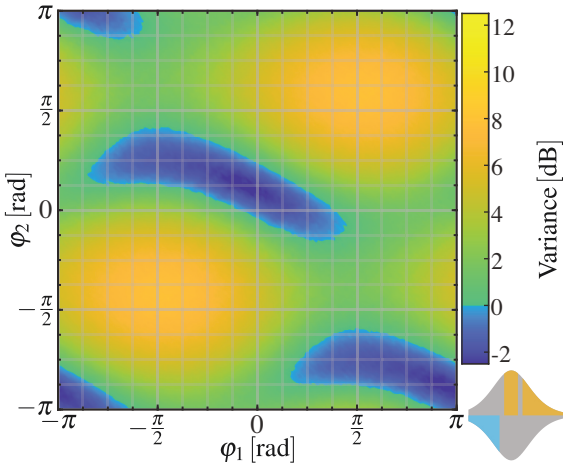

(M.7c) Variances for [RG] [B] at 100 K

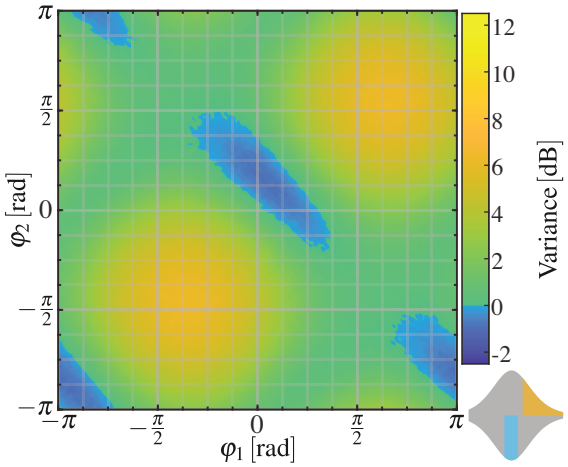

(M.7d) Variances for [R] [G] at 100 K

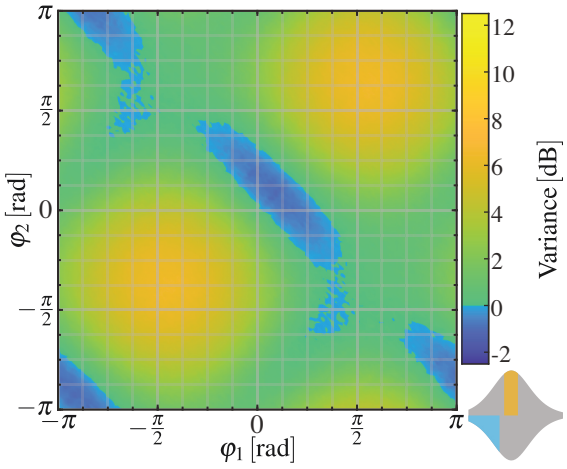

(M.7e) Variances for [G] [B] at 100 K

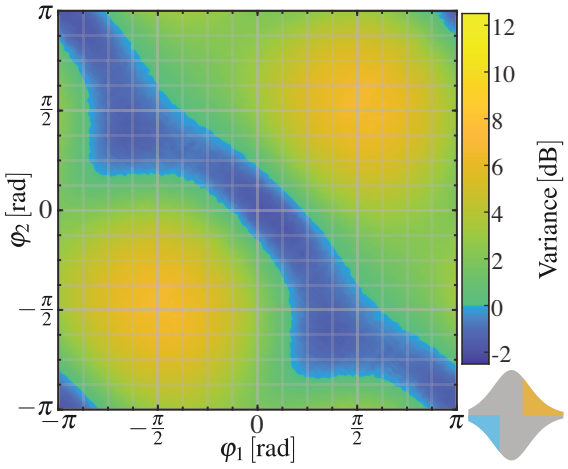

(M.7f) Variances for [R] [B] at 100 K

Figure M.7 Simulated variances for three-mode measurement at 100 K

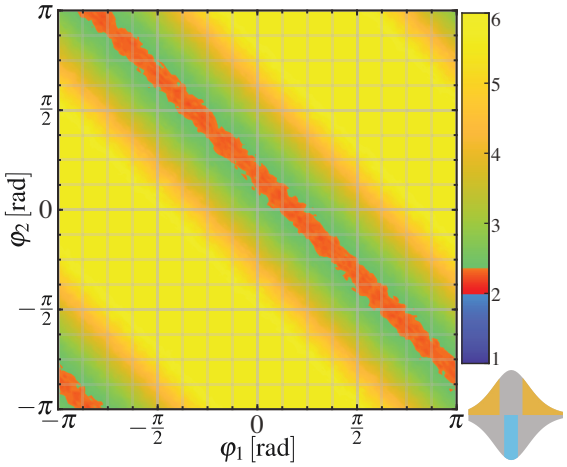

(M.8a) Comparison with Duan limit for [RB] [G] at 100 K

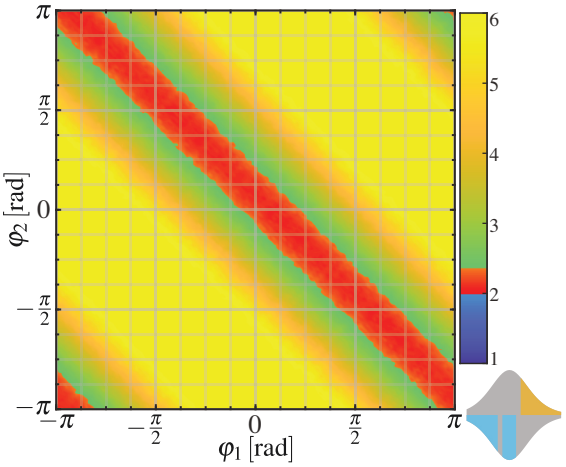

(M.8b) Comparison with Duan limit for [R] [BG] at 100 K

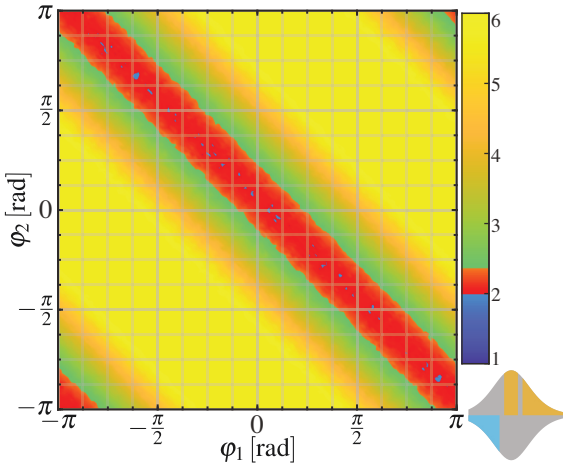

(M.8c) Comparison with Duan limit for [RG] [B] at 100 K

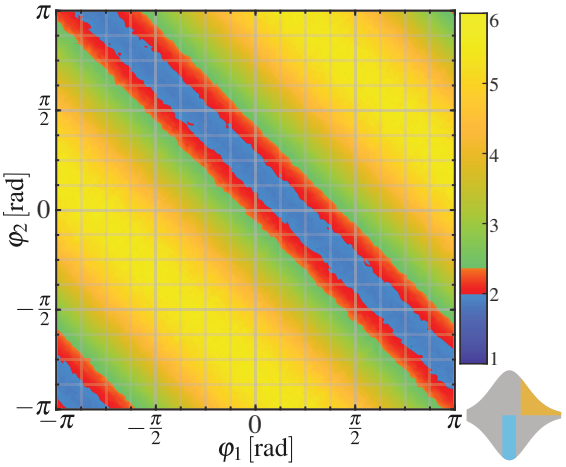

(M.8d) Comparison with Duan limit for [R] [G] at 100 K

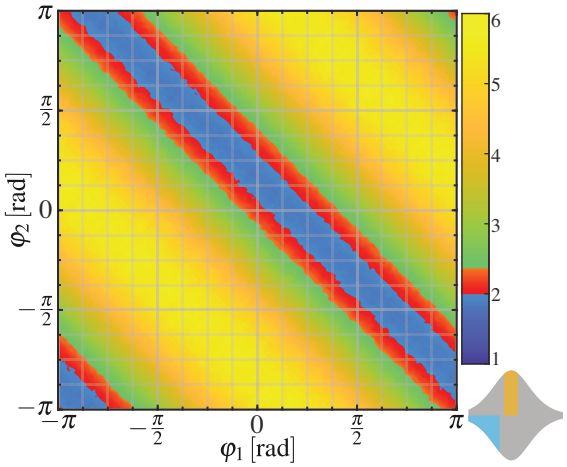

(M.8e) Comparison with Duan limit for [G] [B] at 100 K

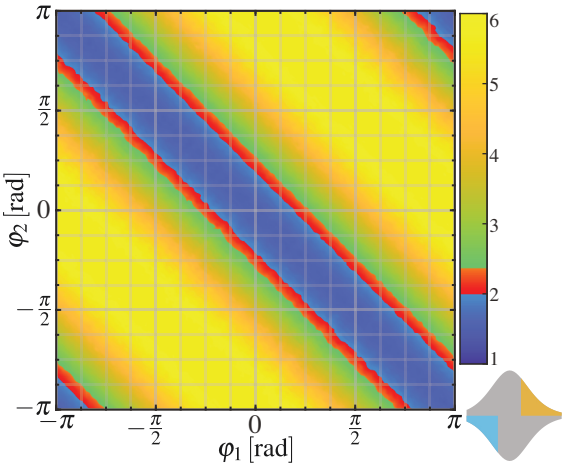

(M.8f) Comparison with Duan limit for [R] [B] at 100 K

Figure M.8 Comparison to the Duan limit for inseparability for simulated data with three modes at 100 K

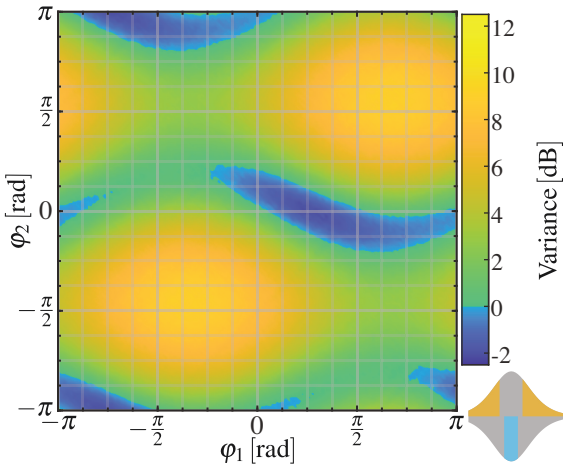

(M.9a) Variances for [RB] [G] at 200 K

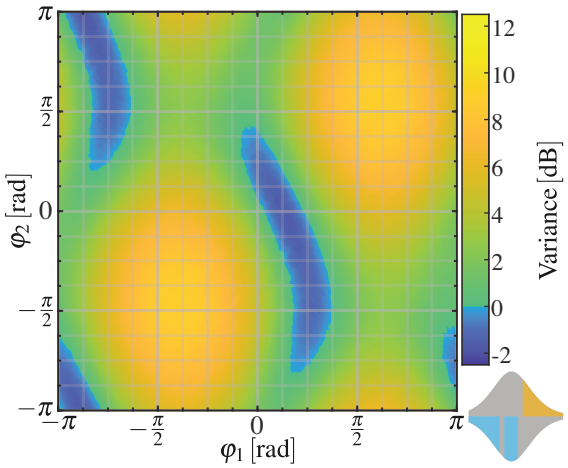

(M.9b) Variances for [R] [BG] at 200 K

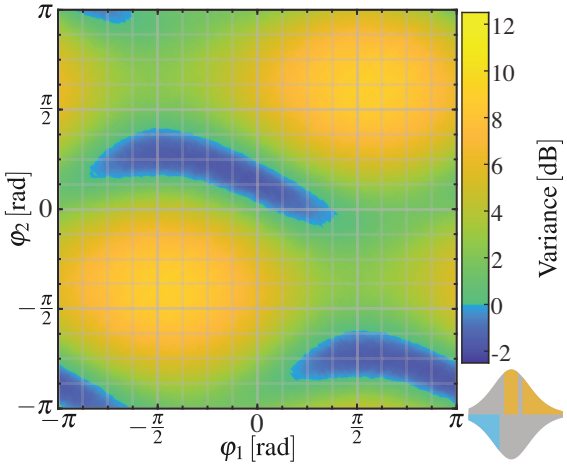

(M.9c) Variances for [RG] [B] at 200 K

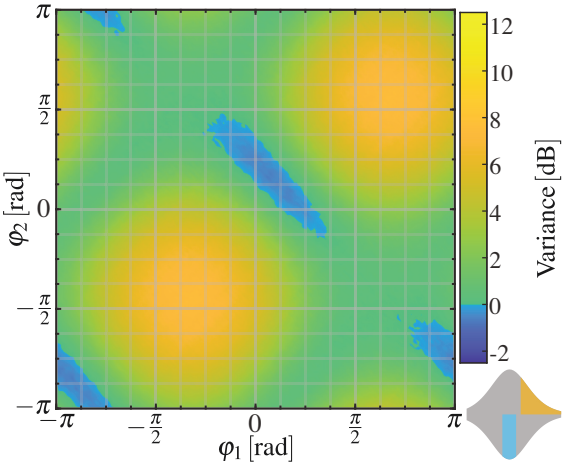

(M.9d) Variances for [R] [G] at 200 K

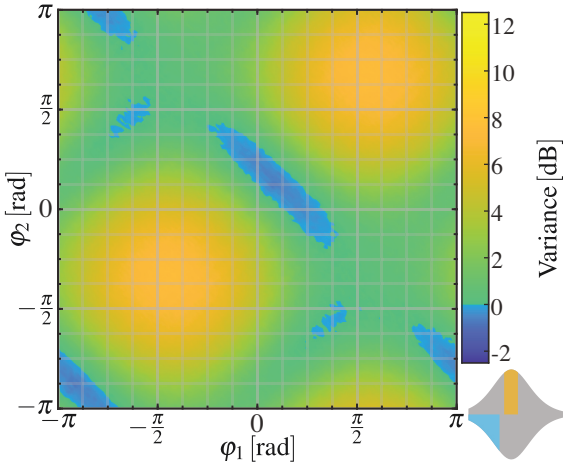

(M.9e) Variances for [G] [B] at 200 K

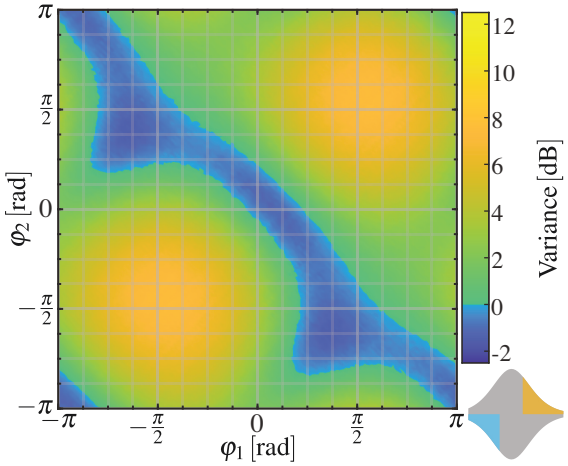

(M.9f) Variances for [R] [B] at 200 K

Figure M.9 Simulated variances for three-mode measurement at 200 K

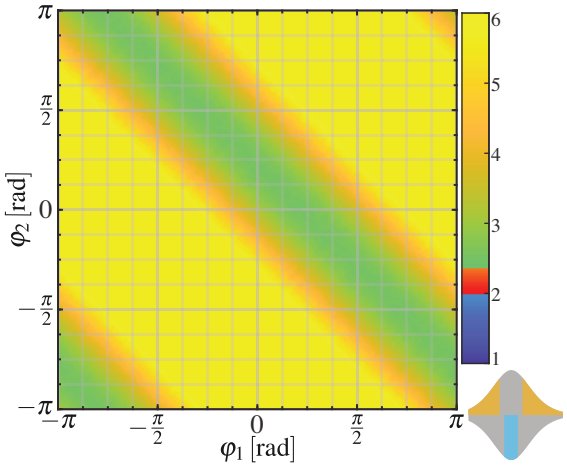

(M.10a) Comparison with Duan limit for [RB] [G] at 200 K

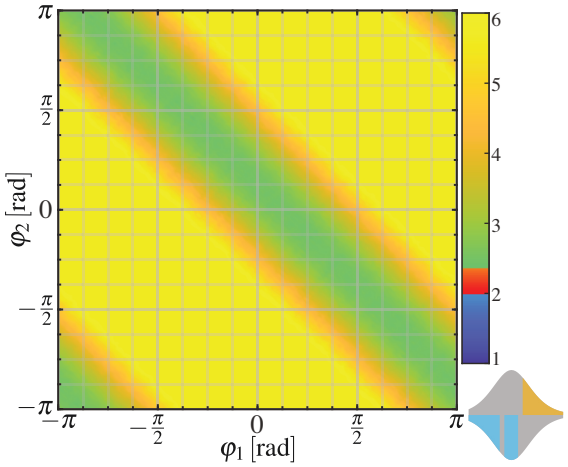

(M.10b) Comparison with Duan limit for [R] [BG] at 200 K

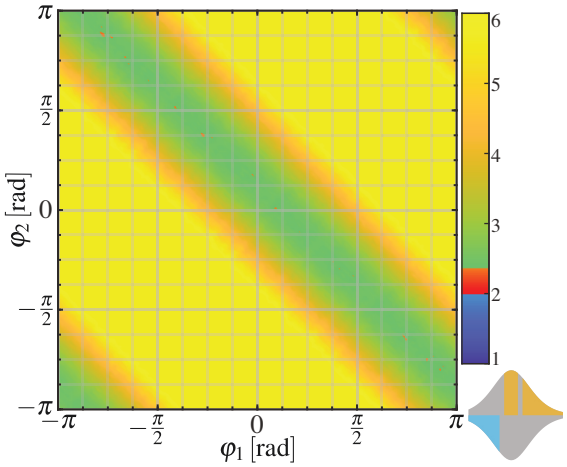

(M.10c) Comparison with Duan limit for [RG] [B] at 200 K

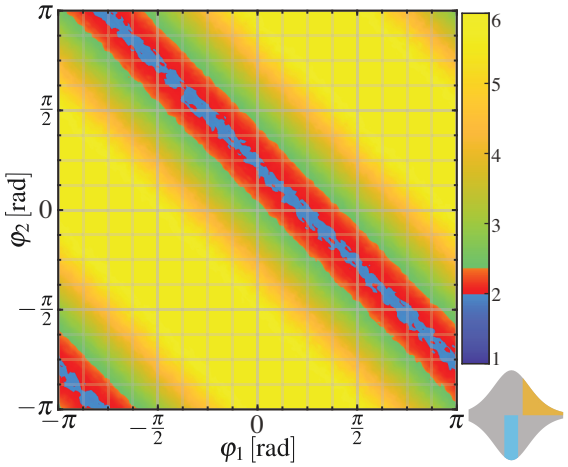

(M.10d) Comparison with Duan limit for[R] [G] at 200 K

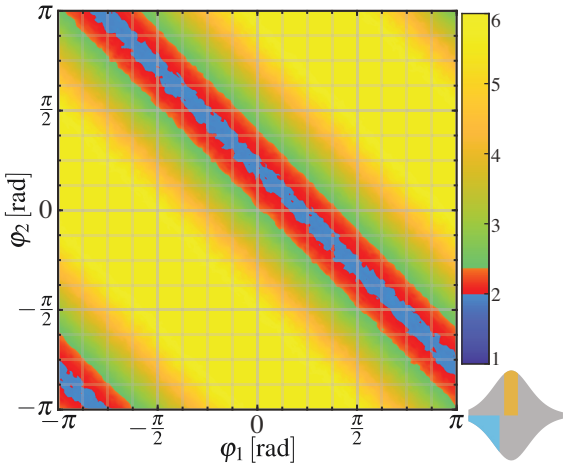

(M.10e) Comparison with Duan limit for [G] [B] at 200 K

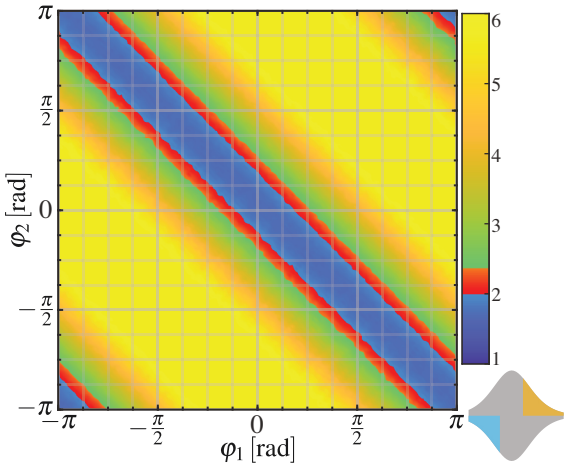

(M.10f) Comparison with Duan limit for [R] [B] at 200 K

Figure M.10 Comparison to the Duan limit for inseparability for simulated data with three modes at 200 K

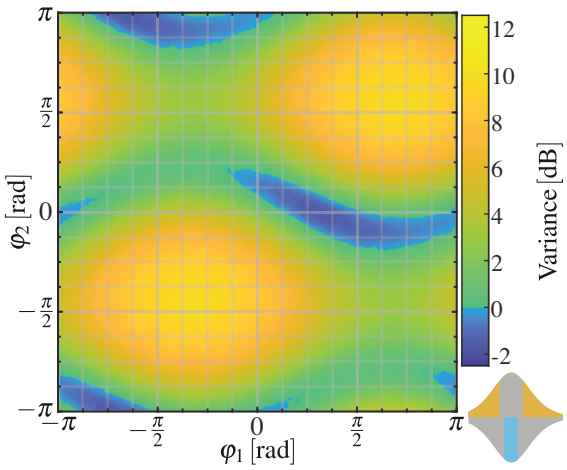

(M.11a) Variances for [RB] [G] at 300 K

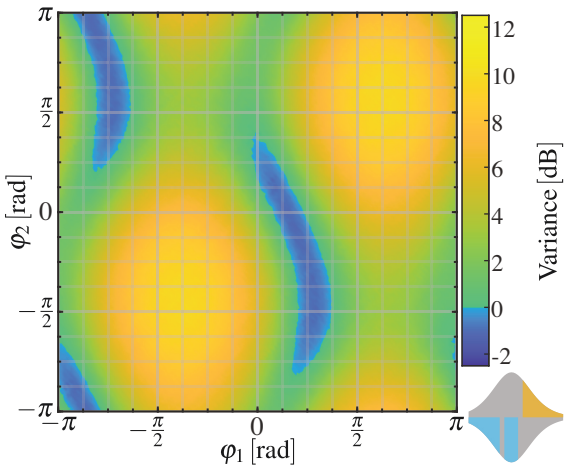

(M.11b) Variances for [R] [BG] at 300 K

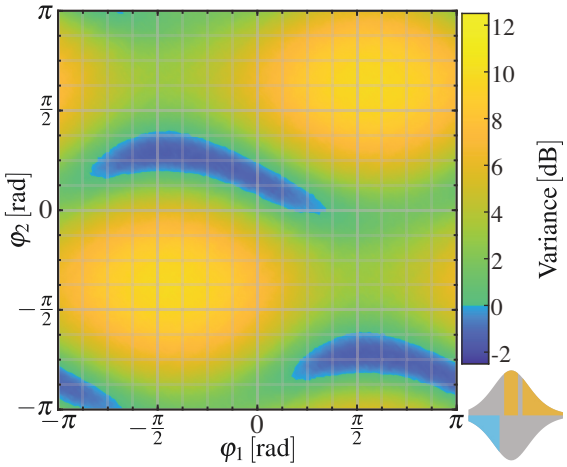

(M.11c) Variances for [RG] [B] at 300 K

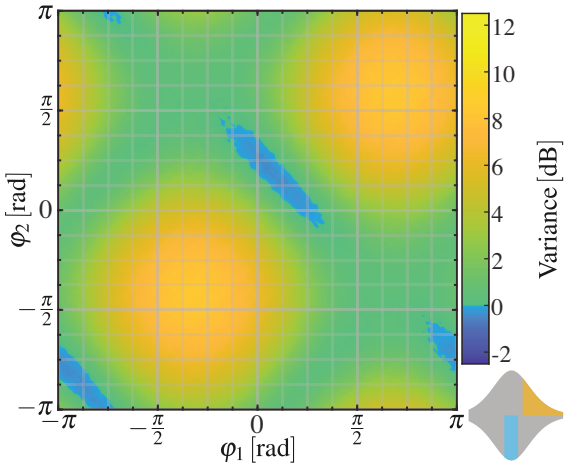

(M.11d) Variances for [R] [G] at 300 K

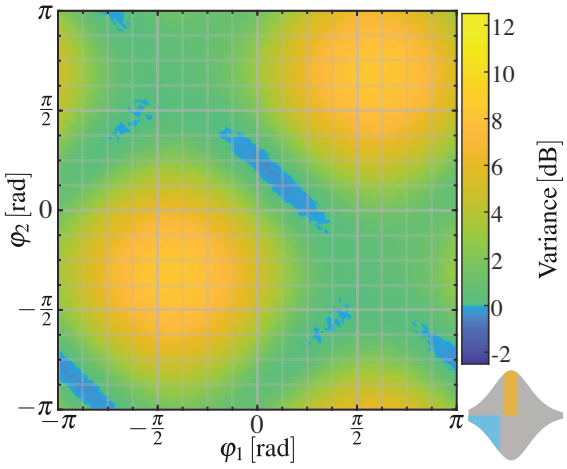

(M.11e) Variances for [G] [B] at 300 K

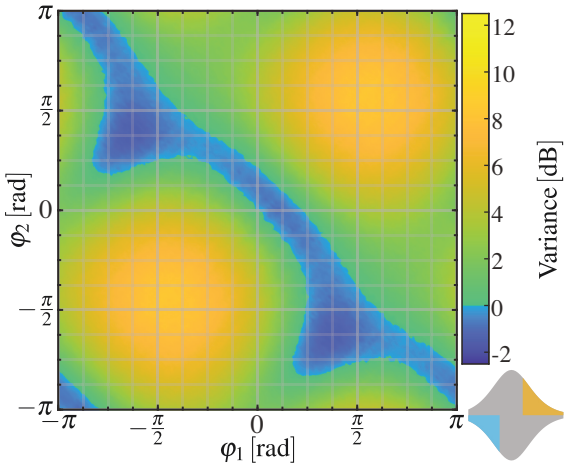

(M.11f) Variances for [R] [B] at 300 K

Figure M.11 Simulated variances for three-mode measurement at 300 K

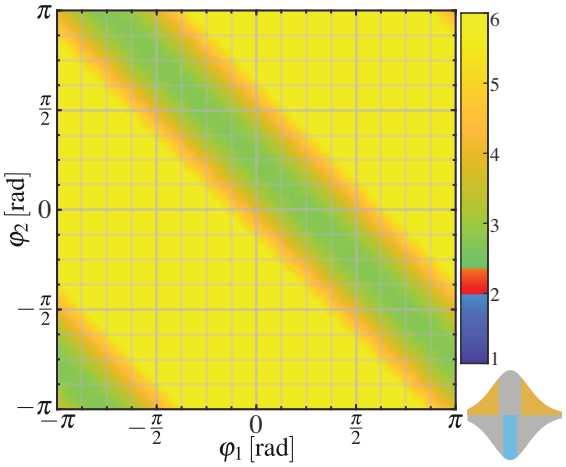

(M.12a) Comparison with Duan limit for [RB] [G] at 300 K

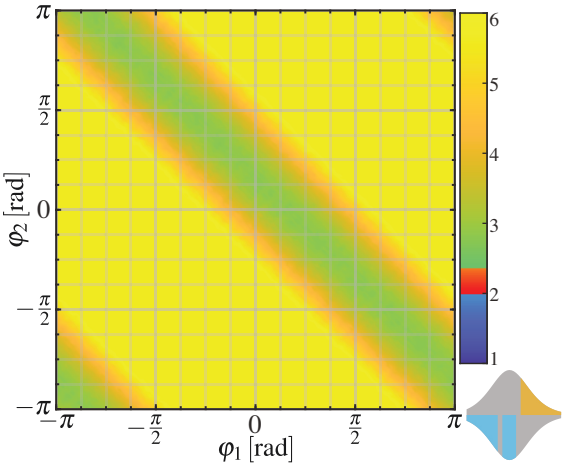

(M.12b) Comparison with Duan limit for [R] [BG] at 300 K

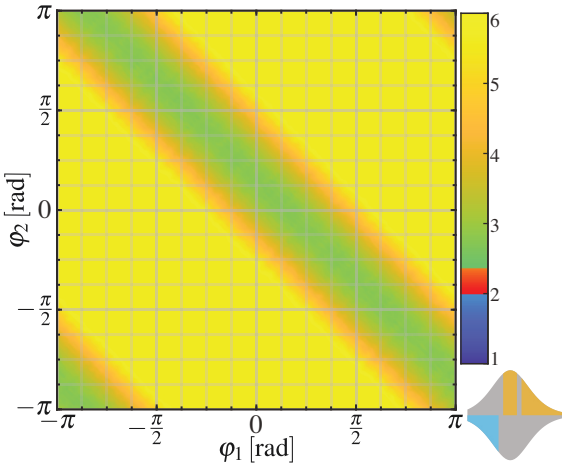

(M.12c) Comparison with Duan limit for [RG] [B] at 300 K

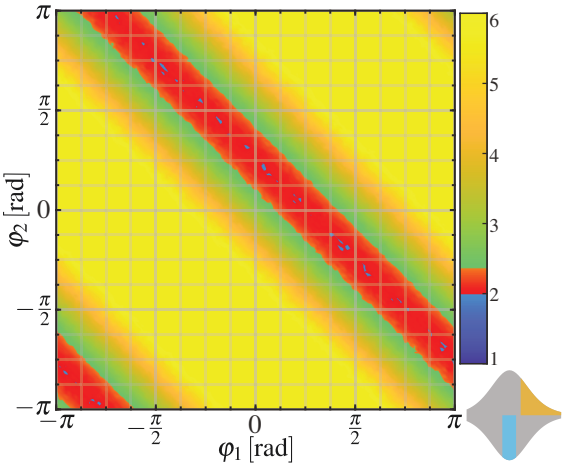

(M.12d) Comparison with Duan limit for[R] [G] at 300 K

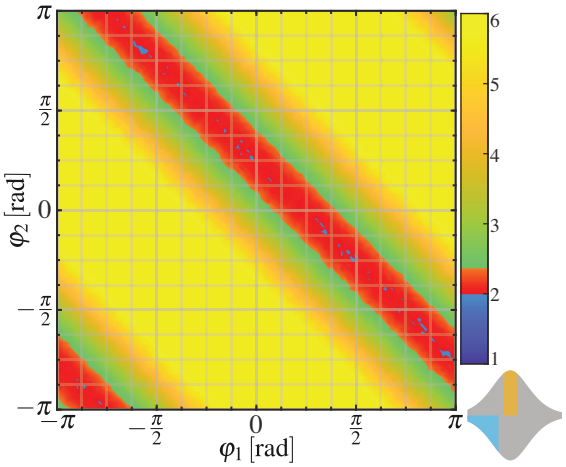

(M.12e) Comparison with Duan limit for [G] [B] at 300 K

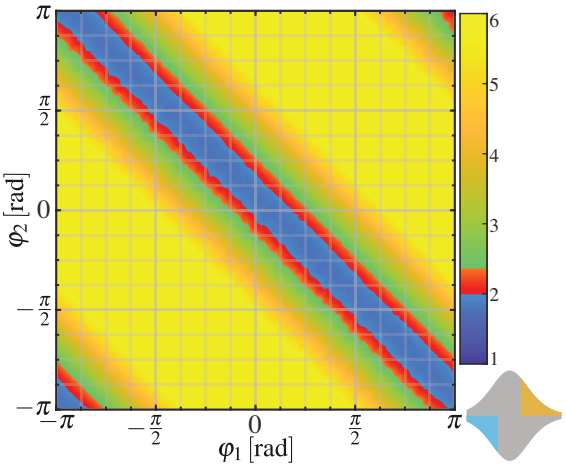

(M.12f) Comparison with Duan limit for [R] [B] at 300 K

Figure M.12 Comparison to the Duan limit for inseparability for simulated data with three modes at 300 K

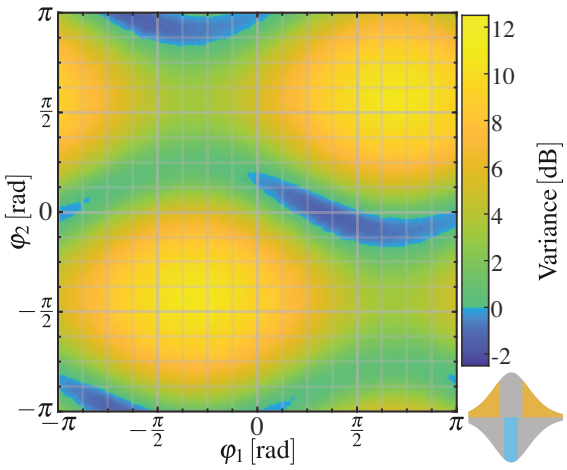

(M.13a) Variances for [RB] [G] at 400 K

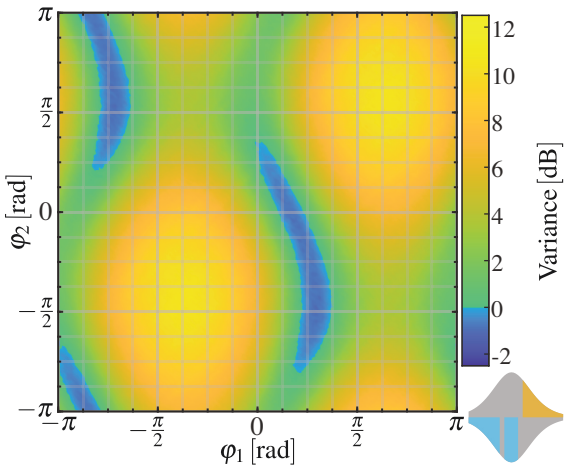

(M.13b) Variances for [R] [BG] at 400 K

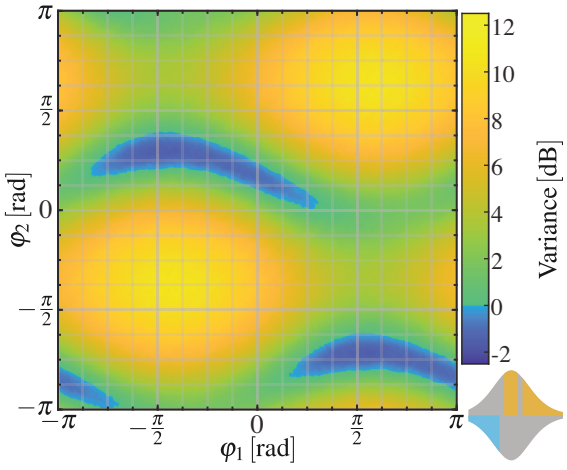

(M.13c) Variances for [RG] [B] at 400 K

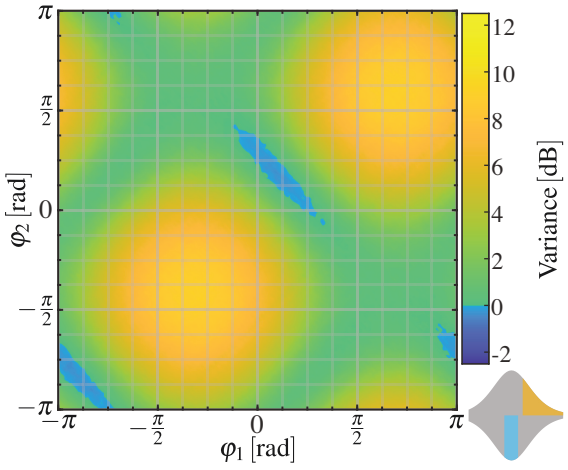

(M.13d) Variances for [R] [G] at 400 K

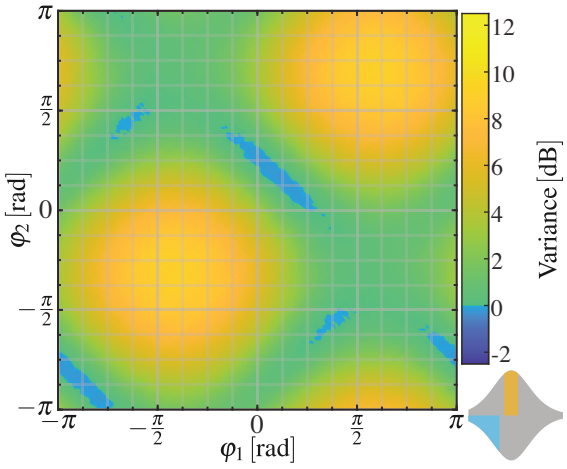

(M.13e) Variances for [G] [B] at 400 K

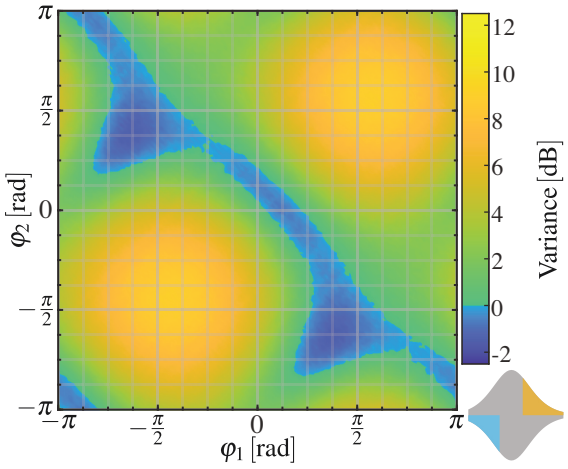

(M.13f) Variances for [R] [B] at 400 K

Figure M.13 Simulated variances for three-mode measurement at 400 K

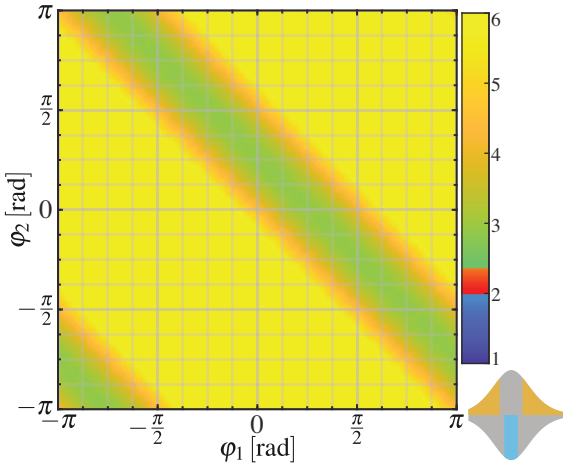

(M.14a) Comparison with Duan limit for [RB] [G] at 400 K

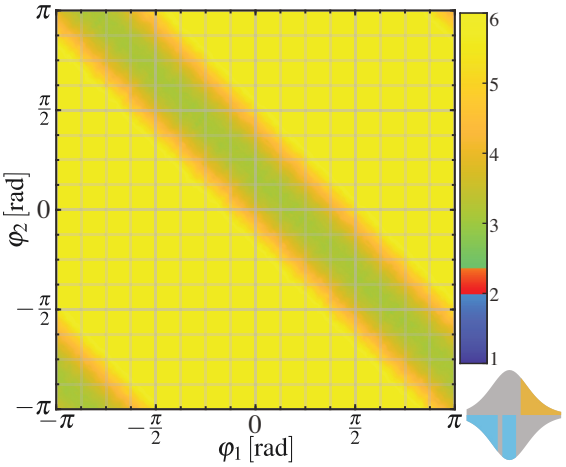

(M.14b) Comparison with Duan limit for [R] [BG] at 400 K

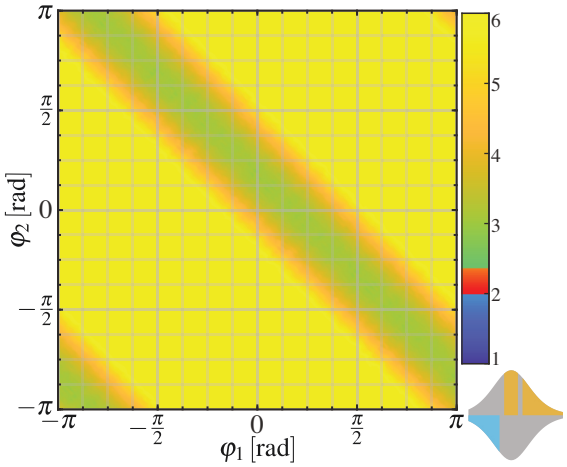

(M.14c) Comparison with Duan limit for [RG] [B] at 400 K

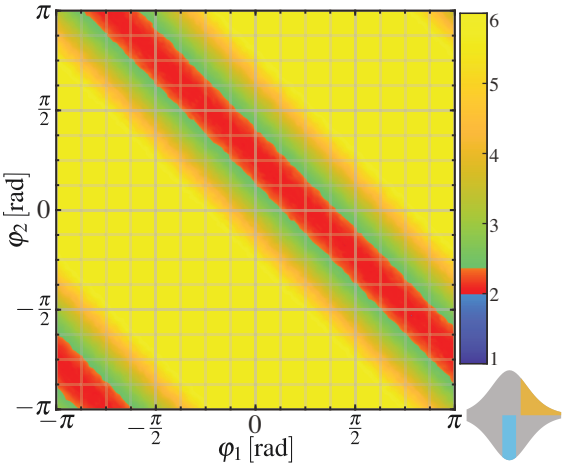

(M.14d) Comparison with Duan limit for[R] [G] at 400 K

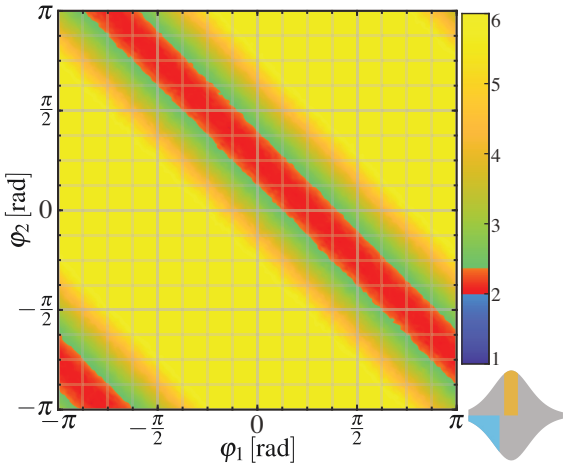

(M.14e) Comparison with Duan limit for [G] [B] at 400 K

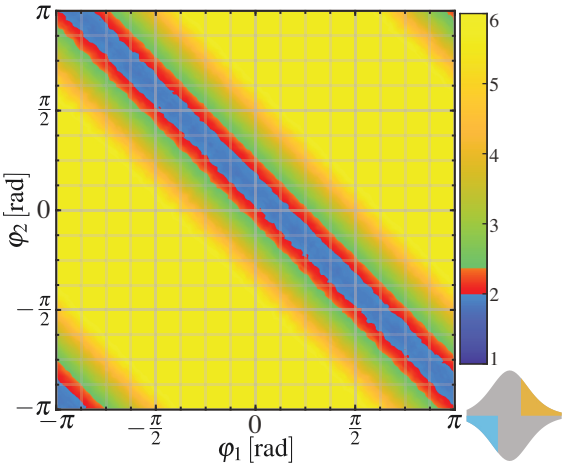

(M.14f) Comparison with Duan limit for [R] [B] at 400 K

Figure M.14 Comparison to the Duan limit for inseparability for simulated data with three modes at 400 K

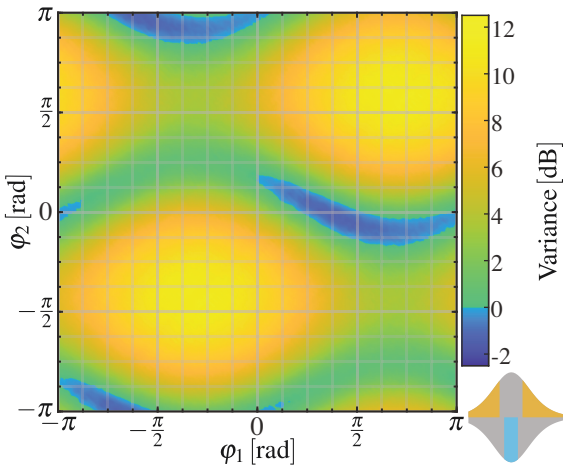

(M.15a) Variances for [RB] [G] at 500 K

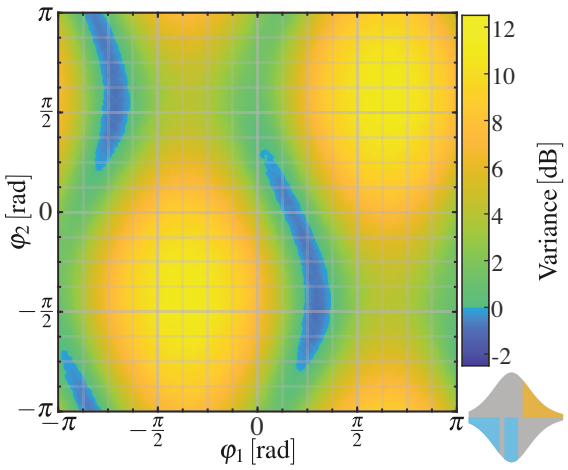

(M.15b) Variances for [R] [BG] at 500 K

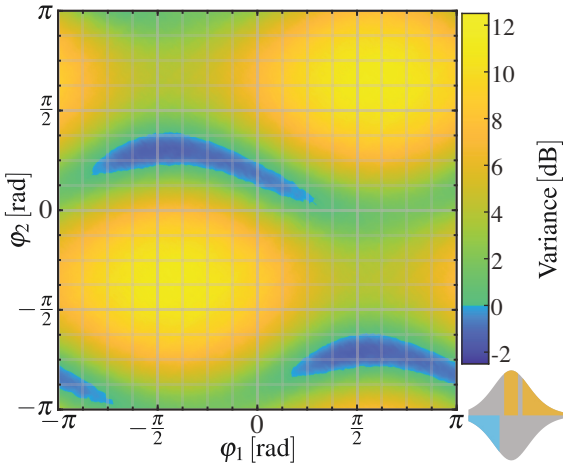

(M.15c) Variances for [RG] [B] at 500 K

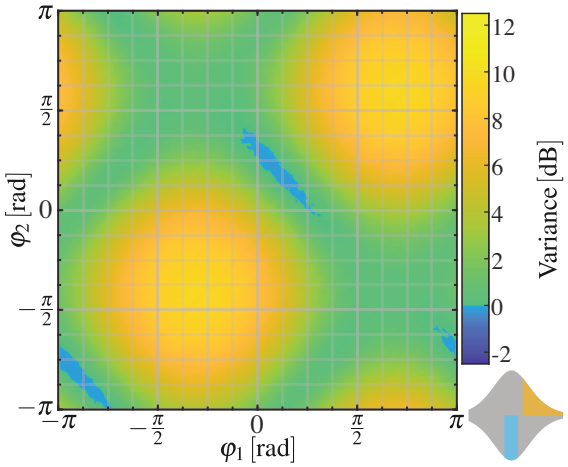

(M.15d) Variances for [R] [G] at 500 K

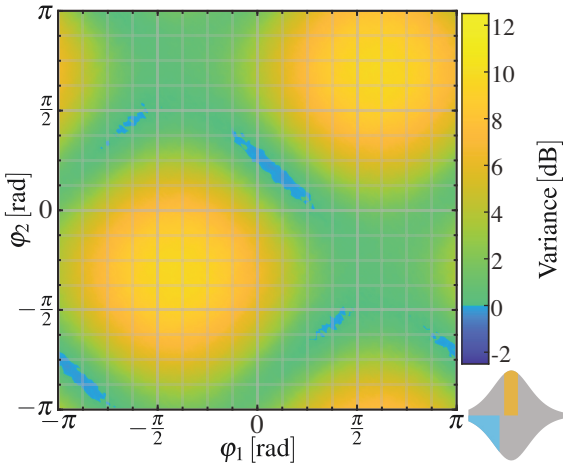

(M.15e) Variances for [G] [B] at 500 K

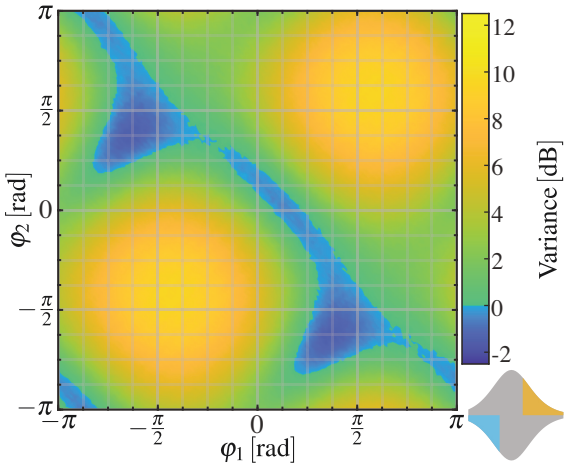

(M.15f) Variances for [R] [B] at 500 K

Figure M.15 Simulated variances for three-mode measurement at 500 K

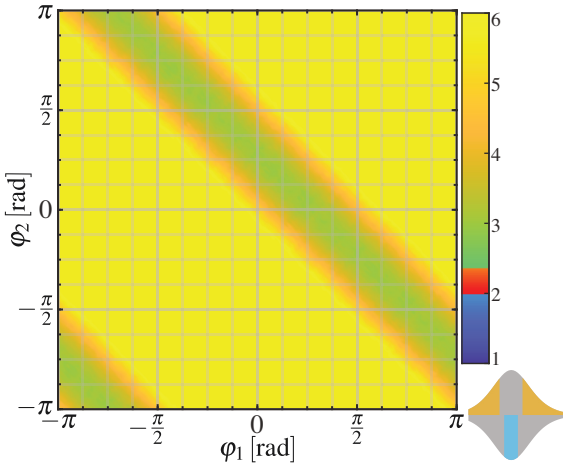

(M.16a) Comparison with Duan limit for [RB] [G] at 500 K

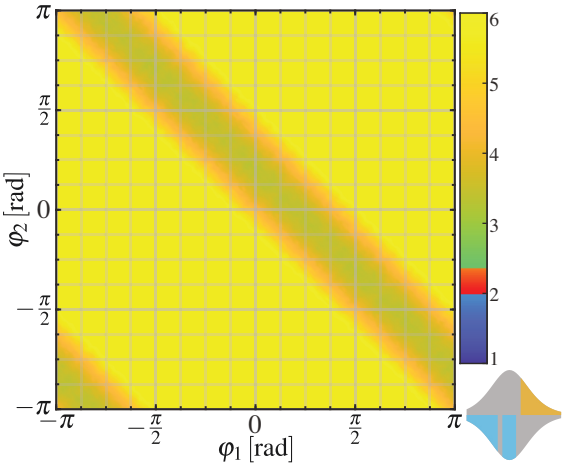

(M.16b) Comparison with Duan limit for [R] [BG] at 500 K

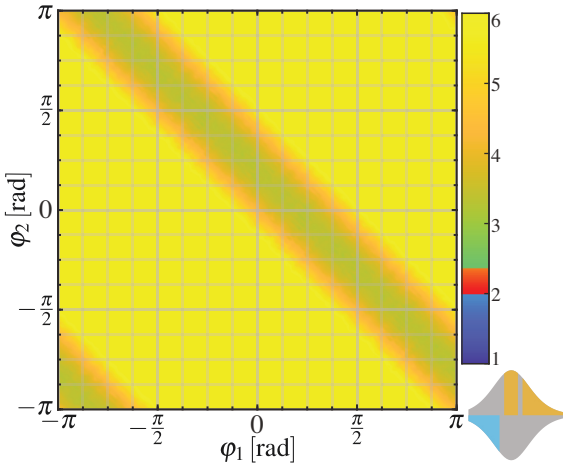

(M.16c) Comparison with Duan limit for [RG] [B] at 500 K

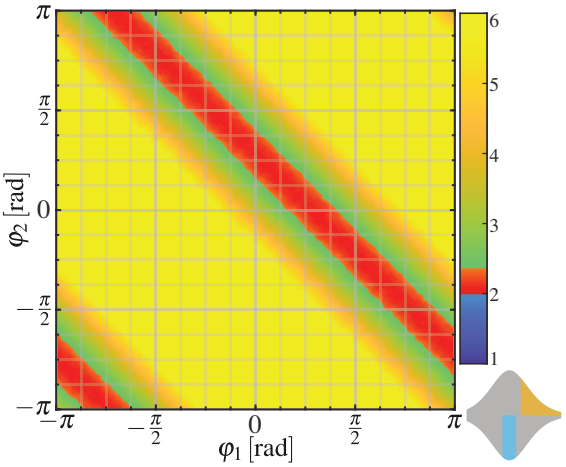

(M.16d) Comparison with Duan limit for[R] [G] at 500 K

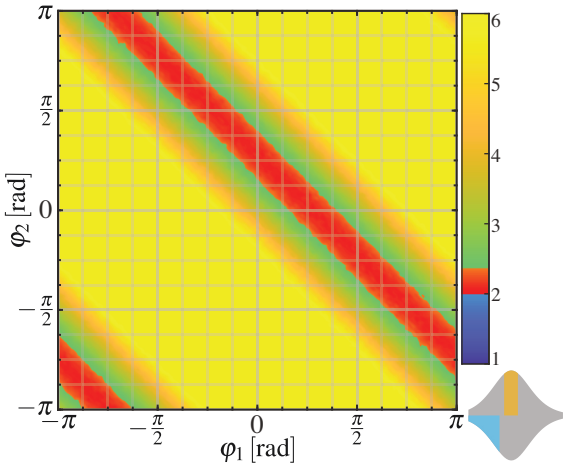

(M.16e) Comparison with Duan limit for [G] [B] at 500 K

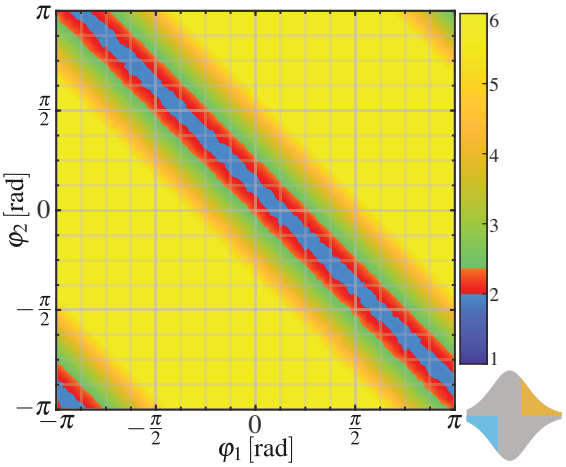

(M.16f) Comparison with Duan limit for [R] [B] at 500 K

Figure M.16 Comparison to the Duan limit for inseparability for simulated data with three modes at 500 K